BLACK HOLE MASS DETERMINATION USING X-RAY DATA

by

Insuk Jang
A Dissertation
Submitted to the
Graduate Faculty
of
George Mason University
In Partial fulfillment of
The Requirements for the Degree
of
Doctor of Philosophy
Physics

Committee:

____________________ Dr. Mario Gliozzi, Dissertation Director

____________________ Dr. Shobita Satyapal, Committee Member

____________________ Dr. Joeseph Weingartner, Committee Member

____________________ Dr. Bijan Jabbari, Committee Member

____________________ Dr. Chi Yang, Interim Director, School of Physics, Astronomy, and Computational Sciences

____________________ Dr. Donna M. Fox, Associate Dean, Office of Student Affairs & Special Programs, College of Science

____________________ Dr. Peggy Agouris, Dean, College of Science

Date: ____________________ Summer 2014
George Mason University
Fairfax, VA

Black Hole Mass Determination Using X-ray Data

A dissertation submitted in partial fulfillment of the requirements for the degree of Doctor of Philosophy at George Mason University

By

Insuk Jang
Master of Science
Pittsburg State University, Kansas, 2008
Bachelor of Art
University of Hawaii at Manoa, 2006

Director: Dr. Mario Gliozzi, Research Assistant Professor
School of Physics, Astronomy, and Computational Science

Summer 2014
George Mason University
Fairfax, VA

Dedication

For my parents, Dr. Yong Kook Chang and Kyung Hee Park

Acknowledgments

Black holes were very interesting and fascinating things to me since I was young but never saw myself becoming an astronomer when I grow up. My astronomer dream started from when I was working on the semester project about active galactic nuclei in my first time astrophysics class in life when I was at Pittsburg State University in Kansas.

Until the stage of accomplishing my dream, there are many people to thank. I would like to thank my thesis advisor Dr. Mario Gliozzi. Without him, this dissertation completion would not have been possible. His office door was always open for me and he always patiently waited and guided me through until today. From him, I had a great opportunity to learn and be into X-ray astrophysics world of black holes. I would also like to thank my master advisor back in Pittsburg, Dr. David Kuehn, who introduced this fascinating astrophysics field and influenced my teaching philosophies when I was teaching labs in PSU and also in GMU.

Along with great professors in my academic career, I also like to thank Rev. Joseph and Eunice No for always being there for me, treating me like a family member, and lots of prayers. I would also like to mention one of my good friends, my best buddy Kyung Ho Moon since high school years who always cheered and always being there for me whenever I was over stressed. I see myself a very lucky person to have such wonderful parents and sisters. Their unlimited support and love always fulfilled, stimulated and kept me concentrating in studies. I also like to thank my lovely wife, Hyejin Yoo, who believed in me and patiently waited with our son, Wookjin Jang, in New Jersey until this time comes.

Lastly, I thank God for providing me opportunities with great people in my life.

Table of Contents

List of Tables

List of Figures

Abstract

BLACK HOLE MASS DETERMINATION USING X-RAY DATA

Insuk Jang, PhD

George Mason University, 2014

Dissertation Director: Dr. Mario Gliozzi

Supermassive black holes are located at the center of basically every galaxy and their mass appears to be tightly correlated with several galaxy properties, suggesting that black hole and galaxy growths are linked together. Determining the mass of black holes provides crucial information on the galaxy evolution and indeed significant progress has been achieved thanks to optically-based methods. However, since these methods are limited by several factors including absorption and galaxy contamination, it is important to develop and test alternative methods that use different energy bands to constrain the black hole mass. In a recent work we demonstrated that a novel X-ray scaling method, originally introduced for stellar mass black holes, can be reliably extended to estimate the mass of highly-accreting supermassive black holes. Here we investigate the limits of applicability of this method to low-accreting black holes, using a control sample of low-luminosity active galactic nuclei with good-quality X-ray data and with dynamically measured black hole masses. We find the threshold value of the accretion rate for which the X-ray scaling method can still be used. Below this threshold, we provide a simple recipe to constrain the black hole mass based on the inverse correlation between X-ray spectral properties and accretion rate, which was found in several low-accreting black holes and confirmed by our sample.

Then, we extend the X-ray scaling method to ultraluminous X-ray sources (ULXs), which are off-nuclear, point-like X-ray sources, whose nature is still debated. Their high X-ray brightness can be equally well explained by stellar mass black holes accreting at extreme rates or by intermediate mass black holes accreting at regular rates, therefore, constraining their mass may shed light on one of the outstanding questions of high energy astrophysics. Currently, no direct optically-based methods can dynamically determine the mass of ULXs, making X-ray methods the only viable option. In this work, we systematically applied the X-ray scaling method to a sample of ULXs with multiple high-quality X-ray observations. This allows us to reconstruct the spectral evolution of ULXs and directly compare it with the spectral trend of stellar mass black holes used as reference sources in the X-ray scaling method. We found that the vast majority of the ULX spectral trends are consistent with those of highly-accreting stellar black holes, suggesting that ULXs are not characterized by exotic spectral states. The black hole masses determined with this scaling technique are in agreement with values obtained from different methods and confirm the existence of some intermediate mass black holes, which may play a crucial role in the formation of the seeds for supermassive black holes. However, the vast majority of the ULX masses appear to be consistent with the hypothesis of massive stellar black holes accreting at very high rate. Our findings highlight the importance of the X-ray scaling method as a robust, scale-independent technique that can be used to constrain the black hole mass from stellar systems up to supermassive black holes at the center of all galaxies.

Chapter 1: Introduction

1.1 Definition of Black Holes

A black hole (BH), by the definition, is a region of spacetime where gravity is so strong that nothing (not even light) can escape and is surrounded by an imaginary surface called "event horizon" beyond which no events can be seen by the outside observer. From the physical point of view, BHs can be considered as giant elementary particles, since they are fully characterized by three parameters: mass, spin, and charge.

The idea of dark star – the escape velocities in excess of the speed of light - was originally suggested by J. Michell and P. S. Laplace in the 18th century. Then the modern theoretical concept of BH grew with Einstein's general relativity theory in 1916. In the same year, Schwarzschild solved Einstein's field equations for a non-spinning black hole (Schwarzschild BH): the escape velocity equals the speed of light (definition of event horizon) at the radius of $R_{\rm S} = 2R_{\rm G} = 2GM_{\rm BH}/c^2$ where $R_{\rm S}$ is the Schwarzschild radius, $R_{\rm G}$ is the gravitational radius, and $M_{\rm BH}$ is the mass of the black hole. Later, in 1963, Kerr solved Einstein's field equations for a spinning BH (Kerr BH; Kerr 1963). Since by definition a BH is isolated from the Universe by its event horizon, we can only infer its presence from the effects of its exceptionally strong gravitational field on its surroundings.

1.1.1 Classification

Over the last 40 years observational studies of BHs at all wavelengths have led to substantial progress in our understanding of these compact objects. Currently, the accepted categories of astrophysical BHs are stellar mass black holes (sMBHs), supermassive black holes (SMBHs), and possibly intermediate mass black holes (IMBHs), which may fill the gap between the first two classes of BHs.

Stellar Mass Black Holes – The simplest way to describe a sMBH is that it is a remnant compact object at the end of massive star's life. Other compact objects are white dwarfs (WDs) and neutron stars (NSs). They are distinguished from normal stars in two ways: 1) they can not support themselves against gravitational collapse by generating thermal pressure and 2) they are exceedingly small for their mass, which yields strong gravitational fields at their surfaces. WDs and NSs are supported by degenerate electron pressure and by degenerate neutron pressure, respectively. BHs are collapsed stars that have no means to hold back the gravitational pull and therefore, they collapse to singularities. If the mass of the original star is relatively small ($M \leq 4\,M_{\odot}$) then it becomes a WD with mass of $\lesssim 1.3\,M_{\odot}$. If the mass exceeds $4\,M_{\odot}$ during the collapse, then a supernova explosion occurs, producing either a NS in a mass range of $1.3 - 3\,M_{\odot}$ or a sMBH at $3 - 20\,M_{\odot}$. Based on stellar population studies, several thousands BHs are expected to reside in our Galaxy, however, only those that are part of X-ray binary systems (XRBs) are easily detected and have been studied for decades. The general structure of XRB consists of a BH surrounded by an accretion disk/corona with a companion star that feeds the accretion disk. There are about 20-30 Galactic BH systems (GBHs) whose properties have been investigated in detail.

Supermassive Black Holes – SMBHs have a mass range of $10^6 - 10^9\,M_{\odot}$ and are found at the center of galaxies; when they are active, these central regions are called active galactic nuclei (AGNs). AGNs are believed to have a similar central structure (an accretion disk/corona) as XRBs with gas accreted from the central region of the galaxy. Based on spectral and temporal properties, AGNs can be considered large-scale analogs of GBHs (e.g., Falcke et al., 2004; Körding et al., 2006; McHardy et al., 2006; Merloni et al., 2003; Sobolewska et al., 2009). The formation of SMBHs is not clearly understood and the origin of seed BHs is currently debated. The main competing scenarios are: direct collapse of large primordial gas clouds, BH formation form large Population III stars, and merging of sMBHs in compact star clusters (e.g., Volonteri et al., 2003a,b).

Intermediate Mass Black Holes – Unlike sMBHs and SMBHs whose existence is now widely accepted, the very existence and the incidence of IMBHs is still debated; their expected mass is in the range of $M_{\rm BH} = 10^2 - 10^4\, M_\odot$ (Miller and Hamilton, 2002). They are believed to reside at the center of globular clusters and in ultraluminous X-ray sources (ULXs). ULXs are off-nuclear sources (i.e., bright X-ray sources that are not located at the center of the galaxy) whose X-ray emission exceeds the Eddington limit for a 10 $M_\odot$ BH ($L_{\rm x} \geq 10^{39}$ erg s^{-1}). The formation of IMBHs is not well understood but it is hypothesized that they originate from primordial black holes in the early universe (Kawaguchi et al., 2008) or by the merging process of sMBHs in sufficiently dense environments. IMBHs may provide a natural way to produce seed SMBHs (Ebisuzaki et al., 2001; Tanaka and Haiman, 2009; Volonteri et al., 2003a).

1.2 X-ray Perspective

The study of BHs in X-rays provides one of the most effective ways to shed light on their nature for the following reasons. First, the X-rays are produced and reprocessed in the innermost, hottest nuclear regions of the source. Therefore, unlike the optical lines that are produced by the reprocessing of the primary emission, the X-ray emission can directly trace the activity of BHs. Second, in BH systems, the X-ray emission appears to be ubiquitous and the penetrating power of (hard) X-rays allows them to carry information from the inner core regions without being substantially affected by absorption.

1.2.1 X-ray Astronomy

X-ray astronomy is the branch of astronomy that studies the X-ray emission from astronomical objects that generally contain extremely hot gas with temperatures ranging from several 10^6 K to 10^{10} K. Due to Earth's atmospheric absorption, X-ray observations need to be performed by instruments in space. The first observations go back to 1912, when Victor Hess (1883-1964) sent a balloon to measure the ionization of atmosphere and opened up the frontier of high-energy astrophysics discovering that some radiation can penetrate the upper layers of the atmosphere. Although the X-ray emission from the Sun was already observed 1949 by Herbert Friedman (1916-2000), the X-ray astronomy actively started in 1962 when the first cosmic X-ray source "Scorpius X-1" was observed by Riccardo Giacconi. The research in high-energy astrophysics became very active from 1970s until today to study binary systems, pulsars, galaxies, and black holes. Several X-ray satellites yield a wealth of information starting from the first X-ray all sky survey performed by the Röntgen Satellite (*ROSAT*) from 1990 to 1999, continuing with detailed spectral studies performed by the Japanese Advanced Satellite for Cosmology and Astrophysics (*ASCA*) and the Italian-Dutch satellite Beppo Satellite per Astronomia X (*BeppoSAX*) with its broadband coverage, and timing variability studies afforded by the Rossi X-ray Timing Explorer (*RXTE*). The current new generation of X-ray satellites comprises *Chandra*, *XMM−Newton*, *Suzaku*, *Swift*, and *NuStar*.

1.2.2 *XMM−Newton* and *Chandra* Satellites

In my thesis work I have utilized data from *Chandra* and *XMM−Newton*. In the following I will describe the main characteristics of these satellites. The image of both satellites is shown in Figure 1.1 with *XMM−Newton* at the top and *Chandra* at the bottom.

The X-ray Multi-Mirror Mission−Newton[1] (*XMM−Newton*) was launched on December 10, 1999 by the European Space Agency (ESA) with an eccentric elliptical orbit − its apogee is nearly 111,4000 km from Earth and the perigee of 7,000 km − with an orbital period of 48 hours. *XMM−Newton* has three aligned X-ray telescopes and one optical/UV telescope. It operates three different types of detectors: 1) three European Photon Imaging Cameras (EPIC) with a focal length of 7.5 m, 2) two reflection grating spectrometers (RGS) with the sensitivity below ~ 2 keV, and 3) a 30 cm diameter Ritchey-Chretien optical/UV telescope. There are two types of EPIC cameras: two MOS arrays of 7 CCDs and one pn consisting of 12 CCDs. The configuration of MOS and pn CCD arrays is shown in Figure 1.2. Each

[1] http://xmm.esac.esa.int

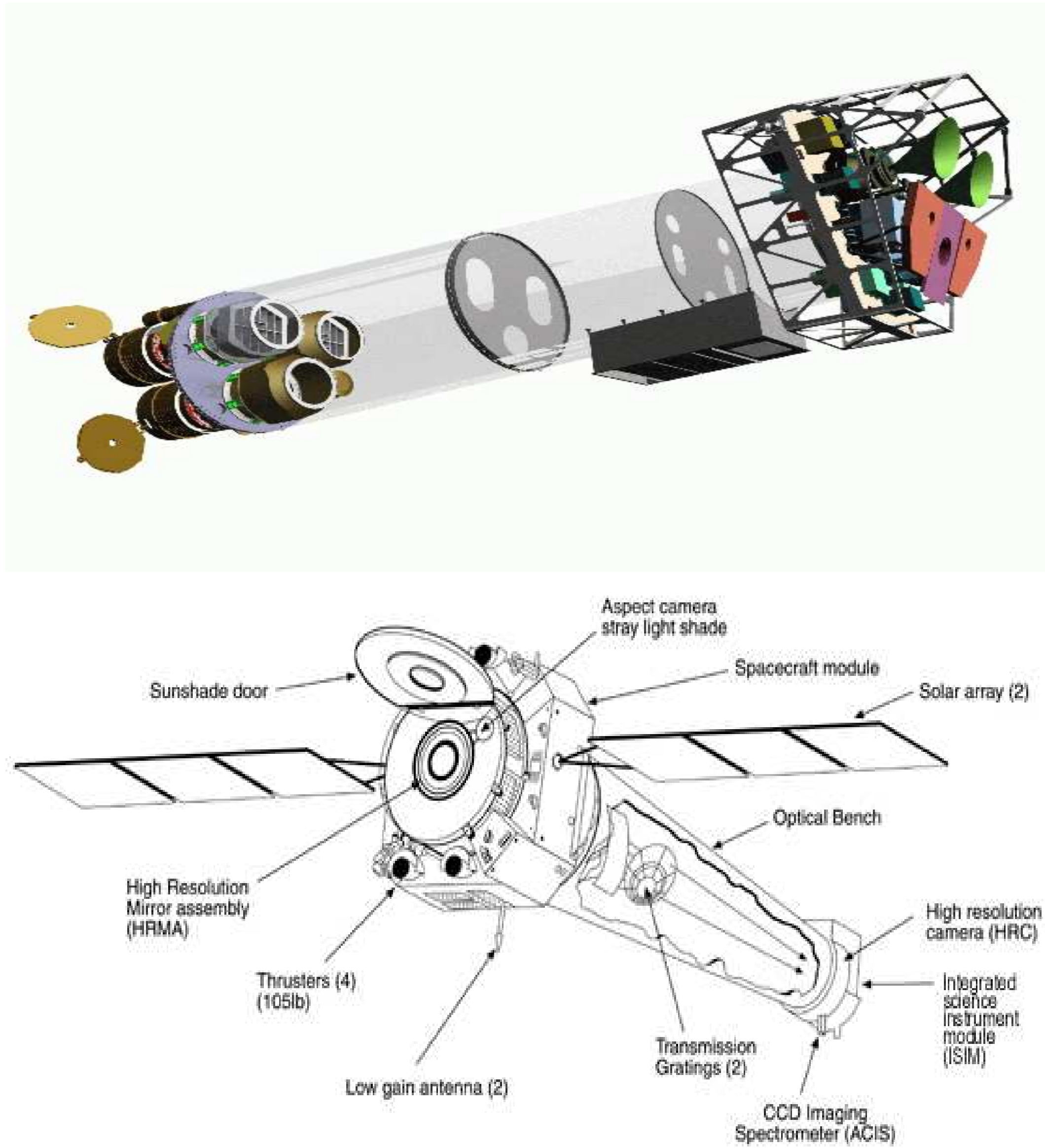

Figure 1.1: Images of the X-ray Satellites *XMM−Newton* and *Chandra*. The images are taken from the user's hand book for each satellite.

detector covers a nominal energy range of $0.15-12$ keV with the total collecting area of 4300 cm^2 (each with 1400 cm^2), with ~ 6 arcsecond full width half maximum (FWHM) spatial resolution across the ~ 30 arcminute field of view. The most important characteristic of

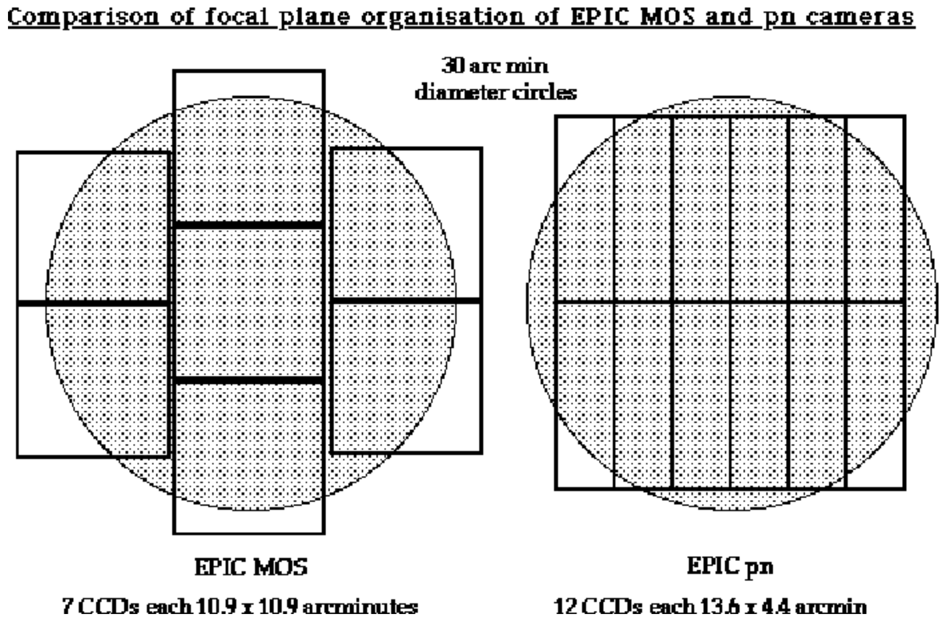

Figure 1.2: *XMM−Newton* EPIC CCD array. The diagram 7 CCD arrays of MOS camera is on the left hand panel and the consists of 12 CCDs for pn on the right hand panel. Each EPIC has 30' field of view. The diagram is taken from *XMM−Newton* user book.

XMM−Newton is its high sensitivity due to the large collecting area and to the fact that all instruments operate simultaneously. This makes it possible to combine the spectra (and light curves) from the different EPIC cameras and hence improve the photon statistics and reducing the signal-to-noise ratio.

The Chandra X-ray Observatory[2] (*Chandra*) was launched on July 23, 1999 by NASA. It orbits Earth in 64.2 hours with an apogee of 133,000 km and a perigee of 16,000 km. The *Chandra* satellite holds two focal plane instruments − the Advanced CCD Imaging Spectrometer (ACIS) and the High Resolution Camera (HRC), and two High Resolution Spectrometers: the High Energy Transmission Grating Spectrometer (HETGS) and the Low Energy Transmission Grating Spectrometer (LETGS). The instruments do not operate simultaneously. The instrument mainly used for our study was ACIS (shown in Figure 1.3)

[2]http://cxc.harvard.edu/ciao4.4/manuals.html

which consists of 10 CCD chips (each chip with a dimension of 8.3 arcminute) providing images and spectral information of objects in the energy range of $0.1-10$ keV. The ACIS-I array, mostly used for imaging purposes, contains four CCDs in a 2×2 arrangement, whereas the ACIS-S array consists of six CCDs in a line arrangement which is also used as a read-out array for the HETG (0.4-10 keV) or LETG (0.1-3 keV). The main advantage of *Chandra* is its unsurpassed sub-arcsecond spatial resolution, which allows one to disentangle the X-ray contribution of the numerous components present in the central region of a galaxy (active galactic nucleus, off-nuclear sources, extended emission from hot gas).

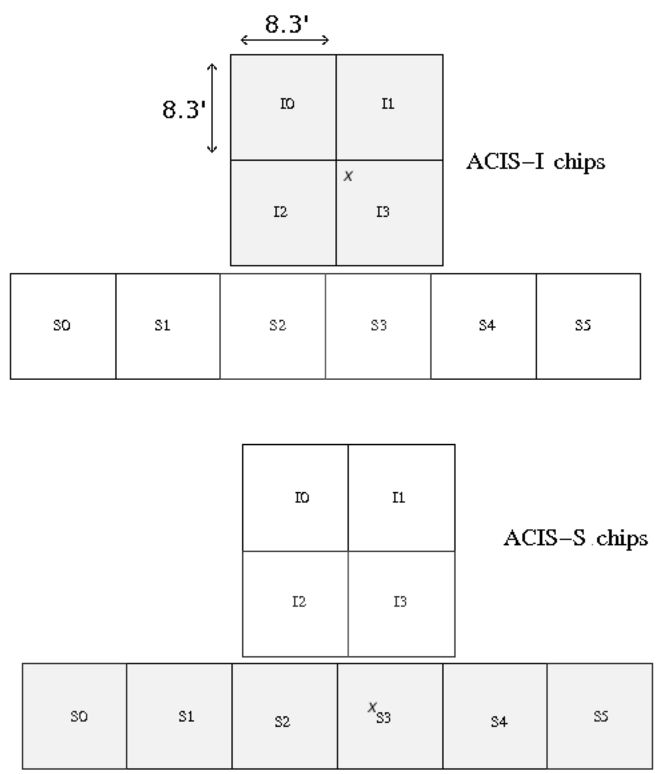

Figure 1.3: *Chandra* ACIS CCD chips arrangement. The 2×2" CCDs (colored in gray on top) are for ACIS-I and 6 CCDs in a line arrangement (bottom) are for ACIS-C. The diagram is taken from *Chandra* user's book.

1.2.3 Radiative Process

We can learn about BH accreting systems from the X-ray emissions it produces. There are two major X-ray emission mechanisms that play an important role in accretion systems: thermal emission and inverse Comptonization. Additional radiative processes as Bremsstrahlung and synchrotron emission are thought to play only a marginal role in the production of X-rays in accreting BH systems. Thanks to their relatively short variability timescales, detailed studies of GBHs indicate that the different radiative processes play different roles in different spectral states with the Comptonization from a putative hot corona dominating in the so-called low/hard state and thermal emission from the accretion disk dominating the high/soft state. Similar interplay between radiative processes is observed in AGNs, that are thought to be large-scale analogs of GBHs.

Thermal Emission

Thermal radiation is the radiation emitted by matter in thermal equilibrium and the spectrum is characterized a blackbody, which can be expressed by *Planck's Law*:

$$B_\nu(T) = \frac{2h\nu^3/c^2}{\exp[h\nu/kT] - 1} \tag{1.1}$$

or in terms of wavelength

$$B_\lambda(T) = \frac{2hc^2/\lambda^2}{\exp[hc/\lambda kT] - 1} \tag{1.2}$$

where h is the Planck's constant 6.63×10^{-34} J s, k the Boltzmann's constant 1.38×10^{-23} J K^{-1}, and c the speed of light 3×10^8 m/s.

Figure 1.4 shows the blackbody spectra of different temperatures ranging from 0.1 K to 10 billion K. At large wavelength, when $h\nu \ll kT$, the intensity can be approximately by

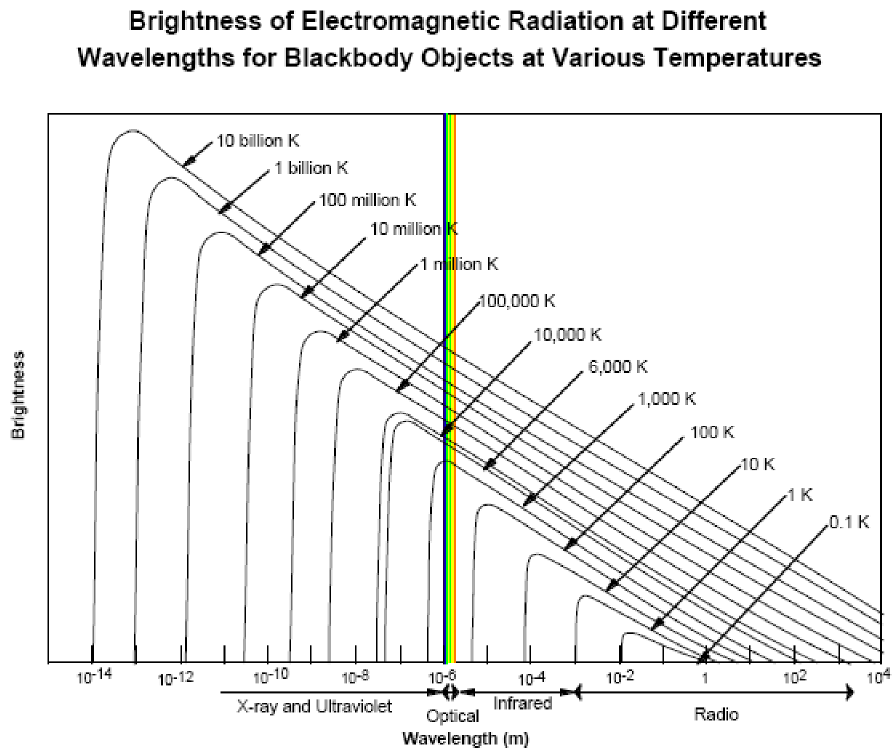

Figure 1.4: Blackbody spectrum diagram. The brightness plotted versus wavelength shows a peak at the certain wavelength and it shifts to shorter wavelength at higher temperature. The straight line part in spectrum can be explained with the *Ryleight-Jeans law* and the rapid drop after the peak can be explained with the *Wein's law*. This figure is taken from AstronomyOnline webpage [3].

the *Rayleigh-Jeans law*:

$$B_\nu(T) = \frac{2\nu^2}{c^2} kT \tag{1.3}$$

In the opposite regime at high frequencies, when $h\nu \gg kT$, the intensity of thermal radiation can be approximated by *Wien's law*:

$$B_\nu(T) = \frac{2\nu^2}{c^2} \exp\left(-\frac{h\nu}{kT}\right). \tag{1.4}$$

Thermal spectra exhibit fundamental properties that provide crucial information on the emitting objects. For example, the shape of the spectra exclusively depends on one parameter, the temperature, and the location of their peak is governed by the Wien's displacement law:

$$\lambda_{\max} T = 0.29 \,\mathrm{cm}\,\mathrm{deg} \tag{1.5}$$

As a result, by measuring the location of the peak, one can determine the temperature of a thermal source. Similarly, a shift of the peak observed during long-term monitoring campaigns, makes it possible to trace the temporal evolution of the system's temperature.

Another fundamental property of thermal radiation is obtained by integrating *Planck's law* over all frequencies. This is called the *Stefan-Boltzmann law* and shows that the flux of a thermal source (i.e., the total energy per unit of time per unit of surface area radiated by the blackbody at that temperature) is directly proportional to the temperature to the fourth power:

$$F = \sigma T^4 \tag{1.6}$$

where the σ is Stefan-Boltzmann constant 5.67×10^{-8} J m^{-2} K^{-4} s^{-1}. Based on this law, a direct measurement of the flux immediately constrains the temperature of the source.

Black holes have no solid surface, therefore they cannot emit directly, and in any case the radiation would not be able to escape from their gravitational field. However, in accreting systems (sMBHs in binary systems and SMBHs at the center of galaxies), thermal emission is thought to be produced by ubiquitous accretion disks present in these systems. Accretion disks are rotating gaseous disks that form around compact objects from accreting material by virtue of the conservation of angular momentum. In the simplest model (see Shakura and Sunyaev, 1973), the disk is geometrically thin ($r/H \ll 1$, where r is the radius and H is the half-thickness of the disk) and optically thick, and can be approximated by a series of rings with Keplerian rotation. The friction between adjacent rings heats up the gas, that releases thermal radiation locally. Since the accretion disk encompasses several temperatures the overall spectrum is generally approximated by a multi-color blackbody.

The total amount of energy per unit of time, i.e., the luminosity of the disk $L_{\rm disk}$, can be described by the following equation

$$L_{\rm disk} = \frac{2\eta G M_{\rm BH} \dot{M}}{R_{in}} = \eta \dot{M} c^2 \tag{1.7}$$

where R_{in} is the radius of the inner edge of the disk, $M_{\rm BH}$ the BH mass, $\dot{M}$ the mass accretion rate, and η the radiation efficiency for the conversion between gravitational energy to radiative energy (η ranges between $0.06 - 0.4$ depending on the BH spin). Combining Equations 1.6 and 1.7 and keeping in mind that R_{in} is measured in units of gravitational radii ($R_G = GM_{\rm BH}/c^2$), yields for the disk temperature an inverse dependence on $M_{\rm BH}$. For this reason, the temperature of an inner disk around a sMBH can reach 10^9 K leading to emission in the X-ray band around $1-2$ keV, whereas in SMBHs the estimated inner disk temperature is of the order of 10^5 K, which implies that the blackbody peak is located in the UV energy range. Observations indicate that BH systems of any scale are strong X-ray emitters with emission extending up to several hundreds of keV. These hard X-rays cannot be directly produced by thermal emission, but require an alternative radiative process that we discuss in the next subsection.

Comptonization

In a classical treatment of electron scattering, an electromagnetic wave interacts with the electron that oscillates and produces dipole radiation. The total cross section of the process (which is proportional to the scattering probability) is called Thomson cross section:

$$\sigma_T = \int \frac{d\sigma}{d\Omega} d\Omega = \frac{8\pi}{3} r_0^2 = 6.65 \times 10^{-25}\,\mathrm{cm}^2 \tag{1.8}$$

where r_0 is a classical electron radius ($r_0 = \frac{e^2}{mc^2}$) and has a value of $r_0 = 2.82 \times 10^{-13}$ cm.

In the quantum treatment of electron scattering, the photon is considered a particle that collides with an electron. In the collision, photon and electron exchange energy and momentum depending on the relative energy of photon ($h\nu$) and electron ($m_e c^2$) measured in the electron rest frame. If $h\nu \ll m_e c^2$, the photon gains energy from the electron; this process is called inverse Compton and the interaction is described by the Thomson cross section. In the opposite case, when $h\nu \gg m_e c^2$, the electron recoils and the scattered photon loses part of its energy; this process is called direct Compton and is regulated by the Klein-Nishina cross section.

In our study, we are mostly interested in the inverse Compton process and in particular in the case where seed photons produced by the accretion disk are up-scattered by multiple scatterings in the corona; this process is called Comptonization. In most models, the corona is in thermal equilibrium, meaning that the electrons follow a Maxwellian energy distribution, which is described by

$$N(\gamma) \propto \gamma^2 \beta [-\gamma m_e c^2 / kT_e]. \tag{1.9}$$

For electrons with $kT_e < m_e c^2$, the photon energy per scattering is $\epsilon_{out} = (1 + 4\Theta)\epsilon_{in}$ where $\Theta = kT_e / m_e c^2$ and the average change of photon energy is

$$\frac{\Delta\epsilon}{\epsilon} = \frac{4kT_e - \epsilon}{m_e c^2} \tag{1.10}$$

where the constant 4 is found by assuming that net energy can not be fully transferred (for details, see Rybicki and Lightman, 1979). The limit to this inverse Compton process is provided by the initial energy of the electrons: the photon cannot gain more energy than that. Photons can interact with electrons only if they collide and the probability of collision ($P_b \propto \exp^{-\tau}$) can be calculated using the optical depth, $\tau = NR\sigma_T$, where N is the electron number density in Equation 1.9, R the path length, and σ_T Thomson scattering cross section. The optical depth also determines the average number of scatterings, $\mathrm{Max}(\tau, \tau^2)$, based on the random walk theory.

The combination of average energy change per scattering and the average number of scattering determines the Comptonization process and hence of the resulting spectrum. Specifically, this is described by the so-called "Compton y parameter"

$$y = < \Delta\epsilon > \times \mathrm{Max}(\tau, \tau^2). \tag{1.11}$$

If $y \ll 1$, the scattering process is negligible and the incoming spectrum remains unaffected. On the other hand, for $y \gg 1$, the inverse Compton scattering becomes important and the spectrum is described by a power law. Based on the steady-state assumption that the probability for a photon to escape per Compton scattering is equal to the inverse of the mean number of scatterings, the energy spectrum is described by

$$I_\nu \propto \nu^{3+m}, \quad m(y) = -\frac{3}{2} \pm \sqrt{\frac{9}{4} + \frac{4}{y}}. \tag{1.12}$$

where $m(y)$ determines the slope of index (for a detrail, see Katz, 1976; Shapiro et al., 1976). When the scattered photon reach a mean energy of $\overline{h\nu} = 3kT_e$, the spectrum will saturate and exhibit the Wien distribution in the form of

$$I_\nu \propto \nu^3 \exp[-h\nu/kT_e]. \tag{1.13}$$

In summary, the Comptonized spectrum extends from $\sim 3kT_\gamma$ to $\sim 3kT_e$ with a spectral index depending on both optical depth and electron temperature.

When the electron number density follows a power law distribution rather than a thermal distribution, i.e., $N(\gamma) \propto \gamma^{-p}$ where γ ranges from 1 to γ_{max}, the process is called non-thermal Comptonization. The average output photon energy is then $\epsilon_{out} = (4/3\gamma^2 - 1)\epsilon_{in} \approx$

$\gamma^2\epsilon_{in}$ for a single order scattering. Multiple scatterings produce a power law spectrum, because the electron energy loss rate is the same as the photon energy gain rate: $F(\epsilon)d\epsilon \propto \dot{\gamma}n\gamma d\gamma = \gamma^2\gamma^{-p}d\gamma$ where $\dot{\gamma}$ is the rate of electron energy loss per scattering ($\dot{\gamma} \propto \gamma^2$). The resulting energy flux is described by $F(\epsilon) \propto \gamma^{-(p-1)} \propto \epsilon^{-(p-1)/2}$ with the spectral index $\alpha = -(p-1)/2$.

An example of non-thermal Comptonization is the bulk motion Comptonization, where the seed photons get scattered off electrons with the bulk relativistic motion plunging in the inner accretion flow. The seed photons gain energy from the bulk and thermal motion electrons regardless of the geometry of the flow (Titarchuk et al., 1997). The average photon energy is directly related to the bulk kinetic energy of electrons since the bulk motion involves high speeds. Then the energy gains and losses in a single scattering can be express as follows

$$\Delta x = \int_0^\infty \left(-\frac{1}{\dot{m}} x^4 \frac{\partial n}{\partial x} + x\Theta f_b \frac{\partial}{\partial x} \left[x^4 \left(f_b^{-1} n + \frac{\partial n}{\partial x} \right) \right] \right) \mathrm{d}x \tag{1.14}$$

where $f_b = 1 + (v_b/c)^2/(3\Theta)$, $\Theta = kT_e/m_ec^2$, $x = \epsilon/kT_e$, $\dot{m}$ is the accretion rate, and v_b is the flow inward speed.

Following Titarchuk et al. (1997) and solving the integration in the dimensionless photon energy density case $x^3n = x\delta(x - x_0)$, yields:

$$\Delta x = \left(\frac{4}{\dot{m}} + 4\left[\Theta + (v_b/c)^2/3\right] - \frac{\epsilon_0}{m_ec^2} \right) x_0 \tag{1.15}$$

where ϵ_0 and x_0 are the initial photon energy components before the scattering. Since the accretion rate $\dot{m}$ is also associated to v_b/c (Blandford and Payne, 1981), the energy change per scattering is associated to the first degree order of the bulk electron velocity, the second order of thermal and bulk electron velocity, and the photon-energy loss due to the recoil of the electron(for details, see Titarchuk et al., 1997). Also in this case, the energy spectrum forms a power law and α is dominated by the bulk velocity rather than the thermal motion of electrons.

Bremsstrahlung

X-ray radiation can also be produced when a charge is accelerated or decelerated in the Coulomb field of another charges. This process of free-free emission is called Bremsstrahlung, which means braking radiation in German. In thermal bremsstrahlung emission, the radiation from positive ions can be neglected because of their high mass, rather the radiation is produced by accelerated positrons and electrons. The spectrum of thermal bremsstrahlung emission can be obtained by averaging the single electron over the thermal distribution and for the detail derivation, see Rieke and Lebofsky (1979). The optically thin bremsstrahlung spectrum is flat for photon energy much smaller than the thermal energy ($h\nu \ll kT$), rolls over at $h\nu \sim kT$, and drops off exponentially at even higher energy. In active black hole systems, Bremsstrahlung radiation plays only a marginal role, since the emission is dominated by thermal processes associated to the accretion flow and Comptonization produced in the corona.

Synchrotron Radiation

High-energy photons can be also produced by energetic electrons spiraling around magnetic field lines. This emission, called synchrotron radiation, is often observed in astrophysical jets, which are observed in both SMBH and sMBH systems. It must be said that most of the times the jet emission is produced in the radio energy band, not in the X-rays. Nevertheless, X-ray jet emission is observed in a specific class of AGN called blazars, which are sources with powerful jets pointing toward the observer. As a result, beaming effects constrain the emission into a narrow cone, increase the intrinsic luminosity and shift the emitted frequency to higher energies. In our study, we do not focus on jet-dominated sources and therefore synchrotron radiation does not play a major role. In GBHs, which have jets that do not point toward the observer, X-ray jet emission has been claimed in some specific spectral states but it is not produced directly by synchrotron emission. Rather, the seed synchrotron emission is thought to be Compton up-scattered by an optically thick, geometrically thin electron region at the base of the jet.

1.2.4 X-ray Data Analysis

X-ray data provide direct and indirect constraints on the properties of accreting BH systems. In the following I describe the main characteristics as well as the advantages and limitations of spatial, temporal, and spectral X-ray analyses.

X-ray Spatial Analysis

In recent years, the outstanding technological progress has provided X-ray astronomers with an additional important tool to complement the spectral and temporal analyses. The analysis of X-ray images of BH systems yields crucial information on different levels. Specifically it allows 1) the unambiguous identification of the central source (current X-ray angular resolution allows a direct comparison with radio, optical, and IR images), 2) the detection of jet-like structures and off-nuclear sources, which, if undetected, may hamper the spectral classification of the central source, and 3) the characterization of the properties of extended diffuse component, which represents the reservoir for BH systems. This progress has been made possible mostly thanks to the sub-arcsecond angular resolution offered by the *Chandra* satellite. Figure 1.5 shows the power of *Chandra* imaging compared with *XMM−Newton*: in the *Chandra* image an off-nuclear dominant source is clearly detected within 10" from the central source, whereas *XMM−Newton* is unable to disentangle the contribution from the off-nuclear source. Despite the important contribution from X-ray imaging and from its combination with spectral analysis, it is important to keep in mind that the X-ray emitting region around BHs of any scale is still well beyond the current best angular resolution, and therefore no direct imaging of the central engine of BH systems is possible with current and next generation of X-ray satellites.

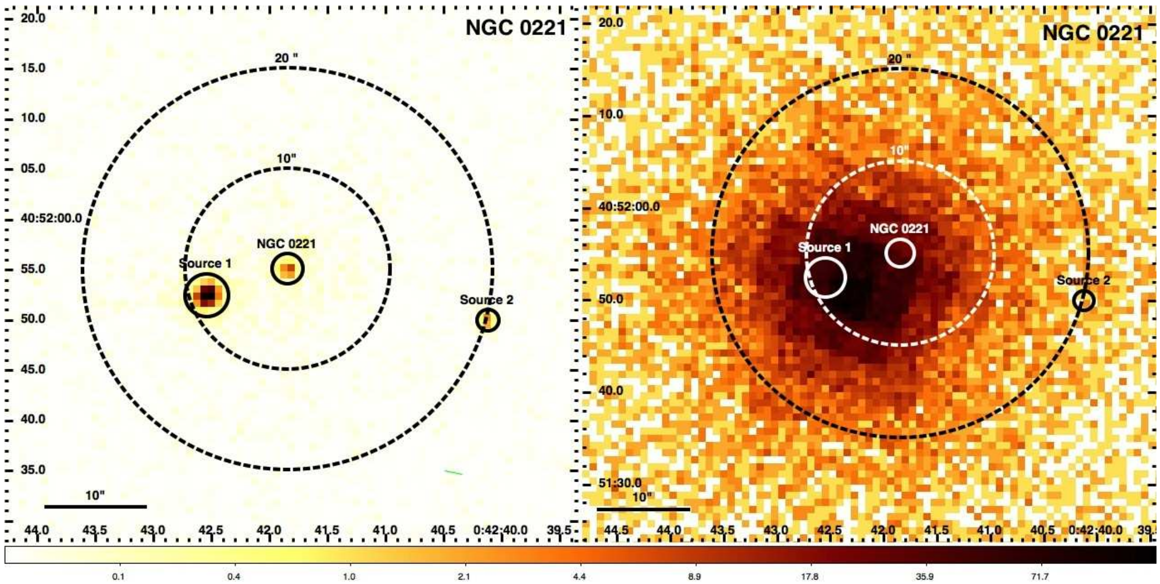

Figure 1.5: An example of CCD images for NGC 221. The left panel shows the *Chandra* image of NGC 221 with the presence of two nearby objects within $10'' - 20''$, whereas the *XMM−Newton* image in right panel shows the combined emissions from "Source 1" and NGC 221.

X-ray Timing Analysis

The study of rapid X-ray variability is one of the best ways to understand the physical environment in the vicinity of accreting compact objects, since the variability is thought to be originated in the inner accretion flow close to the BH. Since current instruments do not allow to spatially resolve the central regions where X-rays are produced (typically, they are produced within few tens of gravitational radii, which translate into angular sizes of the order of $10^{-4} - 10^{-5}$ milliarcsecond), the size of X-ray emitting regions in BHs can only be inferred from temporal variability observations. One of the fundamental principles of the theory of relativity states that nothing can move faster than the speed of light, which has a very high but finite value. As a result, a source of radiation that varies on a timescale Δt will have an upper limit on the size of $c\Delta t$, because the signal that travels through the object cannot travel faster than light. The basic tools to study the temporal properties of any source are the light curves, diagrams where a quantity representing the flux or luminosity is plotted versus the time. Important insights into the properties of the central engine can be obtained by comparing simultaneous light curves from different energy bands. Specifically, coordinated studies in the radio and X-ray bands make it possible to investigate the link between jet and accretion. Similarly, multi-wavelength monitoring campaigns in several optical, UV, and X-ray energy bands allow one to study the link between accretion disk and corona. Long evenly-spaced X-ray light curves yielded by the *RXTE* satellite for over 16 years have played a crucial role in our understanding of stellar BH systems and AGNs. Often, the variability of BHs is investigated using the power-density spectrum (PDS; e.g., Leahy et al., 1983), which use Fourier transforms to describe how the power of the temporal signal is distributed over a large range of frequencies (in the range mHz $-$ kHz). PDS of BHs are generally described by power laws with some frequency break corresponding to typical timescales, and resolved peaks that represent quasi-periodic oscillations (QPOs). QPOs, which are observed almost exclusively in stellar BHs, can be divided into two main classes: 1) low-frequency QPOs (LFQPOs; $0.1 - 30$ Hz), which are strong features fairly common in specific spectral states, and 2) high-frequency QPOs (HFQPOs; $150 - 405$ Hz), which are intrinsically weaker and have been observed only in few objects but are important because they may be directly related to the Keplerian orbital frequencies in the last stable orbit.

X-ray Spectral Analysis

Another common tool used in X-ray astrophysics is the study of energy spectra. At first order, spectra can be represented by a power law, which can be described by $N(E) = N_0 E^{-\Gamma}$, where $N(E)$ indicates the number of photons per second per square centimeter per energy band and Γ is the photon index. In this case, the energy flux of the source is given by $F(E) = EN(E) = N_0 E^{-(\Gamma-1)} = N_0 E^{-\alpha}$, which explains the relationship between photon and spectral index: $\alpha = \Gamma - 1$. $F(E)$ represents the energy spectrum emitted by the source, but it is different from the observed spectrum $C(E)$ (where C stands for photon counts), which must account for the instrument response:

$$C(E) = \int F(E_0)R(E, E_0)dE_0 \tag{1.16}$$

where $R(E, E_0)$ is the detector response, which gives the probability that a photon of input energy E_0 is detected at energy E. Unfortunately, this equation cannot be uniquely inverted because of the complexity of the response matrix. As a result, the X-ray spectral analysis is carried out by fitting the data with different spectral models. Typical X-ray spectra in the $2-10$ keV band are described by a simple power law, that is characterized by a photon index Γ in the range between 1.4 and 3. At very high energies the spectrum sometimes shows a break or exponentially cutoff, whereas it may exhibit a bump between 10 and 30 keV produced when the power law photons get reflected by the accretion disk (e.g., Done and Nayakshin, 2001). More specifically, when some of the X-rays photons are directed toward the disk, two possible processes can occur: either the photons are absorbed by the elements in the disk or they are Compton scattered. The probability of the processes depends on the relative importance of the photo-electric and scattering cross sections. Since the photo-electric cross section decreases with energy and becomes equal to σ_T around 10 keV, at this point the scattering process dominates until the photons are down-scattered in the Klein-Nishina regime, explaining the presence of the so-called Compton bump. In several AGN spectra, an additional component called soft-excess emerges at low energies ($E < 1-2$ keV). The nature of this component is still debated with explanations ranging from reflection from partially ionized material, to complex absorption, or by a second cooler Comptonization component. In XRBs instead, the soft X-ray spectrum is characterized by direct thermal emission from the inner part of the accretion disk, which can be modeled with a multicolor black body. A common spectral feature of BH systems irrespective of their mass is the presence of a fluorescent Fe Kα line around 6.4 keV, whose energy, profile, and strength are function of the geometry and the physical state of the reprocessing medium (e.g., George and Fabian, 1991). Finally, a crucial aspect of X-ray spectra is that they are modified by absorption from material located along the line of sight. In addition to the interstellar absorption, BH systems are often characterized by intrinsic absorption from material in the equatorial plane associated with the torus in AGNs and accretion disk or companion winds for GBHs. When modeling the X-ray spectra, one or more multiplicative models must be included to account for absorption, which is parameterized by $N_{\rm H} = nR$ indicating the number of hydrogen atoms along the line of sight with a cross section area of 1 $\rm cm^2$.

1.3 Black Hole States

To progress in our understanding of BH systems at all scales, it is important to study the complex phenomenology of GBHs in the X-ray band. Since early 70s, systematic spectral variability changes were observed in several systems and were categorized in two main states: the "low/hard" state (LHS), characterized by a hard photon index ($\Gamma \sim 1.7$) and relatively low flux, and the "high/soft" state (HSS), defined by softer spectra dominated by a thermal component around 1 keV and higher X-ray flux (e.g., Tananbaum et al., 1972; Terrell, 1972). After forty years of observational and theoretical studies it is now clear that the changes of X-ray spectral properties are continuous and are associated with specific X-ray temporal properties as well as to systematic changes of the radio properties associated with the jet. General state transitions of GBHs are frequently described using the Hardness- Intensity Diagram (HID) and Hardness-RMS diagram (HRD) (e.g., Belloni, 2010, 2011). The HID is a plot of X-ray intensity (count rate) versus the hardness ratio (HR) which is the ratio between a hard and a soft X-ray band (e.g., Belloni, 2004; Homan et al., 2001; van der Klis, 2005), whereas the fractional rms variability is plotted against HR in HRD. A sketch of the HID (top panel) and HRD (bottom panel) is shown in Figure 1.6. In this section, we describe the spectral and temporal properties of each state as well as the current physical interpretation. A schematic illustration of the coordinated changes in the temporal and spectral properties of GBHs is shown in Figure 1.7.

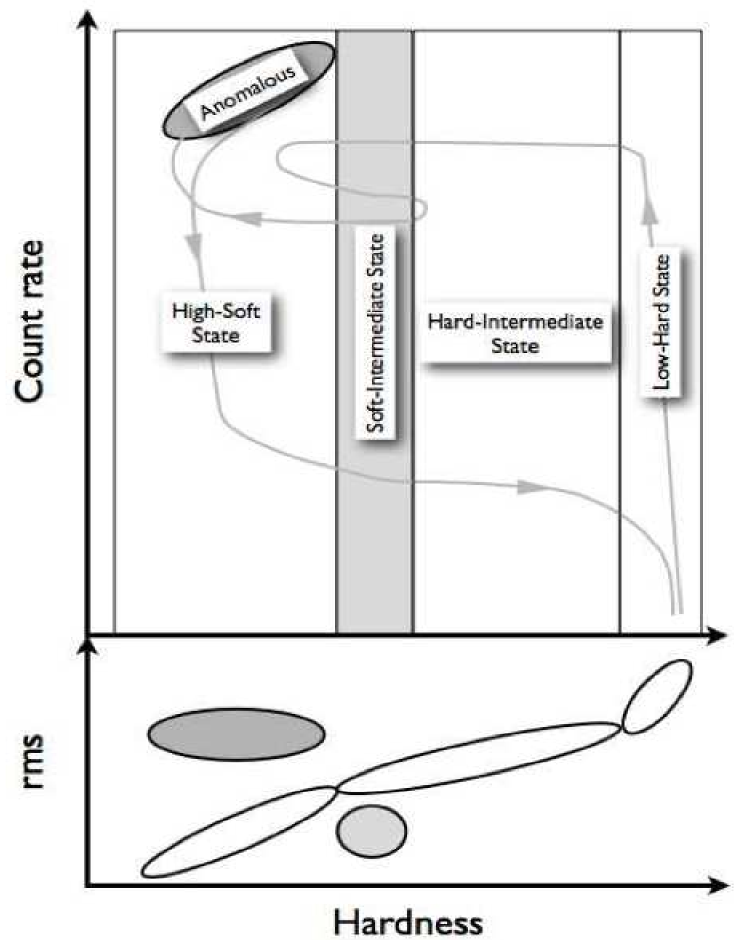

Figure 1.6: General spectral state transition of GBHs. The Hardness-Intensity diagram (top panel) shows the transition of a GBH in the LHS to the HSS and again to its LHS. The Hardness-RMS diagram shows the correlation between RMS and hardness during the transitions. This figure is from Belloni (2010).

1.3.1 Low/Hard State (LHS)

The low/hard state (LHS) is the first and the last stage in GBH evolutions as seen in Figure 1.6. The definition of LHS is based on following properties.

1) The spectrum is well described by a power law with a hard spectrum with photo index

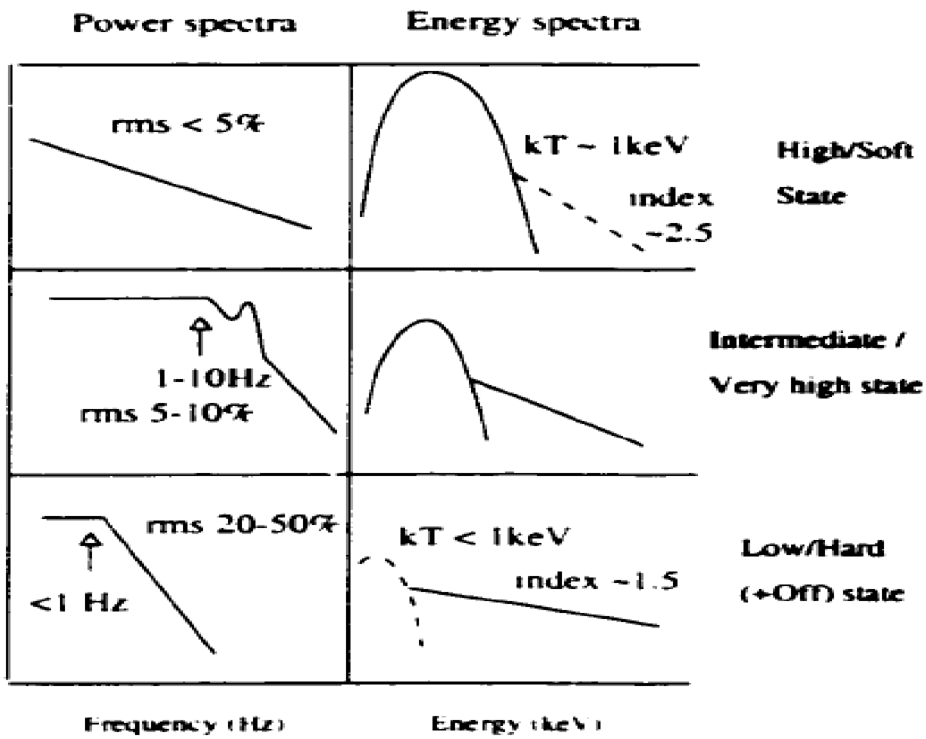

Figure 1.7: PDS and energy spectra in the canonical GBH states. This diagram is taken from Kalemci (2002) (originally from Fender et al. 2001).

$\Gamma = 1.4 - 2.1$ and a high energy cut-off at ~ 100 keV. This high-energy cut-off reflects the temperature of electrons around $50 - 100$ keV responsible for the thermal Comptonization in the accretion flow corona. A low-energy break observed in the spectrum is an indicator of initial energy range of seed photons (somewhere between UV and X-rays) which are probably produced by the accretion disk (see Figure 1.8). Secondary radiative processes contributing to the seed photons in the LHS are Bremsstrahlung and synchrotron emission (Chiang et al., 2010).

2) The PDS is described by a steep power law with high level of aperiodic variability ($20\% - 50\%$) with the possible presence of LFQPOs.

3) Strong radio emission, which exhibits a flat or an inverted spectrum (the emissivity

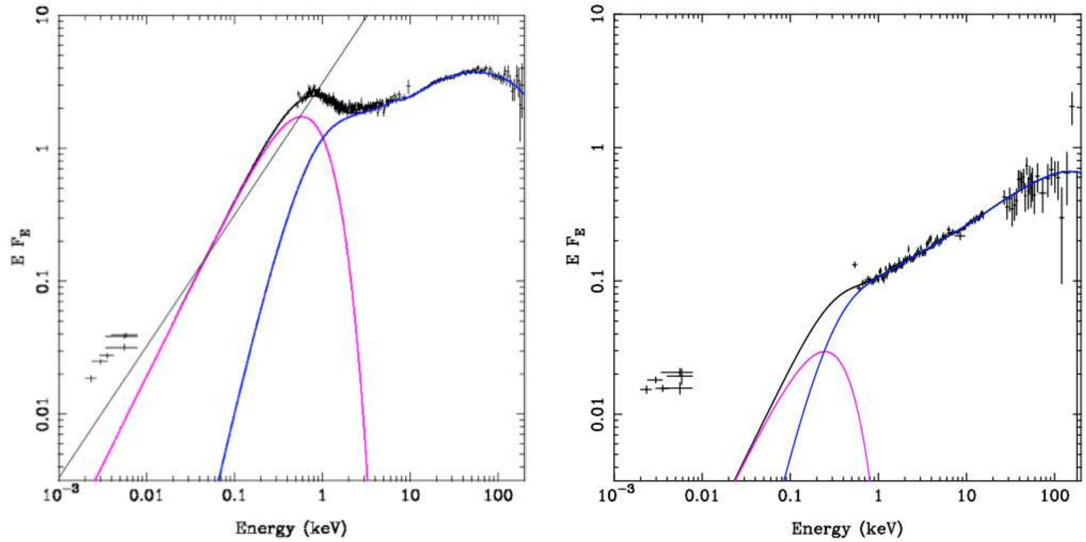

Figure 1.8: The unabsorbed data from the BH transient of 1753.5-0127. The left hand panel shows the HSS spectrum. The right hand panel shows the LHS spectrum. Each spectrum was modeled with the disk (indicated with magenta in color version) and thermal Comptonization of seed photon from the disk (with blue solid line). It was taken from Chiang et al. (2010).

increases with the frequency) and is considered a reliable indicator of optically thick moving material emitting synchrotron radiation. Other lines of evidence (high polarization and spatially resolved structures) confirm the presence of compact jets in the LHS (e.g., Corbel et al., 2000, 2003; Fender, 2001).

A sketch of one of the leading models of GBHs in LHS is shown in the top panel of Figure 1.9. An inner hot accretion flow or corona is thought to cover the truncated accretion disk located far away from the last stable orbit and to be responsible for the base of jets. The dominant radiation ($\sim 80\%$ of the flux) is produced from the accretion flow via thermal Comptonization of soft seed photons from the accretion disk $-$ they get up-scattered off thermal distributed electrons inside the hot flow.

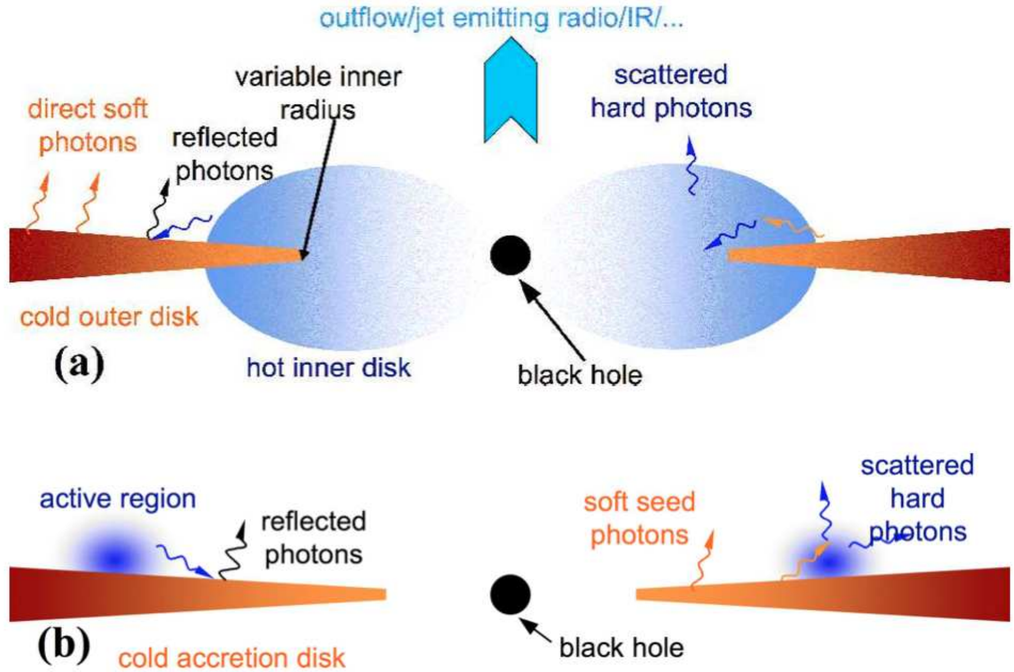

Figure 1.9: Schematic representation of BH states. The LHS in panel (a) shows that the seed photons from the cold disk are intercepted in hot flow and get up-scattered. Panel (b) shows the HSS. This picture is taken from Zdziarski et al. (2004)

1.3.2 High/Soft State (HSS)

The second canonical spectral state, the high soft state (HSS), is characterized by energy spectra dominated by thermal radiation produced by the accretion disk (up to $\sim 75\%$). This emission is generally parameterized by a multicolor blackbody model, which measures the temperature of inner disk and its size under the assumption of blackbody and the radial distribution of $T(R) \propto R^{-3/4}$ (Makishima et al., 1986; Mitsuda et al., 1984). The hard X-ray spectrum is well described by a power law with a steep photon index ($\Gamma = 2 - 2.5$) and without a high-energy break, which may be evidence of non-thermal Comptonization. The hard component can be parameterized by the bulk motional Comptonization (BMC) model (Titarchuk et al., 1997, see next section for a detaii) or by "hybrid" Comptonization models that comprise thermal and non-thermal Comptonization processes. The temporal properties of the HSS, described by the PDS, are characterized by a very low aperiodic variability (RMS$\sim 1\%$), with elusive or absent QPOs (see the top panel in Figure 1.7). No significant radio emission is detected in this spectral state suggesting that there is no jet, as shown in the schematic illustration of this state in the bottom panel of Figure 1.9. The sketch indicates that when GBHs enter the HSS, the corona has cooled down and does not dominate the X-ray emission and the optically thick accretion disk extends to the innermost stable circular orbit.

1.3.3 Other States

Although historically only two canonical states were defined, a wealth of observational data collected over several years (mostly based on *RXTE* observations) has indicated that GBHs continuously evolve from a spectral state to another passing through several intermediate states. The general state transitions (illustrated in Figure 1.6) can be summarized as follows: LHS $\rightarrow$ VHS/SPL $\rightarrow$ HSS $\rightarrow$ IMS $\rightarrow$ LHS and sometimes $\rightarrow$ Off state $\rightarrow$ LHS. In this section, I will briefly explain in the characteristics of the Very High State (VHS), Intermediate State (IMS), and Off state.

Very High State (VHS) and Steep Power Law State (SPL)

Some BHs after LHS becomes extremely bright ($L \geq 0.2L_{\rm Edd}$) with very steep X-ray spectra ($\Gamma \sim 2.4-3$) and $40-90\%$ of their total flux associated with non-thermal Comptonization. The PDS shows QPOs in the range of $0.1-30$ Hz and in some cases HFQPOs in the range of $100-300$ Hz (Remillard et al., 2002). In this state, BHs appear to be radio quiet objects (e.g., GRO J1655$-$40 during 1996 August, Tomsick et al., 1999). This VHS was interpreted as evidence of the highest accretion rate in BH systems (van der Klis, 1994).

Intermediate States (IMS)

The state that GBH passes through from LHS to HSS is called hard-intermediate state (HIMS) where the spectrum becomes softer and the thermal disk component starts to emerge and the numbers of photons up-scattered from thermal electrons is reduced. In the PDS, the aperiodic variability still remains high (although at a lower level compared to the LHS) and strong LFQPOs are present. The soft-intermediate state (SIMS) is characterized by steeper energy spectra and similar PDS where different types of LFQPOs are present: strong and variable type-C QPOs (up to 16% rms) are common in the HIMS, whereas weaker type-A and B QPOs (rms few percent) are observed during SIMs. The state evolution of GBH then switches back and forth between two IS states. Importantly, the SIMS has been associated with the most powerful relativistic jets of GBHs (Fender et al., 2004).

Quiescent State (Off State)

Sometimes BH transition exhibits flat non-thermal spectra ($\Gamma = 1.5 - 2.1$) associated with very weak luminosity of the order of $L = 10^{30-33}$ erg s^{-1} compared to the typical 10^{36-37} erg s^{-1} observed in the LHS. This almost-quiescent state can be described by a very low accretion rate ($\dot{m} = \dot{M}/\dot{M}_{\rm Edd} \ll 1\%$) combined with low radiative efficiency. These physical conditions are readily explained by models where the seed photons are advected into BH without thermal energy transfer to electrons (Menou et al., 1999; Narayan et al., 2002; Narayan and Yi, 1994, 1995). Figure 1.10 illustrates the spectral evolution of GBHs with the quiescent state described by a truncated standard disk and an inner advection dominated accretion flow (ADAF). When the accretion rate increases the standard disk moves inward increasing the overall luminosity and the ADAF will eventually disappear (Esin et al., 1997).

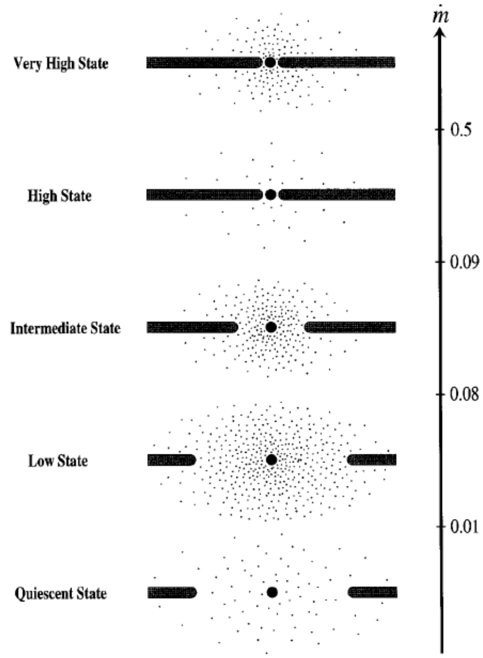

Figure 1.10: Graphic interpretation of state relative to the accretion rate. The Comptonizing plasma in each state is associated the transitional radius and also consequently to the accretion rate. This figure is taken from Esin et al. (1997).

1.4 Black Hole Mass Determination

It is widely accepted that the brightest persistent sources in our galaxy and universe are powered by gravitational accretion onto black holes. The bright and strongly variable emission at high energies associated with accreting BH systems and the presence of relativistic jets that may have a huge impact on the environment over long distances (Fabian et al., 2003; McNamara et al., 2000) are at the forefront of current research in high-energy astrophysics. BH systems can simply be characterized by three parameters from the observational point of view: mass, spin, and charge. The charge does not play a major role because matter is overall neutral. Although measurements of the spin parameter have been reported, the estimators are generally model-dependent and still rely on other parameters such as the inclination angle and mass. On the other hand, the black hole mass can be measured directly in the optical band and provides essential information (e.g., time and length scales) about the BH systems. The mass of supermassive black holes is crucial to understand the formation and evolution of galaxies.

Direct $M_{\rm BH}$ estimators use the dynamics of stars and gas that are accelerated by the BH itself. In the following, I introduce the optically-based methods used to estimate $M_{\rm BH}$ in sMBH and SMBH. Then I review different X-ray-based techniques including the X-ray scaling method, that was developed for stellar BHs and we extend and refinded for supermassive black holes.

1.4.1 Optically Based $M_{\rm BH}$ Determination

Direct Methods

The most reliable black hole mass measurement is based on the dynamics of stars or gas that orbit around a BH. The mass of any black hole in binary systems can be expressed analytically as a function of period, inclination angle, and the velocity of the companion star (e.g., Greene et al., 2001; Herrero et al., 1995). Similarly, the $M_{\rm BH}$ of a SMBHs in quiescent galaxies can be derived from the stellar or gas dynamics via the proper motion and radial velocity of individual sources (e.g., Barth et al., 2001; Genzel et al., 2000; Ghez et al., 2005; van der Marel et al., 1998). The left panel in Figure 1.11 shows an example of proper motion of objects orbiting the center of our Galaxy and their best-fit models to compute the central mass value. For Type 2 active galaxies with heavily obscured emission and high inclination angle, $M_{\rm BH}$ can be measured from megamasers in the gas disk around the BH (Miyoshi et al., 1995). The SMBH in Type 1 active galaxies can be measured via the reverberation mapping method (hereafter RM; Blandford and McKee, 1982; Peterson, 1993) utilizing the time delay (see the right panel in Figure 1.11) between the continuum emission from the AGN and the ionized emission-line from the broad line region (BLR), which is made of clouds revolving close to the central black hole with high speeds and whose spectrum shows broad emission lines due to the Doppler effects. Specifically, measuring the time delay τ that characterizes the size of BLR ($R = \tau c$) and the dispersion velocity ΔV from the full width at half maximum of the line, one can derive the $M_{\rm BH}$ using the following equation

$$M_{\rm BH} = f_G \frac{R \Delta V^2}{G} \tag{1.17}$$

where the unknown f_G parameter describes the BLR geometry and is poorly constrained. Unfortunately, the applicability of direct $M_{\rm BH}$ estimation methods is limited. The stellar

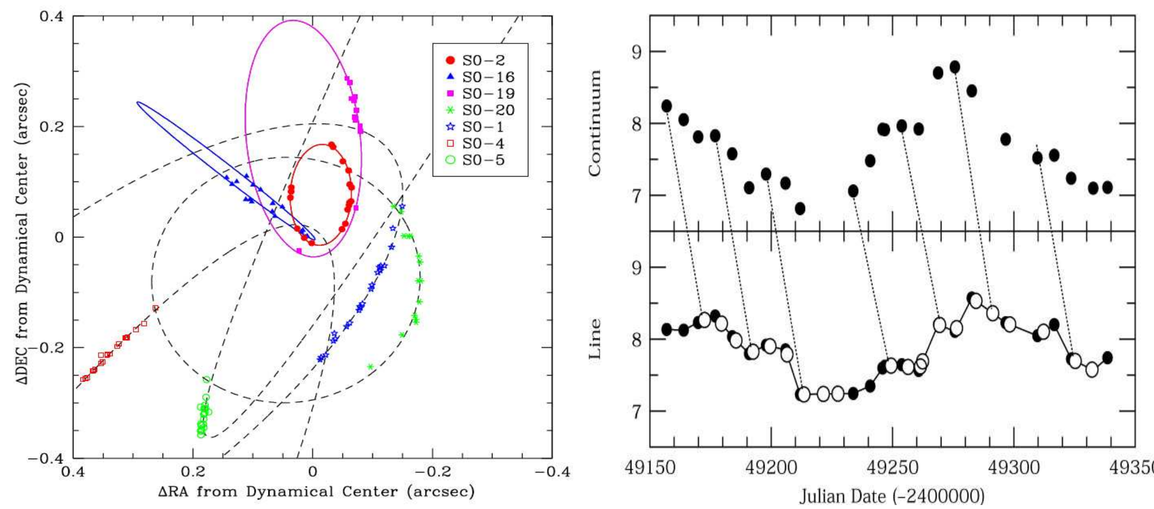

Figure 1.11: A example of $M_{\rm BH}$ direct methods. The left panel shows the stellar orbits around Sgr A*. This figure is taken from (Genzel and Karas, 2007). The right panel shows the time delay between continuum and line emission, which s used in the reverberation mapping method. This figure is taken from (Peterson, 2001).

dynamical method requires the sphere of influence of the BH to be resolved and this is possible only for our own Galaxy and few nearby galaxies. For more distant galaxies, the Keplerian motion is not fully detected due to low signal-to-noise ratio are required. The use of large telescopes with high spatial resolution allows to extend the measurement of $M_{\rm BH}$ to more distant galaxies by observing and modeling the gas dynamics in the inner region of the galaxy. However, gas also respond to non-gravitational forces unlike the stellar motion that only responds to gravitational forces. The RM method, which needs a significant amount of resources and time, does not require any spatial resolutions. However, it is limited to typical AGNs because not all AGNs host a BLR and the variability of very luminous AGNs is typically characterized by small-amplitude flux changes over very long timescales. Further limitations for the RM method come from the parameter f_G in Equation 1.17 which is still poorly constrained because of the unknown dynamics of the BLR.

Indirect Methods

The black hole mass can be measured indirectly by using several empirical relationships e.g., $M_{\rm BH} - \sigma_*$, $M_{\rm BH} - L_{\rm bulge}$. The $M_{\rm BH} - L_{\rm bulge}$ correlation was first obtained by Kormendy and Richstone (1995) and showed a substantial scatter. On the other hand, the correlation found between $M_{\rm BH}$ and the dispersion velocity σ_* showed small scatter (Ferrarese and Merritt, 2000; Gebhardt et al., 2000a). Figure 1.12 shows the linear correlation between $M_{\rm BH}$ and $L_{\rm bulge}$ and σ_* where the closed circles indicate stellar dynamics based $M_{\rm BH}$ value, squares the gas dynamic based values, and triangles the megamasers measurements. These correlations imply that the central black hole mass is linked to the growth of its host galaxy. The $M_{\rm BH} - \sigma_*$ correlation is seen in quiescent (Ferrarese and Merritt, 2000; Gebhardt et al., 2000a) and active galaxies (Ferrarese et al., 2001; Gebhardt et al., 2000b; Nelson et al., 2004). However, the measurement of velocity dispersions is limited to weakly active galaxies whose nuclei are not too bright (Dasyra et al., 2007; Watson et al., 2008). The $M_{\rm BH} - \sigma_*$ correlation also statistically constrains the parameter f_G in Equation 1.17; it turns out to be $< f_G > \sim 5$ using the correlation for quiescent and active galaxies (Onken et al., 2004; Park et al., 2012; Woo et al., 2010). The $M_{\rm BH}$ can also be derived from the empirical relation between the size of BLR R found from the RM method, and the AGN luminosity L, $R \propto L^{1/2}$ (e.g., Laor, 1998; Wandel et al., 1999). Unlike the RM method, this provides a

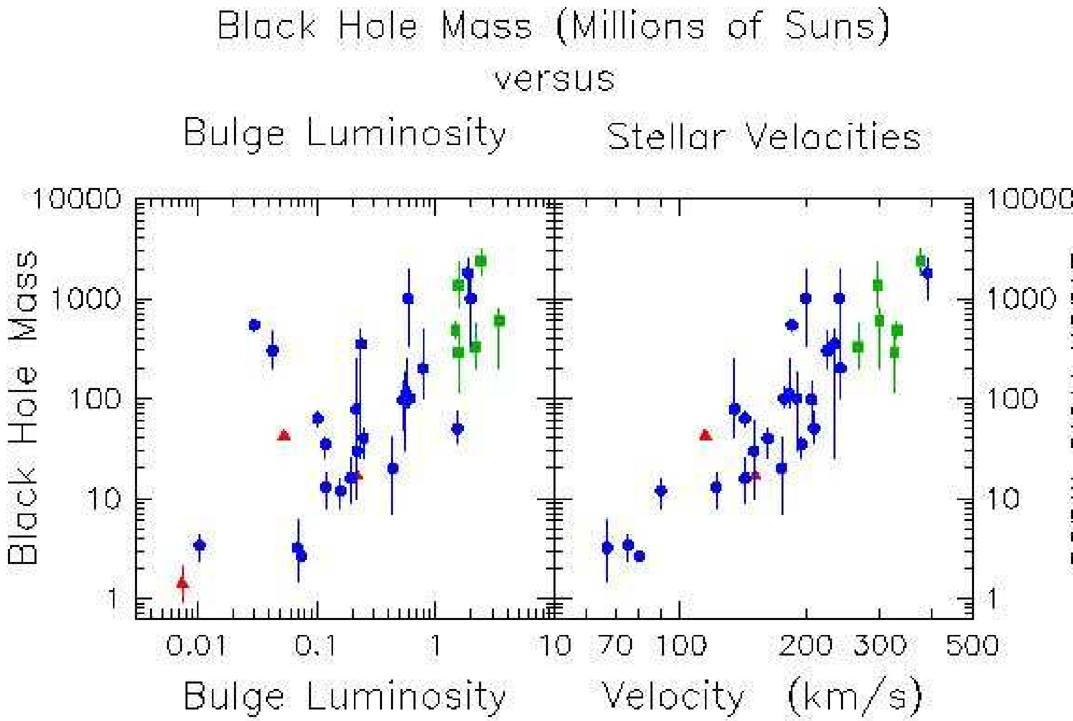

Figure 1.12: $M_{\rm BH}$ versus $L_{\rm bulge}$ and σ_*. The left plot shows the correlation between $M_{\rm BH}$ and $L_{\rm bulge}$ in the units of the total luminosity of the Milky Way. Blue points indicate $M_{\rm BH}$ measured values via star proper motions, green points values based on the gas dynamics, and the red ones the megamaser based values. The right plot shows the correlation between $M_{\rm BH}$ and the dispersion velocity. This diagram is taken from the following website (http://chandra.as.utexas.edu/ kormendy/stardate.html)

simple and quick way to measure the BLR size and $M_{\rm BH}$ from a single spectrum. For this reason, this latter technique has been used for very large samples of AGNs including very distant AGNs, and AGNs spanning a very large range of accretion rates.

1.4.2 X-ray-Based $M_{\rm BH}$ Determination

The optically-based methods for $M_{\rm BH}$ determination are limited to nearby objects with good spatial resolutions and long observation periods. It is therefore essential to measure $M_{\rm BH}$ based on different wavelengths and with different physical assumptions. For example

X-rays methods may provide valid alternative ways to constrain $M_{\rm BH}$.

- $M_{\rm BH}$ in BHs at all scales can be obtained by X-ray variability studies. Generally, the PDS display a "break frequency": the power law becomes steeper at high frequency. It has been shown that the break timescale $T_{\rm break} = 1/\nu_{\rm break}$ is related to $M_{\rm BH}$ by the following equation $T_{\rm break} = M_{\rm BH}/10^{6-7}\ M_{\odot}$ which is valid for XRBs and Seyfert 1 galaxies (Markowitz et al., 2003; McHardy et al., 2006; Papadakis, 2004). The origin of break frequency may be associated with the cooling timescale for Comptonization of electrons in corona (Ishibashi and Courvoisier, 2012). However, it is not fully understood yet as $T_{\rm break}$ may also be associated to the accretion rate. A similar method based on X-ray variability measured by the "excess variance" but limited to AGNs was developed by Nikolajuk et al. (2004); Nikoajuk et al. (2009, 2006) and recently refined by Ponti et al. (2012). These are reliable methods to constrain $M_{\rm BH}$, however they can only be applied to BHs that show significant variability and posses X-ray light curve sufficiently long and with good signal-to-noise ratio.

- The most used X-ray-based method for stellar mass BHs is based on the spectral fitting of X-ray spectra with the multicolor black body model (Kubota et al., 2001a,b), which assumes that at the last stable orbit the disk luminosity and the temperature are correlated by $L_{\rm disk} \propto T^4_{\rm disk}$ is in agreement with the standard accretion disk theory if gas pressure dominates in the disk. Although it is possible to fit the disk model and constrain $M_{\rm BH}$, the disk becomes unstable when disk is radiation pressure dominated. More complex disk models are necessary to adequately describe stable disks, but our understanding of the physical conditions in the inner part of disk is still incomplete. In addition in AGN, the disk emission peaks in the UV band which cannot be observed directly because of the intrinsic absorption.

1.4.3 X-ray Scaling Method

In a recent study, Shaposhnikov and Titarchuk (2009) carried out an extensive analysis of the temporal and spectral X-ray properties of different GBHs during their spectral transitions. They fitted the X-ray spectra with the Bulk Motion Comptonization model (BMC), which is a generic Comptonization model able to describe equally well the thermal Comptonization and the bulk motion Comptonization, where the seed photons are scattered off electrons with bulk relativistic motion (Titarchuk et al., 1997). The BMC model is characterized by 4 free parameters: the temperature of the thermal seed photons kT, the energy spectral index α (which is related to the photon index by the relation $\Gamma = 1+\alpha$), a parameter $\log(A)$ related to the Comptonization fraction f (.i.e., the ratio between the number of Compton scattered photons and the number of seed photons) by the relation $f = A/(1+A)$, and the normalization $N_{\rm BMC} = L_{39}/d_{10}^2$, where L_{39} is the luminosity in units of 10^{39} erg s^{-1} and d is the distance in units of 10 kpc.

Their main findings can be summarized as follows: (1) Two positive correlations were found: the first one involving temporal and spectral properties and specifically relating the quasi periodic oscillation (QPO) frequency and the photon index Γ (see Figure 1.13 left panel); the second one relating 2 spectral parameters: the normalization $N_{\rm BMC}$ and Γ (Figure 1.13 right panel). (2) Both spectral evolution trends (Γ−QPO and $\Gamma - N_{\rm BMC}$) can be adequately parametrized by 2 analytical functions, which are similar for the different GBHs.

By virtue of this similarity, $M_{\rm BH}$ (and the distance) of any GBH can be obtained from a scaling process. Simply speaking, if the $M_{\rm BH}$ is known for a given GBH considered as a reference system, the black hole mass for any other GBH can be determined by shifting its self-similar trend until it matches the reference object's function. In Figure 1.13, this is accomplished by shifting right-ward the gray (red, if printed in color) colored trend until it matches the black one: the difference in $M_{\rm BH}$ between the target of interest and the reference system is directly related to the amount of the shift along the x-axis. The

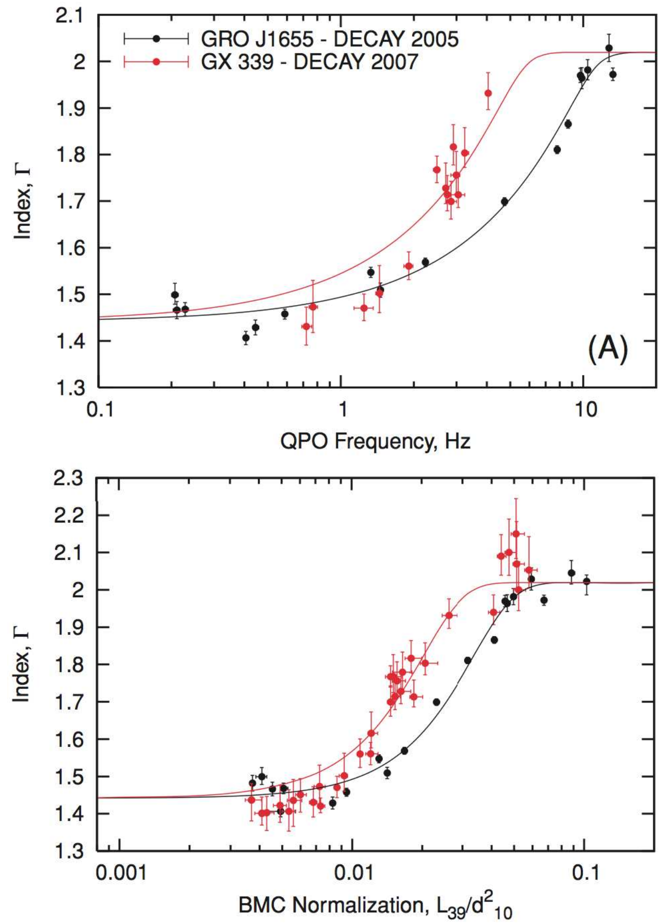

Figure 1.13: Γ−QPO (left panel) and $\Gamma-N_{\rm BMC}$ (right panel) diagrams of GRO J1655−40 and GX 339−4. The data corresponding to the spectral transition of the reference system, GRO J1655−40, are shown in black, whereas the red (gray in black and white) data belong to the target of interest, which in this case is GX 339−4. The saturation at high and low values of Γ is a natural consequence of the Comptonization process (from Shaposhnikov and Titarchuk 2009).

physical basis of these scaling techniques can be summarized as follows: (1) the QPO frequency is inversely proportional to $M_{\rm BH}$. This can be readily understood considering that the larger $M_{\rm BH}$, the larger the gravitational radius $R_G = GM_{\rm BH}/c^2$; this in turns implies larger physical distances of the accretion inflow responsible for the radiation, and hence longer dynamical timescales (which are probed by the inverse of the QPO frequency). (2) The BMC normalization is a function of black hole mass and distance: more specifically,

$N_{\rm BMC} = L/d^2$, where $L \propto \eta \dot{m} M_{\rm BH}$, with η being the radiative efficiency and $\dot{m}$ the accretion rate in Eddington units; therefore, $N_{\rm BMC} \propto \eta \dot{m} M_{\rm BH}/d^2$. The similarity of spectral evolution trends from different BH systems implies that Γ is a reliable indicator of the BH spectral state: BHs in low-accreting states are characterized by X-ray spectra with low values of Γ, whereas in highly accreting states Γ is steep. As a consequence, different BHs characterized by spectra with similar values of Γ should also have similar values of $\dot{m}$ and η (the implicit reasonable assumption here is that similar accretion states have similar radiative efficiencies). Therefore, in the $N_{\rm BMC}$ - Γ diagram, when we compare the values of $N_{\rm BMC}$ of two sources at a given value of Γ, we are actually comparing their $M_{\rm BH}$ (divided by the squared distance).

In simple terms, the necessary steps to derive $M_{\rm BH}$ with this scaling method are:

(1) construct a $\Gamma - N_{\rm BMC}$ plot for a GBH of known mass and distance, which will be used as reference (hereafter denoted by the subscript r);

(2) compute the normalization ratio between the target and the reference object $N_{\rm BMC,t}/N_{\rm BMC,r}$ by shifting in the $\Gamma - N_{\rm BMC}$ plot the target's pattern until it matches the reference one;

(3) derive the black hole mass using the following equation

$$M_{\rm BH,t} = M_{\rm BH,r} \times \left(\frac{N_{\rm BMC,t}}{N_{\rm BMC,r}}\right) \times \left(\frac{d_{\rm t}}{d_{\rm r}}\right)^2 \times f_G \tag{1.18}$$

where $M_{\rm BH,r}$ is the black hole mass of the GBH reference object, $N_{\rm BMC,t}$ and $N_{\rm BMC,r}$ are the respective BMC normalizations for target and reference objects at a fixed value of Γ, $d_{\rm t}$ and $d_{\rm r}$ are the corresponding distances, and $f_G = \cos\theta_{\rm r}/\cos\theta_{\rm t}$ is a geometrical factor that depends on the respective inclination angles and should be included only in the scenario where the X-ray soft photon emitting region has a disk-like geometry.

Table 1.1: Information on the reference sources

Reference Pattern (1)	$M_{\rm BH}(M_{\odot})$ (2)	d(kpc) (3)	A (4)	B (5)	N_{tr} (6)	β (7)
GROJ16550D05	6.3 ± 0.3	3.2 ± 0.2	1.96 ± 0.02	0.42 ± 0.02	0.023 ± 0.001	1.8 ± 0.2
GROJ1655R05			2.35 ± 0.04	0.74 ± 0.04	0.131 ± 0.001	1.0 ± 0.1
GX339D03	12.3 ± 1.4	5.8 ± 0.8	2.13 ± 0.03	0.50 ± 0.04	0.013 ± 0.0002	1.5 ± 0.3
GX339R04			2.10 ± 0.03	0.46 ± 0.01	0.037 ± 0.001	8.0 ± 1.5
XTE1550R98	10.7 ± 1.5	3.3 ± 0.3	2.96 ± 0.02	2.8 ± 0.2	0.055 ± 0.010	0.4 ± 0.1
GRS1915R97	12.9 ± 2.4	9.2 ± 0.2	2.94 ± 0.03	0.9 ± 0.07	0.186 ± 0.005	6.1 ± 1.9

Note. Column (1) Name of Reference Source followed by the phase transition (R as rise and D as Decay) and the occrrence year; (2) $M_{\rm BH}$ value via dynamical measurement; (3) distance in units of kpc; (4), (5), (6), and (7) = best-fit parameter value for A, B, N_{tr}, and β. Each parameters were found by fitting the spectral data from Shaposhnikov and Titarchuk (2009) and Titarchuk and Seifina (2009) using IDL software package LEVENBERG-MARQUART algorithm (Press et al., 1997).

The X-ray Spectral State Transition Diagram

The typical pattern shown in the $\Gamma - N_{\rm BMC}$ diagram can be parameterized by the following function

$$\Gamma(N_{\rm BMC}) = A - B \ln \left[\exp \left(1 - (N_{\rm BMC}/N_{tr})^{\beta} \right) + 1 \right] \tag{1.19}$$

where parameter A characterizes the higher saturation level of $\Gamma(N_{\rm BMC})$, B describes the lower saturation level, N_{tr} is the parameter responsible for the shift of the spectral pattern along the x-axis, and β describes the slope of the spectral trend.

In Figure 1.14, we show $\Gamma - N_{\rm BMC}$ diagrams for the available reference sources during rise (from LHS to HSS) and decay (from HSS to LHS) phases of four different outbursts. The reference sources, GRO J1655−40, GX 339−4, and XTE J1550−564, are used in Shaposhnikov and Titarchuk (2009) and the spectral transition of GRS 1915+105 in Titarchuk and Seifina (2009). The $M_{\rm BH}$ value and its distance as well as best-fit parameter values for each reference pattern is reported in Table 1.1. Each GBH carries its own advantages in this frame work − GRO J1655−40 has the best constrained binary system parameters

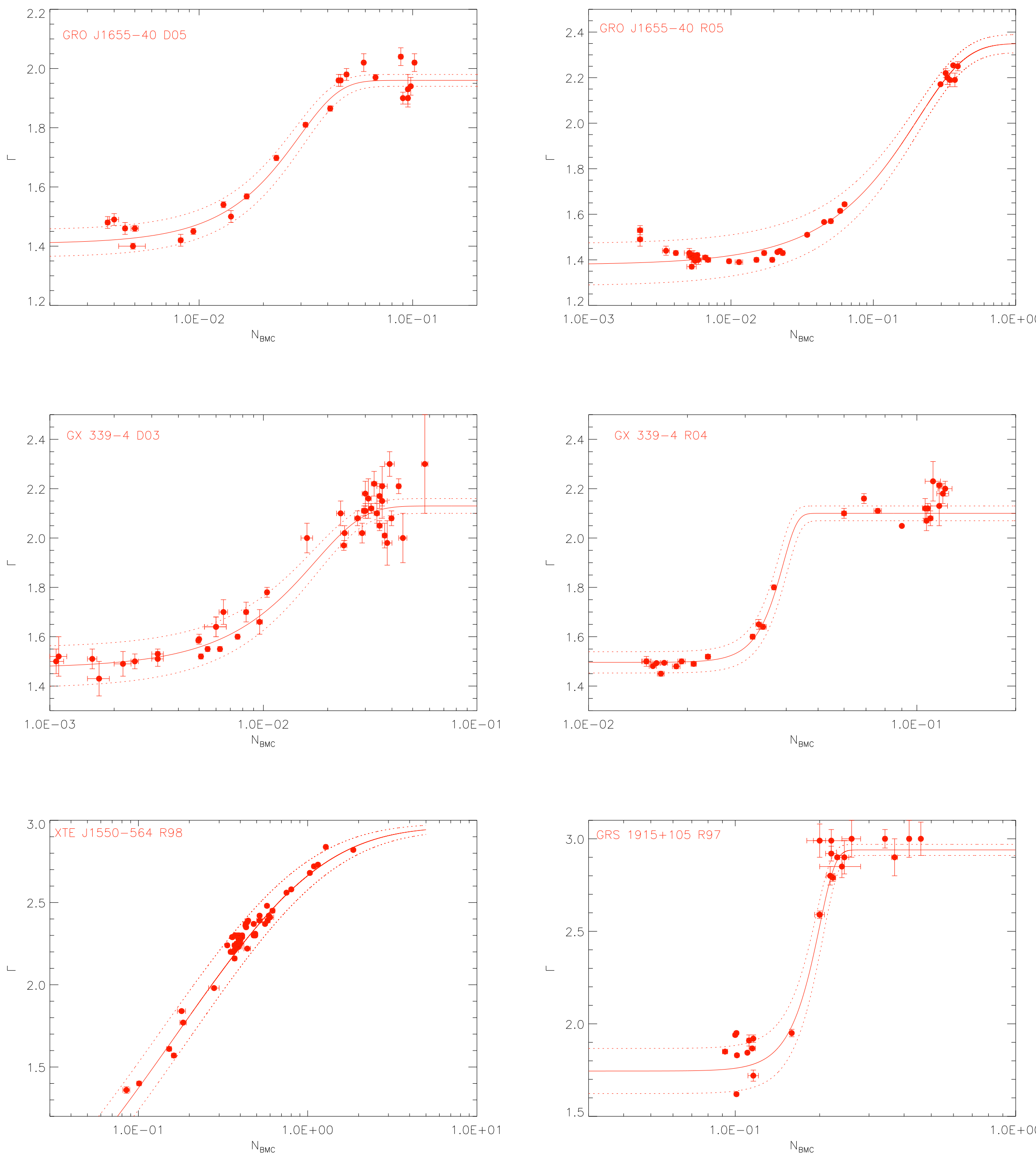

Figure 1.14: Γ–$N_{\rm BMC}$ plots for the reference GBHs. Each outburst is plotted and fitted using Equation (1.19) which is indicated by the solid line and its 1σ uncertainty by dashed lines. R indicates rise outburst and D the decay.

($M_{\rm BH}$, d, inclination angle), GX 339−4 is the prototype of GBHs having very similar spectral variability from different outburst events, XTE J1550−564 is a highly accreting GBH with the largest range spanned by photon index $\Gamma = 1.3-3$, and GRS J1915+105 is another highly accreting GBH with the high photon index saturation level of $\Gamma \sim 3$.

1.4.4 Testing The Scaling Method On Active Galactic Nuclei

There is mounting evidence that AGNs may be considered as large-scale analogs of GBHs (see, e.g., Falcke et al., 2004; Gliozzi et al., 2010; Körding et al., 2006; McHardy et al., 2006; Merloni et al., 2003; Sobolewska et al., 2009, 2011). Despite the large difference in scales, both GBHs and AGNs are believed to harbor the same central engine: a black hole and an accretion disk/corona that sometimes produces relativistic jets. Therefore, the progress made in the field of GBHs can in principle be extended to AGNs (and vice versa).

In the framework of the AGN-GBH unification, it thus appears reasonable to extend to AGNs the scaling method described before. One advantage of AGNs with respect to GBHs is that their distance is relatively well constrained via redshift, Cepheids, or other standard candles. Having only one unknown, $M_{\rm BH}$, implies that we only need one scaling law for AGNs, the $\Gamma - N_{\rm BMC}$ diagram.

To illustrate how this method can be extended to AGNs, in Figure 1.15 we show the $\Gamma - N_{\rm BMC}$ diagram for a hypothetical AGN (dashed line) and the microquasar GRO J1655−40 (thick solid line), which is one of the most reliable reference sources since the parameters of this system are tightly constrained. From Figure 1.15, assuming for the AGN $\Gamma = 1.8$, we infer that the reference normalization is $N_{\rm BMC,r} \simeq 0.3$. Inserting in Equation (1.18) this value and the other known quantities – for the reference source: the mass and distance, for the AGN: the distance and $N_{\rm BMC,t}$ that is obtained from the spectral fit of the X-ray spectrum– we immediately derive $M_{\rm BH}$.

Pilot study on reverberation mapped AGN: In order to test on firm statistical ground whether this scaling method can be successfully extended to AGNs, we applied it to a control sample of AGN with $M_{\rm BH}$ well constrained. We chose a sample with BH mass

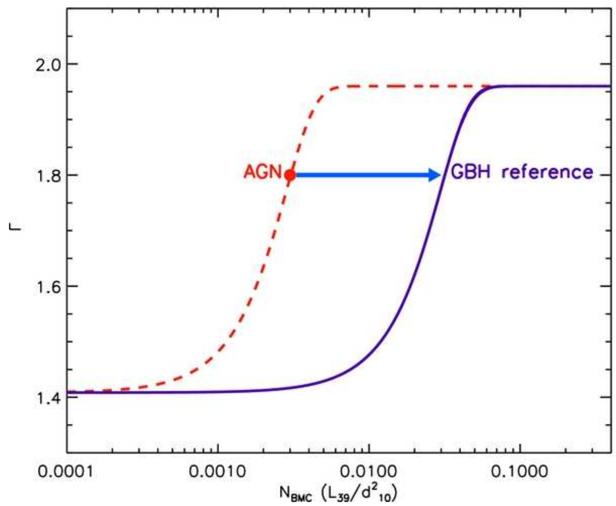

Figure 1.15: $\Gamma - N_{\rm BMC}$ diagram for the microquasar GRO J1655−40 during the decay of the 2005 outburst and for a hypothetical AGN. The thick continuous line represents the best fitting function of the GBH spectral trend. The arrow illustrates how we determine the value of $N_{\rm BMC,r}$ from the value of Γ measured for the AGN. This figure is taken from Gliozzi et al. (2011). See text for further details.

estimates derived from a direct method, and with good quality X-ray data, in order to tightly constrain the parameters of the BMC model. Nearly 30 objects with $M_{\rm BH}$ determined via reverberation mapping by Peterson et al. (2004) have been observed by *XMM−Newton*. The main properties of this sample can be summarized as follows: the sample spans a redshift range of 0.002–0.234; the values of $M_{\rm BH}$ encompass nearly 3 orders of magnitude; the bolometric luminosities, computed by integrating the spectral energy distribution over the 0.001–100 keV interval, span nearly 5 orders of magnitudes; finally, the Eddington ratio $\lambda_{\rm Edd}$, i.e. obtained from the ratio between bolometric and Eddington luminosity, ranges between 0.01–1.14 (Vasudevan and Fabian, 2009). In summary, this sample spans a considerably large region of the parameter space, providing the ideal framework to test the scaling method.

The left panel of Figure 1.16 reveals a general agreement between the $M_{\rm BH}$ values determined via reverberation mapping (solid histogram) and the corresponding ones determined with the X-ray scaling method using two different reference sources (dashed histograms).

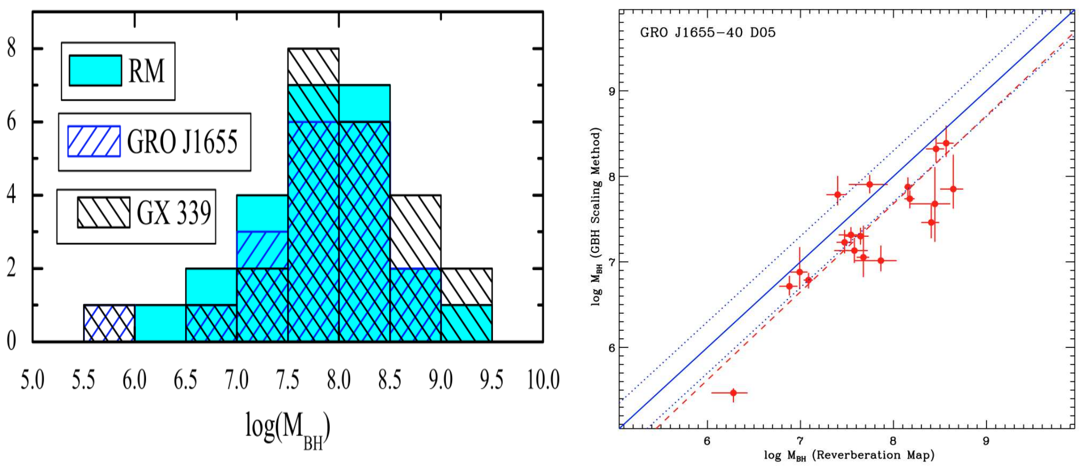

Figure 1.16: **Left:** Distributions of the $M_{\rm BH}$ values obtained with reverberation mapping (filled histogram), and with the X-ray scaling method using as references GRO J1655−40 and GX 339−4. **Right:** The $M_{\rm BH}$ values obtained with the scaling method (y-axis) are plotted versus the reverberation mapping values (x-axis). The thick solid line indicates the one-to-one correlation; the dotted lines represent the 0.3 dex levels, commonly assumed as uncertainty on the reverberation mapping estimates; the dashed line is the linear best-fit (from Gliozzi et al. 2011).

The consistency between the $M_{\rm BH}$ distributions is formally confirmed by a Kolmogorov-Smirnov test, which indicates that the distributions obtained with this new X-ray scaling method are indistinguishable from the reverberation mapping one. Further evidence of the agreement between the X-ray based $M_{\rm BH}$ estimates and the corresponding values determined via reverberation mapping is revealed by the tight correlation (and the associated highly significant linear correlation) obtained when plotting one quantity versus the other (see Figure 1.16 right panel). The detailed findings of this work have been recently published in *ApJ* (Gliozzi et al., 2011) and can be summarized as follows: 1) This novel method, which is completely independent of any assumption on the BLR nature/geometry or host galaxy characteristics, is a robust estimator of $M_{\rm BH}$ in AGN, and provides values that are in good agreement (within a factor of $\sim$2) with the corresponding values obtained with the reverberation mapping technique. 2) The best agreement with reverberation mapping values is obtained assuming a quasi-spherical geometry for the soft photon supply (i.e., $f_G = 1$ in

Equation 1.18), which lends support to the hypothesis that the soft photon emission region is quasi-spherical.

Chapter 2: Constraining Black Hole Masses in Low-accreting Active Galactic Nuclei Using X-ray Spectra

2.1 Introduction

It is now widely accepted that black holes exist on very different scales, with masses that range between 3–20 $M_\odot$ for stellar mass black holes (sMBHs) and $10^6 - 10^9$ $M_\odot$ for supermassive black holes (SMBHs) at the center of galaxies and in active galactic nuclei (AGNs), with possibly intermediate black holes ($M_{\rm BH} = 10^2 - 10^5$ $M_\odot$) whose nature is still a matter of debate.

Recent studies have provided evidence for the presence of supermassive black holes at the center of virtually every galaxy with a prominent bulge and for the existence of tight correlations between $M_{\rm BH}$ and several galaxy parameters such as the velocity dispersion or the mass of the bulge (Ferrarese and Merritt, 2000; Gebhardt et al., 2000a; Magorrian et al., 1998). This bolsters the importance and ubiquity of these systems in the universe and suggests that black hole and galaxy growth may be closely related and that black holes are essential ingredients in the evolution of galaxies.

Black holes are fairly simple objects that are completely described by only three parameters, mass, spin, and charge, with the latter generally negligible in astrophysical studies. However, since active BHs are not isolated systems but feed on the gas provided by a stellar companion or on the gas accumulated at the center of galaxies, the dimensionless accretion rate $\dot{m}$ (defined as $\dot{m} = L_{\rm bol}/L_{\rm Edd}$, where $L_{\rm bol}$ is the bolometric luminosity and $L_{\rm Edd} = 1.3 \times 10^{38}\, M_{\rm BH}/M_\odot$ erg s^{-1} the Eddington luminosity) in Eddington units should be counted as an additional basic parameter.

The determination of $M_{\rm BH}$ is one of the most crucial tasks to shed light on accretion and ejection phenomena in both supermassive and stellar BHs, because $M_{\rm BH}$ sets the time and length scales in these systems, and may play a fundamental role in the formation and evolution of galaxies. The most direct way to determine $M_{\rm BH}$ is via dynamical methods. Under the assumption of Keplerian motion, a lower limit on the mass of the compact object can be determined in GBHs by measuring orbital period and velocity of the visible stellar companion. Similarly, in nearby weakly active or quiescent galaxies the estimate of $M_{\rm BH}$ can be inferred by directly modeling the dynamics of gas or stars in the vicinity of the black hole (e.g., Kormendy and Richstone, 1995; Magorrian et al., 1998). For highly active galaxies that show significant optical variability, the estimate of $M_{\rm BH}$ relies upon the so-called "reverberation mapping" method, where the "test particles" are represented by high-velocity gas clouds, whose dynamics are dominated by the BH gravitational force and are usually referred to as the broad-line region (BLR), since their radiation is dominated by broad emission lines (Peterson, 1993).

These direct methods are the most accurate and reliable ways to constrain $M_{\rm BH}$, but at the same time have severe limitations: the methods applied to semi-quiescent galaxies require the sphere of influence of the black hole to be resolved by the instruments, and hence can be extended only to nearby objects. On the other hand, the reverberation mapping technique requires significant resources and time, and cannot be applied to very luminous sources, whose variability is typically characterized by small-amplitude flux changes occurring on very long timescales, or to sources without a detected BLR. In order to circumvent these limitations, several secondary indirect methods have been developed (see e.g., Vestergaard, 2009). Most of them rely on some empirical relationship between $M_{\rm BH}$ and different properties of the host galaxy or are based on results obtained from the reverberation mapping such as the radius-luminosity relationship (Kaspi et al., 2000). However, the extension of these empirical relationships to systems with $M_{\rm BH}$ and $\dot{m}$ vastly different from the original limited samples is still untested, and the majority of these techniques still requires a detected BLR, significantly restricting the number of possible AGNs and the black hole mass range that can be studied.

In order to perform statistical studies of BHs and understand their evolutionary history and connection to their host galaxies, it is important to explore alternative ways to determine the BH mass that are not dependent on the assumptions of optical-based methods. An important role in this field may be played by X-ray-based methods, since the X-rays are nearly ubiquitous in accreting BH systems regardless of their mass or accretion state, are less affected by absorption than optical/UV emission, and are produced and reprocessed in the vicinity of the BH thus closely tracking its activity.

Recently, Shaposhnikov and Titarchuk (2009) developed a new X-ray scaling method to determine $M_{\rm BH}$ for GBHs. This method is based on the positive correlation between X-ray photon index Γ (which is generally considered as a reliable indicator of the accretion state of the source; (see e.g., Esin et al., 1997; Shemmer et al., 2008) and the source brightness, parameterized by the normalization of the Bulk Motion Comptonization (BMC) model. The self-similarity of this spectral trend, which is observed in different GBHs during different outbursts events, makes it possible to estimate $M_{\rm BH}$ in any GBHs by scaling the dynamically-constrained value of $M_{\rm BH}$ of a GBH considered as a reference source.

With the assumption that AGNs follow the same spectral evolution as GBHs (although on much longer timescales that cannot be directly probed), in our recent work, we tested whether this novel X-ray scaling method could be extended to supermassive BHs. To this end, we utilized a sample of AGNs with good X-ray data and whose BH mass had been already determined via reverberation mapping. The results (on average the $M_{\rm BH}$ values determined with this method are within a factor of 2-3 from the reverberation mapping values) demonstrate that this method is reliable and robust for BH systems accreting at moderate and high rate ($\dot{m} \geq 1\%$) and can be used to determine BH masses at any scale (Gliozzi et al., 2011).

The presence of a positive correlation between Γ and $L_{\rm X}$ (which is at the basis of the X-ray scaling method) has been observed in highly and moderately accreting BH systems at all scales for several decades. For example, a spectral steepening as the source brightens is consistently observed in the evolution between canonical spectral states in GBHs (e.g., Esin et al., 1997; Homan et al., 2001, and references therein). A similar behavior has been also observed in individual and samples of AGNs (e.g., Markowitz and Edelson, 2001; Papadakis et al., 2002; Shemmer et al., 2008). On the other hand, in the very low accreting regime ($\dot{m} \ll 1\%$) convincing evidence of a $\Gamma - L_{\rm X}$ (or $L_{\rm X}/L_{\rm Edd}$) anti-correlation has been revealed only recently (e.g., Constantin et al., 2009; Gu and Cao, 2009; Gültekin et al., 2012; Wu and Gu, 2008; Younes et al., 2011) however for an alternative view (see Trump et al., 2011).

Here, we want to investigate the limits of applicability of this method to low-accreting BH systems, by applying it to a sample of low-accreting AGNs, which possess good-quality X-ray data (either from *Chandra* or *XMM−Newton* satellites) and with $M_{\rm BH}$ determined from direct dynamical methods. In principle, since the direct $\Gamma - L_{\rm X}$ correlation is the foundation of the scaling method and since at very low accreting levels no positive correlation is observed, it is expected that at a certain threshold value of $\dot{m}$ the X-ray scaling method should break down. Nevertheless, it is important to test if this break down actually occurs (this would provide indirect support to the foundation of the method, i.e., the self-similar spectral behavior of BHs at all scales) and at which value of $\dot{m}$ does it occur.

The description of the sample and the data reduction are provided in Sections 2.2 and 2.3, respectively. The X-ray spectral analysis is performed in Section 2.4. In Section 2.5, we apply the X-ray scaling method and show that the overall spectral behavior of our sample is consistent with an anti-correlation in the $\Gamma - L_{\rm X}/L_{\rm Edd}$ plot, which provides an alternative way to constrain $M_{\rm BH}$. The main results and their implications are summarized and discussed in Section 2.6.

2.2 Sample Description

In order to test X-ray-based methods to determine $M_{\rm BH}$ in low-accreting AGNs, we need to select objects that fulfill the following criteria: 1) they must have a direct and robust estimate of $M_{\rm BH}$; 2) they must possess good-quality X-ray data; and 3) they must accrete at low level, $L_{\rm X}/L_{\rm Edd} \ll 1\%$.

Our sample contains a total of 53 low-luminosity AGNs (LLAGNs) with bolometric luminosity less than 10^{42} erg s^{-1} (Ho et al., 2001) and whose black hole mass has been determined via dynamical methods. The physical properties of the sources are listed in Table 2.1, in which column (1) provides the source name, columns (2) and (3) right ascension and declination, (4) the $M_{\rm BH}$ value via the dynamical method, (5) the redshift-independent distance from the NSAS/IPAC Extragalactic Database (NED), (6) the Hα/Hβ ratio, (7) the flux of the narrow component of [O III]λ5007, (8) the radio luminosity, (9) the AGN class (S=Seyfert galaxies, L=LINERs), and (10) the galaxy class. The narrow-line emission and types were gathered from the Palomar Survey (Ho et al., 1997) unless stated otherwise. Based on the optical classification, this sample comprises 16 LINERs, 17 Seyfert galaxies ranging from Type 1 to Type 2, and 20 AGNs that are not optically classified.

The dynamical mass measurements are based on high spatial resolution stellar velocity measurements (Ghez et al., 2008; Gültekin et al., 2009a), gas dynamic measurements (Barth et al., 2001), and maser measurements (Miyoshi et al., 1995). All sources have been observed with *Chandra* and most have also *XMM−Newton* data. *Chandra* with its unsurpassed spatial resolution is ideal to disentangle the different X-ray components, whereas *XMM−Newton* with its large collecting area and consequent higher sensitivity provides tighter constraints on the X-ray spectral parameters for isolated point-like sources.

Table 2.1: $M_{\rm BH}$ of ULXs via the X-ray scaling method using spectral patterns of moderately accreting GBHs

Source name (1)	RA (2)	Dec. (3)	$\log(M_{\rm BH}/M_\odot)$ (4)	d (Mpc) (5)	$\mathrm{H}\alpha/\mathrm{H}\beta$ (6)	$\log(F_{[\rm O\,III]})$ (7)	$\log(L_{\rm 6cm})$ (8)	AGN class (9)	Optical class (10)
IC 1459	22 : 57 : 10.6	-36 : 27 : 44	9.44 ± 0.20[1]	29.2			39.76	L/R	E3[f]
IC 4296	13 : 36 : 39.0	-33 : 57 : 57	9.13 ± 0.07[2]	62.2			38.59	L	E1[g]
NGC 221	00 : 42 : 41.8	40 : 51 : 55	6.49 ± 0.09[3]	0.81			33.3		E2
NGC 224	00 : 42 : 44.3	41 : 16 : 09	8.17 ± 0.16[4]	0.84			32.14	L	SA(s)b
NGC 821	02 : 08 : 21.1	10 : 59 : 42	7.63 ± 0.16[5]	22.4					E6
NGC 1023	02 : 40 : 24.0	39 : 03 : 48	7.66 ± 0.04[6]	9.82					SB(rs)0-
NGC 1068	02 : 42 : 40.7	00 : 00 : 48	6.93 ± 0.02[7]	10.1	5.29	-10.46	39.18	S2	(r)SA(rs)b
NGC 1300	03 : 19 : 41.1	-19 : 24 : 41	7.85 ± 0.29[8]	22.6					SB(rs)bc
NGC 1399	03 : 38 : 29.1	-35 : 27 : 03	8.71 ± 0.06[9]	19.4				S2[b]	E1
NGC 2748	09 : 13 : 43.0	76 : 28 : 31	7.67 ± 0.50[8]	21.0	6.11	-15.00		H	Sabc
NGC 2778	09 : 12 : 24.4	35 : 01 : 39	7.21 ± 0.32[5]	38.1					E2
NGC 2787	09 : 19 : 18.6	69 : 12 : 12	7.64 ± 0.05[10]	7.48	1.89	-13.93	37.22	L	SB(r)0+
NGC 3031	09 : 55 : 33.2	69 : 03 : 55	7.90 ± 0.09[11]	3.65	3.15	-12.65	36.82	L[b]	SA(s)ab
NGC 3115	10 : 05 : 14.0	-07 : 43 : 07	8.98 ± 0.18[12]	9.68				S	SA0- sping
NGC 3227	10 : 23 : 30.6	19 : 51 : 54	7.18 ± 0.23[13]	21.1	2.9	-12.02	37.72	S1.5	SAB(s)a pec
NGC 3245	10 : 27 : 18.4	28 : 30 : 27	8.35 ± 0.11[14]	27.4	4.76	-13.42	36.98	L	SA(r)0?
NGC 3377	10 : 47 : 42.3	13 : 59 : 09	8.06 ± 0.16[5]	11.3		-10.20[c]			E5+
NGC 3379	10 : 47 : 49.6	12 : 34 : 54	8.09 ± 0.25[15]	12.6		-14.16		L	E1
NGC 3384	10 : 48 : 16.9	12 : 37 : 45	7.25 ± 0.04[5]	10.8		-10.60[c]			SB(s)0-
NGC 3585	11 : 13 : 17.1	-26 : 45 : 17	8.53 ± 0.12[16]	20.2					S0
NGC 3607	11 : 16 : 54.6	18 : 03 : 06	8.08 ± 0.15[16]	22.8	5.56	-13.26		S2[b]	SA(s)0:
NGC 3608	11 : 16 : 58.9	18 : 08 : 55	8.32 ± 0.17[5]	23.1		-14.16		L	E2
NGC 3998	11 : 57 : 56.1	55 : 27 : 13	8.37 ± 0.43[17]	19.4	4.72	-13.13	38.03	L[b]	SA(r)0?
NGC 4026	11 : 59 : 25.2	50 : 57 : 42	8.33 ± 0.11[16]	11.7	3.4	-10.95			(R')SAB(rs)ab:
NGC 4151	12 : 19 : 23.2	05 : 49 : 31	7.65 ± 0.05[18]	3.89			38.2	S1.5	SA0 spin
NGC 4258	12 : 18 : 57.5	47 : 18 : 14	7.58 ± 0.00[19]	7.59	3.94	-12.98	36.03	S1.9	SAB(s)bc
NGC 4261	12 : 19 : 23.2	05 : 49 : 31	8.74 ± 0.09[20]	24.0	4.9	-13.43	39.21	L	E2+
NGC 4278	12 : 20 : 06.8	29 : 16 : 51	9.20 ± 0.00[21]	10.0	2.5	-13.17	37.91	L	E1+
NGC 4291	12 : 20 : 18.2	75 : 22 : 15	8.51 ± 0.34[5]	31.2					E
NGC 4303	12 : 21 : 54.9	04 : 28 : 25	6.65 ± 0.35[22]	12.2	3.92	-12.97	38.46	S2[b]	SAB(rs)bc
NGC 4342	12 : 23 : 39.0	07 : 03 : 14	8.56 ± 0.19[23]	16.8					S0
NGC 4374	12 : 25 : 03.7	12 : 25 : 04	9.18 ± 0.23[24]	17.5	4.68	-13.46	38.77	S2	E1
NGC 4395	12 : 25 : 48.8	33 : 32 : 49	5.04 ± 0.00[25]	4.83	2.13	-12.46	35.56	S1.8	SA(s)m:
NGC 4459	12 : 29 : 00.0	13 : 58 : 42	7.87 ± 0.08[10]	16.6	3.24	-14.64		L	SA(r)0+

Table 2.1 – continued from previous page

Source name (1)	RA (2)	Dec. (3)	$\log(M_{\rm BH}/M_\odot)$ (4)	d (Mpc) (5)	Hα/Hβ (6)	$\log(F_{[\rm O\,III]})$ (7)	$\log(L_{\rm 6cm})$ (8)	AGN class (9)	Optical class (10)
NGC 4473	12 : 29 : 48.9	13 : 25 : 46	8.11 ± 0.35[5]	15.2					E5
NGC 4486	12 : 30 : 49.4	12 : 23 : 28	9.56 ± 0.13[26]	15.9	4.29	-12.97	39.83	L	E0+pec
NGC 4486A	12 : 30 : 57.7	12 : 16 : 13	7.13 ± 0.15[27]	15.1					E2
NGC 4564	12 : 36 : 27.0	11 : 26 : 21	7.84 ± 0.05[5]	15.8					E
NGC 4594	12 : 39 : 59.4	-11 : 37 : 23	8.76 ± 0.41[28]	13.7	3.37	-12.46[a]	37.89	Sy1.9[b]	SA(s)a spin
NGC 4596	12 : 39 : 55.9	10 : 10 : 34	7.92 ± 0.16[11]	16.8	2.12	-15.35		L	SB(r)0+
NGC 4649	12 : 43 : 40.0	11 : 33 : 10	9.33 ± 0.12[5]	14.0			37.45		E2
NGC 4697	12 : 48 : 35.9	-05 : 48 : 03	8.29 ± 0.04[5]	20.9		-15.90[d]			E6
NGC 4742	12 : 51 : 48.0	-10 : 27 : 17	7.18 ± 0.15[29]	15.5					E[h]
NGC 4945	13 : 05 : 27.5	-49 : 28 : 06	6.15 ± 0.18[30]	4.50			38.17	S[b]	
NGC 5077	13 : 19 : 31.7	-12 : 39 : 25	8.90 ± 0.22[31]	39.8	2.89	-13.82		L	E3+
NGC 5128	13 : 25 : 27.6	-43 : 01 : 09	8.48 ± 0.04[32]	4.09	3.72[a]	-13.15[e]	39.85	S2	
NGC 5252	13 : 38 : 15.9	04 : 32 : 33	9.00 ± 0.34[33]	99.3	3.72[a]	-12.41	39.05	S2[b]	S0
NGC 5576	14 : 21 : 03.7	03 : 16 : 16	8.26 ± 0.09[16]	25.8					E3
NGC 5845	15 : 06 : 0.80	01 : 38 : 02	8.46 ± 0.22[5]	24.1					E3
NGC 6251	16 : 32 : 32.0	82 : 32 : 16	8.78 ± 0.15[34]	97.6	15.1[a]	-11.90	41.01	S2	E1
NGC 7052	21 : 18 : 33.0	26 : 26 : 49	8.60 ± 0.22[35]	56.7			39.43		E3
NGC 7457	23 : 00 : 59.9	30 : 08 : 42	6.61 ± 0.17[5]	12.3		-16.18		S	SA(rs)0-?
NGC 7582	23 : 18 : 23.5	-42 : 22 : 14	7.74 ± 0.10[36]	22.2	7.6[a]	-11.35	38.55	S2[b]	Sbab

Note. $M_{\rm BH}$ reference: [1]Cappellari et al., 2002; [2]Dalla Bontá et al. 2009; [3]Verolme et al. 2002; [4]Bender et al. 2005; [5]Gebhardt et al. 2000a; [6]Bower et al. 2001; [7]Lodato and Bertin 2003; [8]Atkinson et al. 2005; [9]Gebhardt et al. 2007; [10]Sarzi et al. 2001; [11]Devereux et al. 2003; [12]Emsellem et al. 1999; [13]Hicks and Malkan 2008; [14]Barth et al. 2001; [15]Gebhardt et al. 2000b; [16]Gültekin et al. 2009b; [17]de Francesco et al. 2006; [18]Onken et al. 2007; [19]Herrnstein et al. 2005; [20]Ferrarese et al. 1996; [21]Cardullo et al. 2009; [22]Pastorini et al. 2007; [23]Cretton and van den Bosch 1999; [24]Bower et al. 1998; [25]Edri et al. 2012; [26]Macchetto et al. 1997; [27]Nowak et al. 2007; [28]Kormendy 1988; [29] listed as M. E. Kaiser et al. 2002 in preparation in Tremaine et al. 2002 but never published; [30]Greenhill et al. 1997; [31]de Francesco et al. 2008; [32]Silge et al. 2005; [33]Capetti et al. 2005; [34]Ferrarese and Ford 1999; [35]van der Marel et al. 1998; [36]Wold et al. 2006; [a]Bassani et al. 1999; [b]Véron-Cetty and Véron 2006; [c]Ciardullo et al. 1989; [d]Méndez et al. 2005; [e]Walsh et al. 2012; [f]Fabbiano et al. 2003; [g]Younis et al. 1985; [h]Naim et al. 1995.

2.3 Data Reduction

2.3.1 *Chandra* Observations

In the *Chandra* archive, for each source we selected the observations with the longest exposures and the smallest pointing offset with respect to the nominal position of the AGN. Most of the observations are the same as those analyzed by Gültekin et al. (2009a). Adding six new sources observed more recently by Gültekin et al. (2012) and 2 described by Gu and Cao (2009), the total number of sources with *Chandra* data is 53.

The data reduction was carried out homogeneously for each source as described below. Source's spectra and light curves were extracted from circular regions with a radius of 1" − 2", and their background from nearby source-free circular regions with a radius of 10" − 20". Sometimes, extraction regions were extended to $\sim$ 3" for brighter sources. The data reduction followed the standard pipeline, using *Chandra* data reduction software package version CIAO 4.4, and the nuclear source regions were confirmed after running WAVDETECT (Freeman et al., 2002). Background flares were cut above 3σ from the mean value. The positions of source and background were given as input to the SPECEXTRACT tool to create the response matrix file (RMF) and ancillary response file (ARF).

2.3.2 *XMM−Newton* Observations

36 sources (nearly 70% of the *Chandra* sample) also possess *XMM−Newton* data. We performed the data reduction following the standard procedures of Science Analysis System (SAS) version 12.0.1. We only selected good X-ray event ("FLAG=0") with patterns $0-4$ and $0-12$ for pn and MOS, respectively. The positions inferred from *Chandra* were used as center of the extraction regions with a radius of $\sim$ 10" or larger for brighter and extended sources. When the nuclear source was located at the edge of a CCD or between two CCDs, we utilized the second longest *XMM−Newton* observation. The background regions were chosen in nearby empty spaces on the same CCD for both pn and MOS cameras. We used *Chandra* images and spectra to account for the presence of additional X-ray components (e.g., diffuse

emission, jet-like structures, off-nuclear sources) in the *XMM−Newton* extraction regions. The SAS RMFGEN and ARGEN task were used to generate RMF and ARF files, respectively. Of the 36 sources observed at least once by *XMM−Newton*, 33 of them have sufficient statistics for a meaningful spectral analysis.

2.3.3 Image Inspection

Since the point spread function (PSF) of *XMM−Newton* EPIC does not allow one to firmly distinguish between point-like and extended emission in low-luminosity sources, a systematic comparison of *XMM−Newton* and *Chandra* images was done to investigate the presence of additional X-ray components in the extraction region.

To this end, we overlapped *Chandra* image contours on the corresponding *XMM−Newton* images. From the *Chandra* images, we also measured source counts using different extraction regions (with radii of 10" and 20"), in order to estimate the contribution of off-nuclear components encompassed by the larger extraction region of *XMM−Newton*.

We illustrate this procedure in Figure 2.1 using NGC 4151 as an example of a clearly isolated nuclear source, NGC 221 (also known as M32) as an example of a LLAGN surrounded by bright nearby objects, NGC 1399 as an example of diffuse emission, and NGC 5128 showing a LLAGN with a jet-like structure. *Chandra* and *XMM−Newton* images are in the left and right hand panels, respectively.

NGC 4151 (the panel in the first row of Figure 2.1) is a well-known nearby ($D \sim 13.3$ Mpc; Mundell et al., 1999) Seyfert 1.5 galaxy (Osterbrock and Koski, 1976). Both images show that it is an isolated source. The *Chandra* net count difference of $\sim 20\%$ between the extraction region with radius of 1.5" (1.3×10^5) and that with radius of 20" ($\sim 1.7 \times 10^5$) confirms that in NGC 4151 the contribution from the extended emission is negligible. Out of 53 LLAGNs, 22 sources appear to have an isolated central source.

The *Chandra* image of NGC 221 (the panel in the second row of Figure 2.1) shows the presence of two additional sources inside of the 20" radius. They are indicated by solid lined circles. A source brighter than the AGN in NGC 221, 'Source 1' in Figure 2.1, is located 8.3" southeast of NGC 221 and a dimmer source ('Source 2') 20" away in the western direction. Although 'Source 1' and the nucleus of NGC 221 are clearly distinguishable with the sub-arcsecond spatial resolution of *Chandra*, the *XMM−Newton* image on the right hand panel reveals a single emission component. In this case, the *XMM−Newton* spectrum is dominated by the brightest off-nuclear source. As a consequence, the *XMM−Newton* observation of NGC 221 cannot be used to characterize the properties of the LLAGN. Using *Chandra* data, we find that 92% of total counts (1.4×10^4) in 10" are from source 1 whereas the counts of NGC 221 are 6.1×10^2. There were a total of 23 objects containing off-nuclear sources within 10" − 20" radii from the central source. For six objects (NGC 2787, NGC 4278, NGC 4374, NGC 4945, NGC 4649, and NGC 5576) the central source emission dominates and the contribution from off-nuclear sources appears to be negligible. Therefore, in these cases, the *XMM−Newton* data can be used for the spectral analysis. For the remaining 5 sources (NGC 221, NGC 224, NGC 1023, NGC 3585, and NGC 4291) only *Chandra* data can be used to investigate the AGN spectral X-ray properties given the significant contamination in the *XMM−Newton* data.

The left and right bottom panels of Figure 2.1 show the cases of two sources (NGC 1399 and NGC 5128) whose X-ray emission in the *XMM−Newton* extraction region is severely contaminated by extended emission and jet emission, respectively. Despite the fact that 12 sources are also classified as radio galaxies, only 3 (NGC 4486, NGC 4594, and NGC 5128) show the presence of an extended jet-like structure in the *Chandra* images.

In summary, after the visual inspection of all *Chandra* images of our sample, 22 appear to be isolated sources (indicated by "iso" in the X-ray morphology classification reported in Table 2.2), 23 LLAGNs contain off-nuclear sources within 20" ("off" in Table 2.2), and the remaining have either significant extended emission ("ext" in Table 2.2) or jet-like structures ("jet").

2.4 X-ray Spectral Analysis

We extracted spectra in the energy range from 0.3 to 10 keV for all isolated sources and for those without significant off-nuclear contribution with *XMM−Newton* data (24 sources), and for the remaining 29 sources we used *Chandra* data. We grouped 20 or 15 counts per bin, which is appropriate for the use of the χ^2 statistics. To increase the statistics for the *XMM−Newton* observation, we fitted simultaneously the EPIC pn, MOS1, and MOS2 spectra. For *Chandra* spectra if the number of counts per extraction region was low (e.g., ≤ 100), the spectra were kept ungrouped and the C-statistic was used (Cash, 1979). Overall, we used the C-statistics for 24 *Chandra* spectra and 2 *XMM−Newton* spectra. All sources in our sample were systemically fitted with a base-line model comprising a power law (PL) and two absorption models, one fixed at the Galactic value and the other left free to vary to mimic the intrinsic local absorption. When necessary, Gaussian components were added to fit line-like features.

The spectral results are reported in Table 2.2. For sources with unconstrained intrinsic absorption value, we reported the upper limits. The vast majority of the sample have X-ray photon indices in the range from 1 to 3, with a few objects yielding very hard values ($\Gamma < 1$). Unabsorbed luminosities $L_{\rm X}$ are in the range of $10^{38} - 10^{43}$ erg s^{-1}, with the exceptions of NGC 221, NGC 224, and NGC 4486A that have low luminosities of order of $10^{36} - 10^{37}$ erg s^{-1}. Overall, the spectral fits of 53 sources were in the range of $0.8 \leq \chi^2_{\rm red} \leq 1.5$ for the χ^2 statistics and the C-statistic/degree-of-freedom also was in a similar range.

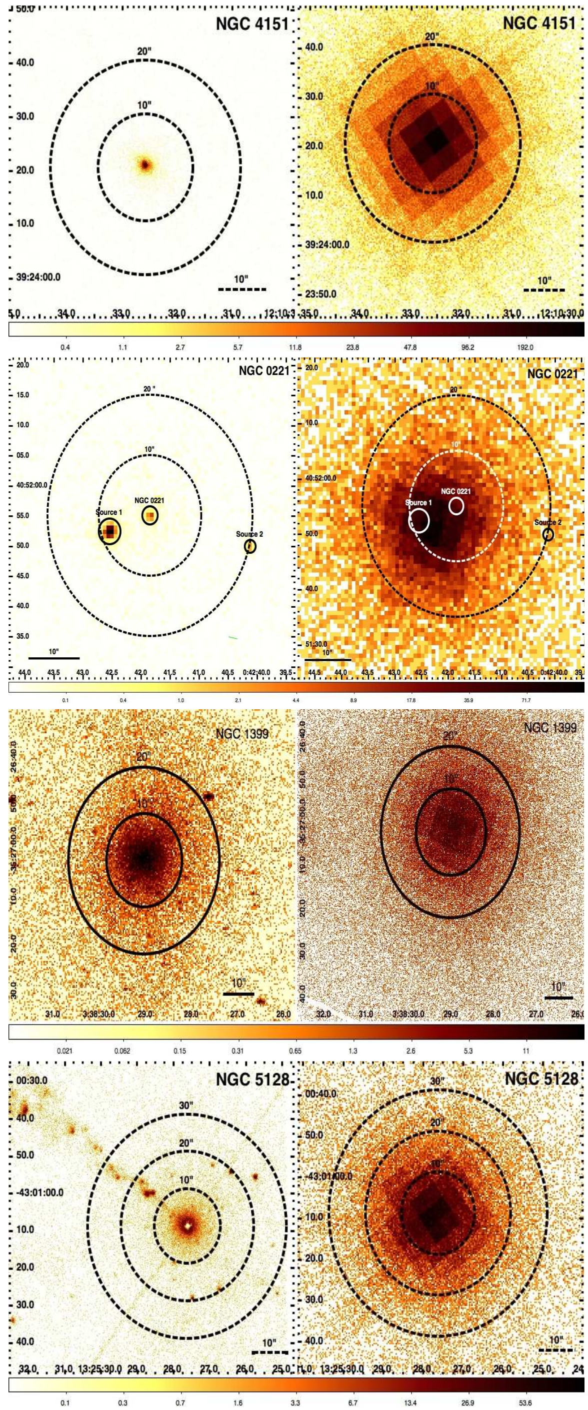

Figure 2.1: Images of NGC 4151, NGC 221, NGC 1399, and NGC 5128. The left hand panels are *Chandra* images and the right hand panels *XMM−Newton* images. Circles with different lines and colors indicate the extended regions for count estimations and nearby sources for the NGC 221 case. NGC 4151 is an example of a clear nuclear source, NGC 221 of a LLAGN surrounded by nearby objects, NGC 1399 of an AGN with substantial extended emission, and NGC 5128 of a LLAGN with jet-like emission presences.

Table 2.2: Spectral analysis

Source name (1)	Instrument (2)	Osb ID (3)	N_{H} (4)	Γ (5)	$\log(L_{\mathrm{X}})$ (6)	Statistics (7)	X-ray mor. (8)	$\log(L_{\mathrm{X}}/L_{\mathrm{Edd}})$ (9)	R_{X} (10)
IC 1459	X	0135980201	0.16 ± 0.01	1.99 ± 0.02	40.76	576.06/574	iso	-6.79	-1.00
IC 4296	X	0672870101	0.09 ± 0.01	1.49 ± 0.02	41.47	733.20/630	iso	-5.77	-2.88
NGC 221	C	5690	≤ 0.02	2.29 ± 0.16	35.92	32.90/24	off	-8.68	-2.62
NGC 224	C	1575	0.03 ± 0.01	2.50 ± 0.09	36.77	63.86/56	off	-9.51	-4.63
NGC 821	C	6314	≤ 0.16	1.76 ± 0.48	38.67	$38.70/35^{a}$	off	-7.07	
NGC 1023	C	8464	0.08 ± 0.03	2.14 ± 0.12	38.66	$135.36/179^{a}$	off	-7.11	
NGC 1068	C	344	≤ 0.001	2.56 ± 0.02	40.77	305.01/210	ext	-4.27	-1.59
NGC 1300	C	11775	3.83 ± 0.77	2.24 ± 0.14	39.68	$85.37/107^{a}$	iso	-6.28	
NGC 1399	X	0400620101	0.17 ± 0.01	3.02 ± 0.05	39.87	1000.58/753	iso	-6.95	
NGC 2748	C	11776	0.15 ± 0.14	2.34 ± 0.65	38.30	$11.75/17^{a}$	off	-7.48	
NGC 2778	C	11777	≤ 0.20	2.29 ± 0.57	38.43	$30.36/28^{a}$	off	-6.89	
NGC 2787	X	0200250101	0.06 ± 0.02	2.03 ± 0.06	39.09	131.82/115	off	-6.66	-1.87
NGC 3031	X	0657801801	0.05 ± 0.01	2.06 ± 0.01	40.27	999.93/896	iso	-5.74	-3.45
NGC 3115	C	11268	0.03 ± 0.03	2.11 ± 0.20	38.35	$97.60/125^{a}$	off	-8.74	
NGC 3227	X	0400270101	$\cdots$	1.41 ± 0.003	42.06	2050.46/1890	iso	-3.23	-4.34
NGC 3245	C	2926	≤ 0.23	1.83 ± 0.36	39.27	$39.93/57^{a}$	iso	-7.19	-2.29
NGC 3377	C	2934	0.15 ± 0.05	2.06 ± 0.23	38.29	$66.62/93^{a}$	off	-7.88	
NGC 3379	C	7076	0.10 ± 0.04	2.26 ± 0.21	38.33	$89.83/113^{a}$	off	-7.87	
NGC 3384	C	11782	≤ 0.21	1.83 ± 0.27	38.55	$51.15/73^{a}$	off	-6.81	
NGC 3585	C	9506	0.08 ± 0.03	2.39 ± 0.20	38.78	$103.00/115^{a}$	off	-7.86	
NGC 3607	X	0099030101	0.06 ± 0.04	2.63 ± 0.22	38.85	33.15/35	iso	-7.34	
NGC 3608	C	2073	≤ 0.23	2.44 ± 0.31	38.58	$42.98/63^{a}$	ext	-7.85	
NGC 3998	X	0090020101	0.01 ± 0.01	1.85 ± 0.01	41.43	1159.15/1163	iso	-5.05	-3.40
NGC 4026	C	6782	≤ 0.33	2.11 ± 0.55	38.06	$21.05/29^{a}$	ext	-8.38	
NGC 4151	X	0143500301	≤ 0.08	-0.46 ± 0.00	42.79	1899.16/1594	iso	-2.97	-4.59
NGC 4258	X	0400560301	0.38 ± 0.01	2.10 ± 0.34	40.45	1253.17/1142	iso	-5.24	-4.42
NGC 4261	X	0056340101	≤ 0.02	0.82 ± 0.03	40.94	561.75/441	iso	-5.91	-1.73
NGC 4278	X	0205010101	0.02 ± 0.01	2.06 ± 0.01	40.26	934.64/929	off	-7.05	-2.35
NGC 4291	C	11778	≤ 0.10	2.11 ± 0.23	39.12	$75.50/87^{a}$	off	-7.50	
NGC 4303	X	0205360101	≤ 0.18	2.90 ± 0.37	39.06	49.45/43	iso	-5.70	-0.60
NGC 4342	C	12955	≤ 0.08	1.90 ± 0.15	38.62	$159.76/182^{a}$	off	-8.05	
NGC 4374	X	0673310101	≤ 0.02	2.16 ± 0.05	39.68	347.37/315	off	-7.61	-0.91
NGC 4395	X	0142830101	0.24 ± 0.01	0.96 ± 0.01	40.16	3030.09/2394	iso	-2.99	-4.60
NGC 4459	X	0550540101	0.20 ± 0.02	1.99 ± 0.09	39.37	147.63/162	iso	-6.61	

Table 2.2 – continued from previous page

Source name (1)	Instrument (2)	Osb ID (3)	$N_{\rm H}$ (4)	Γ (5)	$\log(L_{\rm X})$ (6)	Statistics (7)	X-ray mor. (8)	$\log(L_{\rm X}/L_{\rm Edd})$ (9)	$R_{\rm X}$ (10)
NGC 4473	C	4688	≤ 0.28	1.70 ± 0.52	38.97	$22.96/28^{a}$	ext	-7.25	
NGC 4486	C	2707	≤ 0.001	1.67 ± 0.01	41.24	582.59/400	jet	-6.43	-1.41
NGC 4486A	C	11783	≤ 0.21	1.47 ± 0.29	37.00	$57.15/61^{a}$	ext	-8.24	
NGC 4564	C	4008	≤ 0.15	1.75 ± 0.29	38.89	$64.17/61^{a}$	off	-7.06	
NGC 4594	X	0084030101	0.14 ± 0.01	1.85 ± 0.02	40.51	551.35/574	jet	-6.36	-2.62
NGC 4596	C	11785	≤ 0.16	1.48 ± 0.24	39.28	$58.83/69^{a}$	off	-6.75	
NGC 4649	X	0502160101	0.06 ± 0.02	2.55 ± 0.02	40.06	1254.12/811	off	-7.38	-2.61
NGC 4697	C	4730	≤ 0.16	1.41 ± 0.19	39.00	$68.99/94^{a}$	off	-7.40	
NGC 4742	C	11779	0.04 ± 0.04	1.76 ± 0.17	39.15	$95.84/135^{a}$	off	-6.14	
NGC 4945	X	0204870101	≤ 0.03	0.03 ± 0.03	40.13	633.61/502	off	-4.13	-1.96
NGC 5077	C	11780	0.14 ± 0.06	1.88 ± 0.23	39.73	$78.05/83^{a}$	iso	-7.28	
NGC 5128	C	3965	5.50 ± 0.13	-0.27 ± 0.02	40.89	183.32/216	jet	-5.70	-1.04
NGC 5252	X	0152940101	2.08 ± 0.01	1.11 ± 0.01	43.11	2226.37/2050	iso	-4.00	-4.06
NGC 5576	X	0502480701	$\cdots$	1.83 ± 0.19	39.21	$295.30/325^{a}$	off	-7.16	
NGC 5845	X	0021540501	≤ 0.07	2.27 ± 0.34	38.85	$163.04/209^{a}$	iso	-7.72	
NGC 6251	X	0056340201	0.04 ± 0.01	1.93 ± 0.02	42.67	1211.77/1069	iso	-4.22	-1.66
NGC 7052	C	2931	0.06 ± 0.04	2.71 ± 0.27	40.24	$68.57/79^{a}$	iso	-6.47	-0.81
NGC 7457	C	11786	≤ 0.19	1.41 ± 0.33	38.36	$25.89/39^{a}$	iso	-6.36	
NGC 7582	X	0204610101	0.12 ± 0.01	0.07 ± 0.03	41.13	1581.04/1044	iso	-4.72	-2.58

Note. Column (1) source name; (2) observation ID; (3) counts in source region; (4) intrinsic absorption value in units of 10^{22} cm^{-2}, (5) photon index; (6) unabsorbed luminosity in $2-10$ keV; (7) χ^2/degree-of-freedom (^{a}C-statistic/degree-of-freedom); (8) X-ray morphology (iso – central AGN; off – presence of nearby objects within 10 arc sec; ext – diffused emission, jet – jet-like structure emission); (9) $\log(L_{\rm X}/L_{\rm Edd})$; (10) X-ray radio-loudness parameter, $R_{\rm X}(=\log(L_{\rm R}/L_{\rm X}))$.

For completeness, for sources with both *Chandra* and *XMM−Newton* observations, we have compared the photon index and X-ray flux measured by the two satellites at different epochs. The vast majority of the AGNs shows consistent values with variations within the 3σ level. The only discrepancies are observed in objects that have poorly constrained *Chandra* spectra with Γ either very steep (> 3) or very flat (< 1 or inverted spectra). We can therefore conclude that flux and spectral variability does not significantly affect our analysis.

Combining the X-ray luminosities inferred from the spectral analysis with the black hole masses from dynamical measurements, we derive the X-ray Eddington ratio, $L_{\mathrm{X}}/L_{\mathrm{Edd}}$ ($L_{2-10\,\mathrm{keV}}/L_{\mathrm{Edd}}$), for all the sources. Throughout the paper we use L_{X} to indicate the luminosity in the $2 - 10$ keV energy range, which is the most common band used in X-ray studies and allow a direct comparison with literature results. These values of $\log(L_{\mathrm{X}}/L_{\mathrm{Edd}})$, reported in Table 2.2, range between -10 and -3, with a mean of -6.5 ± 1.5. The distribution of $\log(L_{\mathrm{X}}/L_{\mathrm{Edd}})$ for each optical class is plotted in Figure 2.2. Assuming a bolometric correction of $15 - 30$, which is appropriate for low-accreting AGNs (see, e.g., Vasudevan and Fabian, 2009), we obtain Eddington ratio values $\log(L_{\mathrm{bol}}/L_{\mathrm{Edd}})$ ranging between -8.8 and -1.8 with a mean of -5.3, which confirms that this sample comprises only low-accreting AGNs.

Very flat X-ray spectra are often associated with heavily absorbed AGNs. In the most extreme cases (i.e., for Compton-thick sources with $N_{\mathrm{H}} > 10^{24}\,\mathrm{cm}^{-2}$), the direct coronal emission is completely absorbed and the detected X-rays are thought to be produced by reflection. Since in these sources the estimated L_{X} is severely underestimated and Γ is not representative of the direct emission, it is not possible to extend the X-ray scaling method to Compton-thick AGNs. For this reason, it is crucial to identify (and exclude from further analysis) Compton-thick sources. Typically, two different approaches are used to find Compton-thick candidates: 1) the detection of Fe Kα lines with large equivalent width (EW$>$ 1keV) and 2) the use of the $T_{\mathrm{ratio}} = F_{2-10\mathrm{keV}}/F_{[\mathrm{O\,III}]}$ parameter (where $F_{[\mathrm{O\,III}]}$ is corrected for optical reddening), with the assumption that the X-ray flux is associated with

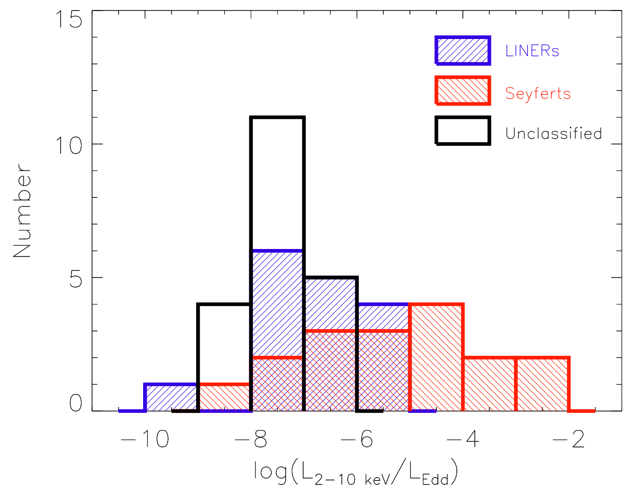

Figure 2.2: Distribution of L_X/L_{Edd}. The histogram filled with positive slopes indicates LINERs, the negative slopes filled represents Seyferts, and the empty one unclassified AGNs.

the absorbed AGN component, whereas the [O III] flux is considered a reliable indicator of the isotropic emission since it is mostly produced in the unobscured narrow line region (Bassani et al., 1999). Past studies have shown that Compton-thick objects are characterized by values of T_{ratio} below 1.

We have computed the T_{ratio} factor for all the objects of our sample with optical line measurements. The results are plotted in Figure 2.3 where the lines represent the expected correlation between T_{ratio} and N_H for Seyfert galaxies under the assumption that the X-ray flux is absorbed by the measured N_H. Figure 2.3, combined with results from the spectral analysis showing flat spectra and in some cases a Fe Kα line with large EW, suggests that 8 sources (NGC 1068, NGC 2748, NGC 3607, NGC 3245, NGC 4303, NGC 4374, NGC 4945, and NGC 7582) may be genuine Compton-thick candidates, in agreement with independent findings in the literature (Bianchi et al., 2009; González-Martín et al., 2009; Marinucci et al., 2012; Yaqoob, 2012). To be conservative, we exclude from further analysis these 8 objects.

Sources with flat spectra but without evidence for Compton thickness and sources that

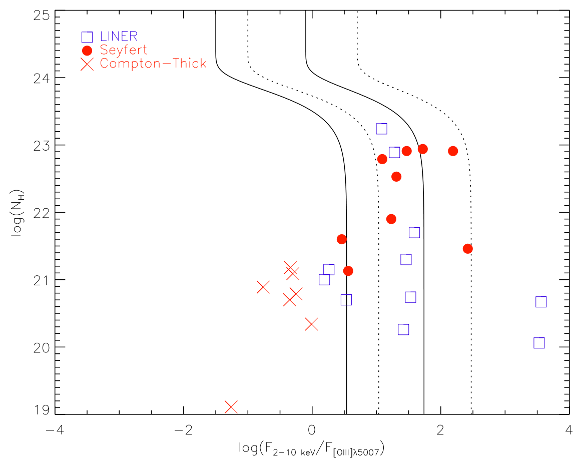

Figure 2.3: Plot of $\log(N_{\mathrm{H}})$ vs. $\log(F_{2-10\,\mathrm{keV}}/F_{[\mathrm{OIII}]})$. The filled circles indicate Seyfert galaxies and the open squares LINERs. The cross mark "x" was used to indicate the Compton-thick candidates. The solid lines indicate the expected correlation derived by Cappi et al. (2006) assuming that L_{X} is absorbed by the measured N_{H} and a 1% reflected component. Similarly the dashed lines indicate the correlation derived by Maiolino et al. (1998).

showed substantial residuals when fitted with our simple base-line model were re-fitted with more complex models. These spectral models may comprise a thermal component (APEC in XSPEC) to account for galaxy contribution, a blackbody to mimic a soft excess, a partial covering model (ZPCFABS) to account for absorbers with patchy geometry and a reflection component (PEXRAV). This additional spectral analysis yielded steeper photon indices as indicated by Table 2.3 that reports the most relevant spectral parameters.

In summary, all sources were reasonably well fitted by either an absorbed power law or slightly more complex models, yielding Γ values in the range $1.3 - 3$ and L_{X} between 10^{37} and 10^{43} erg s^{-1}.

Table 2.3: Spectral analysis − for objects with very flat spectra

Name (1)	Model (2)	$N_{\rm H}$ (3)	R (4)	$E_{\rm break}$ (5)	CF (6)	kT (7)	Γ (8)	Fe Kα (9)	EW (10)	$\log(L_{\rm X})$ (11)	χ^2/dof (12)
NGC 1300	pcfabs(pow)	3.83 ± 0.77			0.96 ± 0.02		2.24 ± 0.14			39.68	85.37/107[a]
NGC 3031	wabs(bb+pow)					0.29 ± 0.02	1.90 ± 0.01			39.38	985.49/895
NGC 3115	pcfabs(pow)	0.13 ± 0.08			0.70 ± 0.33		2.34 ± 0.24			38.09	80.94/126
NGC 3227	pcfabs(pow)+gauss	6.16 ± 0.15			0.91		1.39 ± 0.01	6.38 ± 0.01	0.06 ± 0.02	41.77	1866.78/1739
NGC 4151	pcfabs(pow+apec+gauss)	3.38 ± 0.02			0.95	0.14	1.33 ± 0.01	6.37 ± 0.01	0.06 ± 0.02	42.88	2617.68/1892
NGC 4258	pow+wabs(pow)	8.74 ± 0.20					1.70 ± 0.02			40.51	966.56/945
NGC 4261	pow+pcfabs(pow)	7.71 ± 0.62					1.65 ± 0.03			41.16	457.95/442
NGC 4342	pcfabs(pow)				0.78 ± 0.02		1.61 ± 0.12			39.81	172.65/173[a]
NGC 4395	pcfabs(apec+pow)	0.79 ± 0.02			0.72	0.19	1.11 ± 0.01			39.96	3197.11/2394
NGC 4596	pcfabs(pow)	17.20			0.05		1.89 ± 0.36			38.86	36.87/67
NGC 4649	pcfabs*apec*pow	0.13 ± 0.01			0.82 ± 0.02	0.87	1.64 ± 0.03			40.12	1250.62/798
NGC 4697	pcfabs(pow)	0.19 ± 0.07			≤ 0.79		2.08 ± 0.30			38.25	50.27/91
NGC 5128	abs(apec+pow)	8.14 ± 0.16				0.11	0.32 ± 0.01			40.40	245.92/216
NGC 5128	wabs(bknpo+pexrav)	8.09 ± 0.27	0.63 ± 0.09	4.68 ± 0.07			0.22 ± 0.01	6.42 ± 0.03	0.03	40.88	191.36/200
NGC 6251	pcfabs*apec*pow	0.40 ± 0.03			0.54 ± 0.02	0.61 ± 0.03	1.83 ± 0.01			42.72	1143.05/1059
NGC 7052	pcfabs(bb+pow)					0.16 ± 0.03	1.76 ± 0.36			40.43	13.46/15
NGC 7457	wabs(apec+pow)	0.29 ± 0.09				0.13 ± 0.02	1.52 ± 0.39			38.50	11.17/12

Note. Column (1): source name; (2): model used; (3): intrinsic absorption value in units of 10^{22} cm^{-2}; (4): reflection factor ($0 \leq R \leq 1$: 0 - no reflection component: 1 - isotropic source above disc); (5): energy break (keV); (6): dimensionless coverage fraction; (7): temperature of soft excess in units of keV. (8): photon index; (9): Fe Kα line (keV); (10): equivalent width (keV); (11): unabsorbed luminosity in 2-10 keV; (12): χ^2/degree-of-freedom.

[a]Indicates C-statistic/degree of freedom.

2.4.1 X-ray Radio-loudness

Combining the X-ray luminosity inferred from the spectral analysis and the radio luminosity from the literature, we computed the X-ray radio loudness parameter, $R_{\rm X} = L(6\,{\rm cm})/{\rm L}_{2-10\,{\rm keV}}$, which was introduced by Terashima and Wilson (2003) to reduce the extinction that affects the optical emission used in the classical radio-loudness parameter. The values of $R_{\rm X}$ for each objects are reported in Table 2.2. For the 26 sources (9 LINERs, 14 Seyferts, 3 unclassified) for which the radio data are available, $\log(R_{\rm X})$ ranges between -5 and 0 with a mean of -2.5 ± 1.3. These values are consistent with those of the sample of low-luminosity Seyfert galaxies analyzed by Panessa et al. (2007). Similar to Panessa et al. (2007) we did not find any correlation between $R_{\rm X}$ and $L_{\rm X}$, whereas there is suggestive evidence for an anti-correlation between $R_{\rm X}$ and $L_{\rm X}/L_{\rm Edd}$. However, unlike Panessa et al. (2007) the anti-correlation in our sample is not statistically significant: the negative slope is consistent with 0 within 2σs. This can be explained either but the limited number of objects with radio data in our sample or by the fact that our objects are accreting at a much lower level and in this regime no correlation is expected between radio-loudness and Eddington ratio, as demonstrated by Sikora et al. (2007).

We also looked for any correlation between Γ and $R_{\rm X}$ and plotted of Γ versus $R_{\rm X}$ is in Figure 2.4. When all objects with $R_{\rm X}$ are included, there is no evidence for any correlation (the Spearman's $\rho-$rank is 0.45 with a probability of $P = 0.03$). If we exclude the Compton-thick candidates and the source with very low Γ, then a weak positive correlation of $\Gamma = (0.17 \pm 0.05)R_{\rm X} + (2.16 \pm 0.22)$ with the RMS value of 0.22 is found.

2.5 Estimation Of $M_{\rm BH}$ With X-rays

2.5.1 X-ray Scaling Method

In a recent study on GBHs, Shaposhnikov and Titarchuk (2009) showed that spectral transitions of different GBHs present two similar positive correlations between temporal and

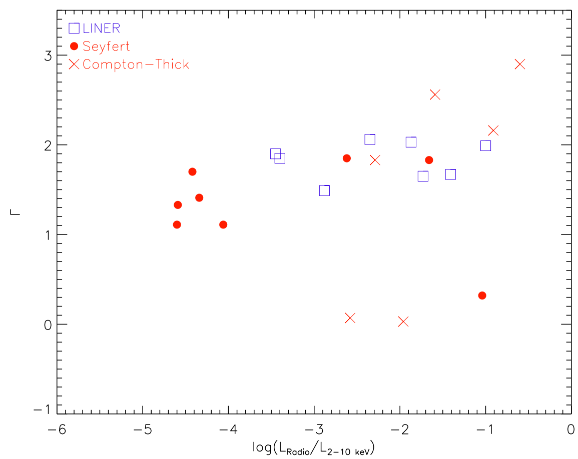

Figure 2.4: Plot of Γ vs. $\log(L(6\text{cm})/\mathrm{L}_{2-10\,\mathrm{keV}})$. Open squares were used to indicate LINERs, filled circles for Seyferts, and crosses for Compton-thick candidates.

spectral properties: 1) a correlation between the quasi periodic oscillation (QPO) frequency and the photon index and 2) a correlation between N_{BMC}, the normalization of the bulk Comptonization (BMC) model, and the photon index. Because different BHs show similar trends in the $\Gamma-\mathrm{QPO}$ and $\Gamma-N_{\mathrm{BNC}}$ diagrams, it can be shown that M_{BH} (and distance) of any GBH can be determined by simply shifting this self-similar function until it matches the spectral pattern of a GBH of known M_{BH} and distance (considered as a reference source).

In the following, we briefly describe the Comptonization model used in the X-ray scaling method, the basic characteristics of the technique utilized to estimate M_{BH}, and the main results obtained applying this method to AGNs.

It is widely accepted that the X-ray emission associated with BH systems is produced by the Comptonization process in the corona. The BMC model is a simple and robust Comptonization model which equally well describes thermal and bulk Comptonization (Titarchuk et al., 1997). The BMC model is characterized by four parameters: (1) the temperature of the thermal seed photons, kT, (2) the energy spectral index α (related to the photon index by the relation $\Gamma = \alpha + 1$), (3) $\log(A)$ which is related to the Comptonization fraction by

$f = A/(1 + A)$ (where f is the ratio between the number of Compton scattered photons and the number of seed photons), and (4) the normalization, $N_{\rm BMC}$ which depends on the luminosity and the distance, ($N_{\rm BMC} \propto L/d^2$).

The X-ray scaling method, based on two diagrams $\Gamma -$ QPO and $\Gamma - N_{\rm BMC}$, allowed the estimate of $M_{\rm BH}$ and distance in several GBHs by scaling the temporal and spectral properties of a reference GBH. However, the much longer timescales of AGNs and the absence of detectable QPOs do not allow the use of the $\Gamma -$ QPO diagram. On the other hand, the $\Gamma - N_{\rm BMC}$ plot can be easily extended to AGNs assuming that AGNs follow a similar spectral evolution as GBHs. This method relies on the direct dependence of the BMC normalization on $M_{\rm BH}$: $N_{\rm BMC} = L/d^2$, where $L \propto \eta \dot{m} M_{\rm BH}$ is the accreting luminosity, η is the radiative efficiency and $\dot{m}$ the accretion rate in Eddington units. Therefore, the normalization, $N_{\rm BMC}$, can be expressed as a function of M_{BH}: $N_{BMC} \propto \eta \dot{m} M_{\rm BH}/d^2 = M_{\rm BH}/d^2$, which is derived assuming that different BHs in the same spectral state (defined by the value of Γ) are characterized by similar values of η and $\dot{m}$.

With this X-ray scaling method, Gliozzi et al. (2011) estimated $M_{\rm BH}$ for a well defined sample of AGNs accreting at moderate/high level ($\dot{m} \gg 1\%$) whose BH mass was determined via reverberation mapping and which had good quality *XMM−Newton* archival data. The good agreement between the $M_{\rm BH}$ values determined by these two methods (the RMS around the one-to-one correlation between $\log M_{\rm BH,Scale}$ and $\log M_{\rm BH,RM}$ is 0.35 using GRO J1655−40 as a reference) confirmed the validity of this novel technique that can be successfully used for both sMBHs and SMBHs.

At very low accreting rate however, X-rays are likely to be produced by different mechanisms (for example by advection dominated accretion flows, ADAFs, or can be directly related to jet emission). Moreover, the applicability of the X-ray scaling method is questionable, since it is based on the similarity of the spectral transition of BHs at relatively high accretion rate ($L_{\rm X}/L_{\rm Edd} \geq 10^{-2}$), which is described by a positive correlation in the $\Gamma-$flux diagram.

To test whether the scaling method can be applied to LLAGNs, we fitted their spectra with the BMC model. LLAGNs with $\Gamma = 1.3 - 3$ were compared to different spectral evolution trends of GBHs. The X-ray scaling method results are shown in Figure 2.5. There is a clear inconsistency between the values from the scaling method and those obtained from dynamical methods.

The vast majority of the $M_{\rm BH}$ inferred from the scaling methods lie well below the one-to-one correlation (indicated by the solid line), and appear to be underestimated by $2-4$ orders of magnitude. This indicates that the X-ray scaling method cannot be used to constrain the $M_{\rm BH}$ of very low-accreting AGNs. The only noticeable exceptions are NGC 3227 and NGC 4151, which appears to be fully consistent with their corresponding dynamical estimate, and NGC 4395 and NGC 5252, that are marginally consistent. Importantly, these sources have the highest $L_{\rm X}/L_{\rm Edd}$ values in our sample and suggest that the scaling method is still valid for $L_{\rm X}/L_{\rm Edd}$ of the order of $10^{-3} - 10^{-4}$.

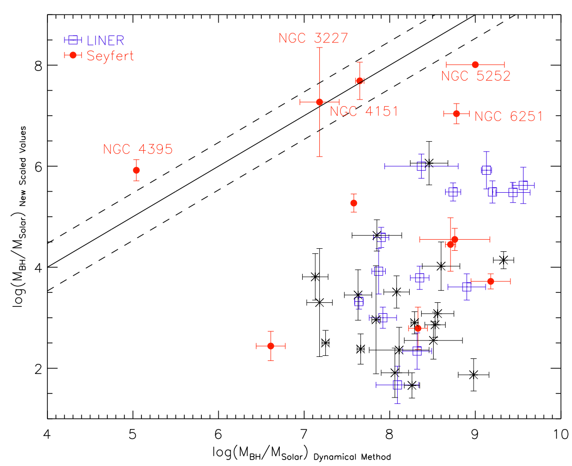

Figure 2.5: $M_{\rm BH}$ values obtained with the scaling method plotted vs. $M_{\rm BH}$ values measured by dynamical method. The Seyfert sample is plotted with filled circles, open squares for LINERs, and crosses for unclassified LLAGNs. The solid line is to indicate the one-to-one correlation. Five objects with $L_{\rm X}/L_{\rm Edd} \lesssim 10^{-4}$ are labeled next to the data points.

2.5.2 $\Gamma - L_{\rm X}/L_{\rm Edd}$ Anti-correlation

We tested whether our LLAGN sample showed any evidence for an anti-correlation in the Γ vs. $L_{\rm X}/L_{\rm Edd}$ plot. The results, obtained using the photon index and the luminosity in the $2-10$ keV range, are shown in Figure 2.6 and support the existence of an anti-correlation, whose best-fit is indicated by the solid line and the 1σ uncertainty with dashed lines.

The slope and y-intercept of best-fit results of LINERs, Seyferts, unclassified AGNs, and the combination of LINERs and Seyferts and all are reported in Table 2.4. There is suggestive evidence for an anti-correlation for LINERs, Seyferts, and the combination of all, when the results from the fitting of a simple PL model are used (Case 1 Table 2.4) and of more complex spectral models (Case 2 Table 2.4). When all AGN classes are combined, the significant negative correlations are confirmed by a non-parametric correlation analysis based on Spearman's $\rho-$rank coefficient which yields a value of -0.42 ($P = 8.19 \times 10^{-3}$) for Case 1, and -0.65 ($P = 1.44 \times 10^{-6}$) for Case 2. We also tested the anti-correlation test for Case 2 without NGC 1399 ($\Gamma \approx 3$) and NGC 5128 (< 1) and the best-fit parameters remained consistent within the 1σ uncertainty. For completeness, in Table 2.4 we also report the results of the correlation analysis between Γ and $L_{\rm X}$ (e.g., Emmanoulopoulos et al., 2012) and show the $\Gamma - L_{\rm X}$ plot in Figure 2.7.

The existence of a robust anti-correlation between Γ and $L_{\rm X}/L_{\rm Edd}$ offers an alternative X-ray-based method to estimate $M_{\rm BH}$ in low-accreting BHs. Since $L_{\rm Edd}$ is a linear function of $M_{\rm BH}$, one can solve the equation for $M_{\rm BH}$, and hence constrain it by plugging the values of Γ and $L_{\rm X}$ as well as the intercept and the slope of the anti-correlation:

$$\log(M_{\rm BH}) = \log(L_{\rm X}) - 38.11 - \left[\frac{\Gamma - B}{A}\right] \tag{2.1}$$

where A is the best-fit slope, B is the best-fit y-intercept, and the constant 38.11 comes from the definition $L_{\rm Edd} = 1.3 \times 10^{38} (M_{\rm BH}/M_{\odot})$ erg s^{-1}.

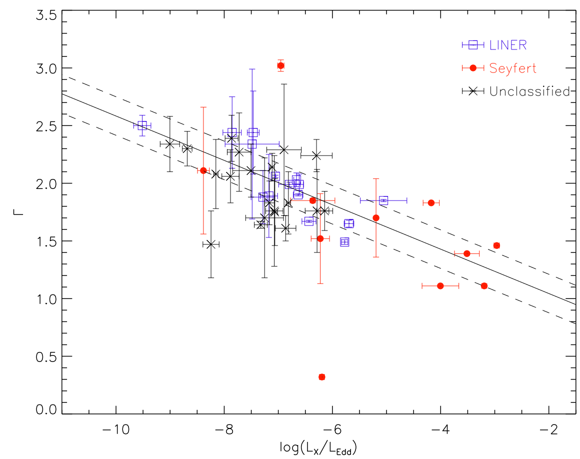

Figure 2.6: Anti-correlation of $\Gamma - L_{\rm X}/L_{\rm Edd}$. The LINER data are indicated by open squares whereas the filed circles represent Seyferts and crosses unclassified ones. The best-fit (with parameters in Table for Case 2 ALL in Table 2.4) is indicated with the solid line with the dashed lines showing the 1σ uncertainty.

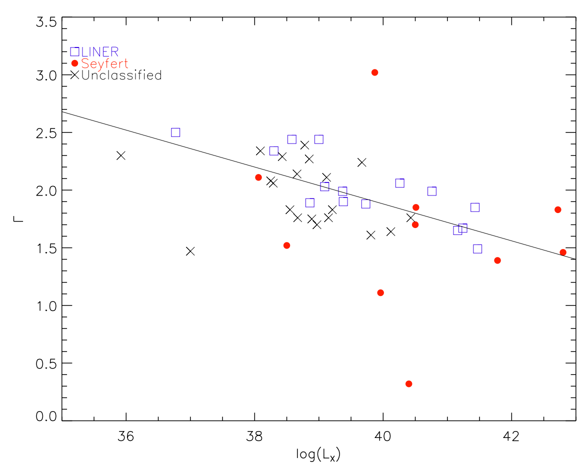

Figure 2.7: Anti-correlation of $\Gamma - L_{\rm X}$. The LINER data are indicated by open squares whereas filled circles represent Seyferts and crosses for unclassified ones. The best-fit (with parameters for Case 2 ALL in Table 2.4) is indicated with the solid line.

Table 2.4: X-ray properties correlation analysis results

AGN class (1)	Slope (2)	Y-int. (3)	RMS (4)
$\Gamma - L_X/L_{Edd}$ Analysis Results			
Case 1 − use of results from the base-line model			
LINER	-0.25 ± 0.09	0.19 ± 0.62	0.33
Seyfert	-0.30 ± 0.16	-0.17 ± 0.88	0.84
L+S†	-0.29 ± 0.08	-0.11 ± 0.49	0.61
Unclassified	-0.20 ± 0.15	0.49 ± 1.11	0.45
ALL	-0.26 ± 0.06	0.03 ± 0.39	0.55
Case 2 − use of results from the complex model			
LINER	-0.22 ± 0.05	0.46 ± 0.32	0.16
Seyfert	-0.17 ± 0.11	0.68 ± 0.63	0.58
L+S†	-0.20 ± 0.05	0.56 ± 0.34	0.41
Unclassified	-0.13 ± 0.08	0.97 ± 0.60	0.26
ALL	-0.18 ± 0.04	0.66 ± 0.25	0.35
$\Gamma - L_X$ Analysis Results			
Case 1			
LINER	-0.21 ± 0.07	10.41 ± 2.77	0.32
Seyfert	-0.24 ± 0.18	11.24 ± 7.50	0.90
L+S†	-0.26 ± 0.09	12.11 ± 3.58	0.66
Unknown	-0.01 ± 0.12	2.34 ± 4.74	0.47
Comb	-0.20 ± 0.06	9.63 ± 2.40	0.60
Case 2			
LINER	-0.19 ± 0.04	9.43 ± 1.39	0.17
Seyfert	-0.10 ± 0.13	5.71 ± 5.26	0.62
L+S†	-0.17 ± 0.06	8.72 ± 2.39	0.45
Unknown	-0.08 ± 0.06	5.08 ± 2.47	0.27
Comb	-0.16 ± 0.04	8.28 ± 1.45	0.27

Note. Column (1) AGN class; (2) a best-fit slope; (3) a best-fit intercept; (4) RMS for the best-fit. All Compton-thick sources are excluded during the anti-correlation between Γ and L_X/L_{Edd} confirmation.
† − LINERs and Seyfert galaxies only.

2.5.3 M_{BH} Computation

We estimated M_{BH} for the sources in Table 2.1 (except for 8 Compton-thick candidates) using the Equation 1 with the best-fitting parameters corresponding all AGN classes for both Case 1 (spectral results from the PL model) and Case 2 (spectral results from more complex models).

The $M_{\rm BH}$ values for the 47 LLAGNs from the anti-correlation of $\Gamma - L_{\rm X}/L_{\rm Edd}$ ($M_{\rm BH,X}$) and the ratio between the $M_{\rm BH,X}$ and the corresponding values determined with dynamical methods ($M_{\rm BH,dyn}$) are reported in Table 2.5, with columns 2 and 3 referring to Case 1 and columns 4 and 5 to Case 2. The uncertainty of $M_{\rm BH,X}$ was derived from the parameter's uncertainty in Equation 2.1.

Table 2.5: $M_{\rm BH}$ estimation of LLAGN

LLAGN (1)	$\log(M_{\rm BH,X})$ (2)	$\log(\frac{M_{\rm BH,X}}{M_{\rm BH,dyn}})$ (3)	$\log(M_{\rm BH,X})$ (4)	$\log(\frac{M_{\rm BH,X}}{M_{\rm BH,dyn}})$ (5)
I 1459	9.78 ± 0.02	0.34 ± 0.20	9.56 ± 0.10	0.12 ± 0.22
I 4296	8.86 ± 0.38	-0.27 ± 0.38		
N 224	7.98 ± 0.22	-0.19 ± 0.27		
N 2748	8.52 ± 1.79	0.85 ± 1.85		
N 2787	8.25 ± 0.07	0.61 ± 0.09	8.07 ± 0.25	0.43 ± 0.25
N 3031	9.54 ± 0.29	1.64 ± 0.30	7.89 ± 0.03	-0.01 ± 0.10
N 3608	9.14 ± 0.44	0.82 ± 0.47		
N 3998	9.90 ± 0.16	1.53 ± 0.46	9.60 ± 0.19	1.23 ± 0.47
N 4261	5.99 ± 1.01	-2.75 ± 1.01	8.84 ± 0.58	0.10 ± 0.58
N 4278	9.53 ± 0.29	0.33 ± 0.29	9.38 ± 0.02	0.18 ± 0.02
N 4459	8.39 ± 0.30	0.52 ± 0.31	8.17 ± 0.43	0.30 ± 0.44
N 4486	9.31 ± 0.18	-0.25 ± 0.22		
N 4596	6.64 ± 1.26	-1.28 ± 1.27	7.77 ± 1.38	-0.15 ± 1.39
N 5077	8.60 ± 0.87	-0.30 ± 0.90		
		Seyfert galaxies		
N 1399	12.32 ± 3.68	3.61 ± 3.68		
N 3227	9.11 ± 0.33	1.93 ± 0.40	7.70 ± 0.66	0.52 ± 0.70
N 4026	7.80 ± 1.94	-0.53 ± 1.95	8.28 ± 2.34	-0.05 ± 2.34
N 4151	3.72 ± 4.88	-3.93 ± 4.88	8.48 ± 0.73	0.83 ± 0.73
N 4258	9.85 ± 0.88	2.27 ± 0.88	8.02 ± 2.00	0.44 ± 2.00
N 4395	5.55 ± 0.79	0.51 ± 0.79	4.56 ± 1.13	-0.48 ± 1.13
N 4594	9.06 ± 0.04	0.30 ± 0.41	8.77 ± 0.09	0.01 ± 0.42
N 5128	2.45 ± 4.44	-6.03 ± 4.44	3.91 ± 2.96	-4.57 ± 2.96
N 5252	9.07 ± 0.66	0.07 ± 0.75		
N 6251	11.49 ± 0.12	2.71 ± 0.19	10.88 ± 0.07	2.10 ± 0.16
N 7457	5.48 ± 1.67	-1.13 ± 1.68	6.01 ± 1.82	-0.60 ± 1.83
		Unclassified AGNs		
N 221	6.38 ± 0.19	-0.11 ± 0.21	6.41 ± 0.15	-0.08 ± 0.18
N 821	7.08 ± 1.97	-0.55 ± 1.97		
N 1023	8.20 ± 0.04	0.54 ± 0.06		
N 1300	3.69 ± 1.75	-4.16 ± 1.77	9.55 ± 0.01	1.70 ± 0.29
N 2778	8.48 ± 1.54	1.27 ± 1.57		
N 3115	8.48 ± 0.93	-0.50 ± 0.95	8.78 ± 0.57	-0.20 ± 0.60
N 3377	8.17 ± 1.76	0.11 ± 1.77		
N 3384	7.25 ± 4.40	0.00 ± 4.40		
N 3585	9.17 ± 0.09	0.64 ± 0.15		

Table 2.5 – continued from previous page

LLAGN (1)	$\log(M_{\mathrm{BH,X}})$ (2)	$\log(\frac{M_{\mathrm{BH,X}}}{M_{\mathrm{BH,dyn}}})$ (3)	$\log(M_{\mathrm{BH,X}})$ (4)	$\log(\frac{M_{\mathrm{BH,X}}}{M_{\mathrm{BH,dyn}}})$ (5)
N 4291	8.56 ± 0.47	0.05 ± 0.58		
N 4342	7.68 ± 2.28	-0.88 ± 2.29	7.66 ± 0.63	-0.90 ± 0.66
N 4473	7.16 ± 2.18	-0.95 ± 2.21		
N 4564	7.27 ± 1.22	-0.57 ± 1.22		
N 4649	10.99 ± 0.73	1.66 ± 0.74	8.08 ± 0.29	-1.25 ± 0.31
N 4697	6.09 ± 1.12	-2.20 ± 1.12	8.35 ± 2.72	0.06 ± 2.72
N 4742	7.39 ± 0.60	0.21 ± 0.62	7.11 ± 1.14	-0.07 ± 1.15
N 5576	7.91 ± 3.42	-0.35 ± 3.42		
N 5845	8.83 ± 0.72	0.37 ± 0.75		
N 7052	11.72 ± 0.03	3.12 ± 0.22	8.67 ± 1.29	0.07 ± 1.31
N 4486A	4.32 ± 1.46	-2.81 ± 1.47	4.32 ± 1.46	

With few exceptions, we found a good agreement between the M_{BH} values determined with this anti-correlation and their corresponding dynamical values. These findings are illustrated in Figure 2.8 where we plot the M_{BH} values obtained with these two methods along the y- and x-axis, respectively. The apparent visual correlation is formally confirmed by the statistical analysis performed using the MPFITEXY routine (Markwardt, 2009; Williams et al., 2010). The best-fit parameters, the slope and intercept, with their 1σ uncertainty and the RMS from the one-to-one correlation for each LLAGN class and for the combination of all are reported in Table 2.6. The distribution of the ratio between computed $M_{\mathrm{BH,X}}$ and its corresponding $M_{\mathrm{BH,dyn}}$ for Case 2 is shown Figure 2.9.

We also investigated whether X-ray radio-loudness plays a role in the mass determination. To this end, we have divided our sample between radio-quiet and radio-loud objects using as the threshold $\log R_{\mathrm{X}} \geq -2.8$ (Panessa et al., 2007). The values of $\log(M_{\mathrm{BH,X}}/M_{\mathrm{BH,dyn}})$ for radio-quiet and radio-loud objects are respectively 0.29 ± 0.54 and 0.55 ± 1.17, which are consistent within the errors. This suggests that radio-loudness does not affect the mass determination with this X-ray method.

In summary, we computed M_{BH} for 47 LLAGNs based on the anti-correlation between

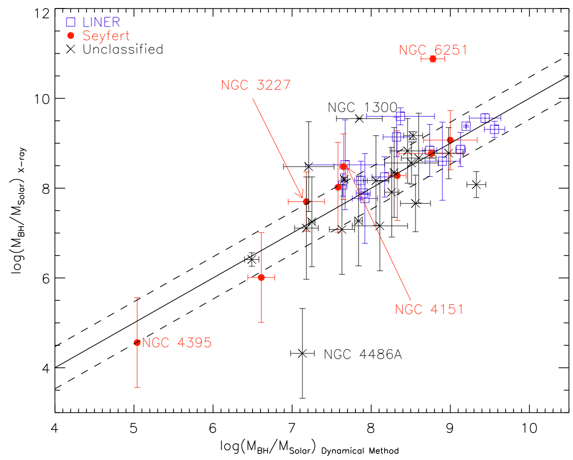

Figure 2.8: M_{BH} values obtained using the $\Gamma - L_{\mathrm{X}}/L_{\mathrm{Edd}}$ anti-correlation parameters vs. dynamically measured M_{BH} values. The open squares are used to indicate LINERs, filled circles for Seyferts, and X marks for unclassified sources. The one-to-one correlation is represented by the solid line whereas the dashed lines indicate the uncertainty.

$\Gamma - L_{\mathrm{X}}/L_{\mathrm{Edd}}$. The vast majority of the M_{BH} values are in good agreement with their dynamical values within a factor of $5-6$ (RMS ~ 0.8).

2.6 Discussion

In this work, we performed a systematic and homogeneous re-analysis of the X-ray spectra for a sample of LLAGNs with M_{BH} dynamically constrained with the aim to test the validity and the limitations of two X-ray-based methods to determine M_{BH}. The first method is based on the scale-invariance of X-ray spectral properties of BHs at all scales, whereas the second one is based on the anti-correlation of Γ vs. $L_{\mathrm{X}}/L_{\mathrm{Edd}}$ at very low accretion rates.

Table 2.6: $M_{\rm BH}$ correlation analysis results

Class (1)	Slope (2)	Y-int. (3)	Spearman(Prob.) (4)	RMS (5)
		Case 1		
LINER	0.56 ± 0.46	4.06 ± 3.96	$0.45(1.06 \times 10^{-1})$	1.09
Seyfert	1.16 ± 0.36	-0.15 ± 2.82	$0.36(2.72 \times 10^{-1})$	2.75
Unclassified	1.70 ± 0.41	-5.41 ± 3.32	$0.64(2.37 \times 10^{-3})$	1.54
ALL	1.08 ± 0.22	-0.23 ± 1.80	$0.55(9.53 \times 10^{-5})$	1.81
		Case 2		
LINER	0.77 ± 0.45	2.12 ± 3.89	$0.72(3.48 \times 10^{-3})$	0.50
Seyfert	1.38 ± 0.37	-2.52 ± 2.94	$0.97(2.16 \times 10^{-5})$	0.83
Unclassified	0.91 ± 0.38	0.68 ± 3.05	$0.61(4.37 \times 10^{-3})$	0.93
ALL	1.00 ± 0.23	0.23 ± 1.89	$0.74(1.50 \times 10^{-8})$	0.79

Note . Column (1) AGN class; (2) best-fit slope; (3) best-fit intercept; (4) Spearman's $\rho-$rank and its following probability; (5) RMS from the one-to-one correlation.

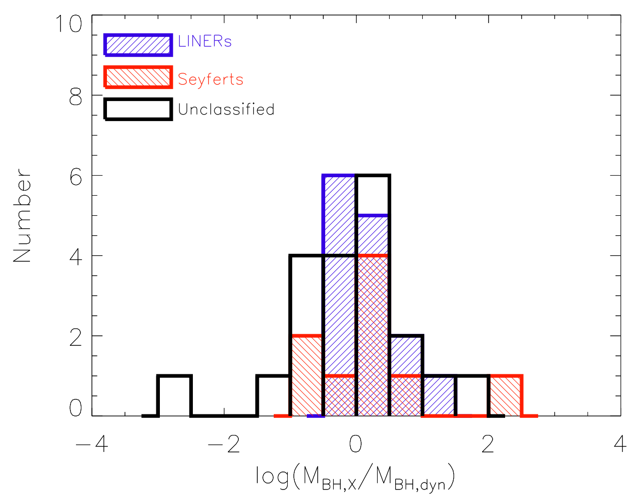

Figure 2.9: Histogram of $\log(M_{\rm BH,X}/M_{\rm BH,dyn})$ where $M_{\rm BH,X}$ refers to Case 2 (spectral results from more complex models). The histogram filled with positive slopes indicate LINERs, the negative slopes filled one is used for Seyferts, and the empty one for unclassified AGNs.

2.6.1 X-ray Scaling Method

In our recent work, we demonstrated that the X-ray scaling method, developed for and tested on GBHs (Shaposhnikov and Titarchuk, 2009), can be successfully applied to AGNs with moderate/high accretion rate (Gliozzi et al., 2011). Specifically, using self-similar spectral patterns from different GBH reference sources we derived the $M_{\rm BH}$ values of a selected sample of bright AGNs and then compared them with the corresponding values obtained from the reverberation mapping technique. The tight correlation found in the $\log(M_{\rm BH,scal})$ and $\log(M_{\rm BH,RM})$ plane (RMS $= 0.35$ for the most reliable reference source, GRO J1655$-$40, and RMS$_{\rm avg}$ $= 0.53$ obtained by taking the average of five different reference patterns) demonstrates that the values of $M_{\rm BH}$ obtained with the scaling method are fully consistent with the reverberation mapping results within the respective uncertainties.

In this work, we have tested the limits of applicability of this scaling method to low accreting AGNs with typical $L_{\rm X}/L_{\rm Edd}$ ratio of the order of $10^{-6}-10^{-7}$, which correspond to very low Eddington ratios ($< 10^{-4}$) for any reasonable bolometric correction. In our starting sample, only three objects have $L_{\rm X}/L_{\rm Edd}$ that are not extremely low: NGC 3227, NGC 4151, and NGC 4395 (all have $L_{\rm X}/L_{\rm Edd} \sim 10^{-3}$ and thus $L_{\rm bol}/L_{\rm Edd} \sim 10^{-2}$). The resulting $M_{\rm BH}$ values derived for the LLAGN sample from the X-ray scaling method are systematically lower than the dynamically inferred values by three or four orders of magnitude, indicating that the X-ray scaling method cannot be utilized for BHs in the very low accreting regime. The only notable exceptions are NGC 3227, NGC 4151, and NGC 4395 for which the derived $M_{\rm BH}$ are consistent with the dynamical values.

Paradoxically, the apparent failure of the scaling method, when applied to AGNs accreting at very low accretion rates, provides indirect support to this method. Indeed, it demonstrates that the agreement between $M_{\rm BH}$ values determined with the scaling method and the reverberation mapping values is not obtained by chance but is based on a common spectral evolution (the steeper when brighter spectral trend), which is systematically seen in highly-accreting AGNs and GBHs in their transition between the low-hard state and the soft-high state. This conclusion is further reinforced by the agreement between $M_{\rm BH,scal}$ and their dynamical values that was obtained for NGC 3227, NGC 4151, and NGC 4395, the only sources of this sample with accretion rate close to 10^{-2}.

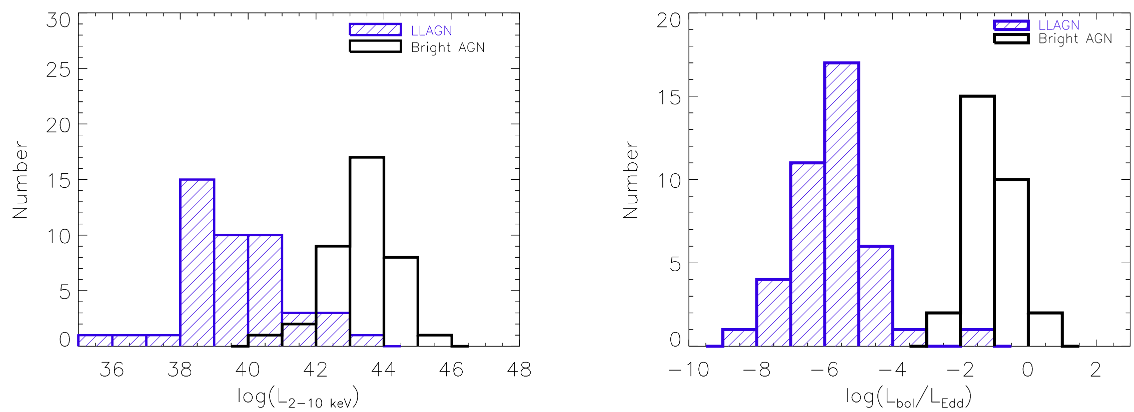

Figure 2.10: Histogram of $\log(L_{\rm X})$ and $\log(L_{\rm bol}/L_{\rm Edd})$ for our sample of LLAGNs and reverberation mapping AGNs in Gliozzi et al. (2011). The histogram filled with negative slopes indicates LLAGNs and the empty one for bright AGNs in both panels.

In Figure 2.10 we show the histogram of the X-ray luminosity (left panel) and of $L_{\rm bol}/L_{\rm Edd}$ (right panel) for the reverberation mapping sample used by Gliozzi et al. (2011) and the LLAGN sample utilized in the present work. The two distributions appear to be distinct as formally demonstrated by a Kolmogorov-Smironv (K-S) test that yields a probability of 1.2×10^{-13} and 1.7×10^{-15} that the two $L_{\rm X}$ and the two $L_{\rm bol}/L_{\rm Edd}$ distributions are drawn from the same populations. These combined findings suggest that the X-ray scaling method provides reliable estimates of $M_{\rm BH}$ for moderately/highly accreting AGNs with $L_{\rm X} > 10^{42}$ erg s^{-1} and $L_{\rm bol}/L_{\rm Edd} \gtrsim 10^{-3}$.

2.6.2 Inverse Correlation of $\Gamma - L_X/L_{Edd}$

Since LLAGNs represent the vast majority of AGNs and many of them have X-ray observations it is important to find an alternative way to constrain M_{BH} in these systems exploiting their X-ray properties. Recent studies of large samples of LLAGNs with X-ray data have provided solid evidence in favor of this anti-correlation in the $\Gamma - L_X/L_{Edd}$ diagram (e.g., Constantin et al., 2009; Gu and Cao, 2009; Gültekin et al., 2012), which has been recently confirmed in an individual LLAGN monitored for several years (Emmanoulopoulos et al., 2012).

Before comparing the results from our work to similar studies in the literature, it is important to underscore the differences of these studies. In this paper, we have performed a thorough and systematic analysis of the highest quality spectra available for a sizable sample of LLAGNs with M_{BH} dynamically determined. Starting with a simple power-law absorption model we progressively increased the complexity of the spectral model to account for partial absorption, thermal emission, soft excess, reflection, and emission lines when necessary. In this way, the vast majority of the sources yielded photon indices in the physical range from $1 - 3$ that followed the $\Gamma - L_X/L_{Edd}$ anti-correlation.

Gültekin et al. (2009a) used a similar sample but limited themselves to Chandra data in the $2 - 10$ keV and used a relatively simple spectral model that for some sources yielded negative photon indices and for other values steeper than 3. This resulted into an anti-correlation described by a slope of -0.24 ± 0.12 which is not statistically significant but consistent with our results when using a power-law model (Case 1).

Constantin et al. (2009) used a very large sample of LLAGNs candidates obtained by cross-matching the Sloan Digital Sky Survey (SDSS) catalog with X-ray selected sources from the *Chandra* Multiwavelength Project (ChaMP). With such a large sample and the relatively low number of counts (the mean source count of the sample was 76 counts) only a basic spectral analysis can be performed providing Γ values ranging from -2 to 6. The anti-correlation derived from this study combining Seyfert galaxies, LINERs and transition objects is again consistent with our results from the power law analysis.

The study more similar to ours in terms of statistical significance of the anti-correlation, quality of the spectra and reasonable values of Γ (although with a considerably smaller sample) is the one from Younes et al. (2011), who studied a sample of 13 LINERs with *Chandra* and *XMM−Newton* data. Their anti-correlation -0.31 ± 0.06 is fully consistent with our correlation for LINERs, but slightly steeper than the correlation obtained combining all classes of AGNs in Case 2. In summary, several previous studies based on different samples and spectral quality have provided findings fully consistent with the anti-correlation derived in this work.

Note that the existence of a positive $\Gamma{-}L_{\mathrm{X}}/L_{\mathrm{Edd}}$ correlation has been widely accepted for more than two decades and is generally explained in the framework of Comptonization models by the cooling of the corona produced by an higher flux of soft photons caused by the increased accretion rate in the disk. On the other hand, substantial evidence of a negative $\Gamma{-}L_{\mathrm{X}}/L_{\mathrm{Edd}}$ correlation has been presented only recently and its explanation is still a matter of debate. In the framework of Comptonization models, this anti-correlation can be explained by a decrease of the number of scatterings associated with very low-accreting, low-density flows and the change of the source of Comptonized seed photons (e.g., Esin et al., 1997; Gardner and Done, 2012; Qiao and Liu, 2013). Alternatively, it can be explained by the dominance of the jet emission in the X-ray range that emerges in the very low accreting regime (e.g., Yuan and Cui, 2005). Independently of the physical reason, the sole presence of this inverse trend in the $\Gamma{-}L_{\mathrm{X}}/L_{\mathrm{Edd}}$ diagram makes it possible to constrain M_{BH}, because L_{Edd} is a direct function of M_{BH}. As a consequence, by using the best fitting parameters of the inverse correlation and the values of Γ and L_{X}, which are obtained from the X-ray analysis, it is possible to determine M_{BH} for any LLAGNs.

With the parameters derived from our best-fitting anti-correlation we derived the M_{BH} values for our sample of LLAGNs. The vast majority of the objects have M_{BH} consistent with the corresponding dynamical values within a factor of 10 with a substantial fraction (26/43) within a factor of 3.

2.6.3 Summary

In conclusion, we can summarize our main results as follows.

- The X-ray scaling method provides $M_{\rm BH}$ values in good agreement with the corresponding dynamically determined values not only for BH systems accreting at high level (as demonstrated by the reverberation mapping sample) but also at moderately low level ($L_{\rm X}/L_{\rm Edd} \sim 10^{-3}$) as shown by NGC 3227, NGC 4151, and NGC 4395.

- We have also computed the X-ray radio-loudness parameter $R_{\rm X}$ for our sample to test whether it plays a relevant role in the $\Gamma - L_{\rm X}/L_{\rm Edd}$ anti-correlation. We found that $R_{\rm X}$ does not play any significant role in the anti-correlation (and hence in the $M_{\rm BH}$ determination). This is in agreement with the findings of Sikora et al. (2007), who found that all AGN classes follow two similar trends (named radio-loud and radio-quiet sequences) when the radio loudness is plotted versus the Eddington ratio. For moderately high values of the Eddington ratio, there is an inverse trend between R and $L_{\rm bol}/L_{\rm Edd}$, which flattens at low values of $L_{\rm bol}/L_{\rm Edd}$. Our sample, which is characterized by very small values of $L_{\rm bol}/L_{\rm Edd}$, appears to be fully consistent with the flat part of the trend shown by the radio-quiet sequence.

- For very low accreting AGNs (typically, with $L_{\rm X} < 10^{42}$ erg s^{-1} or $L_{\rm X}/L_{\rm Edd} < 10^{-4}$), the scaling method fails to properly constrain $M_{\rm BH}$ because its basic assumption (the steeper when brighter trend) no longer holds. Nevertheless, for very-low-accreting AGNs, to get a reasonable estimate of $M_{\rm BH}$ (within a factor of ~ 10) we can use the equation $\log(M_{\rm BH}) = \log(L_{\rm X}) - (\Gamma\ - B)/A - 38.11$ (where B is the intercept and A the slope of the anti-correlation; their vales are provided in Table 2.4).

- The possibility to constrain the $M_{\rm BH}$ in low-accreting systems with this simple X-ray method may have important implications for large statistical studies of AGNs. This is because the $L/L_{\rm Edd}$ appears to play a crucial role in defining the properties and the evolution of AGNs. However, in current studies $L_{\rm Edd}$ uniquely relies on $M_{\rm BH}$ estimates from optically-based indirect methods, which may not be appropriate for all AGN classes and accretion regimes. The X-ray approach, which is based on assumptions completely different from those used in the optically-based indirect methods, can be thus used as a sanity check. In addition, it may expand the range of the investigation of the cosmic evolution of galaxies, since it can be applied to very low accreting systems, which represent the majority of the AGN population.

Chapter 3: Black Hole Mass Determination in Ultraluminous X-ray Sources Using The *XMM−Newton* Satellite

3.1 Introduction

An ultraluminous X-ray source (ULX) is an off-nuclear, point-like source that accretes above the Eddington limit of a sMBH ($L_{\rm X} \geq 10^{39}$ erg s^{-1}). Their importance stems from the fact that ULXs may contain the missing population of intermediate mass black holes (IMBHs).

ULXs were first discovered in nearby star-forming galaxies by the *Einstein* Observatory satellite in the 1980s (Fabbiano, 1988, 1989; Fabbiano and Trinchieri, 1987; Long and van Speybroeck, 1983; Stocke et al., 1991a,b). However, the relatively crude spatial resolution and lack of long-term monitoring prevented to distinguish between steady luminous sources and transient events (e.g., young supernovae, SNe). Repeated observations of nearby galaxies with X-ray satellites such as *ROSAT* and *ASCA* with superior spatial resolution and spectral coverage suggested that some of these luminous off-nuclear sources were actually SNe and some were super-Eddington sMBHs. Despite the progress achieved with detailed modeling of the X-ray spectral and temporal high-quality data gathered by the new generation of X-ray satellites (*Chandra*, *XMM−Newton*, *Suzaku*, and *Swift*), the nature of ULXs (IMBHs versus sMBHs with extreme properties) is still a matter of debate. Many different names have been used to identify this class of accreting BHs and recently the community consensus has settled to call this type of objects as ultraluminous X-ray sources as firstly proposed by Japanese *ASCA* teams (Makishima et al., 2000; Mitzuno et al., 1999; Okada et al., 1998).

The first catalog of off-nuclear luminous X-ray sources from *ROSAT* observations linked observational results with the theoretically-predicted IMBHs (Colbert and Mushotzky, 1999). Later, a catalog of ULXs with 106 X-ray sources at $L > 10^{39}$ erg s^{-1} was compiled by Liu and Bregman (2005). With longer *Chandra* observations, 266 ULXs were presented in the catalog by Liu and Mirabel (2005). Currently, the largest catalog of ULXs that is based on *XMM−Newton* observations (2XMM Serendipitous Survey), comprises 470 ULXs with 367 sources newly discovered (Walton et al., 2011).

When in a spherical accreting compact object the inward-directed gravitational force and the outward-directed radiation force are balanced out, the object is at its maximum radiative luminosity or the Eddington limit. The Eddington luminosity can be expressed as

$$L_{\rm Edd} = \frac{4\pi c G M_{\rm BH} m_p}{\sigma_T} \approx 1.3 \times 10^{38} \left(\frac{M_{\rm BH}}{M_\odot}\right) \,\mathrm{erg\,s^{-1}} \tag{3.1}$$

where σ_T is the Thomson scattering cross section, m_p the proton mass, and $M_{\rm BH}$ the BH mass (Frank et al., 2002). The Eddington argument has provided very valuable information from the early stage of X-ray astrophysics. First, it showed that most Galactic X-ray binaries are neutron stars (Margon and Ostriker, 1973) and later on, it suggested the existence of a population of Galactic BHs with mass $\approx 5-15\,M_\odot$. Also in modern X-ray astronomy $L_{\rm Edd}$ plays an important role by providing a lower limit on the mass of the accreting compact object.

The apparent luminosity of an accreting BH assuming solar abundances and allowing for non-isotropic emission can be expressed as follows (Poutanen et al., 2007; Shakura and Sunyaev, 1973):

$$\begin{array}{ll} L \approx \frac{1.3\times10^{38}}{b}\dot{m}\left(\frac{M_{\rm BH}}{M_\odot}\right)\,\mathrm{erg\,s^{-1}} & \dot{m} \leq 1 \\ L \approx \frac{1.3\times10^{38}}{b}\left(1+\frac{3}{5}\ln\dot{m}\right)\left(\frac{M_{\rm BH}}{M_\odot}\right)\,\mathrm{erg\,s^{-1}} & 1 \leq \dot{m} \leq 100 \end{array} \tag{3.2}$$

where $b \leq 1$ is the beaming factor ($b = \gamma^{-1}(1-\beta\cos\theta)^{-1}$ with the Lorentz factor, $\gamma = 1/\sqrt{1-\beta^2}$, and $\beta = v/c$) and $\dot{m}$ is the dimensionless accretion rate at large radii.

These equations indicate that an apparent luminosity $> 10^{39}$ erg s^{-1} can be explained by increasing either the $M_{\rm BH}$, the beaming factor, the accretion rate, or combination of all three factors. In the framework of the standard accretion theory (Shakura and Sunyaev, 1973), ULXs can be explained by the following different scenarios.

Strong beaming effect ($1/b \gg 1$) – Massive outflows and anisotropically emitting relativistic jets have been frequently observed in specific classes of AGNs commonly named blazars that are characterized by strongly beamed emission (e.g., Urry and Shafer, 1984). In this scenario, the strong beaming effects cause the apparent luminosities of ULXs to be larger than 10^{39} erg s^{-1}. However, statistical studies based on the luminosity function rule out this hypothesis. Moreover, the strong beaming scenario is disfavored for ULXs that are surrounded by photoionized bubbles which require quasi-isotropic X-ray emission with luminosities $\approx 10^{40}$ erg s^{-1} (e.g., HoII X-1: Kaaret et al. 2004; Lehmann et al. 2005; Pakull and Mirioni 2002; NGC 5408 X-1: Kaaret and Feng 2009).

Mild beaming and/or super-Eddington accretion ($1/b \leq 10$, $\dot{m} \gg 1$) – At super-Eddington accretion rate, the disk becomes geometrically thick with radiatively-driven outflows from the inner part (King, 2009; Poutanen et al., 2007; Shakura and Sunyaev, 1973). The bulk of the emission is concentrated along the normal to the accretion disk because of the scattering and collimation process along the funnel wall (King, 2009; King et al., 2001). This implies that ULXs can be luminous up to $\approx 10^{41}$ erg s^{-1} with $M_{\rm BH} \leq 20\, M_{\odot}$. Recent results of radiation-hydrodynamical simulations showed that super-Eddington accretion with $\dot{m} \approx 5$ can produce the luminous ULXs with $\approx 1.7 L_{\rm Edd}$ and apparent luminosities at $\approx 22 L_{\rm Edd}$ (Mineshige and Ohsuga, 2011; Ohsuga and Mineshige, 2011).

Quasi-isotropic sub-Eddington luminosity ($1/b \sim 1$, $\dot{m} < 1$) – An alternative scenario hypothesizes that ULXs are sub-Eddington accreting and nearly isotropically emitting objects with masses in the range of $10^2 \leq M_{\rm BH}/M_{\odot} \leq 10^4$ (Colbert and Mushotzky, 1999;

Kaaret et al., 2003; Liu and Di Stefano, 2008; Makishima et al., 2000; Miller et al., 2003; Yuan et al., 2007).

3.1.1 Characteristics of ULXs

Spectral studies of ULXs have revealed behaviors similar to XRBs, although some authors have suggested the possible presence of new states with sMBHs accreting at super-Eddington rate distinct from the well-known states in XRB systems (Dewangan et al., 2010, 2006; Feng and Kaaret, 2006, 2009). If ULXs host IMBHs, then standard transitions are expected (Feng and Soria, 2011). According to their X-ray spectral properties ULXs can be divided into two groups: ULXs with spectra consistent with a simple power law and those described by more complex models (for example, soft excess below 2 keV and a break or steepening above $\sim$ 2 keV). Some ULXs with $\Gamma \geq 2.5$ may be similar to the steep power-law states in GBHs. These appear to be similar to highly accreting GBHs such as XTE J1550$-$564 (Feng and Kaaret, 2005; Soria, 2007; Winter et al., 2006). The strong variability of the flux (sometimes an order of magnitude) at a constant Γ observed in some ULXs appears to be similar to the LHS of GBH systems (Belloni et al., 2005; Feng and Kaaret, 2009; Kaaret and Corbel, 2009; Remillard and McClintock, 2006; Soria and Ghosh, 2009).

ULXs with soft excess below 2 keV and high energy curvature above 2 keV have been classified as belonging to an ultraluminous state distinct from well-known states of GBHs (Gladstone et al., 2009). Berghea et al. (2008) found that some ULXs tend to have harder spectra as the luminosity increases and Soria (2011) pointed out the same behaviors with some ULXs having $L_X \geq 10^{40}$ erg s^{-1} at $\Gamma \leq 1.8$ (described as high/hard state). Many ULXs were found in the canonical hard state ($\Gamma \approx 1.5 - 2$) but also in extremely hard and soft states, $\Gamma \sim 1$ and $\Gamma \sim 3$, respectively. However, no clear evidence of spectral transitions between two states was found (Berghea et al., 2008; Swartz et al., 2004; Winter et al., 2006).

Only recently, systematic variability studies of ULXs have been carried out. For example, Heil et al. (2009) studied 16 bright ULXs. The sources can be divided into two groups: ULXs having either a weak or absent variability on timescales of 100s and ULXs having variability levels (and power spectra) similar to luminous GBHs or AGNs in frequency band of $10^{-3} - 1$ Hz. Only two out of 16 ULXs, one from each group, had QPO detections. Although there are more ULXs with QPOs, the detection of QPOs is difficult and hence relatively rare in ULXs.

3.1.2 M_{BH} Estimators

The black hole mass (M_{BH}) is a crucial parameter in observational studies of accreting objects and many authors have tried to constrain M_{BH} in different ways. Unlike the X-ray binary systems (XRBs) or AGNs, ULXs are often observed in the X-ray band only and therefore, there are not well-defined direct methods to measure M_{BH} inside ULXs such as the dynamical methods for XRBs and the reverberation mapping method for AGNs. The two most frequently used methods are based on the inner disk temperature (e.g., Feng and Kaaret, 2009) and on the QPO frequency (e.g., Kaaret et al., 2009; Rao et al., 2010). If ULXs are assumed to have standard accretion disks extending to the last stable orbit, ULXs are expected to follow the standard disk trend of $L_{\mathrm{disk}} \propto T^4$. Indeed this behavior has been observed in NGC 5204 X-1 (Feng and Kaaret, 2009). However, the same authors also found some ULXs that did not show this standard trend (e.g., IC 342 X-1). The second method based on the M_{BH}–QPO^{-1} relation is fairly limited because the QPO features are elusive due to low signal-to-noise ratio in ULX light curves.

ULXs host either sMBHs and IMBHs and hence are expected to spectrally evolve on much shorter timescales than AGNs. As a consequence, multiple observations of the same ULXs over a time interval of several months/years have the potential to probe their spectral evolution. By applying the X-ray scaling method to a sample of ULXs with multiple observations, we can determine M_{BH}, probe their spectral evolution, and compare it with typical trends observed in GBHs (e.g., Feng and Kaaret, 2005, 2007, 2009; Soria, 2007; Soria and Ghosh, 2009; Winter et al., 2006).

3.2 Scaling Method Application to ULXs

Since QPO features have been detected only in a few ULXs, the $M_{\rm BH}$ determination using the $\Gamma-$QPO correlation is fairly limited. Hence, to determine $M_{\rm BH}$ we rely on $\Gamma-N_{\rm BMC}$ diagram that we already used in the study of AGNs. The shorter time scales expected in ULXs (in comparison to those associated with AGNs) have the potential to probe the spectral evolution of ULXs over time intervals of months/years and to allow a direct comparison with GBH reference sources. The X-ray scaling method application to ULXs can be summarized as follow:

1) Construct a $\Gamma-N_{\rm BMC}$ diagram with measured values from the BMC model spectral fitting over multiple observations of the same ULX and compare it to the self-similar trend observed in GBHs.

2) Determine the best-fit N_{tr} value, which is the parameter that describes the shift the ULX trend along the x-axis ($N_{\rm BMC}$) with respect to the GBH reference trend.

3) Determine the $M_{\rm BH}$ value from the following equation:

$$M_{\rm BH,t} = M_{\rm BH,r} \times \left(\frac{N_{\rm tr,t}}{N_{\rm tr,r}}\right) \times \left(\frac{d_{\rm t}}{d_{\rm r}}\right)^2. \tag{3.3}$$

Note that we assumed the geometric factor f_G was equal to 1 in this study because the geometry of ULX is unknown.

3.2.1 Sample Collection

The sample of ULXs used in this study was compiled starting from the ULXs reported in the literature as of *January 2012*. Ae searched the *XMM−Newton* archive for sources with multiple observations and exposure longer than 10 ks. We found 47 ULXs located in 30 nearby galaxies that satisfy these criteria and reported them in Table 3.1. Specifically, column (1) provides the ULX name, (2) and (3) the equatorial coordinates Right Ascension and declination, (4) the distance in units of Mpc, (5) the Galactic absorption value in units of 10^{22} cm^{-2} from Dickey and Lockman (1990), (6) the numbers of observations that meet the exposure requirement and the total number in parenthesis, (7) the minimum and maximum values of $M_{\rm BH}$ in the literature, and (8) the references.

3.2.2 Data Reduction

We perform the data reduction following the standard procedures of Science Analysis System (SAS) version 12.0.1. We only selected good X-ray event ("FLAG= 0") with patternsof $0-4$ and $0-12$ for the pn and MOS, respectively. Most of ULXs in our sample were isolated point-like sources, whose emission can be clearly separated from the galactic nuclear contribution. For those targets, we used source extraction regions with a radius of 10" $-$20" and background regions of $\sim$ 60" located in a nearby source$-$free zone. Some observations captured the source either at the edge of the CCD or partially in the gap between CCDs for the pn and/or MOS. In this case, the source extraction region was reduced accordingly. When the source in the *XMM$-$Newton* image did not appear to be isolated (e.g., when the ULX emission could be contaminated by diffuse emission or by nearby sources), we used *Chandra* images to guide our source extraction and assess the possible contamination. In general, the spectral analysis was performed by simultaneously fitting the spectra from the three EPIC cameras. Only for very bright sources the analysis was limited to the EPIC pn data. The SAS RMFGEN and ARGEN tasks were used to generate RMF and ARF files, respectively. To use the χ^2 statistics, each spectrum was grouped with 20 counts per bin or 15 counts per bin in case of relatively short observations (net exposure $\sim$ 10 ks).

Table 3.1: The ultraluminous X-ray source sample

Name		RA	Dec.	d (Mpc)	$N_{\rm H}$ (10^{22} cm^{-2})	Number	$\log(M_{\rm BH})$ (Min, Max)
(1)		(2)	(3)	(4)	(5)	(6)	(7)
NGC 55	ULX	00:15:28.9	-39:13:19.1	1.94	1.71	3	
M31	X-1	00:42:22.9	41:15:35.1	0.82	6.60	23(47)	
NGC 253	X-1	00:47:22.6	-25:20:51.0	3.19	1.41	8(9)	0.39, 1.97[1,2,3,4,5]
	X-2	00:47:33.0	-25:17:50.0		1.42	9	1, 1.98[1,2,3]
	XMM4	00:47:23.3	-25:19:06.5		1.42	2(9)	
	XMM5	00:47:17.6	-25:18:21.1		1.42	6(9)	
NGC 300	XMM1	00:55:09.9	-37:42:13.9	1.98	3.19	5	1.26, 1.60[6]
	XMM2	00:55:10.6	-37:48:36.7		3.20	4(5)	
	XMM3	00:54:49.7	-37:38:53.8		3.24	2(5)	
M33	X-8	01:33:50.9	30:39:37.2	0.89	5.58	13(21)	1, 3.18[7,8]
NGC 1313	X-1	03:18:20.0	-66:29:11.0	4.03	3.90	17	2.78, 3.34[1,2,9,10,11,18]
	X-2	03:18:22.3	-66:36:03.8		3.90		2.81,3.11[1,2,9,10,11,18]
	XMM2	03:17:38.8	-66:33:05.3		3.82		
	XMM4	03:18:18.5	-66:30:05.0		3.90		2.06, –[2]
IC 342	X-1	03:45:55.5	68:04:54.2	3.12	31.1	4(6)	2.53, 4.47[1,2,11]
	XMM2	03:46:15.0	68:11:11.2		29.7		3.18, –[2]
	XMM3	03:46:48.6	68:05:43.2		30.2		2.87, –[2]
	XMM4	03:46:57.2	68:06:20.2		30.0		
NGC 2403	X-1	07:36:25.9	65:35:38.9	3.54	4.14	3(5)	1.23, 1.47[2,9]
HoII	X-1	08:19:29.0	70:42:19.0	3.33	3.42	7	1.30, 3[1,2,9,13,14]
M81	X-6	09:55:32.9	69:00:34.8	3.68	4.16	8	0.39, 1.93[2,3,9]
M82	X-1	09:55:50.2	69:40:46.7	3.92	3.98	8(12)	4.08, 4.64[15,16,17,18]
HoIX	X-1	09:57:53.2	69:03:48.3	3.63	4.06	7	1.70, 3.82[1,2,9,10,11,14,19,20]
NGC 4395	XMM1	12:26:01.5	33:31:29.0	4.12	1.37	2(3)	1.36, –[2]
	XMM2	12:25:25.3	33:36:46.4		1.37		
	XMM3	12:25:32.6	33:25:27.9		1.34		
NGC 4490	XMM1	12:30:32.4	41:39:14.6	8.68	1.78	2(3)	0.40, 1.60[2,21]
	XMM2	12:30:36.5	41:38:33.3		1.78		0.30, 1.62[2,21]
	XMM3	12:30:43.3	41:38:11.5		1.78		1.34, 3.14[2,21]
	XMM4	12:30:31.1	41:39:08.1		1.78		0.70, 2.12[2,21]
	XMM5	12:30:30.3	41:41:40.3		1.78		2.99, –[4]
NGC 4736	XMM1	12:50:50.2	41:07:12.0	4.86	1.44	2(3)	2.32, –[2]
NGC 4945	XMM1	13:05:33.3	-49:27:36.3	3.98	15.6	2(9)	
	XMM2	13:05:38.4	-49:25:45.3		15.5		
	XMM3	13:05:18.8	-49:28:24.0		15.7	1(9)	
	XMM4	13:05:22.2	-49:28:27.9		15.7	2(9)	
	XMM5	13:05:25.7	-49:28:32.3		15.7		
NGC 5194	XMM1	13:29:40.0	47:11:36.2	8.73	1.56	5(6)	3.86, –[2,22]
	XMM2	13:30:07.7	47:11:04.8		1.58		1.30, 1.46[2,22]
	XMM3	13:30:01.1	47:13:41.4		1.57		2.21, 3.41[2,22]
	XMM4	13:30:06.0	47:15:38.9		1.57		2.29, –[2,22]
	XMM5	13:29:59.6	47:15:54.0		1.56		
	XMM6	13:29:57.5	47:10:45.3		1.58		1, 2.48[2,22]

$M_{\rm BH}$ *references* – [1]Kajava and Poutanen 2009; [2]Winter et al. 2006; [3]Hui and Krolik 2008; [4]Barnard 2010; [5]Bauer 2005; [6]Carpano et al. 2007; [7]Foschini et al. 2004; [8]Gebhardt et al. 2001; [9]González-Martín et al. 2011; [10]Heil et al. 2009; [11]Wang et al. 2004; [12]Miller et al. 2003; [13]Goad et al. 2006; [14]Zampieri and Roberts 2009; [15]Feng et al. 2010; [16]Kaaret et al. 2001; [17]Yuan et al. 2007; [18]Feng and Kaaret 2010; [19]Dewangan et al. 2006; [20]Tsunoda et al. 2006; [21]Yoshida et al. 2010; [22]Dewangan et al. 2005; [23]Vierdayanti et al. 2006; [24]Soria et al. 2004; [25]Strohmayer et al. 2007; [26]Rao et al. 2010

Table 3.1 – continued from previous page

Name		RA	Dec.	d (Mpc)	$N_{\rm H}$ (10^{22} cm^{-2})	Number	$\log(M_{\rm BH})$ (Min, Max)
(1)		(2)	(3)	(4)	(5)	(6)	(7)
NGC 5194	XMM7	13:29:53.6	47:14:31.5		1.56		1, 1.30[2,22]
NGC 5204	X-1	13:29:38.6	58:25:06.0	5.28	1.39	5(7)	2.46, –[1,2,9,23]
NGC 5408	X-1	14:03:19.6	-41:23:00.0	4.85	5.67	6(16)	1.90, 3.72[24,25]
NGC 6946	X-6	20:35:00.7	60:11:31.0	6.93	2.13	9(10)	–, 3[1,26]

3.3 Results

3.3.1 Spectral Analysis

Each *XMM–Newton* spectrum in the range of $0.5 - 10$ keV was systematically fitted using the X-ray astronomy software package XSPEC V12.0.1. Two absorption models were used; one fixed at the Galactic value and the other one left free to vary to mimic the intrinsic absorption value of the equivalent hydrogen column. The soft X-rays were described by an accretion disk model called *diskpn* (Gierlinksi et al. 1999) that is parameterized by the maximum disk temperature near the black hole ($T_{\rm max}$) in units of keV and the inner disk radius in units of R_G, whereas the hard X-rays are described by the BMC model. Since we assume that the seed photons for the Comptonization process are provided by the disk, we linked the seed photon temperature in the BMC model to $T_{\rm max}$. For simplicity, we fixed the inner disk to be at the last stable orbit of $6R_G$. The Comptonization factor $\log(A)$ is initially left free to vary but was fixed to 2 if it exceeded $\log(A) \gg 2$. For the completeness, we used a F-test to compare spectral results to the case without any assumptions and no significant difference was found.

In Appendix A, we report the spectral results including the observation ID, the net exposure in units of ks, the intrinsic absorption value ($N_{\rm H}$) in units of 10^{22} cm^{-2}, the seed photon temperature kT, the Comptonization factor $\log(A)$, the photon index $\Gamma(= \alpha + 1)$, $N_{\rm BMC}$ normalized at 10^4, $\log(L_{\rm X=2-10\,keV})$, and the χ^2 per degree of freedom for a total of

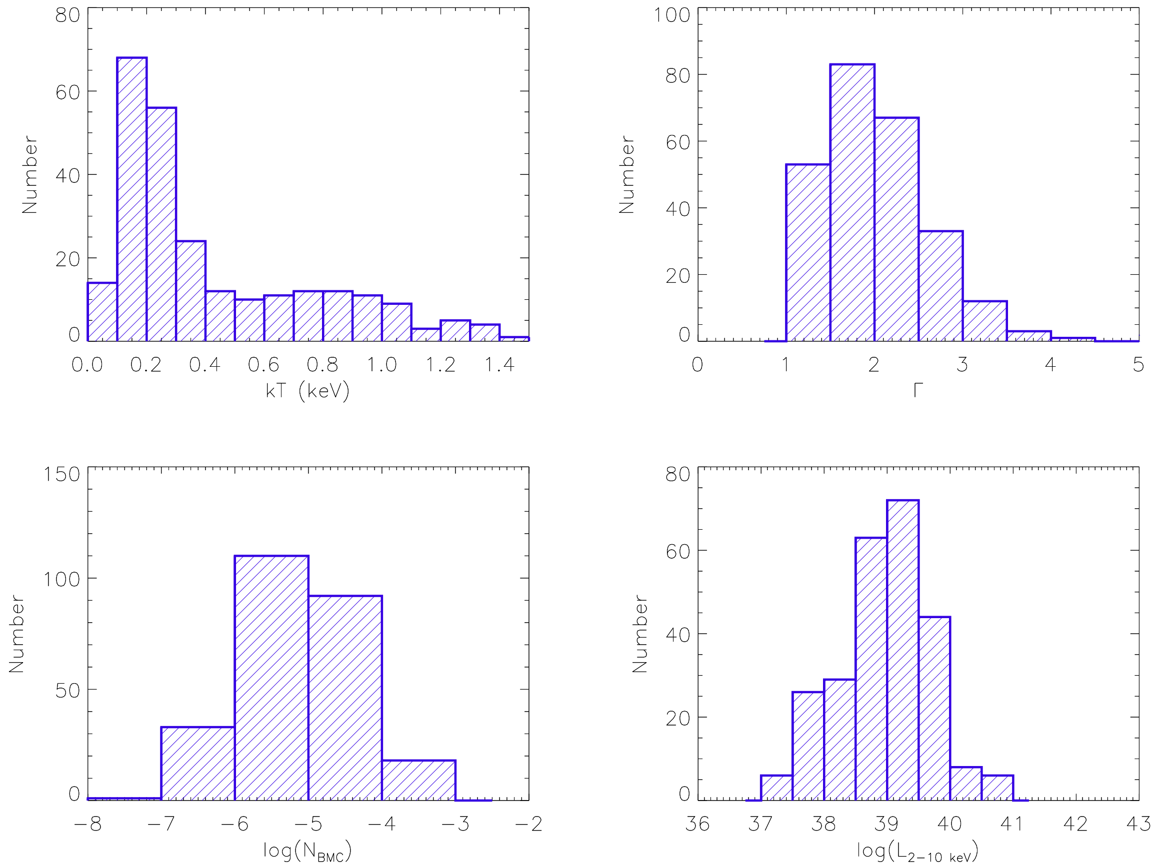

Figure 3.1: Histogram of the spectral BMC model properties. The histograms are in the order of the seed photon temperature, Γ, $\log(N_{\rm BMC})$, and $\log(L_{\rm X})$ for all objects.

260 observations from 47 ULXs. The distributions of kT, Γ, $\log(N_{\rm BMC})$, and $\log(L_{\rm X})$ are illustrated in Figure 3.1. The measured kT ranges between $0.01-1.79$ keV with a mean of 0.43 ± 0.35 keV and a median of 0.26 keV. The vast majority of the spectra (204 out of 260 observations) had $\log(A)$ fixed at 2 and a mean value of 1.64 ± 0.71. The values of Γ are distributed in the $1-6$ range with the mean value of 2.03 ± 0.69 where 242 observations have $\Gamma<3$. The normalization $N_{\rm BMC}$ is distributed in the $10^{-4}-10^{-8}$ range with a mean of $(2.54\pm4.8)\times10^{-5}$ and a median of 7.17×10^{-6}. Finally, the unabsorbed $L_{\rm X}$ in the $2-10$ keV band ranges between $10^{37}-10^{41}$ erg s^{-1}.

3.3.2 $\Gamma - N_{\rm BMC}$ Diagrams

We constructed $\Gamma - N_{\rm BMC}$ diagrams for each ULX utilizing the spectral results to investigate their spectral evolution and constrain their $M_{\rm BH}$. Out of 47 ULXs, 5 ULXs (NGC 55 ULX, NGC 253 XMM4, NGC 4490 XMM2, NGC 4945 XMM4, and XMM5) have values of Γ outside the range of any reference pattern. We did not construct the $\Gamma - N_{\rm BMC}$ daigram for NGC 4945 XMM3 because there was only one observation with the good *XMM−Newton* quality data. Therefore these ULXs were excluded from further analysis since their $M_{\rm BH}$ cannot be constrained with this method. Their $\Gamma - N_{\rm BMC}$ diagrams are shown in Figure B.1 in Appendix B.

27 ULXs showed positive $\Gamma - N_{\rm BMC}$ trends, whereas 15 ULXs had negative patterns. Some ULXs exhibit different values of Γ corresponding to the same value of $N_{\rm BMC}$. Figure 3.2 illustrates the different types of trends shown; NGC 55 ULX has all values of Γ above 3 and therefore cannot be compared to any reference pattern. NGC 5204 X-1 shows a positive spectral pattern in the $\Gamma = 1.7 - 2.5$ range and can be compared to any reference patterns. NGC 1313 X-1 shows a positive spectral trend with two possible outliers. Finally, an anti-correlation of Γ and $N_{\rm BMC}$ is seen in $\Gamma - N_{\rm BMC}$ plot of M81 X-6.

3.3.3 $M_{\rm BH}$ Computation

The spectral trends of each ULX in the $\Gamma - N_{\rm BMC}$ plot were fitted with the same parametric function used to describe each reference trend. The parametric function (see Equation 1.19) used for the fit is characterized by three parameters (A, B, and β) fixed at the reference source values, and by the parameter N_{tr} that describes the shift along the x-axis of $\Gamma - N_{\rm BMC}$ diagram is left free to vary. We tried to compare as many reference patterns as possible to each ULX trend: 13 ULXs were compared to all 6 reference patterns, 12 ULXs to 5, 3 ULXs to 4, 6 to 3, 5 to 2, and 4 ULXs to only one reference pattern. We used the IDL routine LMFIT (Research Systems, 1999)to fit the spectral patterns and determine the shift along the x-axis with respect to the chosen GBH reference, which is used to compute the

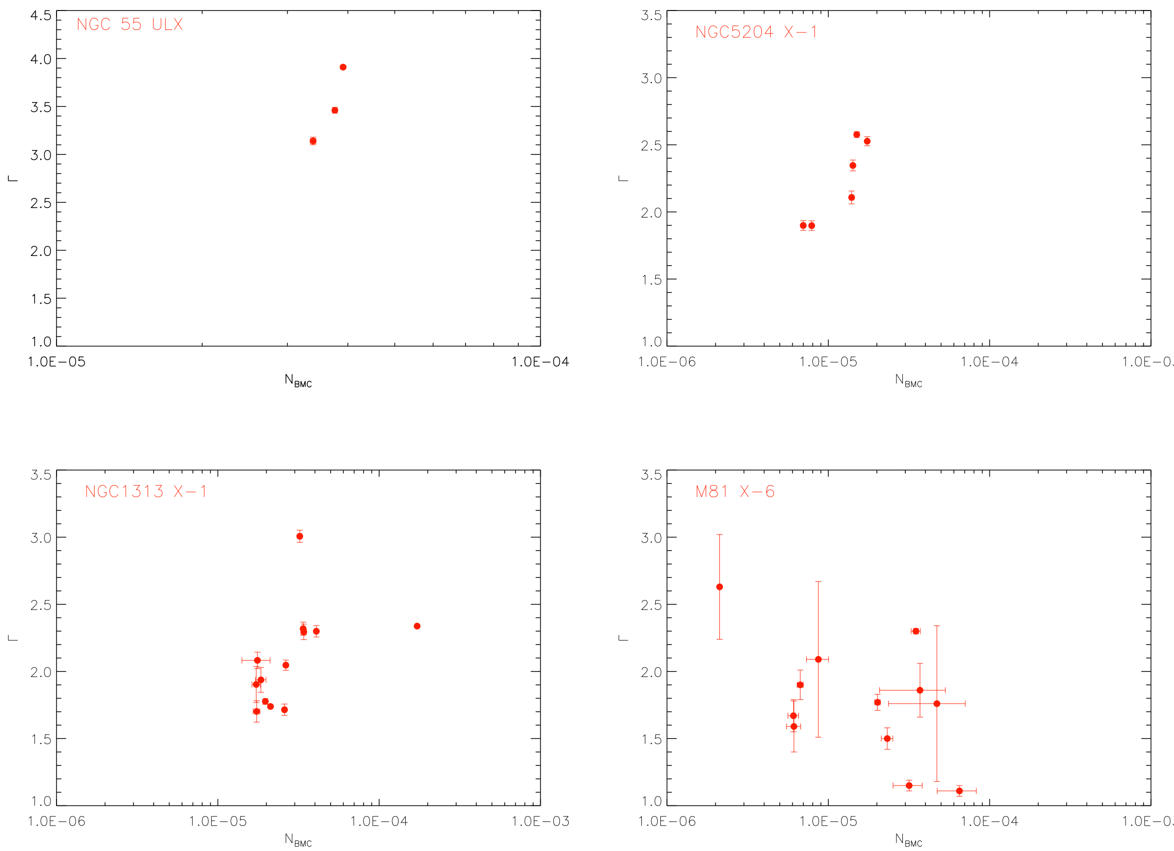

Figure 3.2: $\Gamma - N_{\rm BMC}$ diagram of ULXs. We show different types of $\Gamma - N_{\rm BMC}$ patterns in the order of NGC 55 ULX, NGC 5204 X-1, NGC 1313 X-1, and M81 X-6.

black hole mass.

We then used the best-fit results to compute the black hole mass value using Equation 3.3. The scaled black hole mass ($M_{\rm BH,Scale}$) values were generally distributed in the range of $10 - 10^4$ $M_\odot$ and values obtained from the decay reference episodes were generally larger by a factor of $2 - 3$ compared to those obtained from the rise reference episodes. The average of computed $M_{\rm BH,Scale}$ by the rise patterns ($< \log(M_{\rm BH,Scale}) >= 3.1 \pm 0.8$) was within 1σ from the value of decay patterns ($= 2.4 \pm 0.7$). The distribution of the computed $M_{\rm BH}$ values for each reference pattern is illustrated in Figure 3.3. Table A.3 summarizes the number of ULXs with $M_{\rm BH,Scale} < 100\ M_{\odot}$ and $\geq 100\ M_{\odot}$, as well as the average of $M_{\rm BH,Scale}$ value obtained from each reference pattern.

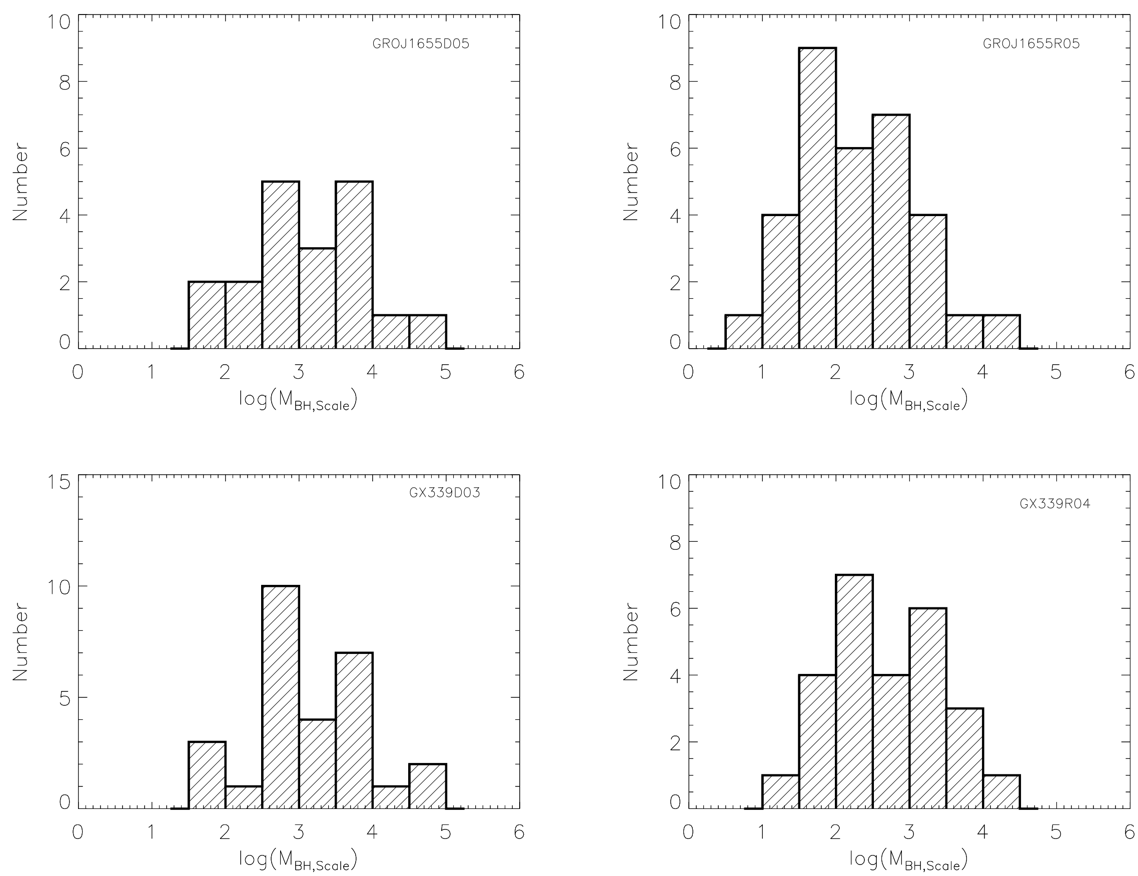

Figure 3.3: The distribution of $M_{\rm BH,Scale}$. The used reference pattern is indicated at the top-right corner of each plot.

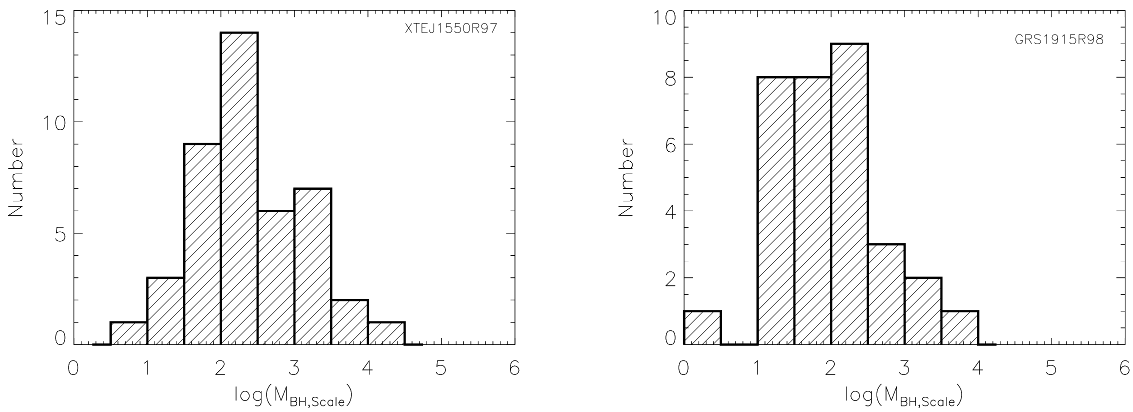

Figure 3.3 − *Continued*

Table 3.2: The summary of X-ray scaling method results

Reference pattern	Number of ULXs with $M_{\rm BH} < 100\ M_{\odot}$	with $M_{\rm BH} \geq 100\ M_{\odot}$	$< \log(M_{\rm BH,Scale}) >$
(1)	(2)	(3)	(4)
GROJ1655D05	2	17	3.11 ± 0.73
GROJ1655R05	14	20	2.32 ± 0.74
GX339D03	3	26	3.10 ± 0.78
GX339R04	6	27	2.66 ± 0.78
XTE1550R98	13	28	2.36 ± 0.70
GRS1915R97	17	15	1.97 ± 0.73

Note. Column (1) reference pattern; (2) number of ULXs with $M_{\rm BH,Scale} < 100M_{\odot}$; (3) number of ULXs with $M_{\rm BH,Scale} \geq 100M_{\odot}$; (4) averge of $M_{\rm BH,Scale}$.

Table 3.3: M_{BH} computation results for ULXs using the X-ray scaling method

Galaxy (1)	ULX (2)	GROJ1655D05 $\log(M_{\mathrm{BH}}/M_{\odot})$ (3)	GROJ1655R05 $\log(M_{\mathrm{BH}}/M_{\odot})$ (4)	GX339D03 $\log(M_{\mathrm{BH}}/M_{\odot})$ (5)	GX339R04 $\log(M_{\mathrm{BH}}/M_{\odot})$ (6)	XTEJ1915R97 $\log(M_{\mathrm{BH}}/M_{\odot})$ (7)	GRS1915R98 $\log(M_{\mathrm{BH}}/M_{\odot})$ (8)
HoII	X-1	···	···	···	···	2.56 ± 0.60	2.41 ± 0.38
HoIX	X-1	4.12 ± 0.01	3.56 ± 0.00	4.32 ± 0.13	3.91 ± 0.16	3.73 ± 0.31	3.11 ± 0.19
IC342	X-1	3.57 ± 0.04	3.19 ± 0.17	3.91 ± 0.18	3.34 ± 0.37	3.16 ± 0.22	2.74 ± 0.02
	XMM2	3.72 ± 0.04	3.31 ± 0.01	4.13 ± 0.29	3.67 ± 0.37	3.38 ± 0.33	3.10 ± 0.02
	XMM3	···	···	···	···	1.85 ± 0.16	1.55 ± 0.02
	XMM4	···	2.00 ± 0.12	···	···	1.95 ± 0.16	1.46 ± 0.02
M31	ULX	2.66 ± 0.34	1.94 ± 0.19	2.51 ± 0.36	2.01 ± 0.56	1.71 ± 0.48	1.11 ± 0.48
M33	X-8	···	1.97 ± 0.17	0.00 ± 0.00	···	2.08 ± 0.16	1.82 ± 0.20
M81	X-6	2.40 ± 0.42	1.90 ± 0.37	2.62 ± 0.37	2.09 ± 0.42	2.09 ± 0.74	0.82 ± 0.62
M82	X-1	4.95 ± 0.03	4.25 ± 0.09	4.95 ± 0.13	4.30 ± 0.34	4.10 ± 0.56	3.75 ± 0.06
NGC1313	X-1	3.70 ± 0.09	3.14 ± 0.27	3.66 ± 0.08	3.52 ± 0.13	3.18 ± 0.21	2.92 ± 0.45
	X-2	3.60 ± 0.37	2.79 ± 0.62	3.76 ± 0.37	3.25 ± 0.58	3.07 ± 0.76	2.14 ± 0.21
	XMM2	···	···	···	···	2.11 ± 0.39	2.26 ± 0.17
	XMM4	2.94 ± 0.28	2.42 ± 0.33	3.14 ± 0.33	2.57 ± 0.21	2.48 ± 0.41	···
NGC2403	X-1	···	···	···	···	3.30 ± 0.16	···
NGC253	X-1	2.41 ± 0.04	1.93 ± 0.08	2.63 ± 0.06	1.98 ± 0.12	1.86 ± 0.29	1.50 ± 0.11
	X-2	3.22 ± 0.04	2.36 ± 0.40	3.34 ± 0.14	···	2.40 ± 0.19	1.92 ± 0.12
	XMM5	2.80 ± 0.20	2.02 ± 0.12	2.75 ± 0.13	2.27 ± 0.15	2.06 ± 0.17	1.59 ± 0.14
NGC300	XMM1	1.79 ± 0.04	1.20 ± 0.01	1.99 ± 0.08	1.51 ± 0.24	1.28 ± 0.16	1.10 ± 0.01
	XMM2	···	0.83 ± 0.17	1.51 ± 0.21	1.14 ± 0.24	0.74 ± 0.16	0.30 ± 0.06
	XMM3	1.72 ± 0.04	1.11 ± 0.10	1.85 ± 0.10	1.52 ± 0.06	1.16 ± 0.08	···
NGC4395	XMM1	···	1.43 ± 0.35	···	···	1.19 ± 0.16	1.33 ± 0.02
	XMM2	···	1.49 ± 0.30	2.22 ± 0.29	1.83 ± 0.18	1.50 ± 0.24	···
	XMM3	···	1.92 ± 0.29	2.68 ± 0.31	2.10 ± 0.06	1.80 ± 0.12	···
NGC4490	XMM1	3.32 ± 0.15	2.79 ± 0.11	3.52 ± 0.10	3.17 ± 0.06	2.83 ± 0.09	2.22 ± 0.08
	XMM3	···	···	···	···	3.07 ± 0.83	2.28 ± 0.02
	XMM4	···	2.64 ± 0.17	···	···	2.31 ± 0.63	2.27 ± 0.18
	XMM5	···	2.75 ± 0.01	3.49 ± 0.01	3.23 ± 0.24	3.22 ± 0.38	2.26 ± 0.02

For details, we report $M_{\mathrm{BH,Scale}}$ values and the ratio between $M_{\mathrm{BH,Scale}}$ and $M_{\mathrm{BH,Lit}}$ in Table A.2 in Appendix.

Table 3.3 – continued from previous pages

Galaxy	ULX	GROJ1655D05 $\log(M_{\rm BH}/M_\odot)$	GROJ1655R05 $\log(M_{\rm BH}/M_\odot)$	GX339D03 $\log(M_{\rm BH}/M_\odot)$	GX339R04 $\log(M_{\rm BH}/M_\odot)$	XTEJ1915R97 $\log(M_{\rm BH}/M_\odot)$	GRS1915R98 $\log(M_{\rm BH}/M_\odot)$
(1)	(2)	(3)	(4)	(5)	(6)	(7)	(8)
NGC4736	XMM1	$\cdots$	1.93 ± 0.08	2.72 ± 0.03	2.42 ± 0.24	2.04 ± 0.16	1.46 ± 0.02
NGC4945	XMM1	$\cdots$	2.16 ± 0.11	2.94 ± 0.06	2.52 ± 0.12	2.19 ± 0.16	1.67 ± 0.02
	XMM2	$\cdots$	$\cdots$	$\cdots$	$\cdots$	2.49 ± 0.43	$\cdots$
NGC5194	XMM1	$\cdots$	1.86 ± 0.37	2.78 ± 0.19	2.53 ± 0.16	2.00 ± 0.30	1.49 ± 0.23
	XMM2	2.78 ± 0.67	2.27 ± 0.73	3.02 ± 0.75	2.43 ± 0.52	2.15 ± 0.57	$\cdots$
	XMM3	3.59 ± 0.36	3.14 ± 0.37	3.89 ± 0.39	3.11 ± 0.34	2.90 ± 0.35	$\cdots$
	XMM4	3.14 ± 0.31	2.68 ± 0.36	3.50 ± 0.46	2.67 ± 0.31	2.34 ± 0.32	$\cdots$
	XMM5	$\cdots$	2.36 ± 0.15	$\cdots$	$\cdots$	2.41 ± 0.37	1.91 ± 0.47
	XMM6	$\cdots$	1.67 ± 0.19	2.51 ± 0.09	$\cdots$	1.91 ± 0.31	1.24 ± 0.15
	XMM7	2.84 ± 0.33	1.95 ± 0.01	2.67 ± 0.01	2.29 ± 0.24	1.96 ± 0.16	1.51 ± 0.02
NGC5204	X-1	$\cdots$	2.89 ± 0.01	3.64 ± 0.01	3.30 ± 0.03	2.90 ± 0.18	2.45 ± 0.13
NGC5408	X-1	$\cdots$	$\cdots$	$\cdots$	$\cdots$	2.84 ± 0.82	2.69 ± 0.86
NGC6949	X-1	$\cdots$	2.75 ± 0.24	$\cdots$	$\cdots$	2.69 ± 0.29	2.43 ± 0.13

The $\Gamma - N_{\rm BMC}$ diagrams for all ULXs with their trend fitted by as many reference patterns as possible are presented in Appendix B, where we also report the derived $M_{\rm BH}$ values and the ratio between $M_{\rm BH,Scale}$ and $M_{\rm BH,Lit}$ values. The results of this analysis are summarized in Table 3.3 with column (1) the host galaxy, (2) ULX, from (3) to (8) the computed $M_{\rm BH,Scale}$ values using the different reference patterns in the order of GROJ1655D05, GROJ1655R05, GX339D03, GX339R04, XTEJ1550R97, and GRS1915R98. In the case where the ULX shows a clear positive correlation between Γ and $N_{\rm BMC}$ with a trend similar to one of the references, the computation of $M_{\rm BH,Scale}$ was straightforward. Irregular patterns can be explained by a combination of different events over several years (keep in mind that also for the reference sources, the spectral pattern during the rise phase of the outburst may be different from the decay trend). Alternatively, irregular patterns can be explained by the presence of statistical outliers or by spurious points obtained from low signal-to-noise spectra. In Figure 3.4, we present the $\Gamma - N_{\rm BMC}$ diagram of NGC 1313 X-1 to show an example of an ULX with two apparent outliers. The left panel in Figure 3.4 shows the spectral transition best-fitted by the GROJ1655R05 pattern (solid line) where the data point at $\Gamma = 3$ (blue open square) was excluded while rest of the observations (red filled circles) follow the reference pattern. The dash lines indicate the 1σ uncertainty of the best fit. The ratio between the data point and the best-fit is also illustrated below the $\Gamma - N_{\rm BMC}$ plot. In the right hand plot, the spectral transition of NGC 1313 X-1 was fitted with the GRS1915R97, pattern where the previously excluded point (at $\Gamma = 3$) is now part of the pattern whereas the point with $N_{\rm BMC} > 1 \times 10^{-4}$ is treated as an outlier. The left panel of Figure 3.5 shows the apparently complex pattern of M81 X-6. However, after we exclude the data points with huge error-bars and those with unphysically low values of Γ, the remaining data can be fitted with the usual positive trend shown by the reference sources. The right panel plot of Figure 3.5 shows the case of NGC 1313 X-2 which appears to have two separate clusters of data. Once again, excluding the data characterized by low values of Γ (which cannot be compared to any reference trend) makes it possible to fit the remaining data with one of the standard patterns shown by the reference sources. Then best-fitting of the inner and outer regions defines the maximum and minimum shift in x-axis which determines the possible $M_{\rm BH}$ values.

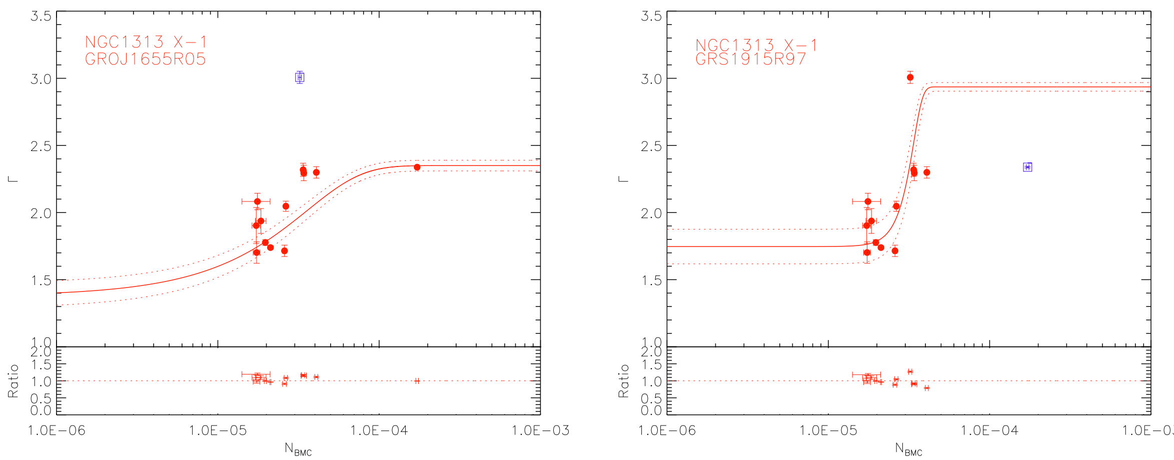

Figure 3.4: Γ–$N_{\rm BMC}$ diagram of NGC 1313 X-1. The $\Gamma - N_{\rm BMC}$ plot best-fitted with GROJ1655R05 pattern is in the left panel and with GRS1915R97 pattern in the right panel. The point considered as an outlier in each panel is indicated by the open square. The ratio between points and the best-fit is also plotted at the bottom of $\Gamma - N_{\rm BMC}$ diagram.

In Figure 3.6 we plot the $M_{\rm BH,Scale}$ values for NGC 1313 X-1, X-2, M81 X-6, and NGC 5204 X-1 versus the corresponding literature values to test how the X-ray scaling method resulted when different types of $\Gamma - N_{\rm BMC}$ patterns in ULXs were applied using different reference patterns. In general, $M_{\rm BH}$ values scaled from rise reference patterns seem to provide a better agreement with the corresponding values reported in the literature.

There were 5 ULXs (IC 345 XMM4, NGC 4395 XMM1, XMM2, NGC 4945 XMM2, and NGC 4490 XMM4) whose $\Gamma - N_{\rm BMC}$ diagrams were constructed with only two data points where one of their Γ values was outside the range of any reference pattern or had a very large uncertainty (e.g., $\sigma_\Gamma \geq 1$). Their $\Gamma - N_{\rm BMC}$ diagrams are presented in Figure B.2. NGC 2403 X-1 had all three measured Γ values below ≈ 1.4 hampering the comparison with any reference trend and consequently the $M_{\rm BH}$ computation. Similarly, NGC 4490 XMM3

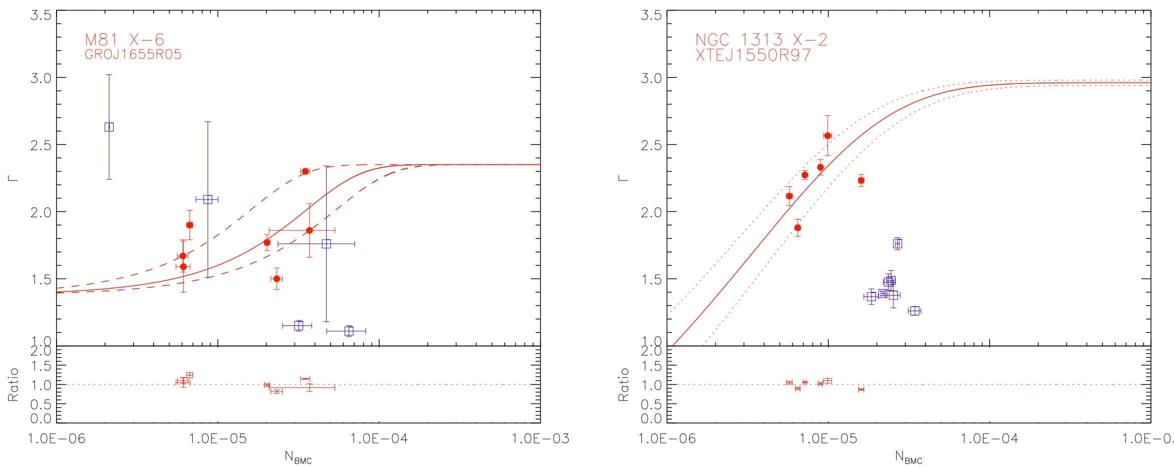

Figure 3.5: $\Gamma - N_{\rm BMC}$ diagram. The $\Gamma - N_{\rm BMC}$ diagram of M81 X-6 fitted by GROJ1655R05 pattern is in the left panel and NGC 1313 X-2 fitted by XTEJ1550R97 in the right panel. The data points used in the best-fitting are indicated with filled circles and the excluded ones with open squares. The ratio between points and the best-fit is also plotted in the bottom of $\Gamma - N_{\rm BMC}$ diagram.

and NGC 4490 XMM5 had 2 out of 3 measusred Γ values ~ 1 and their $\Gamma - N_{\rm BMC}$ ruled out to be compared from any reference pattern (see Figure B.3). These 8 ULXs were excluded from further analysis.

Comparison between $M_{\rm BH,Scale}$ and $M_{\rm BH,QPO}$

Among the methods used to constrain $M_{\rm BH}$ in ULXs, the technique based on QPOs is considered the most reliable, since unlike spectral-based methods, it is model independent. For this reason, we compared our computed $M_{\rm BH,Scale}$ values with those obtained via QPOs for the subsample of ULXs for which QPOs were clearly detected. However, we were able to test only 4 ULXs (HoIX X-1, NGC 5408 X-1, M82 X-1, and NGC 6946 X-1) because the QPO based $M_{\rm BH}$ determination for ULXs is very limited, since secure QPO detections in ULXs are very elusive. In Table 3.4 we report the results of this comparison. The main finding from this comparison is that $M_{\rm BH,Scale}$ values based on different reference patterns (especially those associated with the rising phase of the outburst) show a general good agreement with the QPO based $M_{\rm BH}$ values. The only exception is HoIX X-1 for which

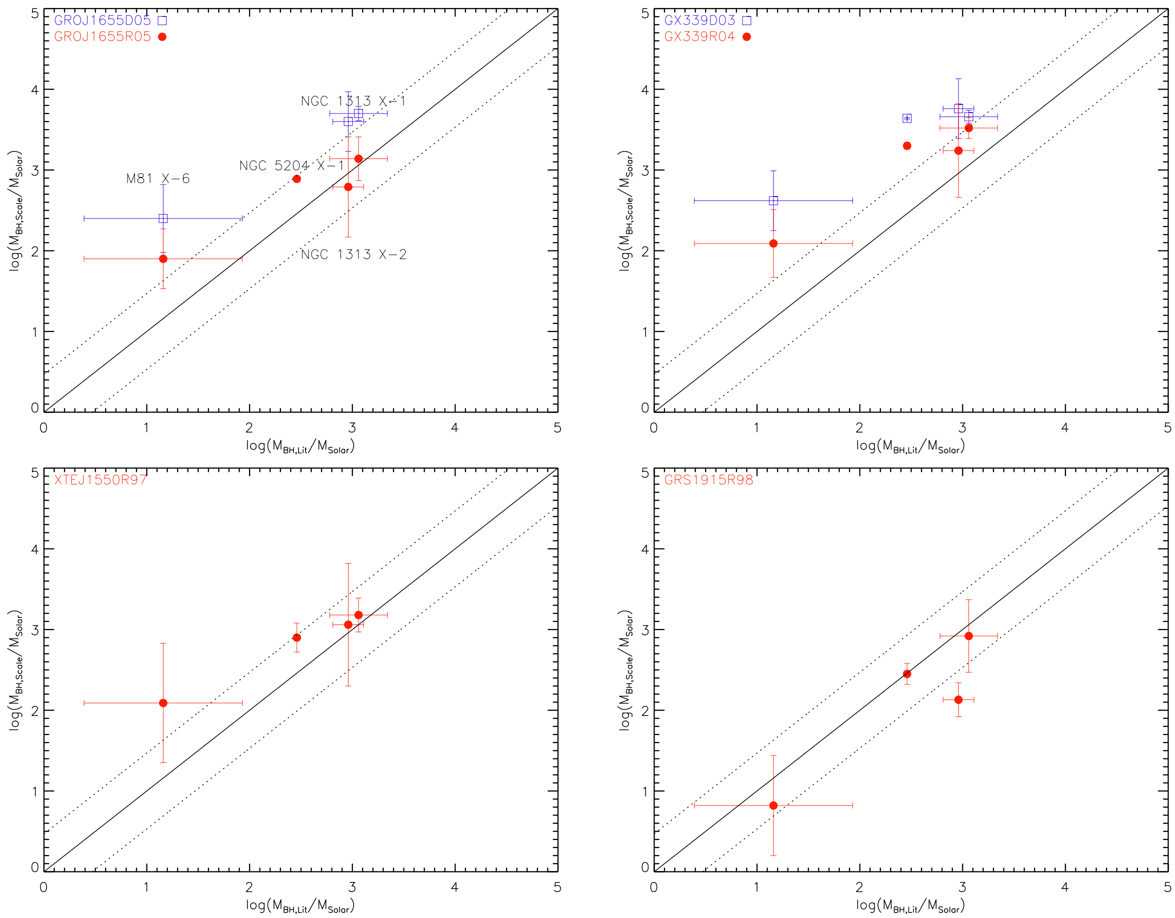

Figure 3.6: Plot of $M_{\mathrm{BH,Scale}}$ versus $M_{\mathrm{BH,Lit}}$. Each plot contains $M_{\mathrm{BH,Scale}}$ values in the y-axis and $M_{\mathrm{BH,Lit}}$ values in the x-axis where open squares are used for values from decay patterns and filled circles for values from rise patterns were used. The solid line indicates the one-to-one correlation and dashed lines for the departure by a factor of 3 (0.47 dex). The name of the used pattern is indicated at the top left corner in each plot.

only GRS1915R97 shows some marginal agreement. For the visual presentation, we plotted $\log(M_{\mathrm{BH,Scale}})$ versus $\log(M_{\mathrm{BH,QPO}})$ of four ULXs by each reference pattern in Figure C.3.

Table 3.4: $M_{\rm BH}$ comparison with values based on QPO

Reference Pattern	HoIX X-1 ($M_{\rm BH}/M_\odot$)	NGC 5408 X-1 ($M_{\rm BH}/M_\odot$)	M82 X-1 ($M_{\rm BH}/M_\odot$)	NGC 6946 X-1 ($M_{\rm BH}/M_\odot$)
$M_{\rm BH,QPO}$	$(0.5-2)\times10^2$	$(1-7)\times10^3$	$(1.2-4.3)\times10^4$	$\approx 1\times10^3$
GROJ1655D05	$(1.3-1.4)\times10^4$		$(8.3-9.6)\times10^4$	
GROJ1655R05	$(3.5-3.7)\times10^3$		$(1.5-2.2)\times10^4$	$(0.3-1)\times10^3$
GX339D03	$(1.6-2.8)\times10^4$	$(0.1-5)\times10^3$	$(6.6-12)\times10^4$	
GX339R04	$(5.6-12)\times10^3$		$(0.9-4.4)\times10^4$	
XTEJ1550R98	$(2.6-11)\times10^3$	$(0.1-4)\times10^3$	$(0.3-4.6)\times10^4$	$(0.2-1)\times10^3$
GRS1915R97	$(0.8-2)\times10^3$		$(5-6.5)\times10^3$	$(2-4)\times10^2$

Note. The first row of table have $M_{\rm BH}$ values in the literature based on QPO.

3.3.4 Correlation Analysis

Comparison with $M_{\rm BH,XTE}$

For all ULXs, we compared the $M_{\rm BH,Scale}$ values obtained from different reference patterns with the corresponding $M_{\rm BH,Scale}$ values based on the XTEJ1550R97 pattern (hereafter, $M_{\rm BH,XTE}$). We used XTEJ1550R97 as primary reference because 1) it provided the best agreement with the $M_{\rm BH}$ values obtained with different methods (see below) and 2) its spectral pattern in the $\Gamma - N_{\rm BMC}$ diagram spans the largest range of Γ allowing the determination of $M_{\rm BH}$ for the vast majority of the ULXs in our sample.

The results of this comparison are shown in Figure 3.7 where $M_{\rm BH,XTE}$ is plotted along the x-axis and the $M_{\rm BH}$ values obtained with the remaining reference patterns along the y-axis with the rising patterns described by filled symbols and decay patterns described by open squares. The solid line indicates the one-to-one correlation and the dashed lines indicate the departure by a factor of 3 (0.47 dex) from the solid line. A visual inspection of Figure 3.7 reveals the presence of tight linear correlations with $M_{\rm BH}$ obtained from the rising patterns of GROJ1655R05 and GX339R04, whereas $M_{\rm BH}$ values from decay patterns are consistently larger than those of XTEJ1550R97 by a factor of ~ 3, and GRS1915R98

Table 3.5: $M_{\rm BH,Scale} - M_{\rm BH,XTE}$ correlation analysis

Reference pattern (1)	Slope (2)	Intercept (3)	Spearman (4)	RMS (5)
GROJ1655D05	1.00 ± 0.06	0.58 ± 0.13	$0.98(1.73 \times 10^{-13})$	0.65
GROJ1655R05	1.03 ± 0.06	-0.06 ± 0.14	$0.97(1.44 \times 10^{-20})$	0.16
GX339D03	1.01 ± 0.06	0.70 ± 0.14	$0.97(5.79 \times 10^{-18})$	0.77
GX339R04	1.00 ± 0.06	0.33 ± 0.14	$0.97(5.74 \times 10^{-17})$	0.31
GRS1915R98	1.00 ± 0.06	-0.44 ± 0.14	$0.93(5.76 \times 10^{-15})$	0.49

Note. Column (1) a reference pattern; (2) a best-fit slope; (3) a best-fit intercept; (4) Spearnan's $\rho-$rank and its following probability; (5) RMS value from the one-to-one correlation

yields values lower by a factor of 2 or 3. The presence of significant linear correlations is formally confirmed by the best-fit values (all slopes are fully consistent with unity, and the intercepts are consistent or close to zero), by a non-parametric Spearman analysis, and by the RMS values. The results of this analysis are reported in Table 3.5.

Comparison with $M_{\rm BH}$ from different methods

We also looked for correlations between $M_{\rm BH,Scale}$ values and the corresponding values reported in the literature. Some ULXs were studied by several authors, who used different methods to constrain $M_{\rm BH}$. As a result, $M_{\rm BH,Lit}$ values for the same source may span a wide range (sometimes with a few orders of magnitude difference). Therefore, we made correlation studies of $M_{\rm BH,Scale}$ values with the minimum and maximum $M_{\rm BH,Lit}$ values ($M_{\rm BH,Lit,Min}$ and $M_{\rm BH,Lit,Max}$, respectively) and also with the mean of $M_{\rm BH,Lit}$ values ($M_{\rm BH,Lit,Mean}$).

We compared $M_{\rm BH,Scale}$ to the corresponding $M_{\rm BH,Lit,Mean}$ for every pattern. The linear correlation results suggest that $M_{\rm BH}$ values for all reference patterns were fully consistent with the corresponding $M_{\rm BH,Lit,Mean}$ within $1-2\sigma$ uncertainty. The RMS value of $M_{\rm BH,Scale}$ using decay reference patterns was 1.21 ± 0.05, and using rise patterns with 0.64 ± 0.11; the average RMS in general was 0.82 ± 0.28. On the other hand, there was no strong correlation

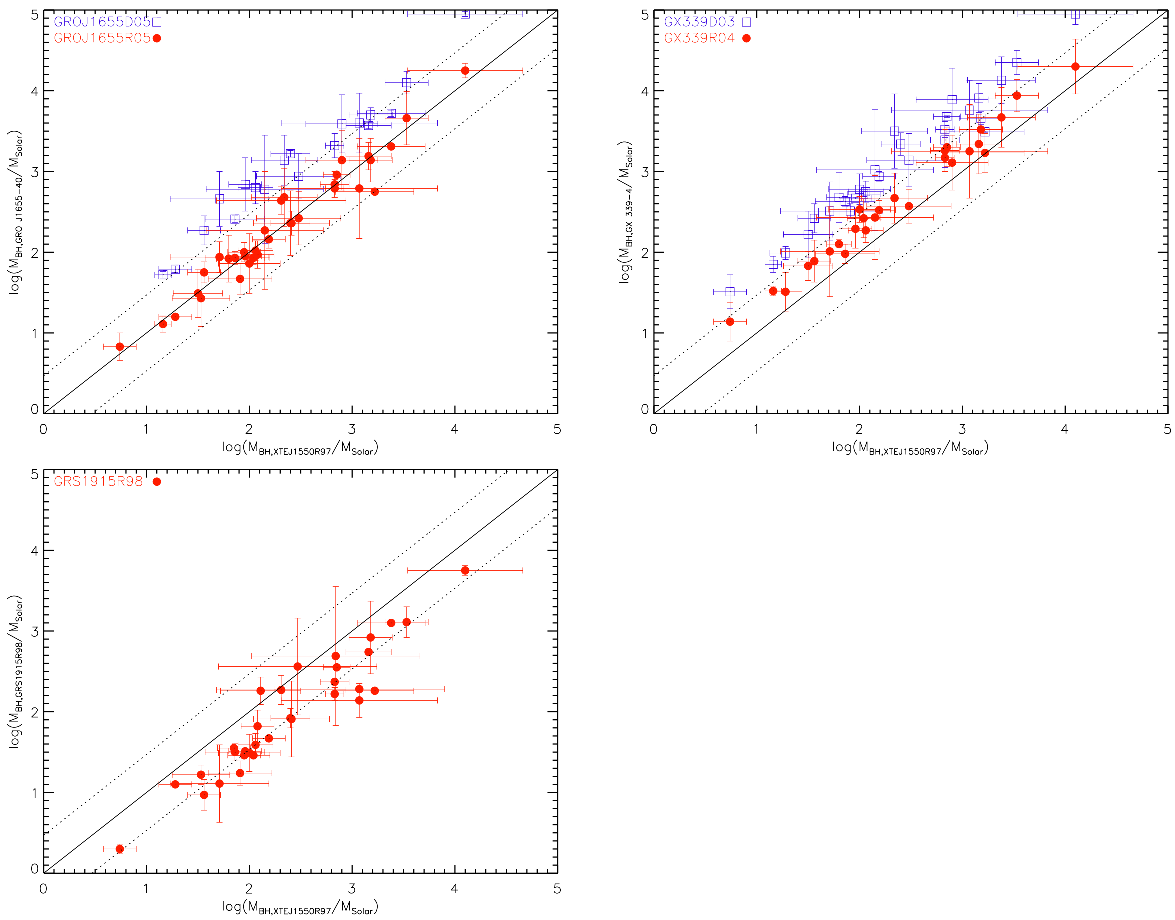

Figure 3.7: $M_{\mathrm{BH,Scale}}$ vs. $M_{\mathrm{BH,XTE}}$. We used filled circles to indicate values computed from rise reference patterns and open squares for the decay patterns.

was found neither between $M_{\mathrm{BH,Lit,Min}}$ and $M_{\mathrm{BH,Scale}}$ for any reference pattern nor between $M_{\mathrm{BH,Lit,Max}}$ and $M_{\mathrm{BH,Scale}}$.

The linear correlation results of $M_{\mathrm{BH,Scale}}$ value from corresponding the $M_{\mathrm{BH,Lit,Min}}$, $M_{\mathrm{BH,Lit,Max}}$, and $M_{\mathrm{BH,Lit,Mean}}$ values are reported in Table 3.6 for each reference pattern with the best-fit slope, the intercept, Spearman's $\rho-$rank and its following probability, and the RMS value. We used the MPFITEXY routine (Markwardt, 2009; Williams et al., 2010) which accounts for errors on both axes for the comparisons. We also plotted $\log(M_{\mathrm{BH,Scale}})$ versus $\log(M_{\mathrm{BH,Lit,Mean}})$ in Figure 3.8 for each reference pattern. The visual inspection of

Table 3.6: $M_{\rm BH}$ correlation analysis

Name (1)	Slope (2)	Intercept (3)	Spearman (4)	RMS (5)
		$\log(M_{\rm BH,Scale})$ versus $\log(M_{\rm BH,Lit,Mean})$		
GROJ1655D05	1.02 ± 0.09	0.70 ± 0.23	$0.80(5.3 \times 10^{-4})$	1.16
GROJ1655R05	1.01 ± 0.10	0.30 ± 0.23	$0.78(6.3 \times 10^{-4})$	0.62
GX339D03	0.92 ± 0.09	1.23 ± 0.22	$0.80(6.3 \times 10^{-4})$	1.26
GX339R04	0.84 ± 0.12	0.93 ± 0.29	$0.82(1.1 \times 10^{-3})$	0.82
XTEJ1550R97	0.93 ± 0.14	0.48 ± 0.33	$0.87(2.8 \times 10^{-5})$	0.56
GRS1915R98	0.83 ± 0.07	0.25 ± 0.17	$0.71(2.1 \times 10^{-3})$	0.56
		$\log(M_{\rm BH,Scale})$ versus $\log(M_{\rm BH,Lit,Min})$		
GROJ1655D05	0.48 ± 0.02	3.01 ± 0.01	$0.75(8.0 \times 10^{-4})$	1.59
GROJ1655R05	0.37 ± 0.01	2.92 ± 0.01	$0.50(1.7 \times 10^{-2})$	1.14
GX339D03	0.59 ± 0.02	2.92 ± 0.01	$0.63(3.0 \times 10^{-3})$	1.64
GX339R04	0.16 ± 0.06	2.85 ± 0.03	$0.66(3.1 \times 10^{-3})$	1.21
XTEJ1550R97	0.05 ± 0.09	2.26 ± 0.04	$0.44(2.3 \times 10^{-2})$	1.11
GRS1915R98	0.68 ± 0.02	0.40 ± 0.01	$0.46(3.5 \times 10^{-2})$	1.01
		$\log(M_{\rm BH,Scale})$ versus $\log(M_{\rm BH,Lit,Max})$		
GROJ1655D05	0.80 ± 0.03	1.03 ± 0.01	$0.80(1.9 \times 10^{-3})$	0.79
GROJ1655R05	0.82 ± 0.01	0.42 ± 0.01	$0.74(6.3 \times 10^{-4})$	0.66
GX339D03	0.49 ± 0.06	2.01 ± 0.02	$0.78(5.9 \times 10^{-4})$	0.94
GX339R04	0.83 ± 0.20	0.57 ± 0.07	$0.79(3.7 \times 10^{-3})$	0.56
XTEJ1550R97	0.34 ± 0.14	1.55 ± 0.05	$0.75(2.8 \times 10^{-5})$	0.61
GRS1915R98	0.54 ± 0.02	0.35 ± 0.01	$0.65(3.2 \times 10^{-3})$	1.03

Note. Column (1) a reference pattern; (2) a best-fit slope; (3) a best-fit intercept; (4) Spearnan's $\rho-$rank and its following probability; (5) RMS value from the one-to-one correlation

these plots confirms that the X-ray scaling method estimates of $M_{\rm BH}$ using the rising patterns are for a good agreement with $M_{\rm BH,Lit,Mean}$ in both sMBHs and IMBHs. For ULXs with $M_{\rm BH,Lit,Mean}$ below 100 $M_\odot$, the scaling values obtained with the GRS1915R97 pattern provided the best agreement, whereas those obtained with the XTEJ1550R98 pattern showed the strongest agreement for ULXs with $M_{\rm BH,Lit,Mean} \geq 100$ $M_\odot$.

The correlation study between $M_{\rm BH,Scale}$ and $M_{\rm BH,Lit}$ values can be summarized as following. The $M_{\rm BH,Scale}$ values obtained with different patterns were compared to the corresponding $M_{\rm BH,XTE}$ values; all the patterns showed a general agreement, suggesting that different patterns provide consistent values of $M_{\rm BH}$, although the values obtained from

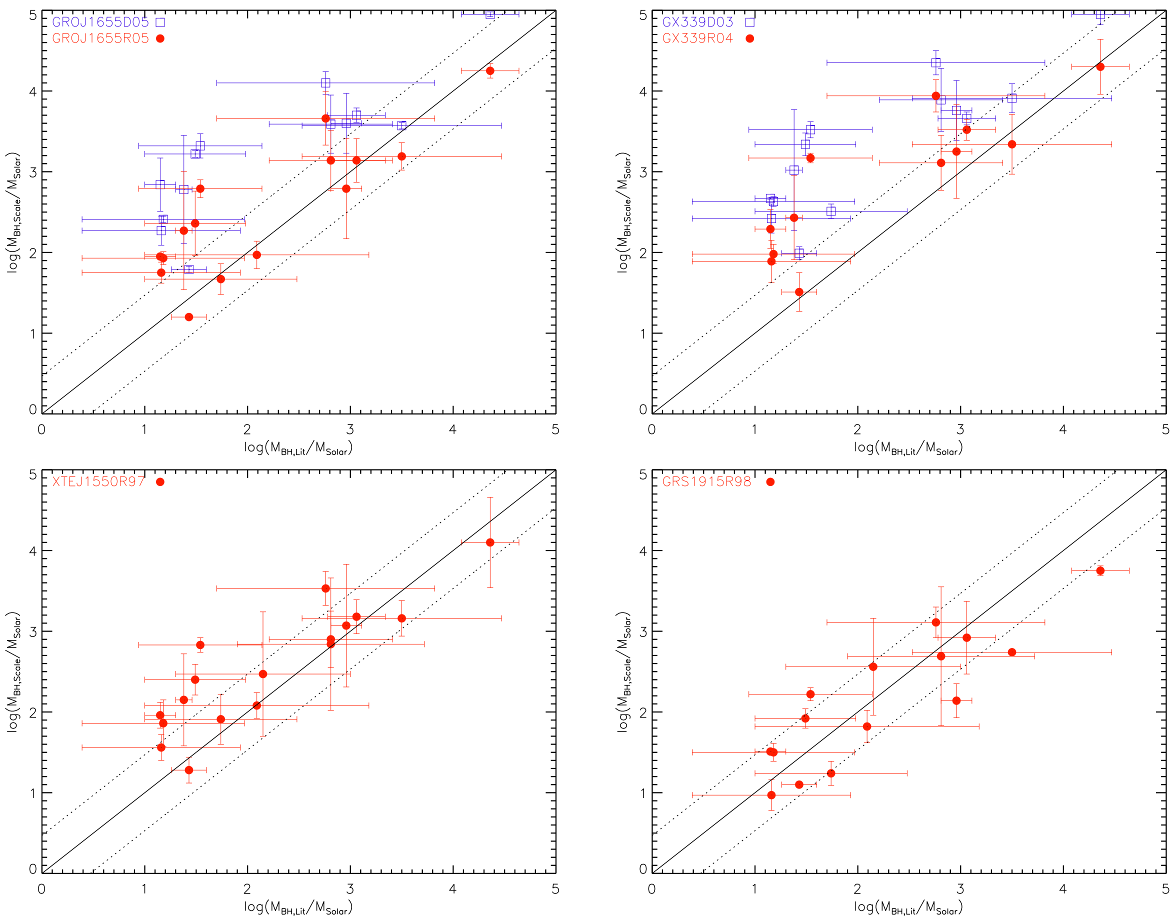

Figure 3.8: Plot of $M_{\rm BH,Scale}$ vs. $M_{\rm BH,Lit}$ for all ULXs. We used filled circles to indicate $M_{\rm BH,Scale}$ values from rising patterns and open squares for decay patterns. The solid line indicates the one-to-one correlation between $M_{\rm BH,Scale}$ and $M_{\rm BH,Lit}$ and the dash lines for the 0.47 dex boundaries. Plots of $M_{\rm BH,Scale}$ vs. $M_{\rm BH,Lit,Min}$ (in Figure C.1) and vs. $M_{\rm BH,Lit,Max}$ (in Figure C.2) in Appendix C.

rising patterns seem to provide a better agreement with $M_{\rm BH,XTE}$ and with the values of $M_{\rm BH}$ obtained with the QPO method. For completeness, we compared the scaled $M_{\rm BH}$ values to the corresponding ones in literature using minimum, maximum, and the mean values when several methods were applied to the same source. We did not find strong correlation for $M_{\rm BH,Scale} - M_{\rm BH,Lit,Min}$ and $-M_{\rm BH,Lit,Max}$ but $M_{\rm BH,Scale} - M_{\rm BH,Lit,Mean}$ had a strong correlation with RMS values within ~ 0.8.

3.4 Discussion

The nature of ULXs is one of the current misteries in X-ray astronomy. They might be stellar mass BHs in a particularly bright state that can be explained by a combination of super-Eddington accretion and beaming effects. This appears to be the favorite interpretation for most of the ULXs with $L_{\rm X} \sim 10^{39}$ erg s^{-1}, because the formation process of sMBHs is well understood and SMBHs are routinely observed in the Milky Way and nearby galaxies. In this framework, what is not completely understood is why this putative ultraluminous spectral state is not regularly observed in X-ray binaries in our Galaxy. There is however a claim that XTE J1550−564 went into this spectral state during the 1998 outburst.

An alternative, perhaps more exciting, interpretation is that ULXs (at least the brightest ones, with $L_{\rm X} \sim 10^{40} - 10^{41}$ erg s^{-1}) host IMBHs and accrete at a regular level. In this case the formation process is under debate (direct collapse vs. BH mergers) but the spectral state would be consistent with the canonical ones regularly observed in GBHs. Finally, one cannot exclude a third intermediate possibility that ULXs are massive stellar BHs ($M_{\rm BH} \sim 100\,M_\odot$) that accrete at high but not extreme level. The formation of these massive BHs can still be explained by the regular stellar evolution process under the assumption of low metallicity ($\sim 1\%$ of the solar value), which should be typical for primordial stars of Population III.

These hypothesis on the nature of ULXs are not mutually exclusive (it is entirely possible that ULXs encompass sMBHs in ultraluminous states as well as highly-accreting massive stellar BHs, and normally-accreting IMBHs) and none can be ruled out until the $M_{\rm BH}$ is dynamically determined. For this to happen, deeper optical spectroscopic observations are necessary to measure radial velocity curves of the binary companion and determine the mass of function. Current optical observations try to disentangle the contribution from the outer part of the accretion disk and the donor star, which in few cases has been identified as a OB supergiant.

For the time being, we need to rely on indirect methods to constrain $M_{\rm BH}$ in ULXs. With our work, we have applied the X-ray scaling method to a sample of ULXs with multiple

X-ray observations. As explained before, this method was introduced to determine M_{BH} and distance in GBHs by scaling the X-ray spectral and temporal trend of a reference source whose properties were well constrained. We then extended this method to AGNs using the reverberation mapping sample with the reasonable assumption that AGNs follow the same spectral transition as GBHs but on much longer timescales. Our choice of a sample of ULXs with multiple observations makes it possible to compare the ULX spectral evolution with the most appropriate reference pattern.

We performed a homogenous spectral analysis of all the available data with sufficient signal-to-noise ratio (exposure ≥ 10 ks) and then a systematic comparison of the spectral trends in the $\Gamma - N_{\mathrm{BMC}}$ plot. The majority of the spectral patterns show a positive trend, which can be directly compared to the reference ones. Some spectral trends appear more complex and can be explained by the presence of statistical outliers or by the fact that the trend may comprise data from different outbursts and/or different outburst phases (typically, the decay spectral pattern is different from the rising one). We cannot rule out that some spectral trends are genuinely different; in that case, it would not be possible to use the reference spectral trends to determine M_{BH}.

The results of our analysis suggests that a substantial fraction of our sample is consistent with the intermediate mass BH hypothesis. At first sight, these findings seem to be at odds with several recent results in this field pointing out that the vast majority of ULXs are "normal" or massive stellar BHs accreting at super-Eddington level with only few strong candidates to be intermediate mass BHs. However, it must be kept in mind that our sample is not complete by any means nor can be considered as representative for the whole ULX population. Indeed, the selection of sources with multiple and good-quality X-ray data is likely to be biased toward the brightest tail of the ULX population, which is more likely to contain larger mass objects. Additionally, taking into account the uncertainties associated with the M_{BH} determination, (which depend on the errors of Γ and N_{BMC} as well as on the uncertainty associated with the fitting procedure of the spectral trend in the $\Gamma - N_{\mathrm{BMC}}$ plot) several sources appear to be consistent with the hypothesis of massive sMBHs accreting at high rate.

The fact that the $M_{\rm BH}$ estimated with the scaling method are largely consistent with the values obtained utilizing very different methods including variability-based methods that are model independent, seems to confirm the validity of this X-ray method at all BH scales. Indeed, since it has been demonstrated that the scaling method can be successfully used to constrain $M_{\rm BH}$ for stellar and supermassive BHs, it is natural to expect that it can also be used in the intermediate range. One may question the applicability of this method to ULXs by claiming that they are in a peculiar ultraluminous spectral state that cannot be compared with the standard reference patterns. However, we must point out that among our reference patterns we include the one referring to 1997 outburst of XTE J1550−564, which has been identified as the Galactic analog of ULXs. We also use the pattern of the historical superluminal source GRS 1915+105, which is known to accrete at super-Eddington rate. Finally, this method has been successfully used to constrain the $M_{\rm BH}$ of PKS 0558−504, a bright radio-loud Narrow Line Seyfert 1 galaxy that accretes at super-Eddington level (Gliozzi et al., 2010).

We therefore conclude that the scaling method can be safely used also for highly accreting objects and hence to constrain $M_{\rm BH}$ in ULXs. The importance of finding IMBHs stems from the fact that these objects may be the local analogs of the BH seeds that grew into supermassive BHs at the center of virtually every galaxy. As a results, strong IMBH candidates offer a complementary way to shed some light on the conditions that led to the formation of SMBHs.

Chapter 4: Conclusion

The black hole mass ($M_{\rm BH}$) is a crucial parameter in astrophysics because it sets the physical properties (e.g., timescales and lengths) of BH systems and is the only BH parameter that is directly measurable. Accreting BHs are categorized into three classes based on the mass range: stellar mass black holes (sMBHs) that reside in binary systems, supermassive black holes (SMBHs) at the center of galaxies and active galactic nuclei (AGNs), and possibly intermediate mass black holes (IMBHs) in ultraluminous X-ray sources (ULXs) that may fill the gap between sMBHs and SMBHs. Studies of SMBHs have proven important to understand the formation and evolution of galaxies where IMBHs may represent the seeds of SMBHs. Currently, we are able to measure $M_{\rm BH}$ values accurately and reliably using optically-based dynamical methods and the reverberation mapping method for supermassive BHs in AGNs. However, the number of BH systems for which dynamical methods are applicable is severely limited and this hampers a comprehensive investigation of the SMBH mass function, which is critical to understand the evolutionary history of BHs and their connection to their host galaxies. Therefore, it is essential to develop and test alternative $M_{\rm BH}$ estimators based on different wavelengths and different physical assumptions. A particularly important role in this context can be played by X-ray based methods, which directly track the BH activity and are less affected by absorption and galaxy contamination.

Recently Shaposhnikov and Titarchuk (2009) introduced a novel X-ray method, the X-ray scaling method, that constrains $M_{\rm BH}$ and distance in sMBHs by scaling the spectral trend of target BH systems to the corresponding trends of reference BHs, whose physical properties are well-known. Observational and theoretical studies indicate that X-rays in BH accreting systems at all scales are produced by the same mechanism (Comptonization) and that stellar-mass and supermassive BHs show the same spectral evolution although on different timescales (specifically, a positive correlation between the slope of the X-ray spectrum, the photon index Γ, and the accretion rate, parameterized by $L_{\rm X}/L_{\rm Edd}$, is observed). This suggests that AGNs can be considered large-scale analog of sMBHs and that the X-ray scaling method can be extended to SMBHs. This is what we demonstrated in our precursor study, where we applied the X-ray scaling method to a sample of moderately/highly accreting AGNs and found that the derived $M_{\rm BH}$ values were fully consistent with those determined dynamically using the reverberation method (Gliozzi et al., 2011).

In the first part of this thesis work (described in Chapter 2), we investigated the limit of applicability of the X-ray scaling method in the low-accreting regime. To this end, we applied this X-ray method to a sample of low luminosity AGNs (LLAGNs) characterized by good X-ray data and $M_{\rm BH}$ values dynamically constrained. The first important result is that we found the lower limit of accretion rate ($L_{\rm X}/L_{\rm Edd} \sim 10^{-3}$) below which the X-ray scaling method cannot be applied. The simple explanation for this limit is that below an accretion rate threshold the nature of the accretion flow changes and so does the mechanism producing X-rays. As a result, we do not see any more the positive correlation between Γ and $L_{\rm X}/L_{\rm Edd}$, which is observed in all BH systems accreting at moderate or high rate and is at the basis of the X-ray scaling method. Specifically, for the vast majority of LLAGNs (43 out of 47) the X-ray scaling method yields $M_{\rm BH}$ values that are underestimated by a few orders of magnitude compared to the dynamical values. The only exceptions are NGC 3227, NGC 4151, NGC 4395, and NGC 6251, which have moderate accretion rates.

At very low accretion rate, a negative correlation between Γ and $L_{\rm X}/L_{\rm Edd}$ was found. This is consistent with recent findings for both stellar ans supermassive black holes and makes it possible to constrain $M_{\rm BH}$ with an alternative X-ray based method. Indeed, exploiting the direct dependence of $L_{\rm Edd}$ on $M_{\rm BH}$, one can use this anti-correlation to determine $\log(M_{\rm BH}) = \log(L_{\rm X}) - (\Gamma - B)/A - 38.11$ (where B is the intercept and A the slope of the anti-correlation). The $M_{\rm BH}$ values determined in this way showed good agreement with the corresponding dynamically measured values typically within a factor 10, with a substantial fraction (26/43) within a factor of 3.

Although sMBHs and SMBHs have been studied for over four decades and are now relatively well-understood, the very existence of IMBHs, that are supposed to fill the gap between these two classes of BHs, is still a matter of debate. The most promising sources to host IMBHs are the so-called ultraluminous X-ray sources (ULXs), off-nuclear point-like X-ray sources whose measured X-ray luminosity surpasses the Eddington limit for a 10 $M_{\odot}$ BH ($L_{\rm X} > 10^{39}$ erg/s). This high X-ray luminosity can be equally well explained by extremely high accreting sMBHs (perhaps in combination with some relativistic beaming effects) or by moderately accreting IMBHs. In principle, the outstanding question about the existence of IMBHs could be answered by measuring the dynamical mass in ULXs. Unfortunately, direct measurements of the optical properties of the elusive star companion in ULXs are still challenging for the current technology hampering a direct measurement of $M_{\rm BH}$. Nevertheless, since in many ULXs the X-ray emission is the only evidence for the BH activity, one can use X-ray based methods to determine $M_{\rm BH}$. In this context, the X-ray scaling method, which yields reliable estimates of $M_{\rm BH}$ for both moderately and highly accreting sMBHs and SMBHs, appears to be an ideal tool to shed some light on the existence of IMBHs and the nature of ULXs.

In the second part of this thesis (described in Chapter 3), we applied the X-ray scaling method to a sample of ULXs with multiple good-quality X-ray observations. This selection criterion allowed us to investigate the spectral evolution of ULXs and to compare their spectral pattern with the corresponding ones observed in sMBHs which are used as references in the scaling method. The first important finding of this analysis is that the vast majority of ULXs appear to have a spectral variability behavior consistent with the typical one observed in sMBHs. This has two important implications: 1) it suggests that in general ULXs behave as “normal” BH systems, and 2) it makes it possible to estimate $M_{\rm BH}$ using the scaling method.

The scaling method results appear to confirm the existence of a substantial fraction of IMBHs, and a the majority of $M_{\rm BH}$ consistent with the hypothesis of massive stellar mass BHs (MsBHs) accreting at high level. Our results are in good agreement with values from literature where different methods with different assumptions were used. We caution, however, that our sample is not complete by any means nor is it representative for the whole ULX population. Indeed, the selection of sources with multiple and good-quality X-ray data is likely to be biased toward the brightest tail of the ULX population, which is more likely to contain larger mass objects.

In summary, we have provided two important X-ray based tools to constrain the $M_{\rm BH}$ in AGNs spanning the entire accretion range. The first is the scaling method, which we demonstrated to be robust and reliable from $L_{\rm X}/L_{\rm Edd} \sim 10^{-3}$ up to the Eddington limit. The second is the method based on the $\Gamma - L_{\rm X}/L_{\rm Edd}$ anticorrelation, which constrains reasonably well $M_{\rm BH}$ in very low-accreting BH systems. The latter is particularly important because LLAGNs represent the vast majority of AGNs and often X-rays are the only measurable sign of the BH activity. Therefore, it may expand the range of the investigation of the AGN population and of the cosmic evolution of galaxies. In addition, being based on assumptions completely different from those used in the optically-based methods, the X-ray based method offers a sanity check for many important results obtained using optically-based indirect methods. We have also successfully applied the X-ray scaling method to ULXs demonstrating that this is a true scale-independent method for all BH systems, as illustrated by Figure 4.1 that shows $\log(M_{\rm BH})$ values determined via the scaling technique on the y-axis and the corresponding literature values (dynamical values for GBHs, reverberation mapping values for AGNs, and values determined with different methods for ULXs) on the x-axis. Finally, this method seems to confirm the existence of IMBHs, which may be relevant for our understanding of the seeds in SMBHs, and to reveal a large population of massive stellar BHs, which are expected to form from large stars with low metallicity. In the future, we plan to investigate the conditions under which ULXs form, by studying the metallicity of the galaxies hosting the ULXs in our sample.

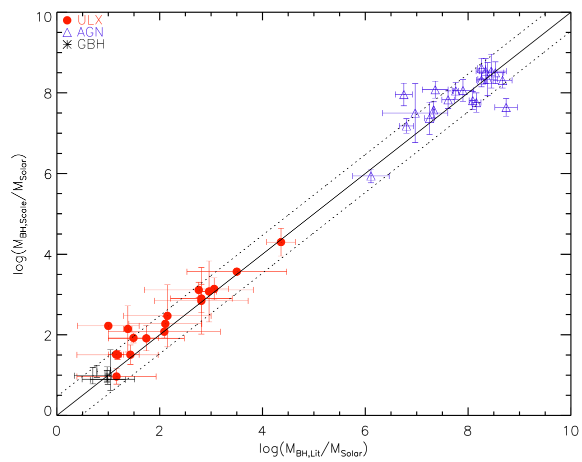

Figure 4.1: Plot of $M_{\rm BH,Scale}$ vs. $M_{\rm BH,Lit}$ for all scales. The obtained $M_{\rm BH}$ values from the scaling methods for GBHs are indicated with stars, ULXs with filled circles, and AGNs with open triangles. The solid line indicates the one-to-one correlation and dash lines for 0.47 dex level.

Tables

Table A.1: ULX spectral results

OsbID	Source Name Date	Exposure	n_{H}	kT	$\log(A)$	Γ	N_{BMC}	$\log(L_{\mathrm{X}})$	χ^2/dof
	HoIIX-1								
0561580401	2010-03-26T09:43:51	53.85	0.02 ± 0.01	0.16 ± 0.01	0.49 ± 0.03	2.52 ± 0.02	17.80 ± 1.61	39.03	946.58/872
0112520601	2002-04-10T14:27:49	12.64		0.27 ± 0.01	2.00	2.47 ± 0.04	34.06 ± 0.75	39.52	600.39/618
0112520701	2002-04-16T12:46:02	13.87	0.06 ± 0.01	0.05 ± 0.01	2.00	2.39 ± 0.01	68.15 ± 1.08	39.55	659.88/623
0200470101	2004-04-15T20:31:48	104.68	0.02 ± 0.01	0.20 ± 0.01	2.00	2.55 ± 0.01	45.08 ± 0.25	39.54	1488.89/1427
0112520901	2002-09-18T02:33:03	6.89		0.12 ± 0.01	2.00	2.81 ± 0.05	13.75 ± 0.38	38.73	213.13/194
	HoIXX-1								
0112521001	2002-04-10T17:37:52	10.71	0.10 ± 0.01	0.26 ± 0.01	2.00	1.65 ± 0.03	36.14 ± 0.66	39.89	816.99/775
0112521101	2002-04-16T17:33:15	11.52	0.07 ± 0.01	0.27 ± 0.01	2.00	1.76 ± 0.02	43.52 ± 0.66	39.94	897.60/898
0200980101	2004-09-26T07:25:12	119.17	0.08 ± 0.01	0.20 ± 0.01	0.70 ± 0.01	1.47 ± 0.01	32.11 ± 0.17	39.85	2388.67/2175
0657801601	2011-04-17T15:31:50	21.10	0.08 ± 0.01	0.52 ± 0.01	2.00	1.47 ± 0.12	115.55 ± 10.50	40.14	234.54/245
0657801801	2011-09-26T04:41:04	25.39	0.02 ± 0.01	0.27 ± 0.01	2.00	1.90 ± 0.02	81.24 ± 32.62	40.09	1119.47/1078
0657802001	2011-03-24T16:03:18	27.46	0.10 ± 0.01	0.32 ± 0.01	2.00	1.35 ± 0.07	44.65 ± 3.30	39.96	314.81/325
0657802201	2011-11-23T01:04:56	23.91	0.04 ± 0.01	0.28 ± 0.01	2.00	1.86 ± 0.02	106.79 ± 55.57	40.22	1206.23/1215
	NGC 55 ULX								
0028740201	2001-11-14T15:11:02	33.62	0.08 ± 0.01	0.23 ± 0.01	2.00	3.46 ± 0.03	37.60 ± 0.34	38.68	1031.29/811
0028740101	2001-11-15T01:15:36	31.52	0.07 ± 0.01	0.26 ± 0.01	2.00	3.14 ± 0.04	33.90 ± 0.46	38.81	836.61/721
0655050101	2010-05-24T07:48:05	127.44	0.14 ± 0.01	0.17 ± 0.01	2.00	3.91 ± 0.02	39.08 ± 39.07	38.14	1350.68/881
	IC 342 X-1								
0093640901	2001-02-11T01:22:16	10.86	0.22 ± 0.03	0.14 ± 0.02	2.00	1.64 ± 0.05	11.74 ± 0.52	39.37	140.06/152
0206890101	2004-02-20T07:22:39	23.91	0.26 ± 0.01	0.47 ± 0.04	2.00	2.10 ± 0.03	43.92 ± 0.50	39.72	1043.72/959
0206890201	2004-08-17T19:49:30	23.91	0.37 ± 0.02	0.26 ± 0.01	2.00	1.73 ± 0.04	16.98 ± 0.43	39.41	428.94/433
0206890401	2005-02-10T18:39:44	23.86	0.19 ± 0.02	0.46 ± 0.06	2.00	1.87 ± 0.05	54.23 ± 1.28	39.83	470.11/459
	IC 342 XMM2								
0093640901	2001-02-11T01:22:16	10.86	0.88 ± 0.14	0.98 ± 0.05	2.00	3.36 ± 0.55	29.89 ± 1.51	39.46	45.83/54
0206890101	2004-02-20T07:22:39	23.91	1.48 ± 0.03	0.83 ± 0.04	2.00	1.87 ± 0.03	115.40 ± 1.42	40.10	1122.74/1001
0206890201	2004-08-17T19:49:30	23.91	0.48 ± 0.05	0.98 ± 0.02	2.00	1.82 ± 0.05	30.56 ± 0.87	39.44	277.15/313
0206890401	2005-02-10T18:39:44	23.86	1.97 ± 0.11	0.08 ± 0.01	0.44 ± 0.08	1.71 ± 0.03	19.37 ± 0.99	39.50	79.87/75
	IC 342 XMM3								
0093640901	2001-02-11T01:22:16	10.86		0.20 ± 0.01	2.00	2.46 ± 0.11	5.04 ± 0.52	38.58	81.90/66
0206890101	2004-02-20T07:22:39	23.91	0.78 ± 0.01	0.09 ± 0.01	0.01 ± 0.01	3.03 ± 0.05	19.44 ± 1.31	38.26	198.24/121
0206890201	2004-08-17T19:49:30	23.91	0.46 ± 0.01	0.12 ± 0.01	2.00	2.50 ± 0.06	3.59 ± 0.24	38.30	216.15/130
0206890401	2005-02-10T18:39:44	23.86		0.21 ± 0.01	2.00	2.18 ± 0.20	1.81 ± 0.24	38.28	47.24/31
	IC342XMM4								
0093640901	2001-02-11T01:22:16	10.86		0.95 ± 0.03	0.66 ± 0.01	2.37 ± 1.29	3.31 ± 0.51	38.69	23.08/30
0206890101	2004-02-20T07:22:39	23.91		1.22 ± 0.02		$5.83\pm$	0.08	38.38	49.10/50
0206890201	2004-08-17T19:49:30	23.91		0.86 ± 0.02	2.00	1.68 ± 0.32	1.78 ± 0.32	38.44	59.29/53
0206890401	2005-02-10T18:39:44	23.86		1.79 ± 0.05		1.01 ± 0.01	1.36 ± 1.64	38.69	20.96/20
	M31 X-1								
0109270101	2001-06-29T06:59:13	57.90		0.20 ± 0.01	2.00	1.65 ± 0.02	26.16 ± 16.68	38.17	1133.17/969
0112570101	2002-01-06T18:44:42	64.32		0.25 ± 0.03	2.00	1.66 ± 0.02	18.06 ± 2.68	38.08	1412.87/1080
0112570401	2000-06-25T11:43:22	46.01		0.19 ± 0.02	2.00	1.55 ± 0.04	5.56 ± 1.11	37.71	296.63/293
0112570601	2000-12-28T00:51:02	13.31		0.35 ± 0.03	2.00	1.44 ± 0.19	16.04 ± 4.02	37.88	73.43/68
0202230201	2004-07-16T16:40:09	20.22		0.40 ± 0.02	2.00	1.39 ± 0.03	7.61 ± 0.32	37.82	237.21/213
0202230401	2004-07-19T01:42:12	21.91	$\leq \pm 0.03$	0.36 ± 0.02	2.00	1.33 ± 0.10	9.73 ± 1.77	37.84	153.29/180
0202230501	2004-07-19T13:11:22	27.31	0.14 ± 0.02	0.14 ± 0.01	2.00	1.54 ± 0.06	7.03 ± 1.49	37.83	100.99/143
0405320501	2006-07-02T14:36:49	21.91	$\leq \pm 0.03$	0.58 ± 0.03	2.00	1.31 ± 0.08	8.76 ± 1.22	37.61	142.75/129
0405320601	2006-08-09T12:21:42	21.92	0.06 ± 0.02	0.17 ± 0.01	2.00	2.20 ± 0.10	6.45 ± 0.92	37.23	81.86/99
0405320701	2006-12-31T14:23:46	15.92	$\leq \pm 0.03$	0.46 ± 0.03	2.00	1.07 ± 0.02	23.15 ± 5.78	37.74	37.89/39
0405320801	2007-01-16T11:46:21	13.91	0.13 ± 0.02	0.17 ± 0.01	2.00	1.67 ± 0.08	4.04 ± 1.17	37.59	92.80/91
0405320901	2007-02-05T03:43:19	16.91		0.24 ± 0.08	2.00	1.47 ± 0.08	5.19 ± 1.87	37.62	92.53/118
0505720201	2007-12-29T13:41:09	27.54	0.14 ± 0.03	0.23 ± 0.02	2.00	1.61 ± 0.08	5.94 ± 1.73	37.99	85.86/105
0505720301	2008-01-08T07:00:01	27.22		0.25 ± 0.05	2.00	1.56 ± 0.05	6.44 ± 3.14	37.63	194.52/204
0505720501	2008-01-27T22:27:17	21.82	0.05 ± 0.02	0.22 ± 0.01	2.00	1.44 ± 0.07	5.54 ± 1.20	37.70	125.82/168
0505720601	2008-02-07T04:55:14	21.92		0.47 ± 0.02	2.00	1.52 ± 0.14	8.38 ± 1.12	37.69	224.22/181

Table A.1 – continued from previous page

OsbID	Source Name Date	Exposure	n_{H}	kT	$\log(A)$	Γ	N_{BMC}	$\log(L_{\mathrm{X}})$	χ^2/dof
0551690301	2009-01-09T06:18:50	21.92		0.16 ± 0.03	2.00	1.39 ± 0.04	7.19 ± 0.01	37.85	265.42/243
0551690401	2009-01-15T21:39:44	27.12		0.81 ± 0.07	2.00	1.22 ± 0.07	16.33 ± 3.95	37.78	53.39/52
0551690501	2009-01-27T07:21:58	21.91		0.19 ± 0.02	2.00	1.47 ± 0.04	8.76 ± 0.01	37.87	261.01/285
0560180101	2008-07-18T06:11:54	21.91		0.35 ± 0.06	0.93 ± 0.15	1.18 ± 0.07	14.83 ± 6.57	37.77	69.44/84
0600660201	2009-12-28T12:41:48	18.82		0.24 ± 0.06	2.00	1.59 ± 0.05	13.56 ± 4.21	37.93	231.98/223
0600660301	2010-01-07T07:45:3	17.32		0.31 ± 0.06	2.00	1.71 ± 0.05	15.35 ± 2.04	38.13	393.79/391
0600660401	2010-01-15T12:42:49	17.22		0.34 ± 0.01	2.00	2.27 ± 0.04	48.97 ± 3.01	38.32	886.87/778
0600660501	2010-01-25T02:38:09	19.72	0.11 ± 0.01	0.15 ± 0.01	0.40 ± 0.05	1.96 ± 0.03	59.11 ± 3.90	38.08	634.24/588
0600660601	2010-02-02T02:40:31	17.32		0.18 ± 0.01	2.00	1.94 ± 0.03	15.76 ± 1.18	38.13	675.40/587
	M33 X-1								
0102640101	2000-08-04T06:06:43	18.56		0.84 ± 0.01	2.00	2.46 ± 0.16	43.76 ± 1.53	38.94	1329.67/1279
0102640301	2000-08-07T02:17:19	14.86	0.01 ± 0.01	0.67 ± 0.01	2.00	2.24 ± 0.20	70.76 ± 3.66	38.96	635.51/569
0102640601	2001-07-05T15:45:49	12.36		0.49 ± 0.02	2.00	2.11 ± 0.13	171.10 ± 14.83	38.97	360.52/341
0102641001	2001-07-08T06:06:59	13.11		0.27 ± 0.02	2.00	2.03 ± 0.03	121.88 ± 28.03	38.99	560.09/547
0102642101	2002-01-25T12:02:31	12.87		0.71 ± 0.03	2.00	2.51 ± 0.15	115.09 ± 5.13	38.97	1053.25/946
0102642301	2002-01-27T10:23:11	12.86	0.01 ± 0.01	0.73 ± 0.03	2.00	2.50 ± 0.16	108.95 ± 4.98	38.96	979014/968
0141980101	2003-07-11T16:28:26	16.72	0.01 ± 0.01	0.76 ± 0.01	2.00	2.29 ± 0.24	73.06 ± 4.13	39.07	671.82/700
0141980301	2003-07-25T07:57:34	25.12		0.65 ± 0.01	2.00	2.81 ± 0.12	74.34 ± 1.81	38.93	484.66/439
0141980501	2003-01-22T21:58:01	13.91	0.01 ± 0.01	0.71 ± 0.01	2.00	2.45 ± 0.16	78.91 ± 3.09	38.99	466.68/452
0141980601	2003-01-23T20:12:42	13.92	0.02 ± 0.01	0.72 ± 0.01	2.00	2.34 ± 0.13	78.08 ± 2.31	39.02	1045.87/825
0141980801	2003-02-12T15:40:40	10.42		0.34 ± 0.04	2.00	2.20 ± 0.03	89.19 ± 1.20	38.90	1263/1114
0650510101	2010-07-09T07:27:58	101.92	0.01 ± 0.01	0.67 ± 0.01	2.00	2.52 ± 0.05	118.98 ± 2.00	39.02	2072.52/1723
0650510201	2010-07-11T07:21:37	101.92		0.78 ± 0.01	2.00	2.35 ± 0.05	81.32 ± 1.22	38.94	2936.35/2039
	M81 X-6								
0111800101	2001-04-22T10:26:40	132.66	0.09 ± 0.01	1.06 ± 0.01	2.00	1.67 ± 0.12	6.08 ± 0.46	39.43	872.26/754
0112521001	2002-04-10T17:37:52	10.71	0.07 ± 0.02	0.34 ± 0.01	2.00	1.77 ± 0.06	20.15 ± 0.78	39.59	207.23/186
0112521101	2002-04-16T17:33:15	11.52	0.11 ± 0.01	0.93 ± 0.01	2.00	1.50 ± 0.08	23.16 ± 1.91	39.59	207.48/205
0200980101	2004-09-26T07:25:12	119.17	NA						
0657801601	2011-04-17T15:31:50	21.10	0.05 ± 0.04	0.25 ± 0.06	0.60 ± 0.39	1.59 ± 0.19	6.12 ± 0.62	39.05	15.66/13
0657801801	2011-09-26T04:41:04	25.39	0.11 ± 0.01	1.07 ± 0.01	2.00	2.09 ± 0.58	8.68 ± 1.36	39.51	142.01/175
0657802001	2011-03-24T16:03:18	27.46	0.19 ± 0.02	0.01 ± 0.01	0.06 ± 0.06	2.30 ± 0.02	34.94 ± 2.29	38.96	28.20/32
0657802201	2011-11-23T01:04:56	23.91	0.12 ± 0.01	0.25 ± 0.01	2.00	1.90 ± 0.11	6.70 ± 0.30	39.10	158.21/171
0693850801	2012-10-23T04:39:59	14.12	0.08 ± 0.02	1.26 ± 0.20	2.00	1.11 ± 0.04	65.02 ± 17.69	39.64	169.39/166
0693850901	2012-10-25T04:32:01	14.01	0.54 ± 0.03	1.39 ± 0.05	0.01 ± 0.01	2.63 ± 0.39	2.12 ± 0.01	39.58	108.48/120
0693851001	2012-10-27T04:27:39	13.92	0.08 ± 0.05	0.45 ± 0.12	2.00	1.86 ± 0.20	37.00 ± 16.21	39.48	107.14/121
0693851101	2012-11-16T03:15:38	13.32	0.09 ± 0.04	1.14 ± 0.29	2.00	1.76 ± 0.58	47.09 ± 23.53	39.58	56.11/54
0693851701	2012-11-12T03:26:59	9.92	NA						
0693851801	2012-11-14T03:18:04	13.82	0.13 ± 0.03	0.90 ± 0.09	2.00	1.15 ± 0.04	31.72 ± 6.50	39.59	84.54/88
	M82 X-1								
0112290201	2001-05-06T09:59:07	30.56	0.92 ± 0.01	0.12 ± 0.01	2.00	1.07 ± 0.01	178.41 ± 1.58	40.56	2733.53/1978
0206080101	2004-04-21T21:59:36	104.35	0.81 ± 0.01	0.13 ± 0.01	2.00	1.63 ± 0.01	51.56 ± 0.34	40.23	3154.54/2114
0560181301	2009-04-03T17:21:10	27.35	0.21 ± 0.07	0.55 ± 0.04	2.00	1.41 ± 0.06	208.12 ± 20.39	40.54	93.08/72
0560590101	2008-10-03T21:05:52	31.91	0.26 ± 0.01	0.81 ± 0.01	2.00	2.11 ± 0.02	397.22 ± 2.19	40.81	2677.03/2311
0560590201	2009-04-17T11:01:41	44.64	0.34 ± 0.01	0.61 ± 0.01	2.00	1.80 ± 0.01	283.04 ± 2.81	40.71	2301.60/2029
0560590301	2009-04-29T08:46:28	52.97	0.33 ± 0.01	0.44 ± 0.01	2.00	1.61 ± 0.01	162.12 ± 1.24	40.52	2099.14/1842
0657800101	2011-03-18T16:55:04	26.66	0.32 ± 0.01	0.03 ± 0.01		1.49 ± 0.01	26.62 ± 0.78	40.41	1547.06/1226
0657801901	2011-04-29T13:39:13	28.22	0.20 ± 0.01	0.24 ± 0.01	2.00	1.77 ± 0.02	120.62 ± 2.25	40.30	2064.03/1292
0657802101	2011-09-24T06:24:26	22.84	1.27 ± 0.01	0.08 ± 0.01		3.30 ± 0.02	127.29 ± 2.93	40.39	2111.00/1459
0657802301	2011-11-21T01:12:26	23.91	0.33 ± 0.01	0.30 ± 0.01	2.00	1.43 ± 0.02	115.35 ± 2.16	40.55	3066.44/1855
	NGC 1313 X-1								
0106860101	2000-10-17T03:20:40	42.42	0.23 ± 0.01	0.17 ± 0.01	0.31 ± 0.02	1.78 ± 0.02	19.67 ± 0.30	39.56	903.02/892
0150280101	2003-11-25T05:20:45	62.42	0.17 ± 0.04	0.02 ± 0.01	2.00	2.08 ± 0.06	17.57 ± 3.49	39.43	45.51/52
0150280301	2003-12-21T02:17:46	16.25	0.15 ± 0.01	0.22 ± 0.02	2.00	2.30 ± 0.04	40.81 ± 0.87	39.79	290.84/312
0150280401	2003-12-23T05:13:42	20.94	0.21 ± 0.01	0.18 ± 0.02	2.00	2.29 ± 0.06	34.06 ± 1.30	39.70	173.32/176
0150280501	2003-12-25T04:47:38	21.46	0.22 ± 0.02	0.25 ± 0.01	2.00	1.94 ± 0.09	18.49 ± 1.40	39.61	129.93/129
0150280601	2004-01-08T03:53:34	53.30	0.20 ± 0.01	0.23 ± 0.01	2.00	2.05 ± 0.04	26.38 ± 0.62	39.72	522.80/548
0205230201	2004-05-01T23:51:25	12.52	0.18 ± 0.02	0.27 ± 0.01	2.00	1.90 ± 0.13	17.32 ± 1.01	39.59	66.39/94

Table A.1 – continued from previous page

Source Name OsbID	Date	Exposure	$n_{\rm H}$	kT	$\log(A)$	Γ	$N_{\rm BMC}$	$\log(L_{\rm X})$	χ^2/dof
0205230301	2004-06-05T06:31:57	11.91	0.29 ± 0.01	0.01 ± 0.01	2.00	2.34 ± 0.01	171.84 ± 3.17	39.97	571.04/610
0205230401	2004-08-23T06:07:43	18.02	0.22 ± 0.01	0.16 ± 0.01	0.34 ± 0.05	3.01 ± 0.05	32.15 ± 0.73	39.11	398.52/383
0205230501(mos)	2004-11-23T07:22:41	16.02	0.16 ± 0.01	0.27 ± 0.01	2.00	1.70 ± 0.08	17.42 ± 0.85	39.65	135.22/151
0205230601	2005-02-07T11:58:14	14.32	0.18 ± 0.01	0.17 ± 0.01	0.08 ± 0.03	1.71 ± 0.04	25.91 ± 0.67	39.61	343.30/304
0301860101	2006-03-06T17:06:07	21.81	0.05 ± 0.01	0.31 ± 0.01	2.00	2.32 ± 0.05	33.78 ± 0.75	39.75	382.29/375
0405090101	2006-10-16T00:07:36	123.15	0.20 ± 0.01	0.17 ± 0.01	0.11 ± 0.01	1.74 ± 0.01	21.18 ± 0.16	39.53	1783.28/1566
NGC 1313 X-2									
0106860101	2000-10-17T03:20:40	42.416	0.11 ± 0.01	0.16 ± 0.01	2.00	2.27 ± 0.03	7.16 ± 0.15	39.01	418.69/400
0150280101	2003-11-25T05:20:45	62.418	0.00 ± 0.03	0.70 ± 0.04	0.53 ± 0.24	1.38 ± 0.09	25.31 ± 2.60	39.59	62.85/72
0150280301	2003-12-21T02:17:46	16.25	0.07 ± 0.01	1.03 ± 0.01	2.00	1.47 ± 0.06	23.58 ± 1.70	39.70	349.20/326
0150280401	2003-12-23T05:13:42	20.94	0.03 ± 0.01	0.37 ± 0.01	2.00	1.76 ± 0.05	26.94 ± 0.79	39.78	263.44/284
0150280501	2003-12-25T04:47:38	21.46	0.30 ± 0.01	0.13 ± 0.01	0.81 ± 0.15	2.23 ± 0.04	15.96 ± 0.60	39.28	145.97/164
0150280601	2004-01-08T03:53:34	53.30	0.05 ± 0.01	0.24 ± 0.01	2.00	2.33 ± 0.06	8.94 ± 0.25	39.14	326.88/321
0205230201	2004-05-01T23:51:25	12.52	0.18 ± 0.02	0.18 ± 0.02	2.00	2.57 ± 0.15	9.91 ± 0.58	39.01	63.93/56
0205230301	2004-06-05T06:31:57	11.91	0.08 ± 0.01	1.13 ± 0.01	0.50 ± 0.01	1.49 ± 0.08	24.50 ± 1.48	39.76	628.98/600
0205230401	2004-08-23T06:07:43	18.02	0.04 ± 0.01	0.22 ± 0.01	0.37 ± 0.07	1.88 ± 0.06	6.47 ± 0.21	39.03	263093/236
0205230501(mos)	2004-11-23T07:22:41	16.02	0.12 ± 0.01	0.24 ± 0.01	2.00	2.12 ± 0.07	5.74 ± 0.24	39.03	148.63/186
0205230601	2005-02-07T11:58:14	14.32	0.08 ± 0.01	1.33 ± 0.01	2.00	1.26 ± 0.03	34.36 ± 3.11	39.77	551.54/518
0301860101	2006-03-06T17:06:07	21.81	0.09 ± 0.01	1.30 ± 0.01	2.00	1.37 ± 0.06	18.54 ± 1.90	39.72	707.56/733
0405090101	2006-10-16T00:07:36	123.15	0.09 ± 0.01	1.01 ± 0.01	2.00	1.39 ± 0.02	21.85 ± 0.61	39.66	1822.92/1559
NGC 1313 XMM2									
0106860101	2000-10-17T03:20:40	42.42	0.18 ± 0.01	0.12 ± 0.01	2.00	2.93 ± 0.03	12.04 ± 0.26	38.77	601.31/360
0150280301	2003-12-21T02:17:46	16.25	0.67 ± 0.02	0.11 ± 0.01		2.80 ± 0.07	23.20 ± 1.77	38.81	78.78/80
0150280401	2003-12-23T05:13:42	20.94	0.70 ± 0.02	0.10 ± 0.01	0.39 ± 0.01	3.01 ± 0.24	19.77 ± 2.13	38.69	30.05/38
0150280601	2004-01-08T03:53:34	53.30	0.66 ± 0.01	0.11 ± 0.01	0.28 ± 0.07	2.79 ± 0.05	18.69 ± 1.05	38.82	180.64/148
0205230301	2004-06-05T06:31:57	11.91	0.45 ± 0.01	1.14 ± 0.01		2.47 ± 0.07	12.31 ± 0.74	38.81	114.39/125
0205230401	2004-08-23T06:07:43	18.02	0.43 ± 0.01	0.13 ± 0.01		2.77 ± 0.06	16.66 ± 0.90	38.74	126.34/139
0205230601	2005-02-07T11:58:14	14.32	0.63 ± 0.01	0.11 ± 0.01		2.66 ± 0.06	18.33 ± 1.18	38.81	117.47/110
0301860101	2006-03-06T17:06:07	21.81	0.61 ± 0.01	0.11 ± 0.01	0.10 ± 0.04	2.84 ± 0.03	20.54 ± 0.80	38.77018902	271.42/268
0405090101	2006-10-16T00:07:36	123.15	0.57 ± 0.01	0.12 ± 0.01		2.71 ± 0.02	18.15 ± 0.39	38.78	641.82/603
NGC 1313 XMM4									
0106860101	2000-10-17T03:20:40	42.42	0.28 ± 0.02	0.13 ± 0.01	2.00	1.78 ± 0.06	1.38 ± 0.08	38.59	88.61/92
0205230301	2004-06-05T06:31:57	11.91	0.07 ± 0.04	0.30 ± 0.04	0.61 ± 0.14	1.14 ± 0.03	3.24 ± 0.33	38.62	18.92/16
0205230501(mos)	2004-11-23T07:22:41	16.02	0.52 ± 0.04	0.14 ± 0.01		1.60 ± 0.16	3.21 ± 0.33	38.75	11.31/25
0301860101	2006-03-06T17:06:07	21.81	0.03 ± 0.01	0.82 ± 0.04	0.82 ± 0.58	1.24 ± 0.07	3.08 ± 0.53	38.59	28.41/32
0405090101	2006-10-16T00:07:36	123.15	0.04 ± 0.01	0.24 ± 0.01	0.76 ± 0.11	1.55 ± 0.05	1.63 ± 0.05	38.60	217.98/207
NGC 2403 X-1									
0150651101	2003-04-30T15:58:22	32.32		0.55 ± 0.09	0.22 ± 0.19	1.28 ± 0.15	10.65 ± 2.15	39.02	57.15/49
0150651201(mos)	2003-09-11T09:26:38	11.41	0.11 ± 0.03	0.92 ± 0.19	2.00	1.23 ± 0.24	19.86 ± 13.51	39.11	28.83/45
0164560901	2004-09-12T17:34:28	80.46	0.11 ± 0.01	0.90 ± 0.01	2.00	1.18 ± 0.24	8.60 ± 0.51	39.16	920.74/886
NGC 253 X-1									
0110900101	2000-12-14T01:33:04	33.73	0.07 ± 0.02	0.32 ± 0.01	2.00	1.77 ± 0.21	1.21 ± 0.12	38.27	47.48/49
0125960101	2000-06-03T10:29:06	60.81	0.03 ± 0.01	0.59 ± 0.03	2.00	2.42 ± 0.19	3.80 ± 0.23	38.67	194.99/210
0125960201	2000-06-04T01:03:43	17.51	0.02 ± 0.04	1.07 ± 0.03	0.49 ± 0.01	1.06 ± 0.36	1.88 ± 1.56	38.40	36.82/38
0152020101	2003-06-19T14:19:22	140.80	0.06 ± 0.01	0.77 ± 0.15	2.00	2.14 ± 0.20	4.42 ± 0.21	38.90	883.96/777
0304850901	2006-01-02T08:09:24	11.81		0.80 ± 0.03	2.00	3.49 ± 1.58	2.47 ± 0.32	38.52	75.32/65
0304851001	2006-01-06T04:35:02	11.85	0.01 ± 0.02	0.35 ± 0.08	2.00	1.93 ± 0.11	3.35 ± 0.20	38.65	68.36/75
0304851101	2005-12-16T20:37:52	23.21	0.02 ± 0.02	0.83 ± 0.02		1.05 ± 0.11	1.91 ± 0.36	38.26	57.82/86
0304851201	2006-01-09T19:09:13	19.92	0.02 ± 0.01	0.73 ± 0.02	2.00	2.61 ± 0.43	3.16 ± 0.25	38.64	132.91/146
0304851301	2006-01-11T02:22:14	20.92	0.03 ± 0.03	0.76 ± 0.03	2.00	1.47 ± 0.17	4.45 ± 0.88	38.73	27.38/30
NGC 253 X-2									
0110900101	2000-12-14T01:33:04	33.73	0.13 ± 0.01	1.50 ± 0.01	2.00	1.35 ± 0.14	5.63 ± 1.48	39.27	590.75/561
0125960101	2000-06-03T10:29:06	60.81	0.11 ± 0.01	1.32 ± 0.01	2.00	1.58 ± 0.20	3.78 ± 0.65	39.14	677.04/654
0125960201	2000-06-04T01:03:43	17.51	0.10 ± 0.01	1.31 ± 0.02	2.00	2.06 ± 1.06	8.68 ± 1.05	39.28	226.42/216
0152020101	2003-06-19T14:19:22	140.80	0.11 ± 0.01	1.45 ± 0.01	2.00	1.12 ± 0.02	12.61 ± 1.47	39.16	1124/1064
0304850901	2006-01-02T08:09:24	11.81	0.10 ± 0.01	1.26 ± 0.02	2.00	1.61 ± 0.25	5.59 ± 1.08	39.08	185.13/191
0304851001	2006-01-06T04:35:02	11.85	0.81 ± 0.02	0.10 ± 0.01	2.00	2.08 ± 0.03	11.74 ± 0.49	39.12	144.35/166

Table A.1 – continued from previous page

Source Name OsbID	Date	Exposure	n_{H}	kT	$\log(A)$	Γ	N_{BMC}	$\log(L_{\mathrm{X}})$	χ^2/dof
0304851101	2005-12-16T20:37:52	23.21	0.14 ± 0.01	0.98 ± 0.02	0.20 ± 0.11	1.21 ± 0.05	10.45 ± 0.78	39.00	224.49/225
0304851201	2006-01-09T19:09:13	19.92	0.10 ± 0.01	1.08 ± 0.01	2.00	3.17 ± 0.91	5.73 ± 0.49	39.05	315.63/294
0304851301	2006-01-11T02:22:14	20.92	0.13 ± 0.03	0.93 ± 0.03	2.00	2.31 ± 0.60	7.28 ± 0.92	39.05	71.78/78
NGC 253 XMM4									
0110900101	2000-12-14T01:33:04	33.73		0.88 ± 0.03	0.32 ± 0.28	1.01 ± 0.12	0.95 ± 0.37	37.83	29.71/31
0152020101	2003-06-19T14:19:22	140.80	0.07 ± 0.02	0.98 ± 0.01	2.00	3.30 ± 1.61	0.38 ± 0.11	38.10	105.37/112
NGC 253 XMM5									
0110900101	2000-12-14T01:33:04	33.73	0.28 ± 0.04	0.15 ± 0.01	2.00	1.56 ± 0.14	1.03 ± 0.12	38.37	42.59/31
0125960101	2000-06-03T10:29:06	60.81	0.08 ± 0.04	0.54 ± 0.02	2.00	2.53 ± 1.72	0.19 ± 0.06	37.47	28.17/18
0152020101	2003-06-19T14:19:22	140.80	0.31 ± 0.01	0.03 ± 0.01	2.00	2.16 ± 0.01	5.85 ± 0.13	38.67	436.76/411
0304850901	2006-01-02T08:09:24	11.81	0.48 ± 0.03	0.16 ± 0.01	2.00	2.08 ± 0.08	3.04 ± 0.23	38.56	68.98/59
0304851001	2006-01-06T04:35:02	11.85	0.22 ± 0.03	0.26 ± 0.01	2.00	1.98 ± 0.15	2.81 ± 0.23	38.57	35.08/49
0304851101	2005-12-16T20:37:52	23.21	0.32 ± 0.02	0.26 ± 0.01	2.00	1.58 ± 0.11	2.83 ± 0.17	38.69	98.54/89
NGC 300 XMM1									
0112800101	2001-01-01T14:21:02	46.71	0.05 ± 0.01	0.17 ± 0.01	2.00	2.41 ± 0.05	2.87 ± 0.07	37.94	332.33/300
0112800201	2000-12-26T19:34:02	36.91	0.02 ± 0.01	0.15 ± 0.01	2.00	1.85 ± 0.08	0.83 ± 0.05	37.71	100.90/109
0305860301	2005-11-25T07:43:45	36.81	0.05 ± 0.01	0.18 ± 0.01	2.00	2.37 ± 0.05	3.96 ± 0.15	38.11	304.32/269
0305860401	2005-05-22T05:12:52	36.81	0.14 ± 0.01	0.15 ± 0.01	2.00	2.22 ± 0.07	1.93 ± 0.14	37.86	144.69/140
0656780401	2010-05-28T14:47:43	18.42	18.42 ± 0.01	0.25 ± 0.01	2.00	1.74 ± 0.35	0.78 ± 0.16	38.06	56.16/48
NGC 300 XMM2									
0112800101	2001-01-01T14:21:02	46.71		0.20 ± 0.01	2.00	2.12 ± 0.17	0.47 ± 0.05	37.32	63.70/63
0112800201	2000-12-26T19:34:02	36.91		0.24 ± 0.01	2.00	1.67 ± 0.30	0.32 ± 0.05	37.32	42.50/42
0305860301	2005-11-25T07:43:45	36.81	0.16 ± 0.02	0.14 ± 0.01	2.00	2.13 ± 0.15	0.51 ± 0.06	37.33	27.25/39
0305860401	2005-05-22T05:12:52	36.81		0.19 ± 0.01	2.00	2.57 ± 0.20	0.75 ± 0.07	37.30	50.86/60
NGC 300 XMM3									
0112800101	2001-01-01T14:21:02	46.71	0.32 ± 0.04	0.17 ± 0.04	2.00	1.98 ± 0.10	0.79 ± 0.06	37.61	40.69/43
0112800201	2000-12-26T19:34:02	36.91	0.23 ± 0.04	0.44 ± 0.04	1.02 ± 0.01	1.89 ± 0.23	1.00 ± 0.09	37.70	43.36/43
NGC4 395 XMM1									
0112521901	2002-05-31T01:01:22	15.87	0.16 ± 0.01	0.17 ± 0.01	2.00	2.87 ± 0.17	1.78 ± 0.17	38.11	86.45/92
0112522001	2002-06-12T18:40:41	17.13	NA						
0142830101	2003-11-30T03:40:59	113.39	0.16 ± 0.01	0.15 ± 0.01	1.60 ± 0.01	3.89 ± 0.07	2.89 ± 0.13	37.71	391.67/291
NGC 4395 XMM2									
0112521901	2002-05-31T01:01:22	18.12	0.08 ± 0.03	0.21 ± 0.01	2.00	1.74 ± 0.51	0.57 ± 0.15	38.20	19.25/10
0112522001	2002-06-12T18:40:41	43.87	NA						
0142830101	2003-11-30T03:40:59	45.89		0.13 ± 0.01	2.00	1.99 ± 0.16	0.29 ± 0.04	37.80	22.08/23
NGC 4395 XMM3									
0112521901	2002-05-31T01:01:22	15.87		0.11 ± 0.04	2.00	1.94 ± 0.14	0.69 ± 0.08	38.22	10.81/16
0112522001	2002-06-12T18:40:41	17.13	NA						
0142830101	2003-11-30T03:40:59	113.39		0.22 ± 0.01	2.00	1.54 ± 0.06	0.64 ± 0.03	38.30	132.49/137
NGC 4490 XMM1									
0112280201	2002-05-27T08:24:13	18.12	0.14 ± 0.03	0.58 ± 0.02	2.00	3.32 ± 0.37	4.40 ± 0.26	39.41	72.41/69
0556300101	2008-05-19T08:52:45	43.87	0.26 ± 0.04	0.55 ± 0.03	2.00	1.95 ± 0.21	2.09 ± 0.17	39.26	77.27/70
0556300201	2008-06-22T06:14:13	45.89	0.64 ± 0.08	0.35 ± 0.02	2.00	1.86 ± 0.33	2.67 ± 0.35	39.40	22.17/21
NGC 4490 XMM2									
0112280201	2002-05-27T08:24:13	18.12	0.25 ± 0.03	0.60 ± 0.03	0.49 ± 0.12	1.13 ± 0.03	5.99 ± 0.58	39.37	50.71/59
0556300101	2008-05-19T08:52:45	43.87	0.22 ± 0.02	0.63 ± 0.03	2.00	3.87 ± 0.31	5.33 ± 0.23	39.50582803	167.29/188
0556300201	2008-06-22T06:14:13	45.89	0.19 ± 0.04	0.45 ± 0.07	0.29 ± 0.09	1.30 ± 0.06	8.41 ± 0.68	39.66	67.12/60
NGC 4490 XMM3									
0112280201	2002-05-27T08:24:13	18.12	0.32 ± 0.06	0.38 ± 0.03	2.00	2.89 ± 0.26	4.08 ± 0.01	39.27	45.14/54
0556300101	2008-05-19T08:52:45	43.87	0.19 ± 0.06	0.83 ± 0.06	0.10 ± 0.01	1.01 ± 0.03	5.70 ± 1.00	39.26	49.43/57
0556300201	2008-06-22T06:14:13	45.89	0.05 ± 0.01	0.68 ± 0.08		1.13 ± 0.06	6.25 ± 0.58	39.34	32.53/28
NGC 4490 XMM4									
0112280201	2002-05-27T08:24:13	18.12	0.34 ± 0.05	0.53 ± 0.03	2.00	2.93 ± 0.48	2.63 ± 0.28	39.28	19.73/25
0556300101	2008-05-19T08:52:45	43.87	0.35 ± 0.04	0.64 ± 0.09	2.00	2.18 ± 0.16	4.23 ± 0.22	39.52	136.20/126
0556300201	2008-06-22T06:14:13	45.89	0.62 ± 0.10	1.00 ± 0.04	2.00	2.28 ± 1.48	2.77 ± 0.61	39.48	26.35/22
NGC 4490 XMM5									
0112280201	2002-05-27T08:24:13	18.12	0.02 ± 0.03	0.42 ± 0.03	0.49 ± 0.09	1.14 ± 0.03	3.51 ± 0.37	39.16	30.91/37

Table A.1 – continued from previous page

Source Name OsbID	Date	Exposure	n_{H}	kT	$\log(A)$	Γ	N_{BMC}	$\log(L_{\mathrm{X}})$	χ^2/dof
0556300101	2008-05-19T08:52:45	43.87	0.09 ± 0.02	0.34 ± 0.07	2.00	2.01 ± 0.12	2.50 ± 0.14	39.32	124.61/126
0556300201	2008-06-22T06:14:13	45.89		1.01 ± 0.03		1.00 ± 0.01	0.85 ± 0.35	39.13	27.76/26
NGC 4736 XMM1									
0094360601	2002-05-23T08:26:55	41.02		0.22 ± 0.07	2.00	2.13 ± 0.28	1.32 ± 0.14	38.56	7.93/12
0094360701	2002-06-26T13:51:34	18.94	0.45 ± 0.03	0.11 ± 0.01	2.00	1.94 ± 0.14	1.19 ± 0.16	38.60	13.62/17
NGC 4945 XMM1									
0112310301	2001-01-21T09:28:45	23.50	0.28 ± 0.04	0.60 ± 0.05	2.00	2.18 ± 0.21	3.43 ± 0.25	38.83	64.86/84
0204870101	2004-01-10T18:51:39	64.92	0.18 ± 0.03	0.43 ± 0.03	2.00	1.88 ± 0.08	2.83 ± 0.12	38.77	168.58/161
NGC 4945 XMM2									
0112310301	2001-01-21T09:28:45	23.50	0.13 ± 0.03	1.04 ± 0.03	2.00	1.33 ± 0.07	4.90 ± 0.69	38.86	65.90/74
0204870101	2004-01-10T18:51:39	64.92	0.10 ± 0.02	0.72 ± 0.03	2.00	2.88 ± 0.24	3.64 ± 0.18	38.83	193.83/203
NGC 4945 XMM3									
0112310301	2001-01-21T09:28:45	23.50	0.18 ± 0.04	0.37 ± 0.08	2.00	1.75 ± 0.10	3.06 ± 0.18	38.85	46.44/62
NGC 4945 XMM4									
0112310301	2001-01-21T09:28:45	23.50	0.13 ± 0.04	0.61 ± 0.02		1.00 ± 3.00	2.27 ± 0.28	38.18	35.13/36
0204870101	2004-01-10T18:51:39	64.92	0.22 ± 0.02	0.81 ± 0.01	2.00	4.18 ± 1.21	1.73 ± 0.18	38.75	208.37/227
NGC 4945 XMM5									
0112310301	2001-01-21T09:28:45	23.50	0.67 ± 0.16	0.54 ± 0.05	2.00	1.66 ± 0.13	2.37 ± 0.21	38.66	26.60/24
0204870101	2004-01-10T18:51:39	64.92		1.21 ± 0.04	2.00	5.84 ± 1.60	2.48 ± 0.16	38.55	64.32/66
NGC 5204 X-1									
0142770101	2003-01-06T01:30:23	31.78	0.03 ± 0.01	0.20 ± 0.01	2.00	1.90 ± 0.04	6.99 ± 0.17	39.44	434.43/471
0142770301	2003-04-25T13:38:46	18.45	0.02 ± 0.01	0.17 ± 0.01	0.37 ± 0.06	2.11 ± 0.05	13.95 ± 0.38	39.49	258.31/249
0150650301	2003-05-01T04:48:30	10.95		0.16 ± 0.01	2.00	2.35 ± 0.04	14.20 ± 0.36	39.50	289.28/305
0405690101	2006-11-16T01:13:41	45.32	0.05 ± 0.01	0.19 ± 0.01	2.00	2.53 ± 0.03	17.42 ± 0.33	39.52	611.06/549
0405690201	2006-11-19T20:30:08	45.32		0.18 ± 0.01	2.00	2.58 ± 0.02	15.00 ± 0.15	39.43	1052.57/893
0405690501	2006-11-25T20:08:43	43.15		0.27 ± 0.01	2.00	1.90 ± 0.04	7.89 ± 0.16	39.49	746.30/716
NGC 5408 X-1									
0112290601	2001-08-08T10:22:14	8.19		0.19 ± 0.01	2.00	2.47 ± 0.08	30.32 ± 2.37	39.10991586	231.77/288
0302900101	2006-01-13T19:03:57	132.25	0.03 ± 0.01	0.15 ± 0.01	2.00	2.82 ± 0.02	10.44 ± 0.11	39.01	1207.32/929
0500750101	2008-01-13T19:28:07	115.69	0.02 ± 0.01	0.14 ± 0.01	0.01 ± 0.01	2.61 ± 0.02	21.17 ± 0.18	39.12	982.65/823
0653380201	2010-07-17T03:36:03	128.91		0.15 ± 0.01	0.17 ± 0.02	2.59 ± 0.02	12.59 ± 1.35	39.22	895.69/718
0653380301	2010-07-19T03:28:20	130.88		0.17 ± 0.01	2.00	2.60 ± 0.01	3.71 ± 0.08	39.21	1422.43/1041
0653380401	2011-01-26T16:32:05	121.02		0.01 ± 0.01		2.67 ± 0.01	197.19 ± 1.30	39.18	1203.12/1035
0653380501	2011-01-28T16:12:08	126.37		0.15 ± 0.01	0.29 ± 0.02	2.60 ± 0.02	16.78 ± 0.12	39.17	593.71/573
NGC 5194 XMM1									
0112840201	2003-01-15T13:35:47	20.92	0.06 ± 0.02	0.22 ± 0.23	2.00	1.98 ± 0.25	0.69 ± 0.08	38.84	56.72/46
0212480801	2005-07-01T07:01:03	49.21	0.36 ± 0.02	0.95 ± 0.02	2.00	3.05 ± 0.07	2.82 ± 0.24	38.49	77.20/67
0303420101	2006-05-20T06:53:57	54.11	0.09 ± 0.02	0.22 ± 0.01	2.00	2.26 ± 0.21	0.41 ± 0.06	38.50	54.98/45
0303420201	2006-05-24T11:35:02	36.81	0.02 ± 0.02	0.27 ± 0.01	2.00	2.02 ± 0.31	0.69 ± 0.10	38.83	65.37/50
0677980701	2011-06-07T05:19:56	13.32		0.21 ± 0.10	2.00	2.28 ± 0.18	0.28 ± 0.03	38.86	25.29/28
NGC 5194 XMM2									
0112840201	2003-01-15T13:35:47	20.92	0.13 ± 0.02	0.30 ± 0.01	2.00	1.54 ± 0.20	1.09 ± 0.15	39.14	41.50/54
0212480801	2005-07-01T07:01:03	49.21		0.21 ± 0.01	2.00	1.55 ± 0.12	1.26 ± 0.12	39.25	30.74/41
0303420101	2006-05-20T06:53:57	54.11	0.07 ± 0.01	0.31 ± 0.01	2.00	1.69 ± 0.14	0.94 ± 0.07	39.05	80.84/96
0303420201	2006-05-24T11:35:02	36.81		0.38 ± 0.01	2.00	1.94 ± 0.18	1.14 ± 0.09	39.07	86.64/81
0677980701	2011-06-07T05:19:56	13.32	0.04 ± 0.01	0.83 ± 0.10	2.00	1.90 ± 0.45	0.14 ± 0.07	39.07	23.53/22
NGC 5194 XMM3									
0112840201	2003-01-15T13:35:47	20.92		0.31 ± 0.02	2.00	1.58 ± 0.15	0.77 ± 0.09	38.97	26.61/32
0212480801	2005-07-01T07:01:03	49.21	0.05 ± 0.01	0.28 ± 0.01	2.00	1.54 ± 0.05	3.49 ± 0.14	39.64	245.28/210
0303420101	2006-05-20T06:53:57	54.11	0.15 ± 0.01	0.26 ± 0.01	2.00	1.37 ± 0.04	2.83 ± 0.13	39.57	190.05/192
0303420201	2006-05-24T11:35:02	36.81	0.14 ± 0.01	0.22 ± 0.01	2.00	1.40 ± 0.04	3.63 ± 0.15	39.72	193.14/195
0677980701	2011-06-07T05:19:56	13.32	0.09 ± 0.03	0.24 ± 0.01	2.00	1.38 ± 0.15	3.09 ± 0.64	39.54	48.84/56
NGC 5194 XMM4									
0112840201	2003-01-15T13:35:47	20.92		0.62 ± 0.04	2.00	1.50 ± 0.17	0.88 ± 0.17	38.90	10.93/18
0212480801	2005-07-01T07:01:03	49.21	0.26 ± 0.05	0.21 ± 0.01	2.00	1.60 ± 0.28	0.31 ± 0.05	38.65	12.84/12
0303420101	2006-05-20T06:53:57	54.11	0.14 ± 0.04	0.22 ± 0.01	2.00	1.49 ± 0.23	0.20 ± 0.04	38.46	9.54/11
NGC 5194 XMM5									

Table A.1 – continued from previous page

OsbID	Source Name Date	Exposure	$n_{\rm H}$	kT	$\log(A)$	Γ	$N_{\rm BMC}$	$\log(L_{\rm X})$	χ^2/dof
0112840201	2003-01-15T13:35:47	20.92	0.86 ± 0.01	0.09 ± 0.01		2.34 ± 0.05	4.62 ± 0.34	39.07	152.94/133
0212480801	2005-07-01T07:01:03	49.21	0.89 ± 0.01	0.09 ± 0.01	2.00	2.31 ± 0.05	2.64 ± 0.19	39.15	294.71/210
0303420101	2006-05-20T06:53:57	54.11	0.85 ± 0.01	0.09 ± 0.01	2.00	2.12 ± 0.05	1.34 ± 0.09	39.02	223.38/181
0677980701	2011-06-07T05:19:56	13.32		0.26 ± 0.02	2.00	1.96 ± 0.32	0.44 ± 0.07	39.11	78.76/80
	NGC 5194 XMM6								
0112840201	2003-01-15T13:35:47	20.92		0.08 ± 0.08	2.00	2.04 ± 0.17	0.41 ± 0.04	38.58	21.36/12
0212480801	2005-07-01T07:01:03	49.21		0.12 ± 0.07	1.19 ± 0.31	2.08 ± 0.18	0.30 ± 0.03	38.40	20.06/25
0303420101	2006-05-20T06:53:57	54.11		0.34 ± 0.01	2.00	1.32 ± 0.10	0.25 ± 0.05	38.41	19.42/18
0303420201	2006-05-24T11:35:02	36.81		0.21 ± 0.02	2.00	2.14 ± 0.37	0.22 ± 0.03	38.28	15.57/13
	NGC 5194 XMM7								
0112840201	2003-01-15T13:35:47	20.92		0.12 ± 0.04	2.00	1.87 ± 0.18	0.32 ± 0.04	38.58	11.45/11
0212480801	2005-07-01T07:01:03	49.21		0.37 ± 0.03	2.00	2.07 ± 0.29	0.55 ± 0.06	38.73	49.44/41
0303420101	2006-05-20T06:53:57	54.11	0.13 ± 0.03	0.16 ± 0.01	2.00	1.51 ± 0.12	0.51 ± 0.05	38.92	32.93/28
0303420201	2006-05-24T11:35:02	36.81		0.76 ± 0.04	2.00	1.32 ± 0.08	1.37 ± 0.25	38.97	24.09/25
	NGC 6946 X-6								
0200670101	2004-06-09T18:58:28	16.41	0.20 ± 0.02	0.17 ± 0.01	2.00	1.78 ± 0.21	3.74 ± 0.47	39.47	48.83/35
0200670201	2004-06-11T19:24:30	14.38	0.21 ± 0.02	$\leq \pm 11.23$	2.00	2.71 ± 0.08	10.13 ± 0.01	39.29	178.59/140
0200670301	2004-06-13T19:17:13	15.61	0.33 ± 0.01	0.17 ± 0.01	2.00	2.36 ± 0.07	5.72 ± 0.32	39.34	148.34/145
0200670401	2004-06-25T16:51:04	21.21	0.24 ± 0.01	0.19 ± 0.01	2.00	2.25 ± 0.09	5.78 ± 0.37	39.43	152.33/125
0401360101	2006-05-23T10:46:07	20.91	NA						
0401360201	2006-06-02T09:08:45	24.42	0.28 ± 0.02	0.17 ± 0.01	2.00	2.25 ± 0.12	6.28 ± 0.57	39.46	56.31/52
0401360301	2006-06-18T08:07:04	24.41	0.29 ± 0.02	0.17 ± 0.01	2.00	2.32 ± 0.12	6.05 ± 0.56	39.40	33.49/52
0500730101	2007-11-08T23:20:25	31.93	0.28 ± 0.01	0.18 ± 0.01	2.00	2.16 ± 0.05	4.67 ± 0.18	39.38	322.34/302
0500730201	2007-11-02T22:51:24	37.30	0.36 ± 0.01	0.15 ± 0.01	2.00	2.37 ± 0.04	6.40 ± 0.26	39.37	228.96/246
0691570101	2012-10-21T19:05:25	119.30	0.27 ± 0.01	0.21 ± 0.01	2.00	2.76 ± 0.06	7.13 ± 0.16	39.42	1130.84/957

Table A.2: M_{BH} of ULXs via the X-ray scaling method using spectral patterns of moderately accreting GBHs

Galaxy	ULX	GROJ1655D05		GROJ1655R05		GX339D03		GX339R04	
		$\log(M_{\mathrm{BH}})$	Ratio	$\log(M_{\mathrm{BH}})$	Ratio	$\log(M_{\mathrm{BH}})$	Ratio	$\log(M_{\mathrm{BH}})$	Ratio
HoII	X-1								
HoIX	X-1	4.12 ± 0.01	1.36 ± 1.07	3.56 ± 0.00	0.80 ± 1.06	4.32 ± 0.13	1.56 ± 1.19	3.91 ± 0.16	1.15 ± 1.22
IC 342	X-1	3.57 ± 0.04	0.07 ± 1.01	3.19 ± 0.17	0.31 ± 1.14	3.91 ± 0.18	0.41 ± 1.15	3.34 ± 0.37	0.16 ± 1.34
	XMM2	3.72 ± 0.04	0.54 ± 0.04	3.31 ± 0.01	0.13 ± 0.01	4.13 ± 0.29	0.95 ± 0.29	3.67 ± 0.37	0.49 ± 0.37
	XMM3								
	XMM4			2.00 ± 0.12					
M31	ULX	2.66 ± 0.34		1.94 ± 0.19		2.51 ± 0.36		2.01 ± 0.56	
M33	X-8			1.97 ± 0.17	0.12 ± 1.26				
M81	X-6	2.40 ± 0.42	1.24 ± 1.19	1.90 ± 0.37	0.74 ± 1.14	2.62 ± 0.37	1.46 ± 1.14	2.09 ± 0.42	0.93 ± 1.19
M82	X-1	4.95 ± 0.03	0.59 ± 0.31	4.25 ± 0.09	0.11 ± 0.37	4.95 ± 0.13	0.59 ± 0.41	4.30 ± 0.34	0.06 ± 0.62
NGC 1313	X-1	3.70 ± 0.09	0.64 ± 0.37	3.14 ± 0.27	0.08 ± 0.55	3.66 ± 0.08	0.60 ± 0.36	3.52 ± 0.13	0.46 ± 0.41
	X-2	3.60 ± 0.37	0.64 ± 0.52	2.79 ± 0.62	0.17 ± 0.77	3.76 ± 0.37	0.80 ± 0.52	3.25 ± 0.58	0.29 ± 0.73
	XMM2								
	XMM4	2.94 ± 0.28	0.88 ± 0.28	2.42 ± 0.33	0.36 ± 0.33	3.14 ± 0.33	1.08 ± 0.33	2.57 ± 0.21	0.51 ± 0.21
NGC 2403	X-1								
NGC 253	X-1	2.41 ± 0.04	1.23 ± 0.83	1.93 ± 0.08	0.75 ± 0.87	2.63 ± 0.06	1.45 ± 0.85	1.98 ± 0.12	0.80 ± 0.91
	X-2	3.22 ± 0.04	1.73 ± 0.53	2.36 ± 0.40	0.87 ± 0.89	3.34 ± 0.14	1.85 ± 0.63		
	XMM5	2.80 ± 0.20		2.02 ± 0.12		2.75 ± 0.13		2.27 ± 0.15	
NGC 300	XMM1	1.79 ± 0.04	0.36 ± 0.21	1.20 ± 0.01	0.23 ± 0.18	1.99 ± 0.08	0.56 ± 0.25	1.51 ± 0.24	0.08 ± 0.41
	XMM2			0.83 ± 0.17		1.51 ± 0.21		1.14 ± 0.24	
	XMM3	1.72 ± 0.04		1.11 ± 0.10		1.85 ± 0.10		1.52 ± 0.06	
NGC 4395	XMM1			1.43 ± 0.35	0.07 ± 0.35				
	XMM2			1.49 ± 0.30		2.22 ± 0.29		1.83 ± 0.18	
	XMM3			1.92 ± 0.29		2.68 ± 0.31		2.10 ± 0.06	
NGC 4490	XMM1	3.32 ± 0.15	2.32 ± 0.75	2.79 ± 0.11	1.79 ± 0.71	3.52 ± 0.10	2.52 ± 0.70	3.17 ± 0.06	2.17 ± 0.66
	XMM3								
	XMM4			2.64 ± 0.17	1.23 ± 0.88				
	XMM5			2.75 ± 0.01	0.24 ± 0.01	3.49 ± 0.01	0.50 ± 0.01	3.23 ± 0.24	0.24 ± 0.24
NGC 4736	XMM1			1.93 ± 0.08	0.39 ± 0.08	2.72 ± 0.03	0.40 ± 0.03	2.42 ± 0.24	0.10 ± 0.24
NGC 4945	XMM1			2.16 ± 0.11		2.94 ± 0.06		2.52 ± 0.12	
	XMM2								
NGC 5194	XMM1			1.86 ± 0.37	2.00 ± 0.37	2.78 ± 0.19	1.08 ± 0.19	2.53 ± 0.16	1.33 ± 0.16
	XMM2	2.78 ± 0.67	1.40 ± 0.75	2.27 ± 0.73	0.89 ± 0.81	3.02 ± 0.75	1.64 ± 0.83	2.43 ± 0.52	1.05 ± 0.60
	XMM3	3.59 ± 0.36	0.78 ± 0.96	3.14 ± 0.37	0.33 ± 0.97	3.89 ± 0.39	1.08 ± 0.99	3.11 ± 0.34	0.30 ± 0.94
	XMM4	3.14 ± 0.31	0.85 ± 0.31	2.68 ± 0.36	0.39 ± 0.36	3.50 ± 0.46	1.21 ± 0.46	2.67 ± 0.31	0.38 ± 0.31
	XMM5			2.36 ± 0.15					
	XMM6			1.67 ± 0.19	0.07 ± 0.93	2.51 ± 0.09	0.77 ± 0.83		
	XMM7	2.84 ± 0.33	1.69 ± 0.48	1.95 ± 0.01	0.80 ± 0.16	2.67 ± 0.01	1.52 ± 0.16	2.29 ± 0.24	1.14 ± 0.39
NGC 5204	X-1			2.89 ± 0.01	0.43 ± 0.01	3.64 ± 0.01	1.18 ± 0.01	3.30 ± 0.03	0.84 ± 0.03
NGC 5408	X-1								
NGC 6949	X-1			2.75 ± 0.24	0.25 ± 0.24				

Table A.3: $M_{\rm BH}$ of ULXs via the X-ray scaling method using spectral patterns of highly accreting GBHs

Galaxy	ULX	XTEJ1550R97		GRS1915R98	
		$\log(M_{\rm BH})$	Ratio	$\log(M_{\rm BH})$	Ratio
HoII	X-1	2.56 ± 0.60	0.41 ± 1.45	2.41 ± 0.38	0.26 ± 1.23
HoIX	X-1	3.73 ± 0.31	0.97 ± 1.37	3.11 ± 0.19	0.35 ± 1.25
IC 342	X-1	3.16 ± 0.22	0.34 ± 1.19	2.74 ± 0.02	0.76 ± 0.99
	XMM2	3.38 ± 0.33	0.20 ± 0.33	3.10 ± 0.02	0.08 ± 0.02
	XMM3	1.85 ± 0.16	1.02 ± 0.16	1.55 ± 0.02	1.31 ± 0.02
	XMM4	1.95 ± 0.16		1.46 ± 0.02	
M31	ULX	1.71 ± 0.48		1.11 ± 0.48	
M33	X-8	2.08 ± 0.16	0.01 ± 1.25	1.82 ± 0.20	0.27 ± 1.29
M81	X-6	2.09 ± 0.74	0.93 ± 1.51	0.82 ± 0.62	0.28 ± 1.39
M82	X-1	4.10 ± 0.56	0.26 ± 0.84	3.75 ± 0.06	0.61 ± 0.34
NGC 1313	X-1	3.18 ± 0.21	0.12 ± 0.49	2.92 ± 0.45	0.14 ± 0.73
	X-2	3.07 ± 0.76	0.12 ± 0.91	2.14 ± 0.21	0.82 ± 0.36
	XMM2	2.11 ± 0.39		2.26 ± 0.17	
	XMM4	2.48 ± 0.41	0.42 ± 0.41		
NGC 2403	X-1	3.30 ± 0.16	1.95 ± 0.28		
NGC 253	X-1	1.86 ± 0.29	0.68 ± 1.08	1.50 ± 0.11	0.32 ± 0.90
	X-2	2.40 ± 0.19	0.91 ± 0.68	1.92 ± 0.12	0.43 ± 0.61
	XMM5	2.06 ± 0.17		1.59 ± 0.14	
NGC 300	XMM1	1.28 ± 0.16	0.15 ± 0.33	1.10 ± 0.01	0.33 ± 0.18
	XMM2	0.74 ± 0.16		0.30 ± 0.06	
	XMM3	1.16 ± 0.08			
NGC 4395	XMM1	1.19 ± 0.16	0.17 ± 0.16	1.33 ± 0.02	0.03 ± 0.02
	XMM2	1.50 ± 0.24			
	XMM3	1.80 ± 0.12			
NGC 4490	XMM1	2.83 ± 0.09	1.83 ± 0.69	2.22 ± 0.08	1.22 ± 0.68
	XMM3	3.07 ± 0.83	0.83 ± 1.73	2.28 ± 0.02	0.04 ± 0.92
	XMM4	2.31 ± 0.63	0.90 ± 1.34	2.27 ± 0.18	0.86 ± 0.89
	XMM5	3.22 ± 0.38	0.23 ± 0.38	2.26 ± 0.02	0.73 ± 0.02
NGC 4736	XMM1	2.04 ± 0.16	0.28 ± 0.16	1.46 ± 0.02	0.86 ± 0.02
NGC 4945	XMM1	2.49 ± 0.43			
NGC 5194	XMM1	2.00 ± 0.30	1.86 ± 0.30	1.49 ± 0.23	2.37 ± 0.23
	XMM2	2.15 ± 0.57	0.77 ± 0.65		
	XMM3	2.90 ± 0.35	0.09 ± 0.95		
	XMM4	2.34 ± 0.32	0.05 ± 0.32		
	XMM5	2.41 ± 0.37		1.91 ± 0.47	
	XMM6	1.91 ± 0.31	0.17 ± 1.05	1.24 ± 0.15	0.50 ± 0.89
	XMM7	1.96 ± 0.16	0.81 ± 0.31	1.51 ± 0.02	0.36 ± 0.17
NGC 5204	X-1	2.90 ± 0.18	0.44 ± 0.18	2.45 ± 0.13	0.01 ± 0.13
NGC 5408	X-1	2.84 ± 0.82	0.03 ± 1.73	2.69 ± 0.86	0.12 ± 1.77
NGC 6949	X-1	2.69 ± 0.29	0.31 ± 0.29	2.43 ± 0.13	0.57 ± 0.13

Figures of $\Gamma - N_{\mathrm{BMC}}$ for all ULXs

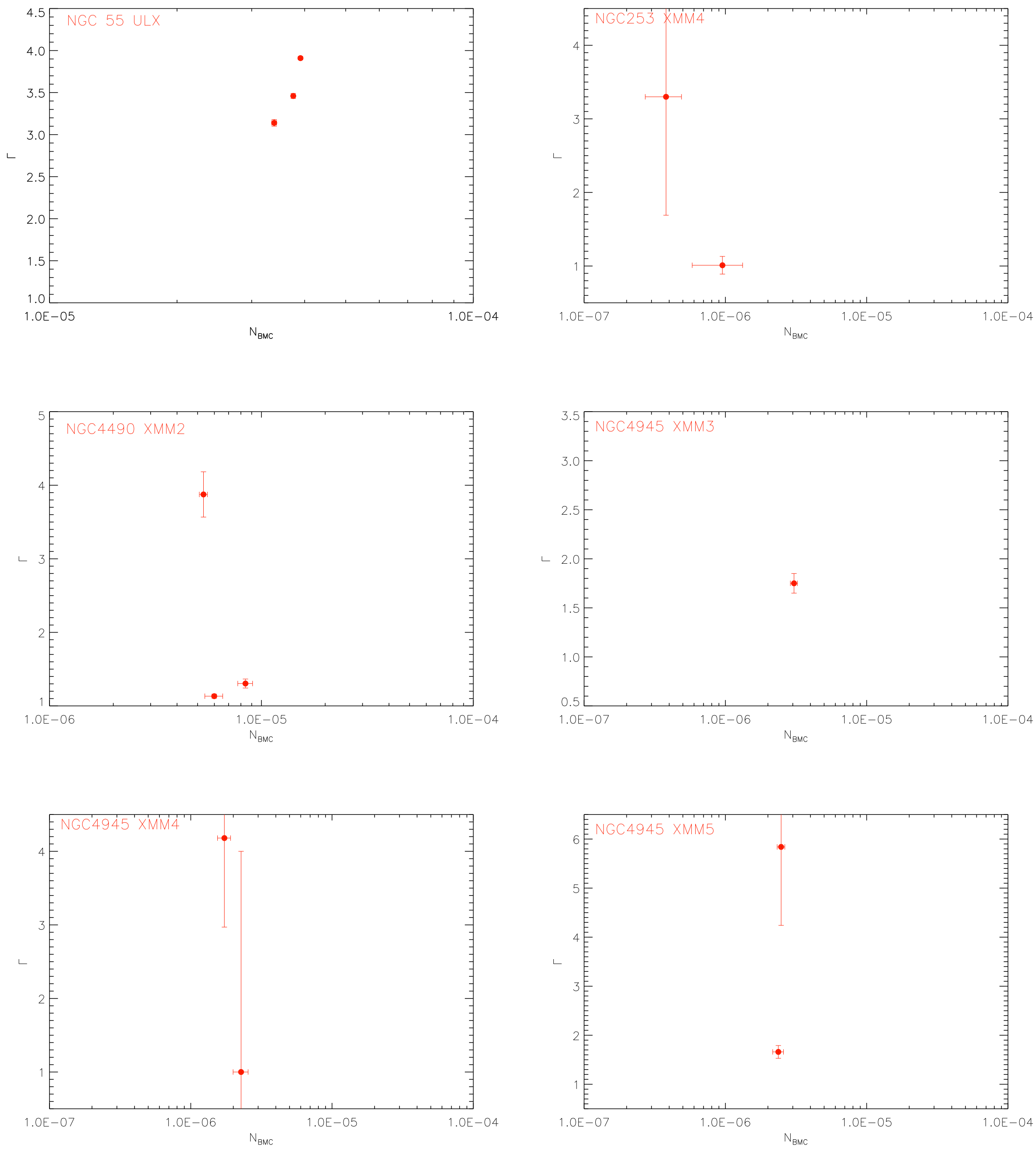

Figure B.1: $\Gamma - N_{\rm BMC}$ diagrams of ULXs which could not be compared to any reference pattern – Example 1. Each ULX had measured Γ values outside the range of any reference pattern and therefore the X-ray scaling method could not been applied. NGC 4945 XMM3 was left out because we were able to make a spectral analysis for only one observation after the systematical data reduction.

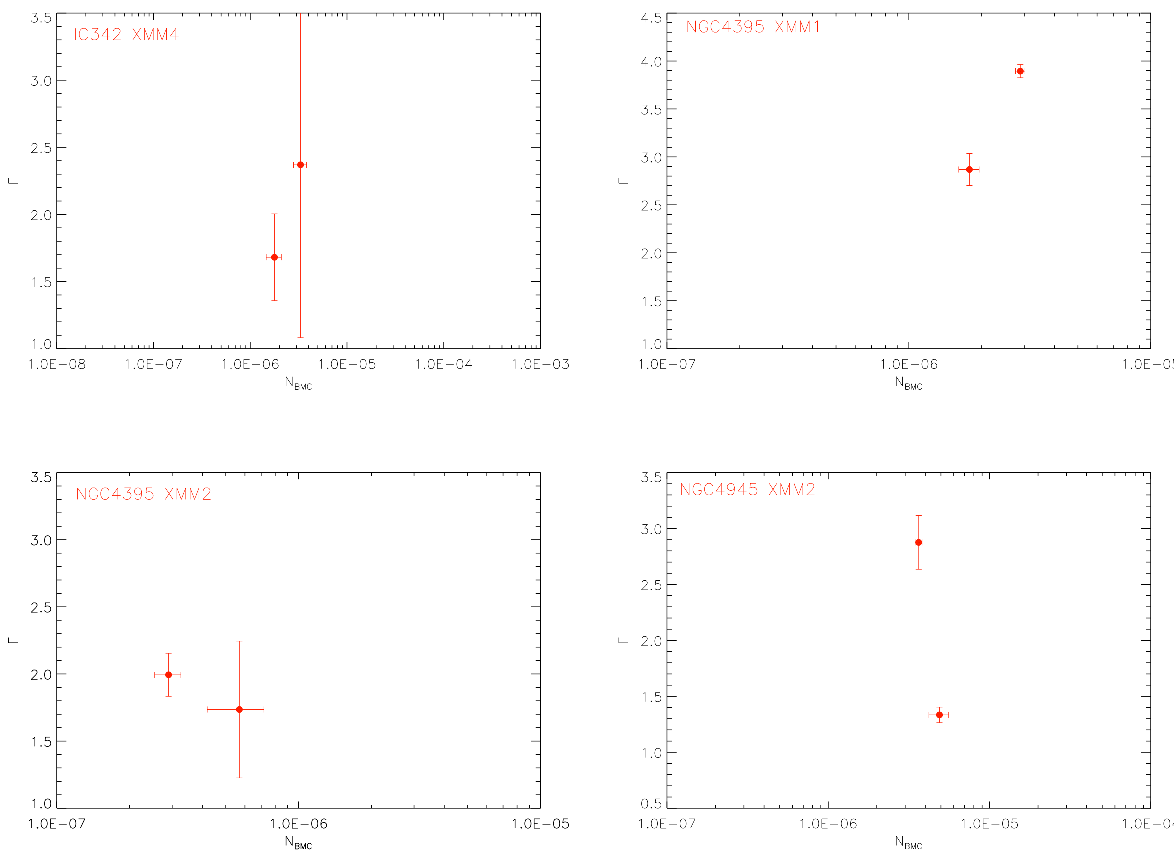

Figure B.2: $\Gamma - N_{\mathrm{BMC}}$ diagrams of ULXs which could not be compared to any reference pattern – Example 2. Their $\Gamma - N_{\mathrm{BMC}}$ trends could not be described by any reference pattern because of one out of two observations either with corrupted date which revealed large uncertainty of Γ or very high Γ (> 3) or low (< 1.3) hampering the comparison to any reference pattern and consequently the M_{BH} computation.

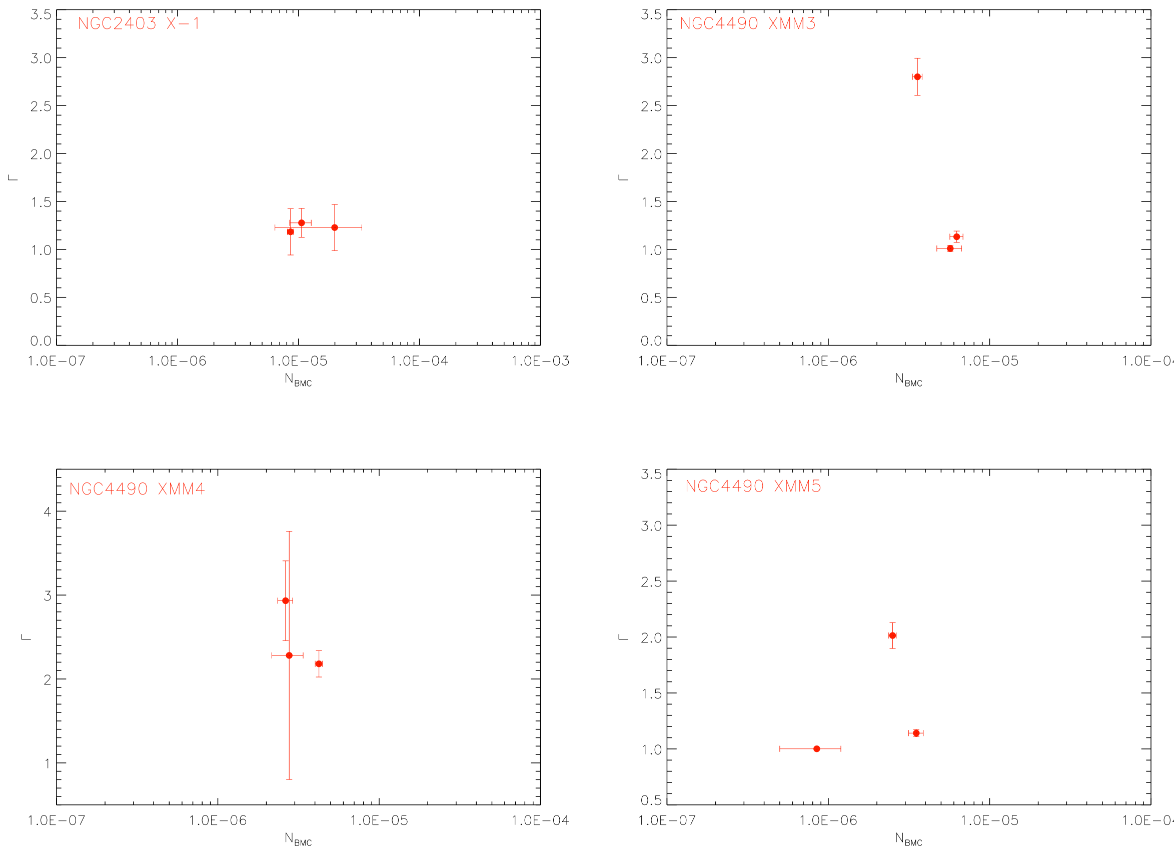

Figure B.3: $\Gamma - N_{\rm BMC}$ diagrams of ULXs which could not be compared to any reference pattern − Example 3. All three measured Γ values of these ULXs near the saturation levels ($\Gamma \approx 1.4$ or ≈ 3) hampering the comparison with any reference trend and consequently the $M_{\rm BH}$ computation. The X-ray scaling method was not applied to NGC 4490 XMM4 and XMM5 because only one data point was left after excluding data points either with $\Gamma \approx 3$ or $\sigma_\Gamma > 1$.

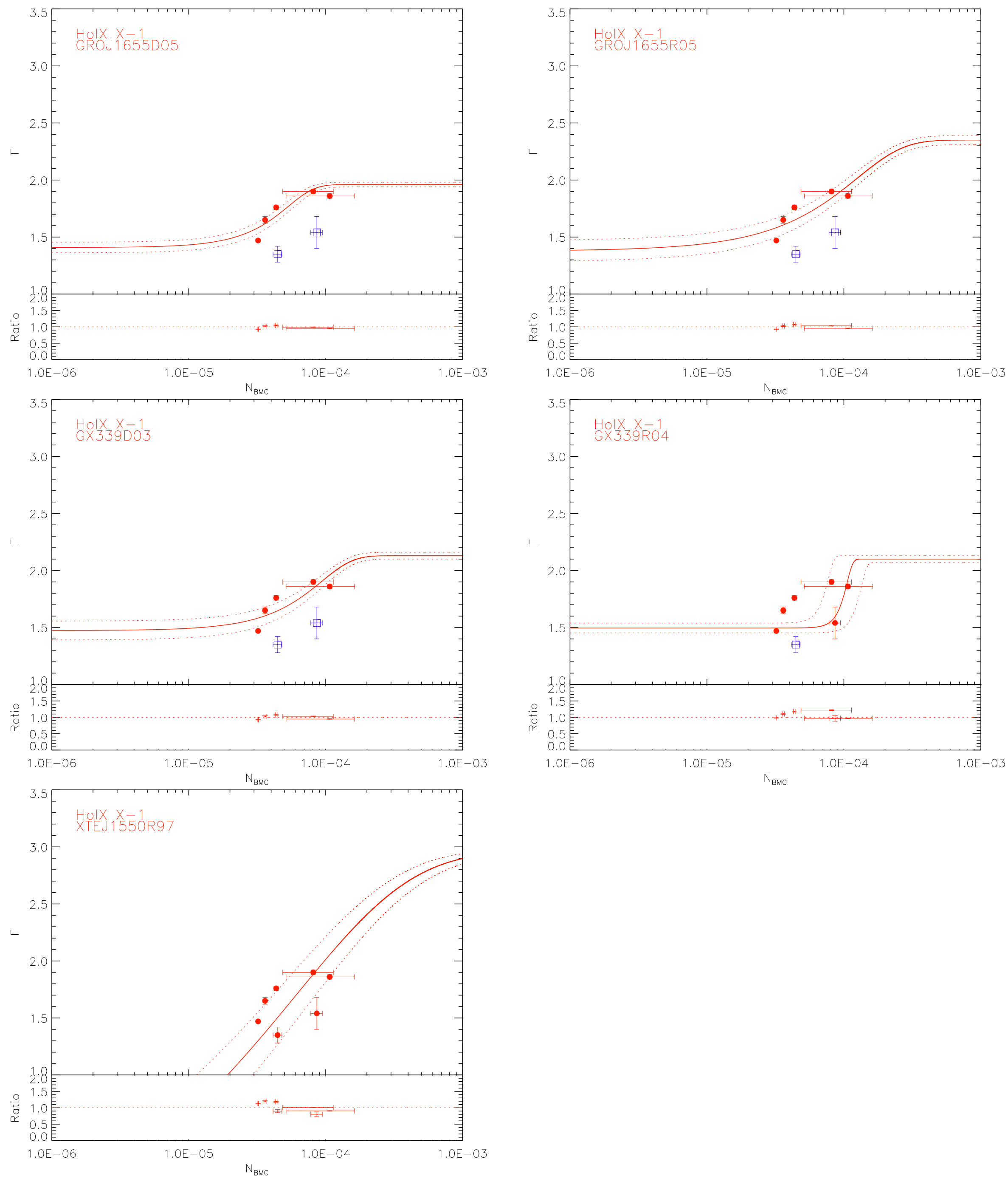

Figure B.4: $\Gamma - N_{\mathrm{BMC}}$ diagram of HoIX X-1. The solid line in each panel shows the best-fit of reference spectral transit pattern and its 1σ uncertainty with the dashed line. Any data point used for the best-fit with the filled red circle and the empty blue box for any excluded point. The name of ULX and the used reference pattern are inidcated at the top-left coner in each panel.

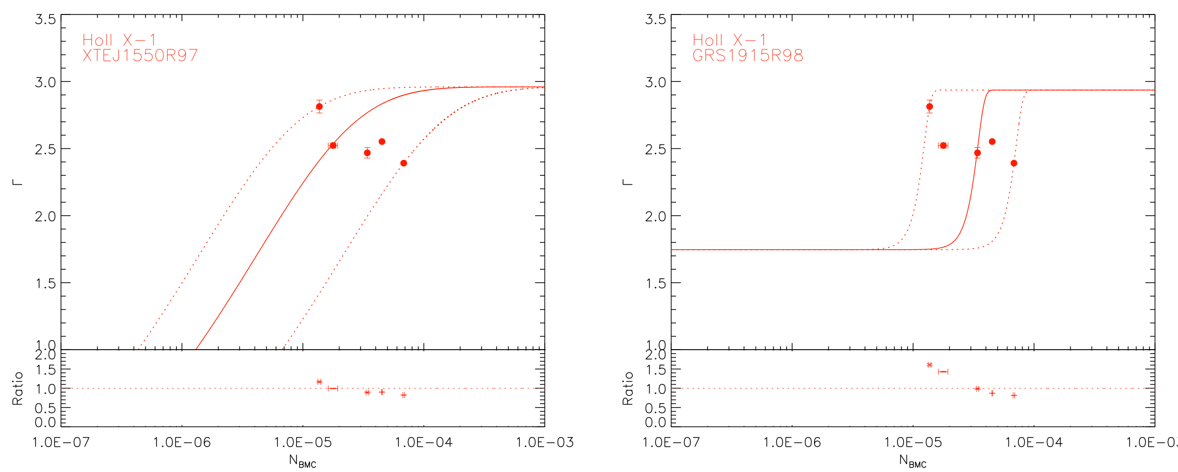

Figure B.5: $\Gamma - N_{\rm BMC}$ diagram of HoII X-1. The solid line in each panel shows the best-fit of reference spectral transit pattern and its 1σ uncertainty with the dashed line. Any data point used for the best-fit with the filled red circle and the empty blue box for any excluded point. The name of ULX and the used reference pattern are inidcated at the top-left coner in each panel.

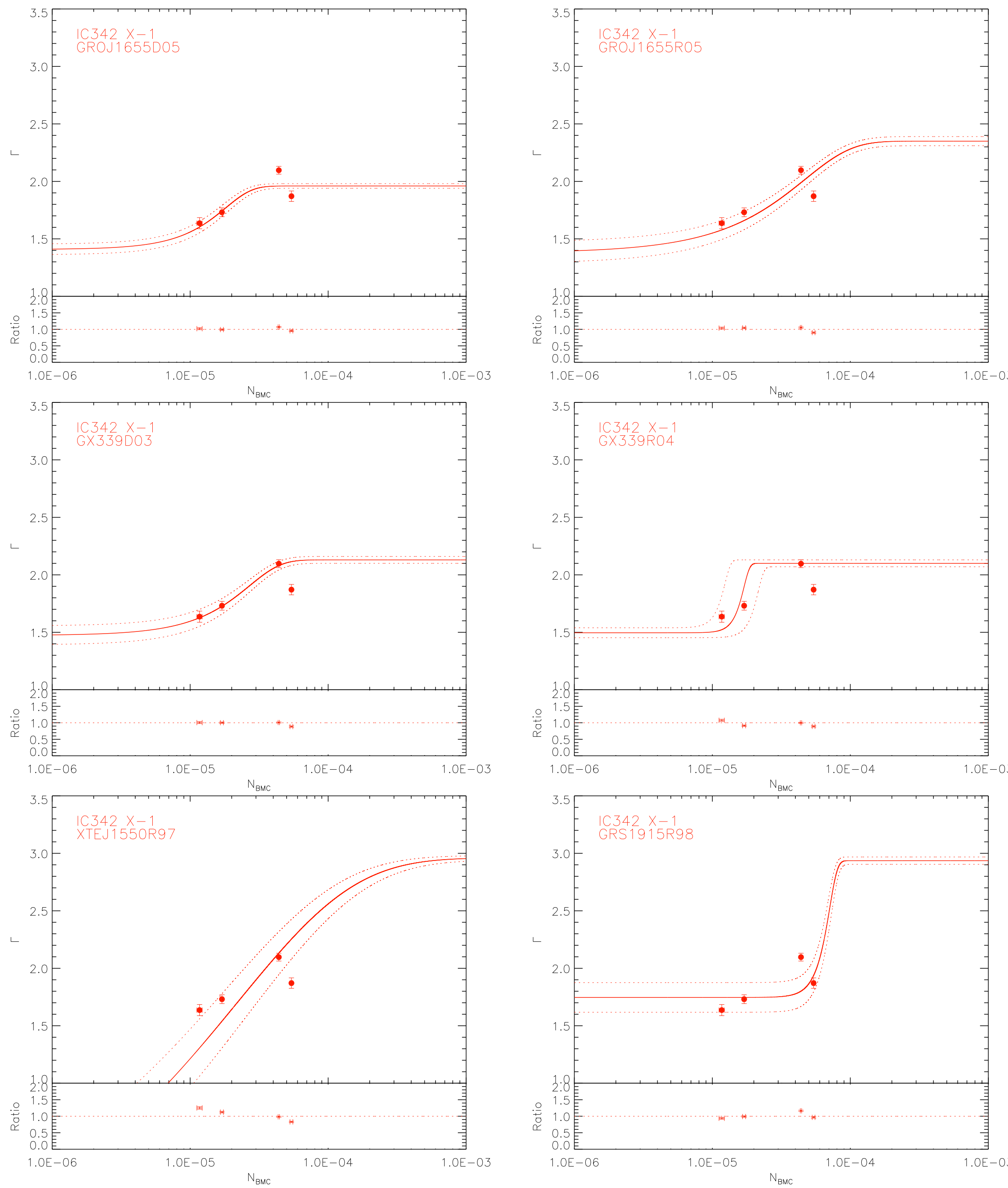

Figure B.6: $\Gamma - N_{\rm BMC}$ diagram of IC 342 X-1. The solid line in each panel shows the best-fit of reference spectral transit pattern and its 1σ uncertainty with the dashed line. Any data point used for the best-fit with the filled red circle and the empty blue box for any excluded point. The name of ULX and the used reference pattern are inidcated at the top-left coner in each panel.

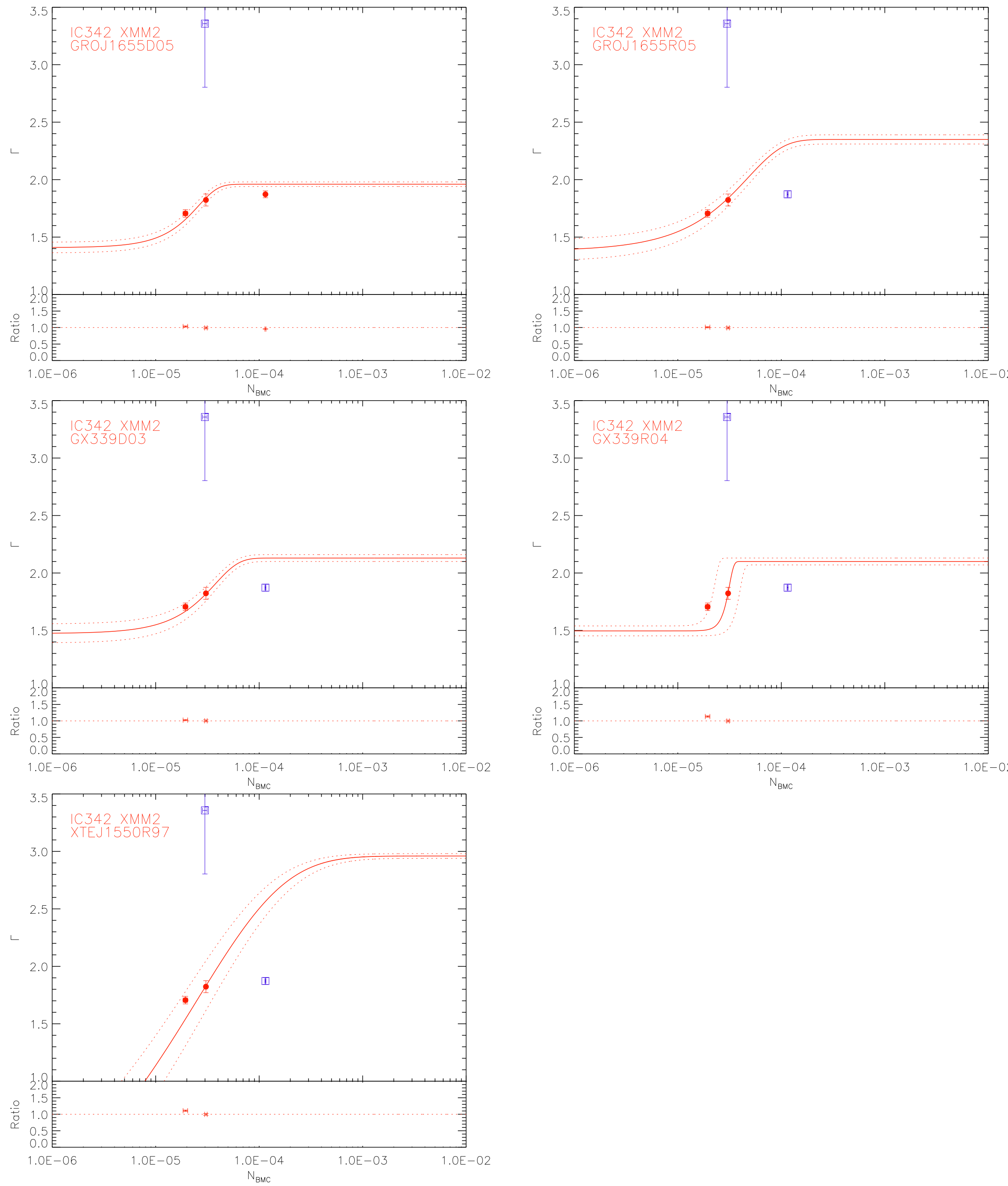

Figure B.7: $\Gamma - N_{\rm BMC}$ diagram of IC 342 XMM2. The solid line in each panel shows the best-fit of reference spectral transit pattern and its 1σ uncertainty with the dashed line. Any data point used for the best-fit with the filled red circle and the empty blue box for any excluded point. The name of ULX and the used reference pattern are inidcated at the top-left coner in each panel.

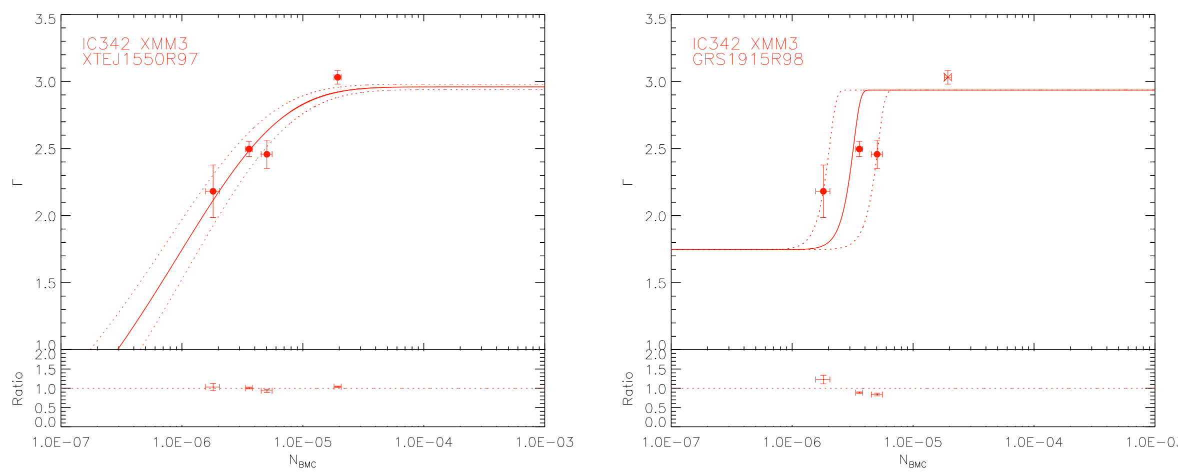

Figure B.8: $\Gamma - N_{\rm BMC}$ diagram of IC 342 XMM3. The solid line in each panel shows the best-fit of reference spectral transit pattern and its 1σ uncertainty with the dashed line. Any data point used for the best-fit with the filled red circle and the empty blue box for any excluded point. The name of ULX and the used reference pattern are inidcated at the top-left coner in each panel.

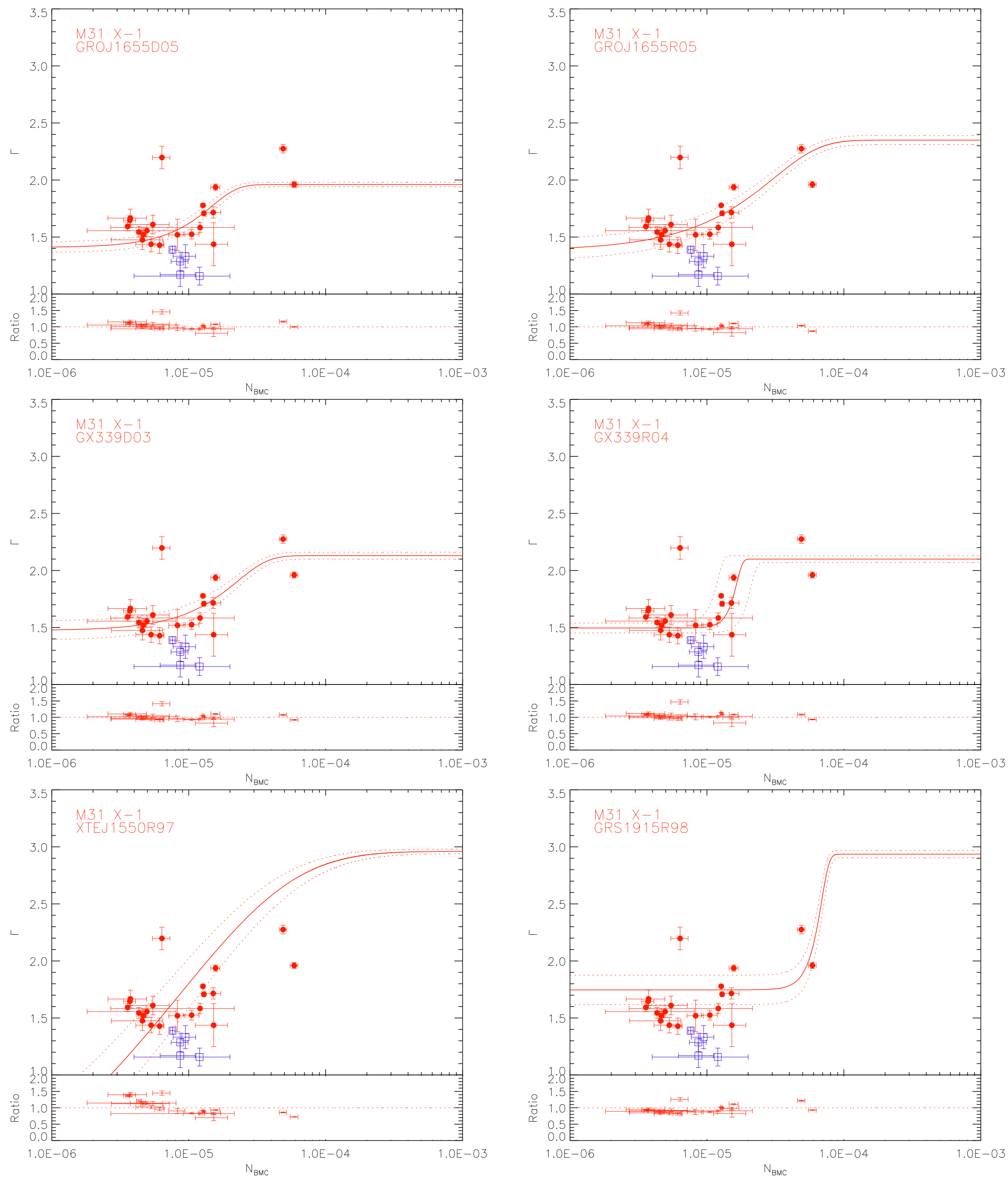

Figure B.9: $\Gamma-N_{\rm BMC}$ diagram of M31 X-1. The solid line in each panel shows the best-fit of reference spectral transit pattern and its 1σ uncertainty with the dashed line. Any data point used for the best-fit with the filled red circle and the empty blue box for any excluded point. The name of ULX and the used reference pattern are inidcated at the top-left coner in each panel.

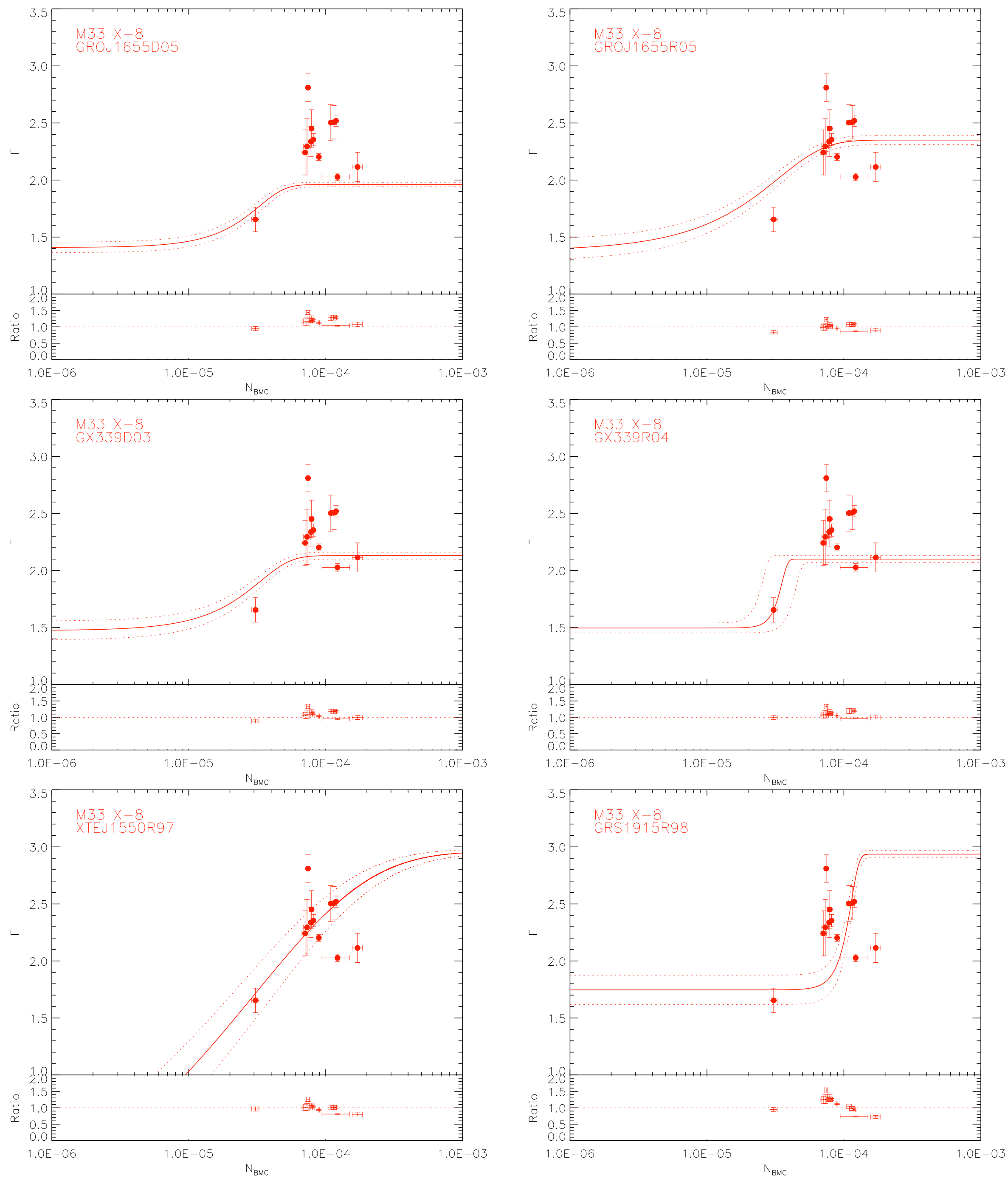

Figure B.10: $\Gamma - N_{\mathrm{BMC}}$ diagram of M33 X-8. The solid line in each panel shows the best-fit of reference spectral transit pattern and its 1σ uncertainty with the dashed line. Any data point used for the best-fit with the filled red circle and the empty blue box for any excluded point. The name of ULX and the used reference pattern are inidcated at the top-left coner in each panel.

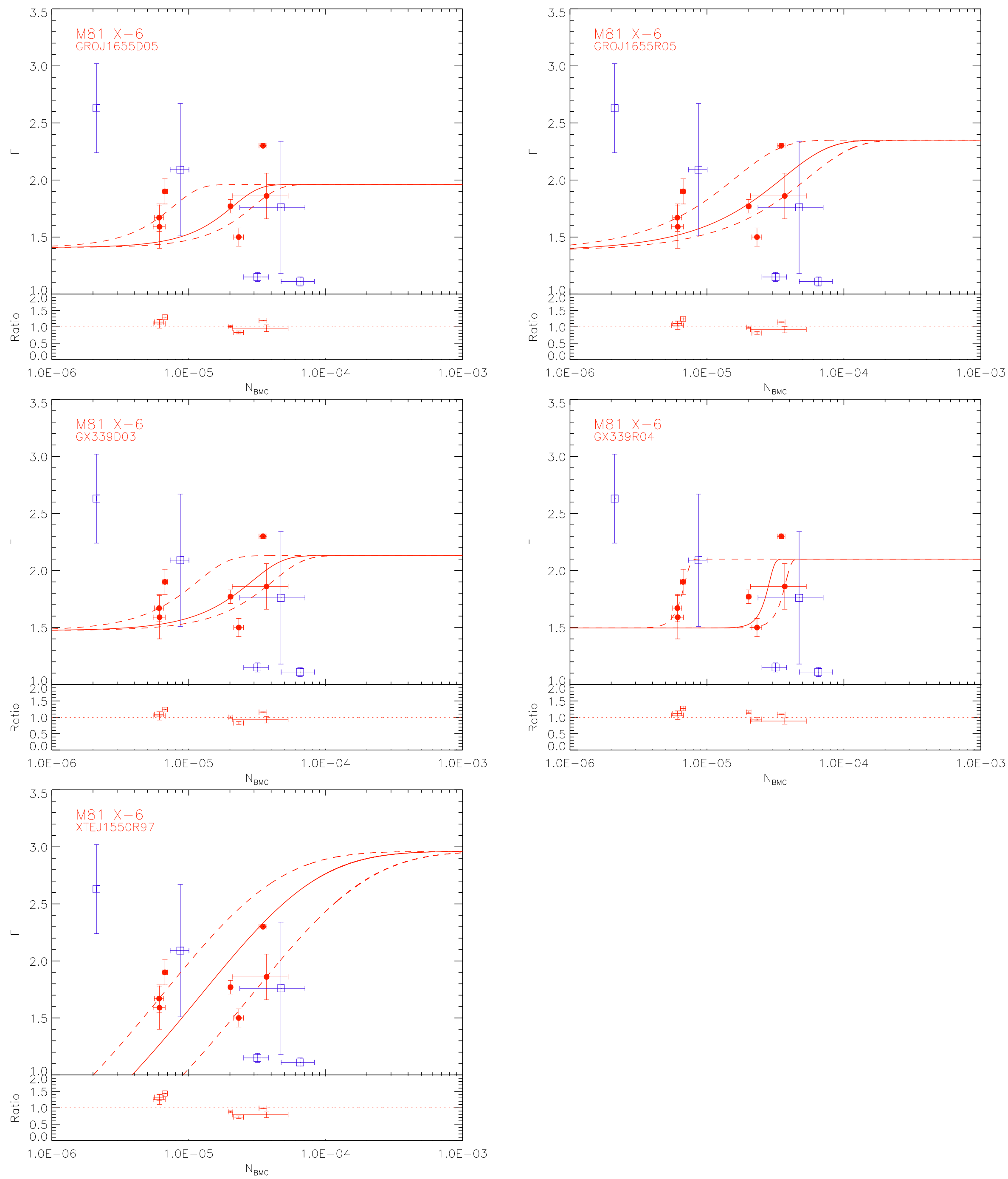

Figure B.11: $\Gamma - N_{\rm BMC}$ diagram of M81 X-6. The solid line in each panel shows the best-fit of reference spectral transit pattern and its 1σ uncertainty with the dashed line. Any data point used for the best-fit with the filled red circle and the empty blue box for any excluded point. The name of ULX and the used reference pattern are inidcated at the top-left coner in each panel.

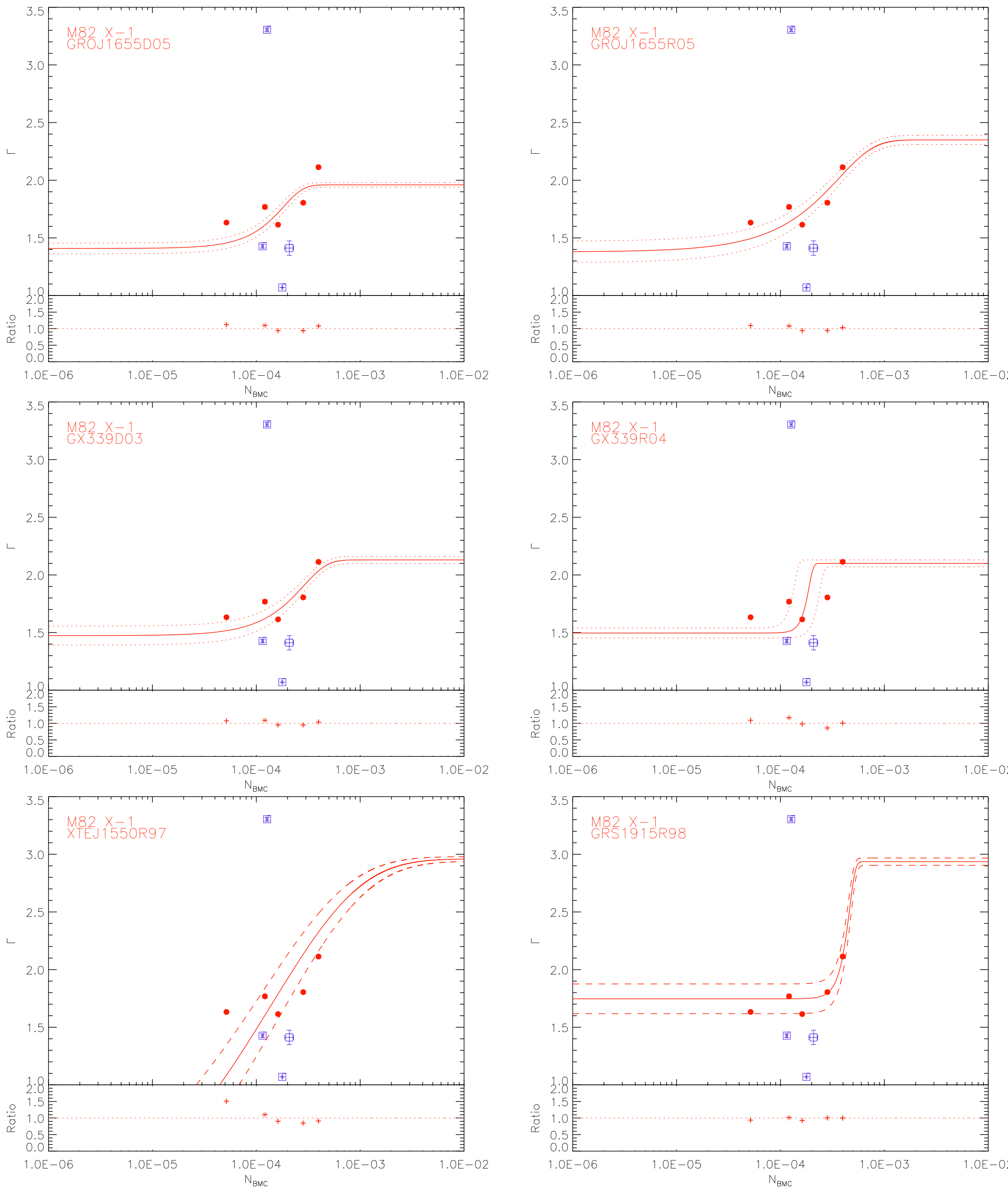

Figure B.12: $\Gamma-N_{\rm BMC}$ diagram of M81 X-6. The solid line in each panel shows the best-fit of reference spectral transit pattern and its 1σ uncertainty with the dashed line. Any data point used for the best-fit with the filled red circle and the empty blue box for any excluded point. The name of ULX and the used reference pattern are inidcated at the top-left coner in each panel.

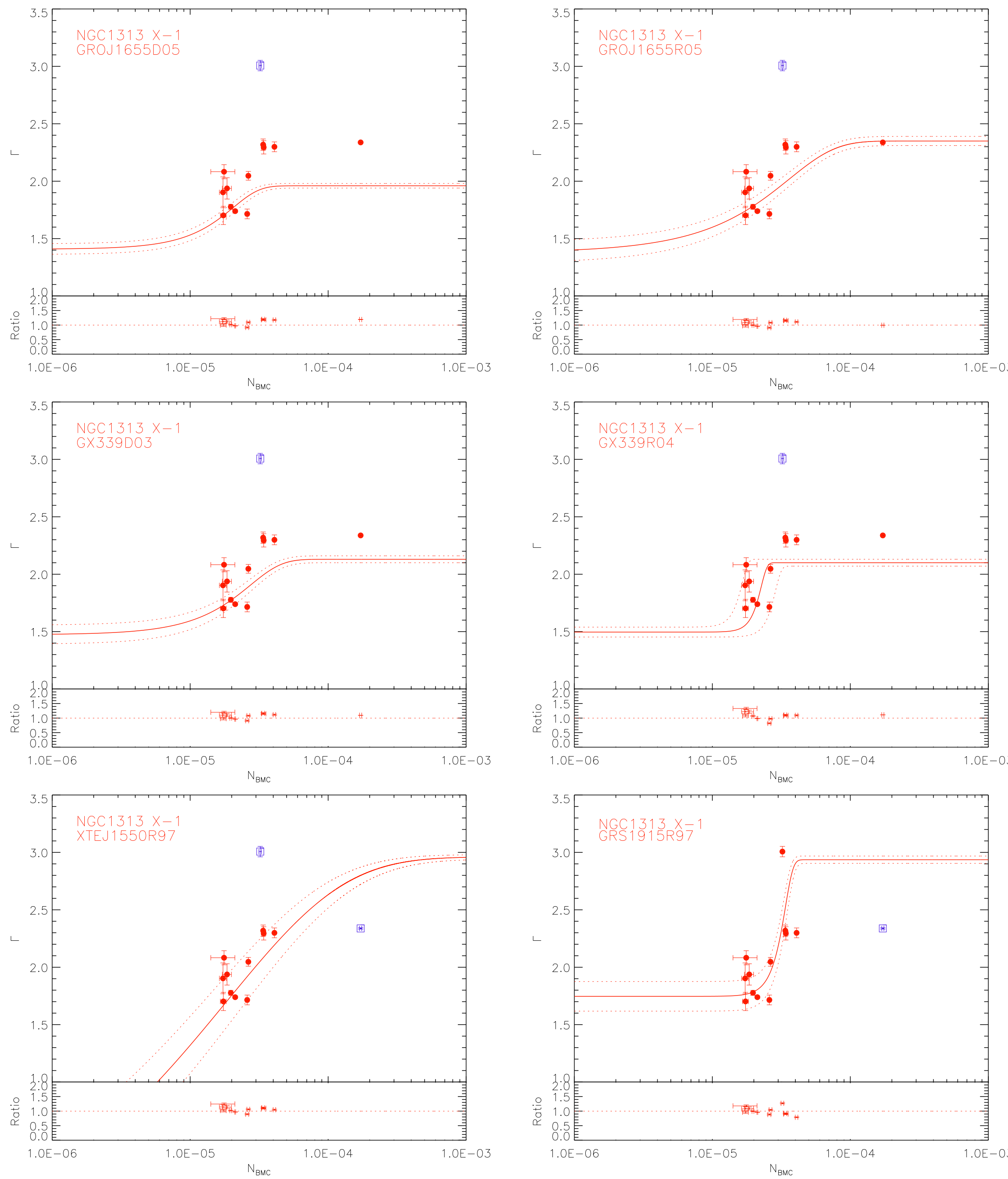

Figure B.13: $\Gamma - N_{\rm BMC}$ diagram of NGC 1313 X-1. The solid line in each panel shows the best-fit of reference spectral transit pattern and its 1σ uncertainty with the dashed line. Any data point used for the best-fit with the filled red circle and the empty blue box for any excluded point. The name of ULX and the used reference pattern are inidcated at the top-left coner in each panel.

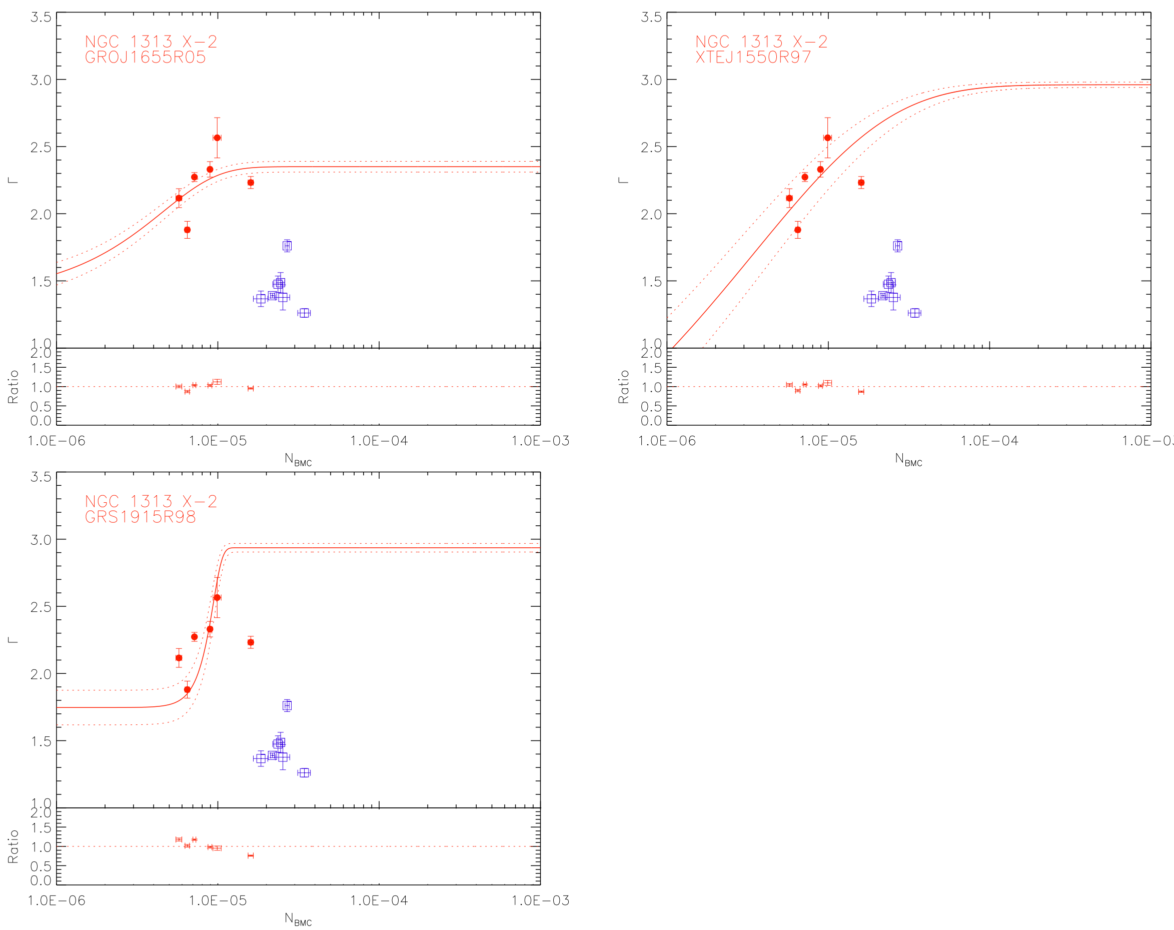

Figure B.14: $\Gamma - N_{\rm BMC}$ diagram of NGC 1313 X-2. The solid line in each panel shows the best-fit of reference spectral transit pattern and its 1σ uncertainty with the dashed line. Any data point used for the best-fit with the filled red circle and the empty blue box for any excluded point. The name of ULX and the used reference pattern are inidcated at the top-left coner in each panel.

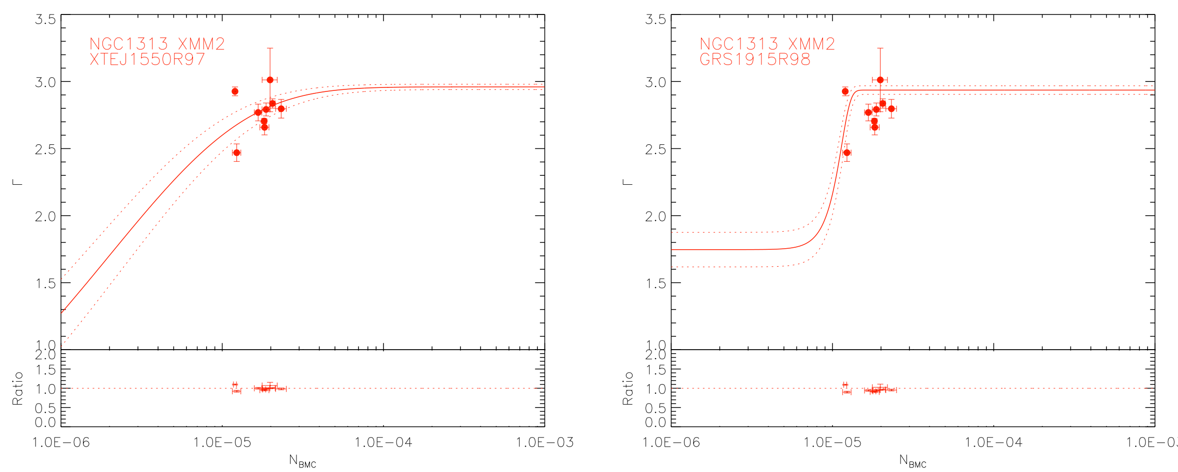

Figure B.15: $\Gamma - N_{\rm BMC}$ diagram of NGC 1313 XMM2. The solid line in each panel shows the best-fit of reference spectral transit pattern and its 1σ uncertainty with the dashed line. Any data point used for the best-fit with the filled red circle and the empty blue box for any excluded point. The name of ULX and the used reference pattern are inidcated at the top-left coner in each panel.

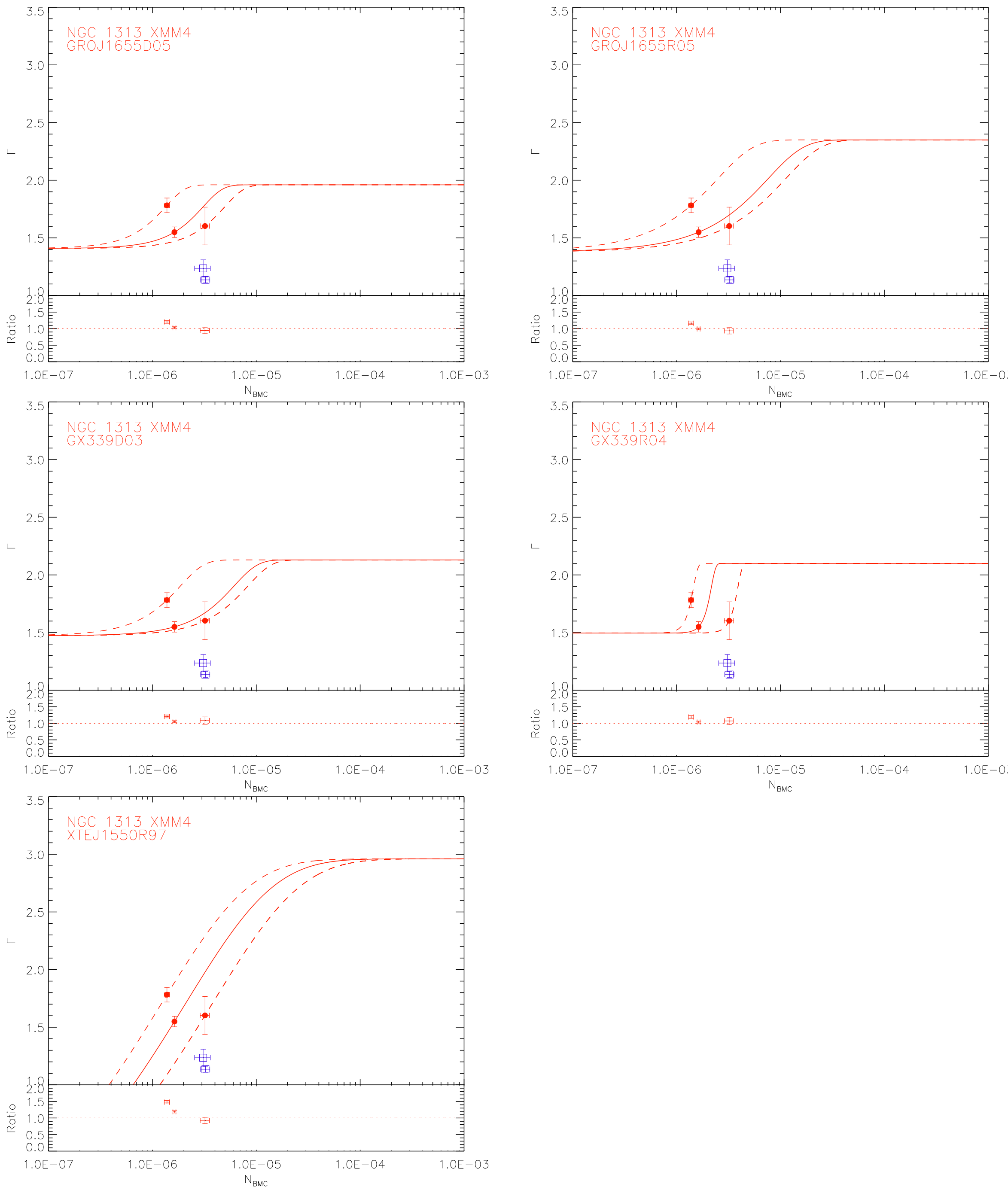

Figure B.16: $\Gamma-N_{\rm BMC}$ diagram of NGC 1313 XMM4. The solid line in each panel shows the best-fit of reference spectral transit pattern and its 1σ uncertainty with the dashed line. Any data point used for the best-fit with the filled red circle and the empty blue box for any excluded point. The name of ULX and the used reference pattern are inidcated at the top-left coner in each panel.

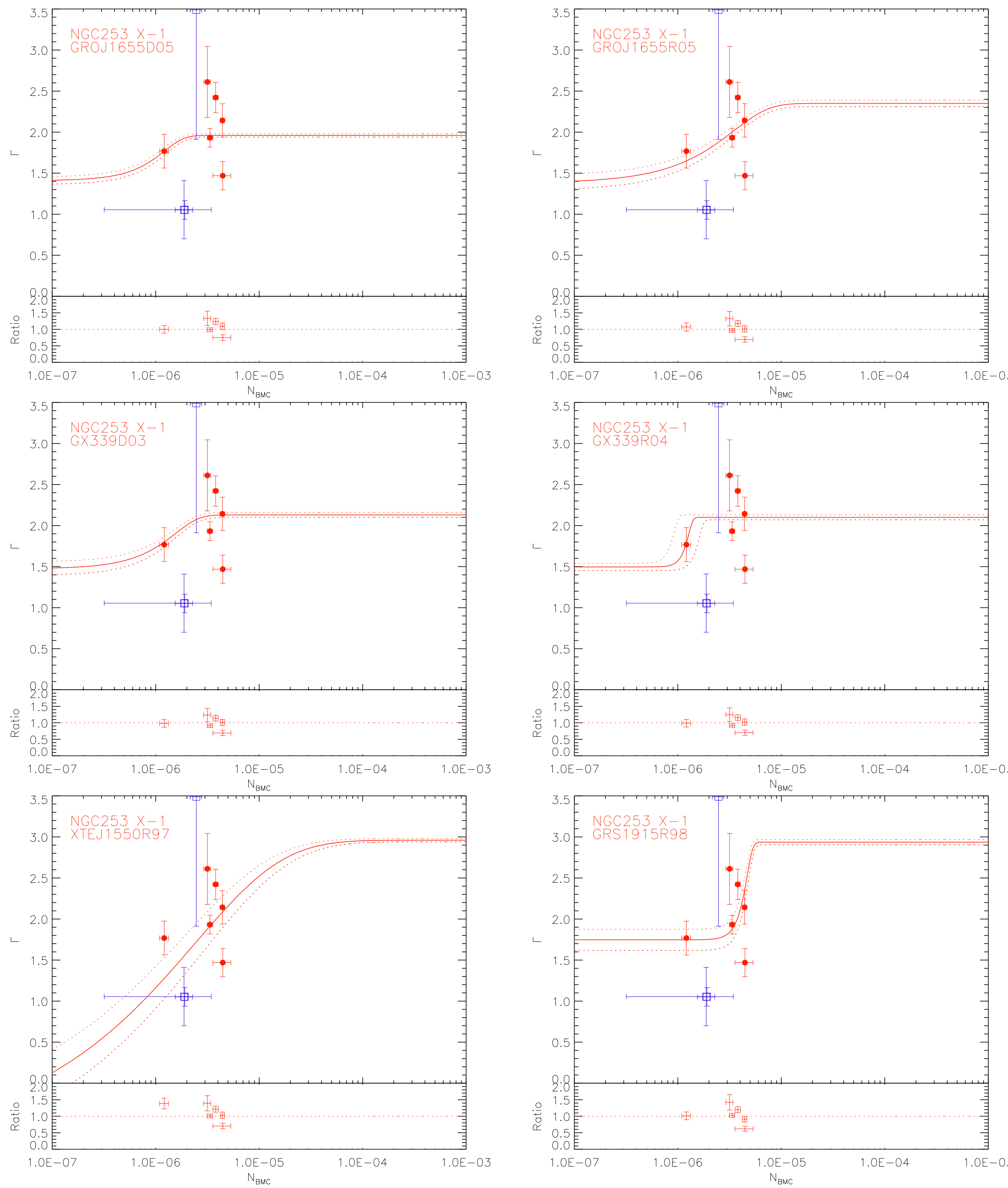

Figure B.17: $\Gamma - N_{\rm BMC}$ diagram of NGC 253 X-1. The solid line in each panel shows the best-fit of reference spectral transit pattern and its 1σ uncertainty with the dashed line. Any data point used for the best-fit with the filled red circle and the empty blue box for any excluded point. The name of ULX and the used reference pattern are inidcated at the top-left coner in each panel.

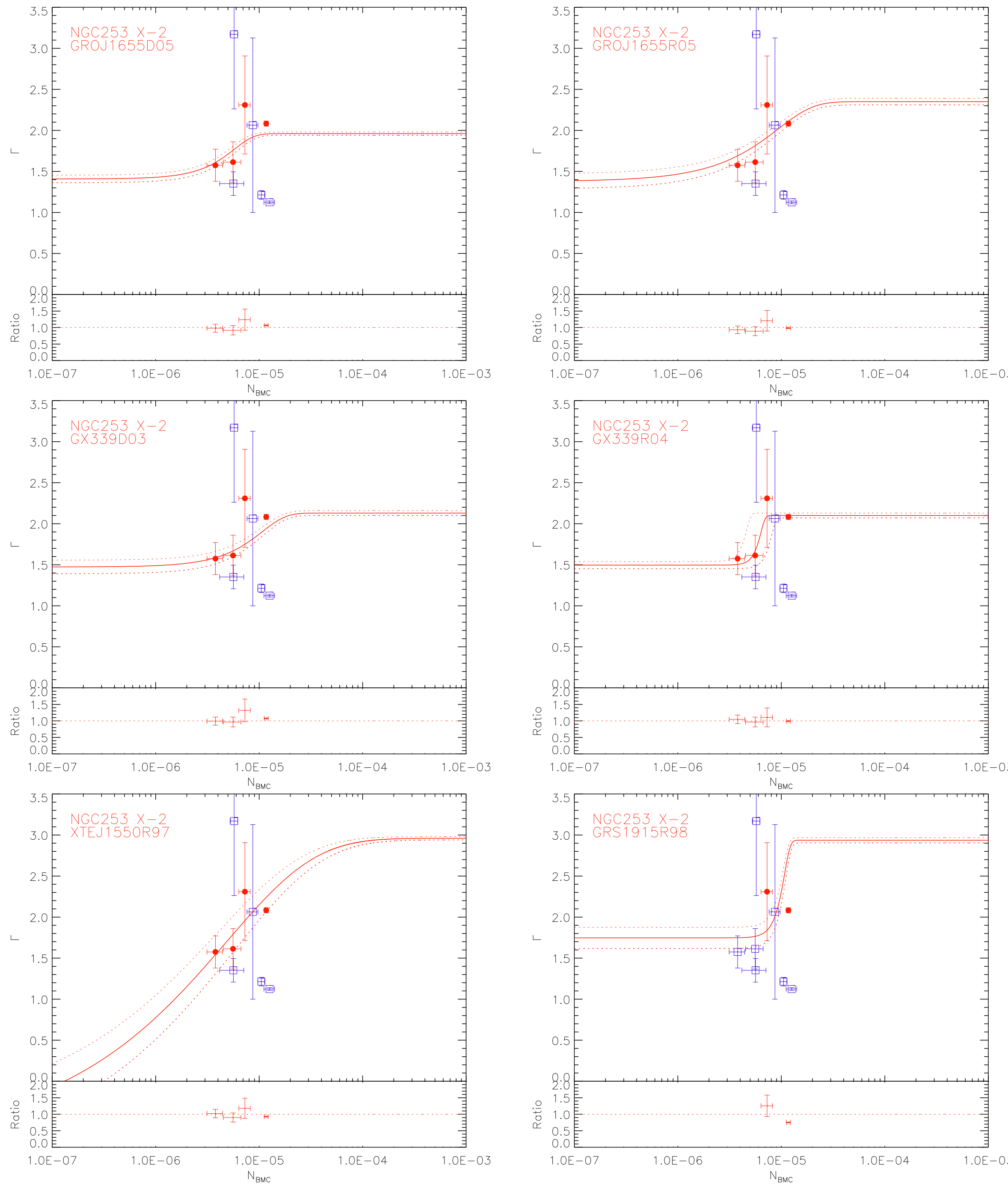

Figure B.18: $\Gamma - N_{\rm BMC}$ diagram of NGC 253 X-2. The solid line in each panel shows the best-fit of reference spectral transit pattern and its 1σ uncertainty with the dashed line. Any data point used for the best-fit with the filled red circle and the empty blue box for any excluded point. The name of ULX and the used reference pattern are inidcated at the top-left coner in each panel.

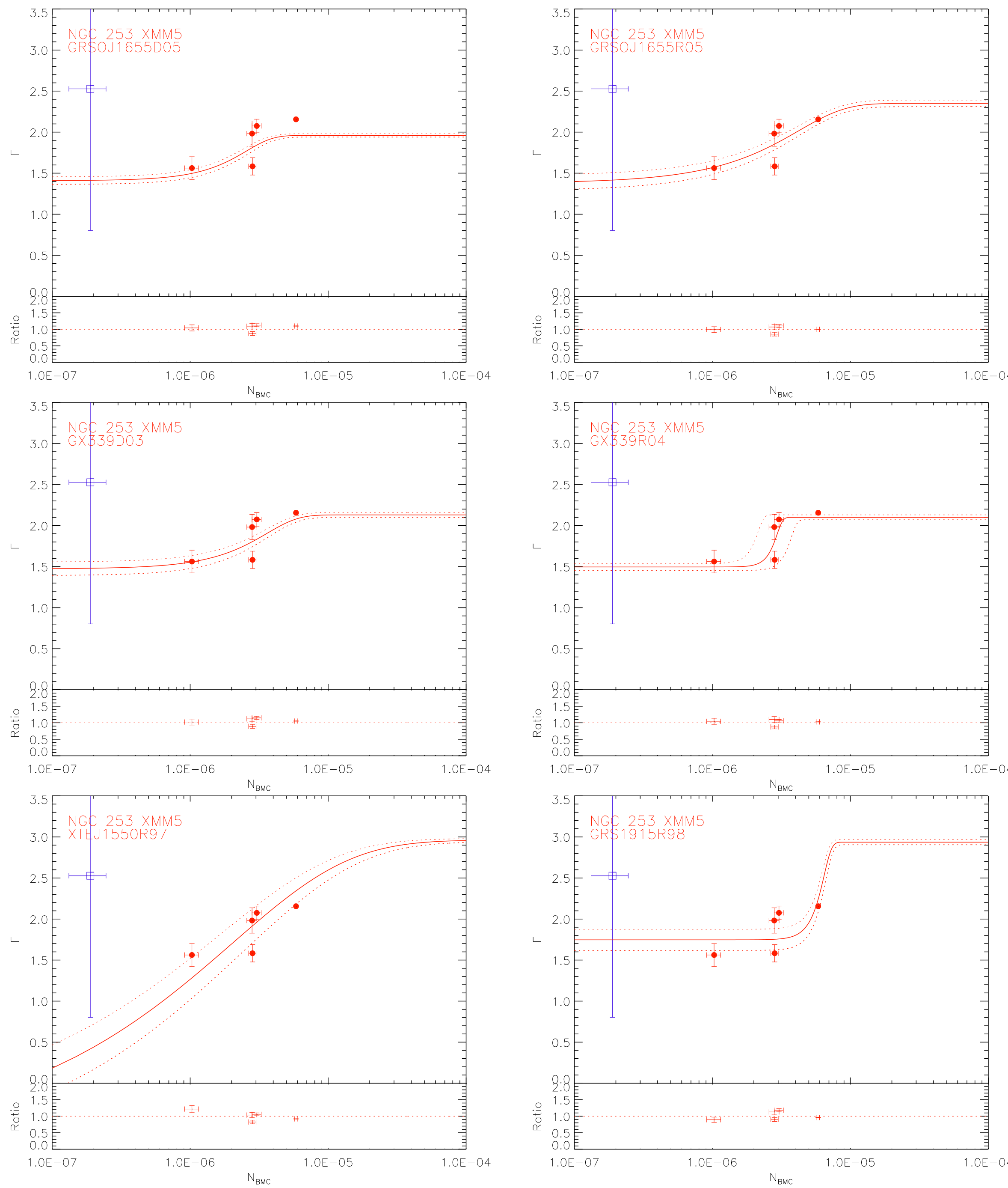

Figure B.19: $\Gamma - N_{\rm BMC}$ diagram of NGC 253 XMM5. The solid line in each panel shows the best-fit of reference spectral transit pattern and its 1σ uncertainty with the dashed line. Any data point used for the best-fit with the filled red circle and the empty blue box for any excluded point. The name of ULX and the used reference pattern are inidcated at the top-left coner in each panel.

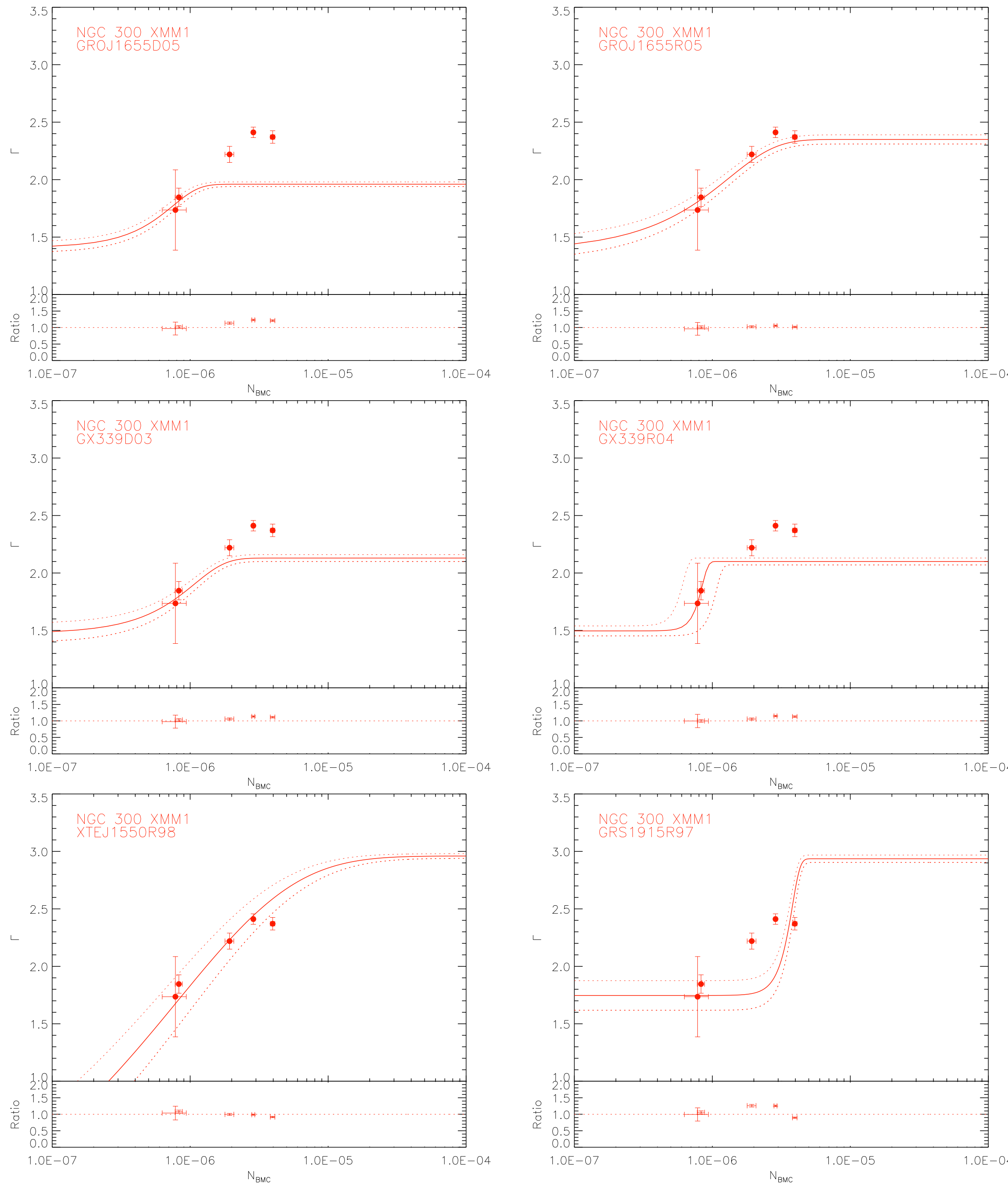

Figure B.20: $\Gamma - N_{\rm BMC}$ diagram of NGC 300 XMM1. The solid line in each panel shows the best-fit of reference spectral transit pattern and its 1σ uncertainty with the dashed line. Any data point used for the best-fit with the filled red circle and the empty blue box for any excluded point. The name of ULX and the used reference pattern are inidcated at the top-left coner in each panel.

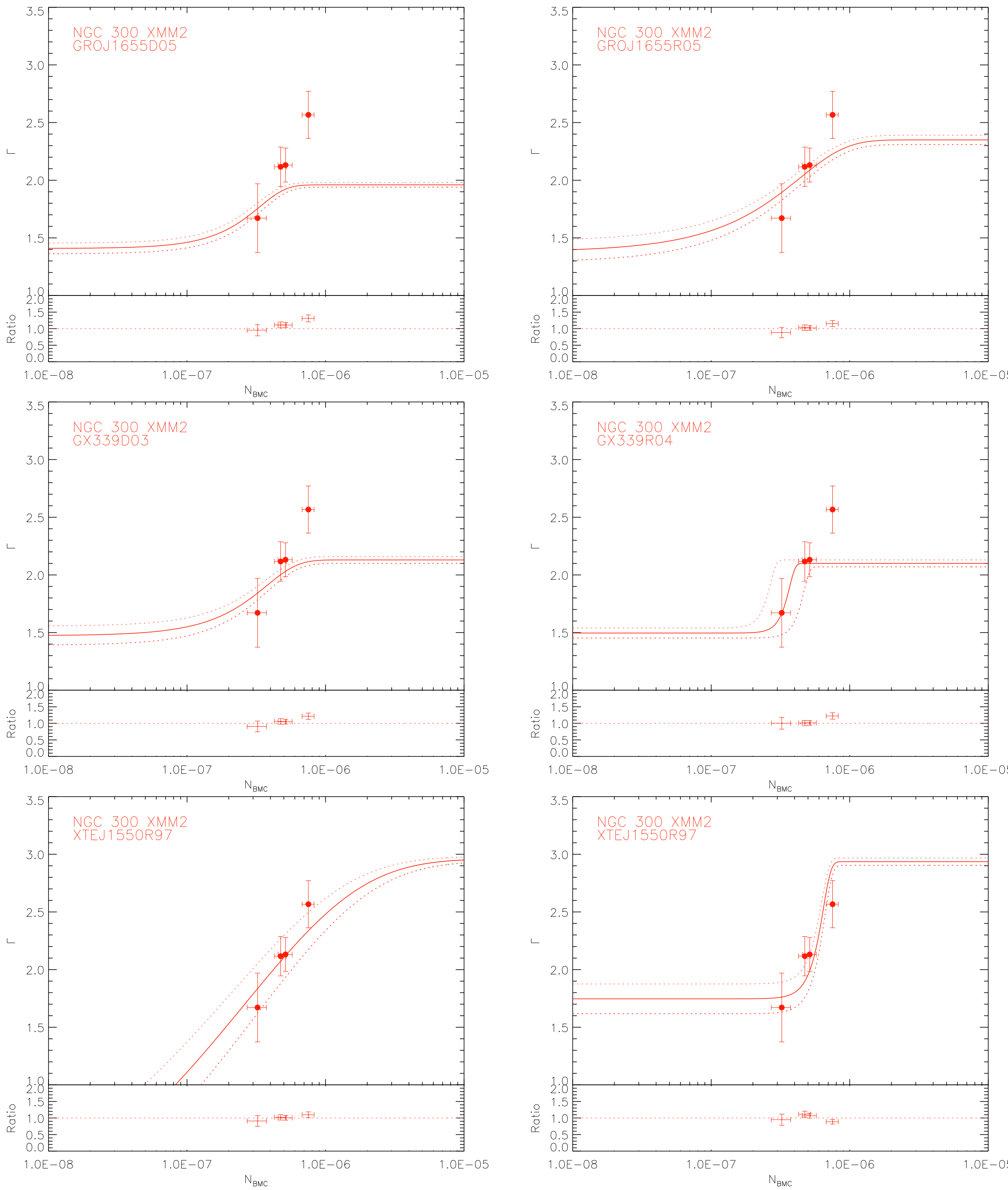

Figure B.21: $\Gamma - N_{\rm BMC}$ diagram of NGC 300 XMM2. The solid line in each panel shows the best-fit of reference spectral transit pattern and its 1σ uncertainty with the dashed line. Any data point used for the best-fit with the filled red circle and the empty blue box for any excluded point. The name of ULX and the used reference pattern are inidcated at the top-left coner in each panel.

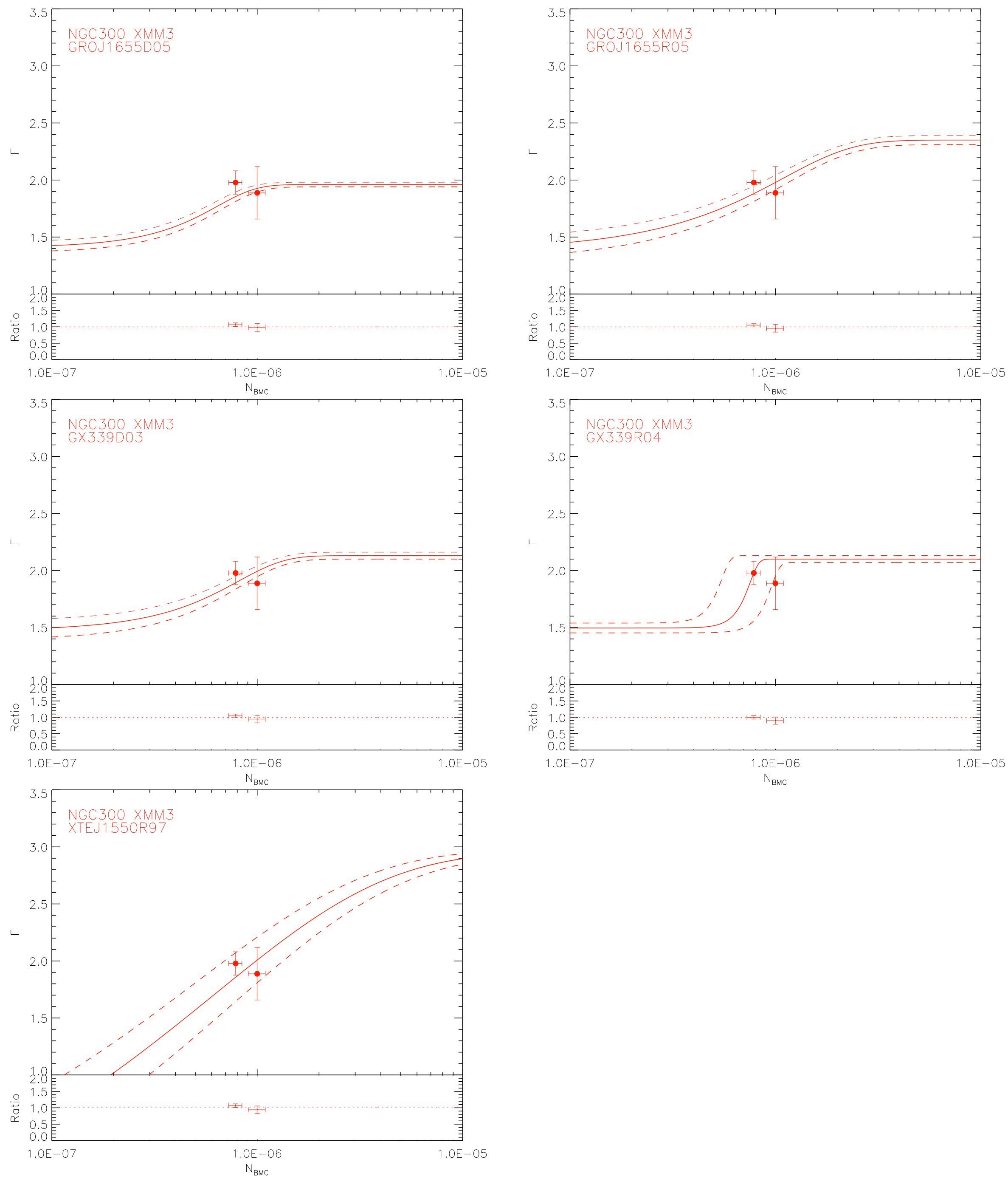

Figure B.22: $\Gamma - N_{\rm BMC}$ diagram of NGC 300 XMM3. The solid line in each panel shows the best-fit of reference spectral transit pattern and its 1σ uncertainty with the dashed line. Any data point used for the best-fit with the filled red circle and the empty blue box for any excluded point. The name of ULX and the used reference pattern are inidcated at the top-left coner in each panel.

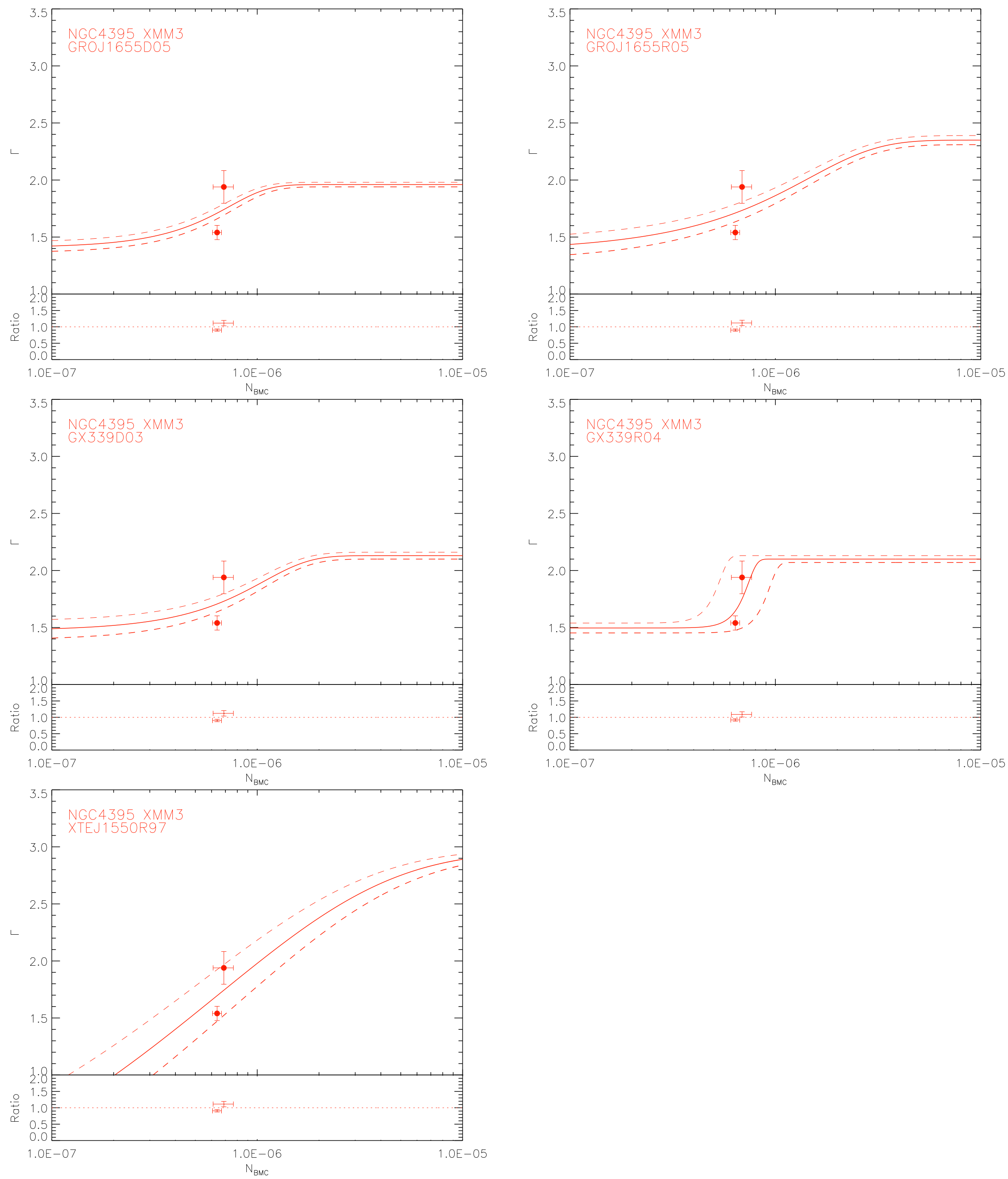

Figure B.23: $\Gamma - N_{\rm BMC}$ diagram of NGC 4395 XMM3. The solid line in each panel shows the best-fit of reference spectral transit pattern and its 1σ uncertainty with the dashed line. Any data point used for the best-fit with the filled red circle and the empty blue box for any excluded point. The name of ULX and the used reference pattern are inidcated at the top-left coner in each panel.

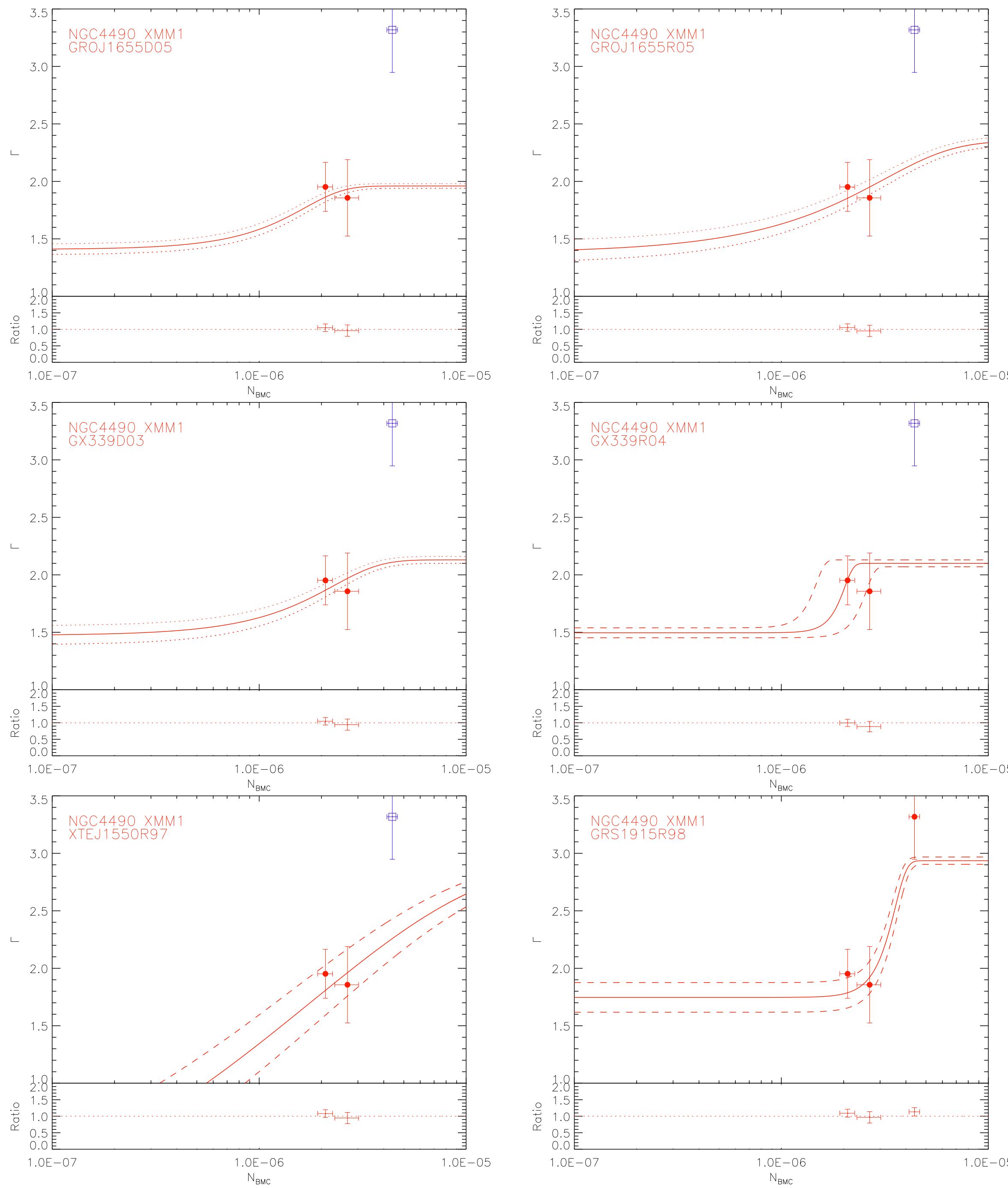

Figure B.24: $\Gamma - N_{\rm BMC}$ diagram of NGC 4490 XMM1. The solid line in each panel shows the best-fit of reference spectral transit pattern and its 1σ uncertainty with the dashed line. Any data point used for the best-fit with the filled red circle and the empty blue box for any excluded point. The name of ULX and the used reference pattern are inidcated at the top-left coner in each panel.

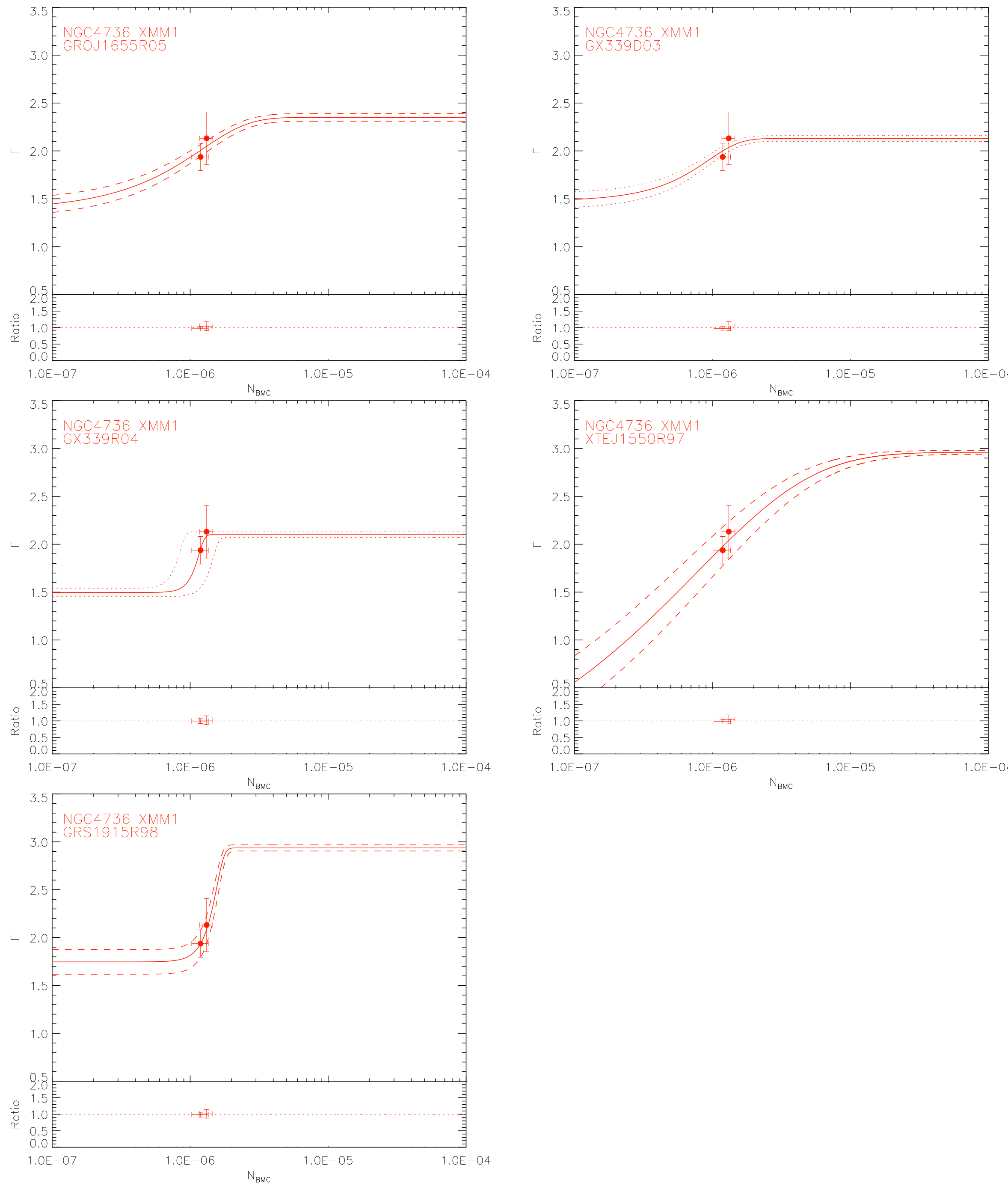

Figure B.25: $\Gamma - N_{\rm BMC}$ diagram of NGC 4736 XMM1. The solid line in each panel shows the best-fit of reference spectral transit pattern and its 1σ uncertainty with the dashed line. Any data point used for the best-fit with the filled red circle and the empty blue box for any excluded point. The name of ULX and the used reference pattern are inidcated at the top-left coner in each panel.

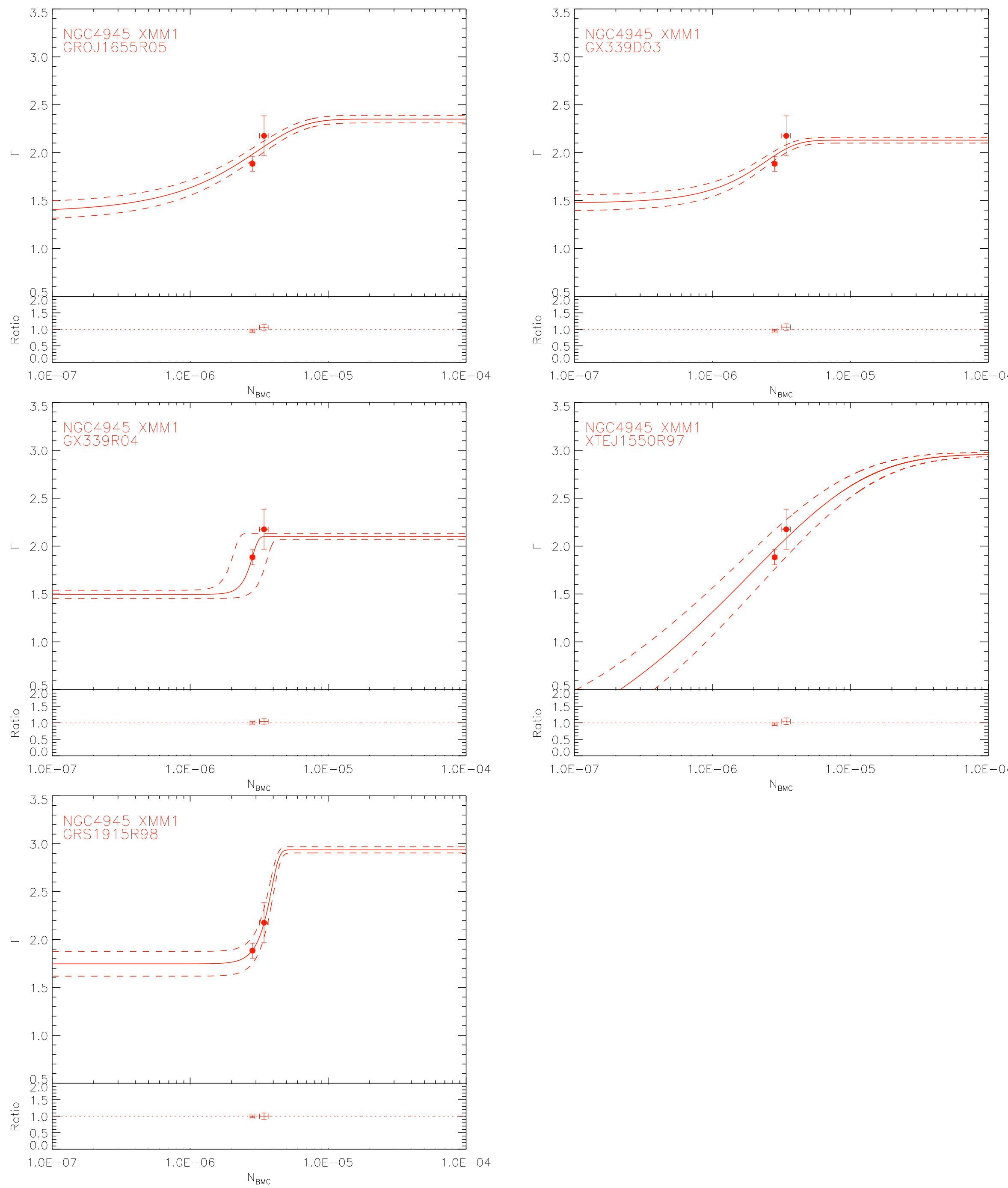

Figure B.26: $\Gamma - N_{\rm BMC}$ diagram of NGC 4945 XMM1. The solid line in each panel shows the best-fit of reference spectral transit pattern and its 1σ uncertainty with the dashed line. Any data point used for the best-fit with the filled red circle and the empty blue box for any excluded point. The name of ULX and the used reference pattern are inidcated at the top-left coner in each panel.

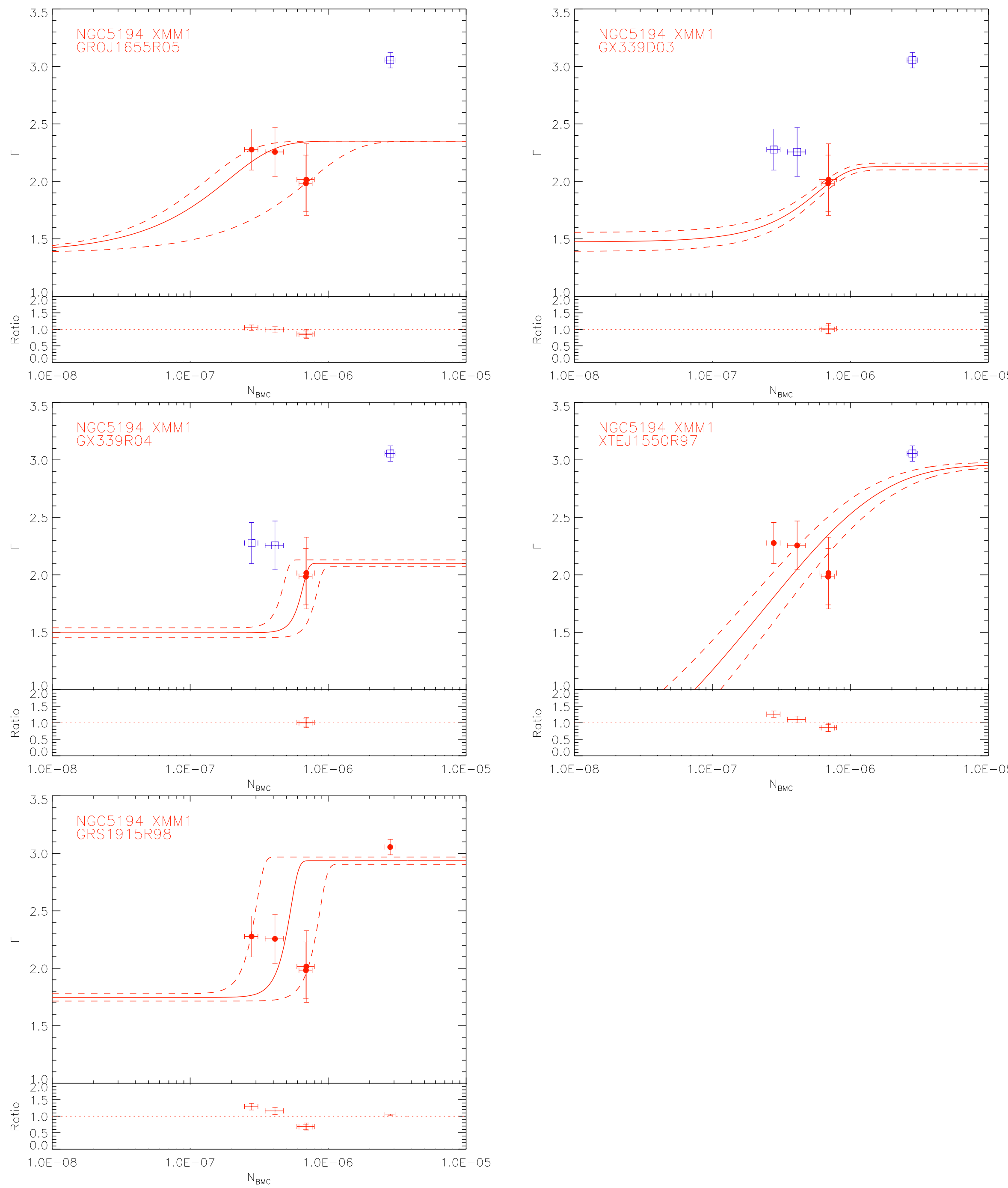

Figure B.27: $\Gamma - N_{\rm BMC}$ diagram of NGC 5194 XMM1. The solid line in aach panel shows the best-fit of reference spectral transit pattern and its 1σ uncertainty with the dashed line. Any data point used for the best-fit with the filled red circle and the empty blue box for any excluded point. The name of ULX and the used reference pattern are inidcated at the top-left coner in each panel.

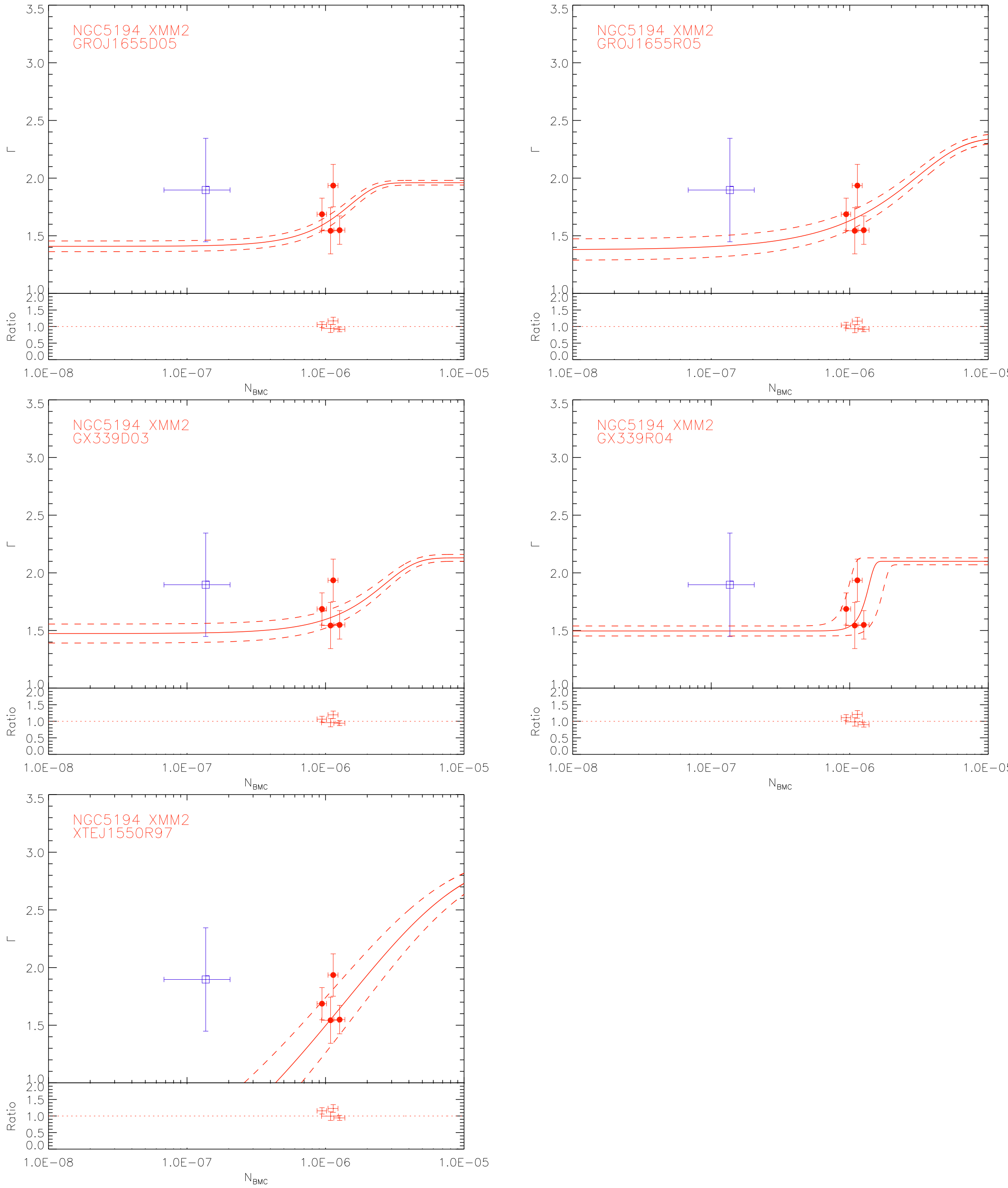

Figure B.28: $\Gamma - N_{\rm BMC}$ diagram of NGC 5194 XMM2. The solid line in aach panel shows the best-fit of reference spectral transit pattern and its 1σ uncertainty with the dashed line. Any data point used for the best-fit with the filled red circle and the empty blue box for any excluded point. The name of ULX and the used reference pattern are inidcated at the top-left coner in each panel.

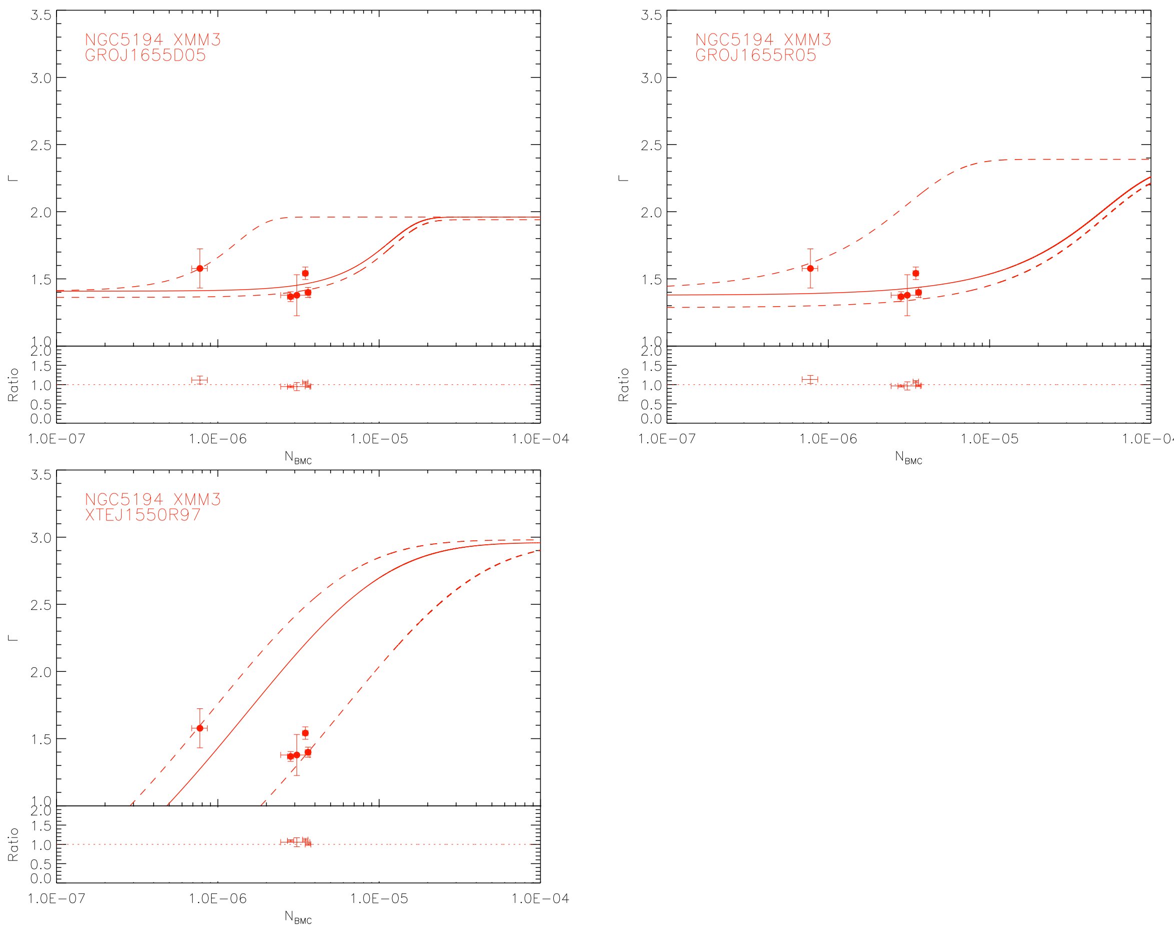

Figure B.29: $\Gamma - N_{\rm BMC}$ diagram of NGC 5194 XMM3. The solid line in aach panel shows the best-fit of reference spectral transit pattern and its 1σ uncertainty with the dashed line. Any data point used for the best-fit with the filled red circle and the empty blue box for any excluded point. The name of ULX and the used reference pattern are inidcated at the top-left coner in each panel.

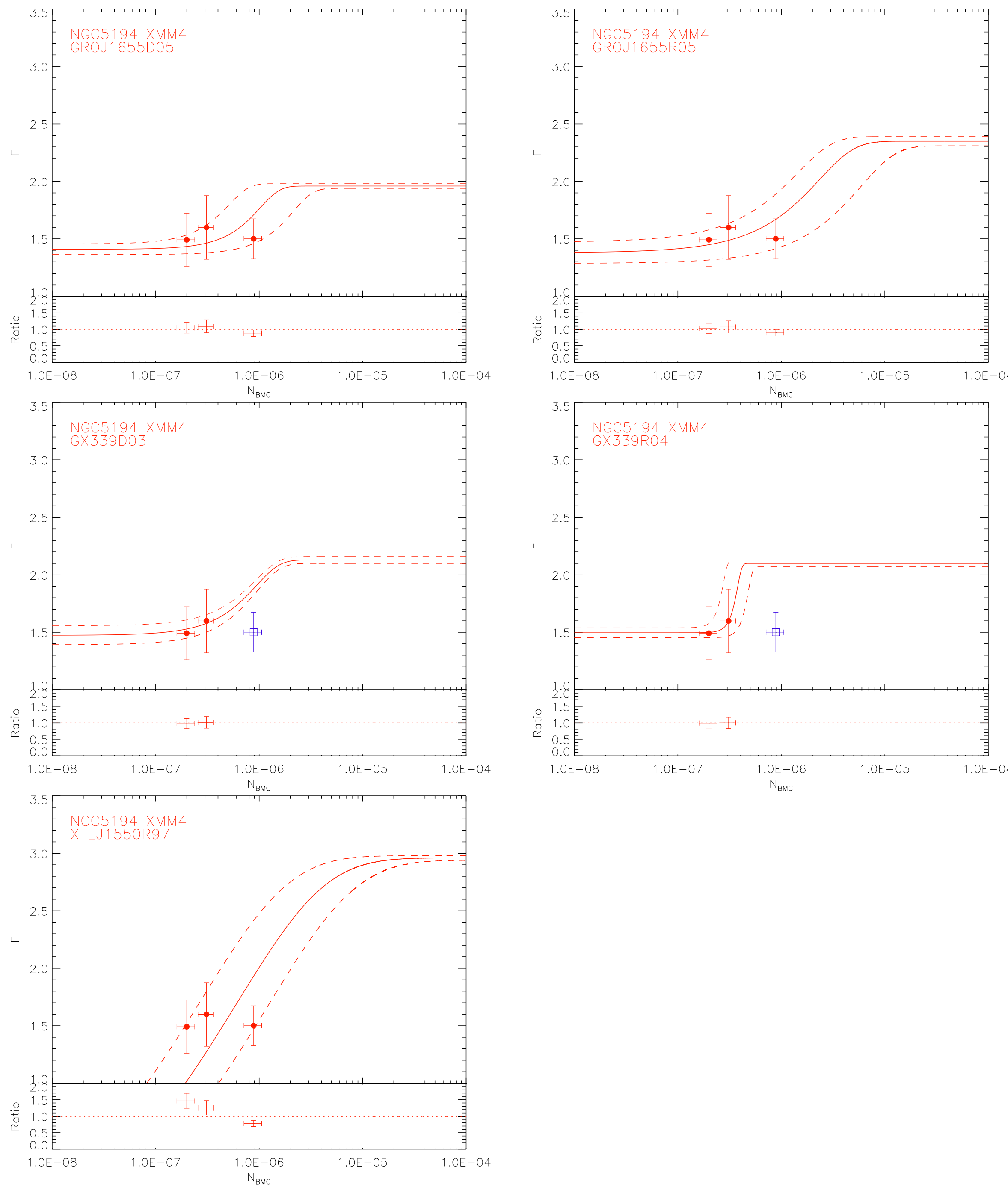

Figure B.30: Γ−$N_{\rm BMC}$ diagram of NGC 5194 XMM4. The solid line in aach panel shows the best-fit of reference spectral transit pattern and its 1σ uncertainty with the dashed line. Any data point used for the best-fit with the filled red circle and the empty blue box for any excluded point. The name of ULX and the used reference pattern are inidcated at the top-left coner in each panel.

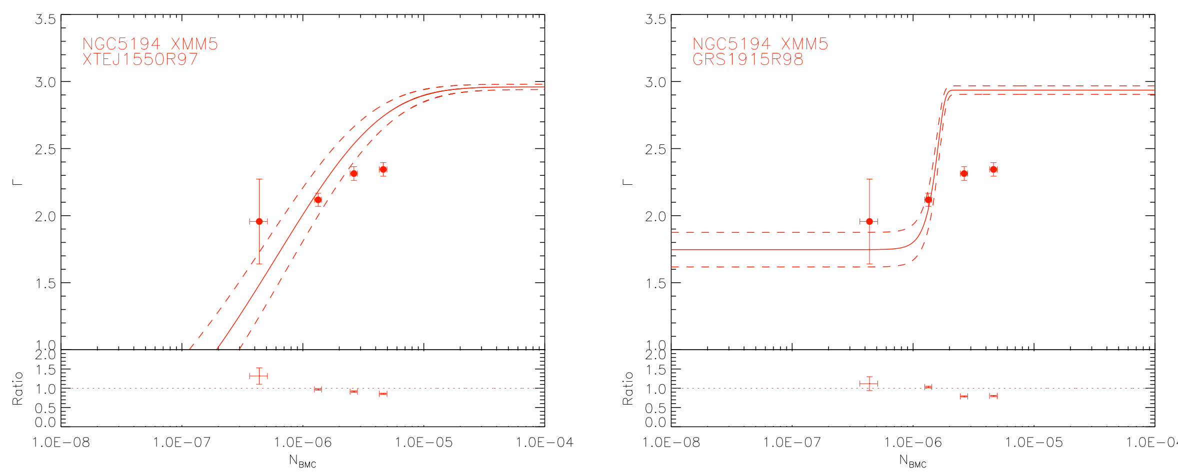

Figure B.31: $\Gamma - N_{\rm BMC}$ diagram of NGC 5194 XMM5. The solid line in aach panel shows the best-fit of reference spectral transit pattern and its 1σ uncertainty with the dashed line. Any data point used for the best-fit with the filled red circle and the empty blue box for any excluded point. The name of ULX and the used reference pattern are inidcated at the top-left coner in each panel.

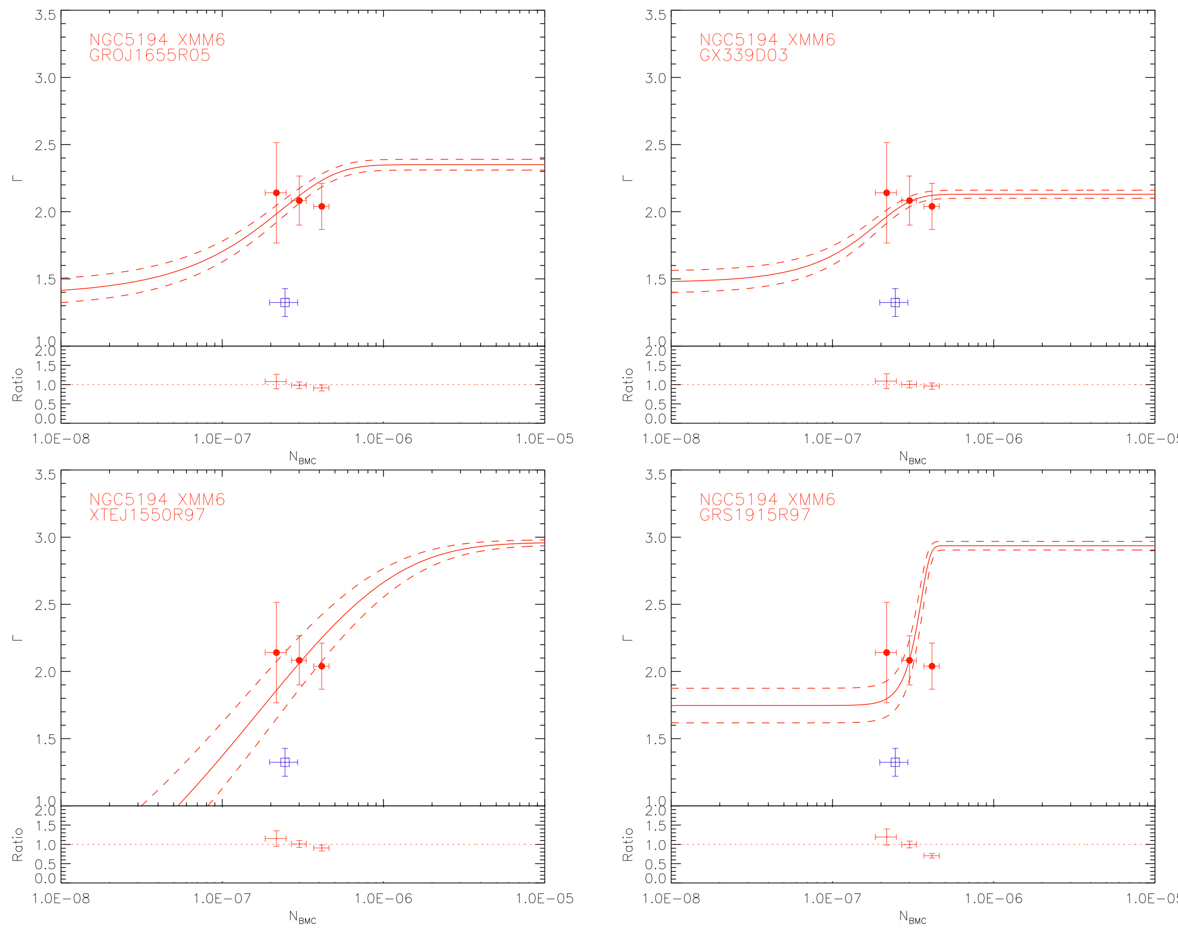

Figure B.32: $\Gamma - N_{\rm BMC}$ diagram of NGC 5194 XMM6. The solid line in aach panel shows the best-fit of reference spectral transit pattern and its 1σ uncertainty with the dashed line. Any data point used for the best-fit with the filled red circle and the empty blue box for any excluded point. The name of ULX and the used reference pattern are inidcated at the top-left coner in each panel.

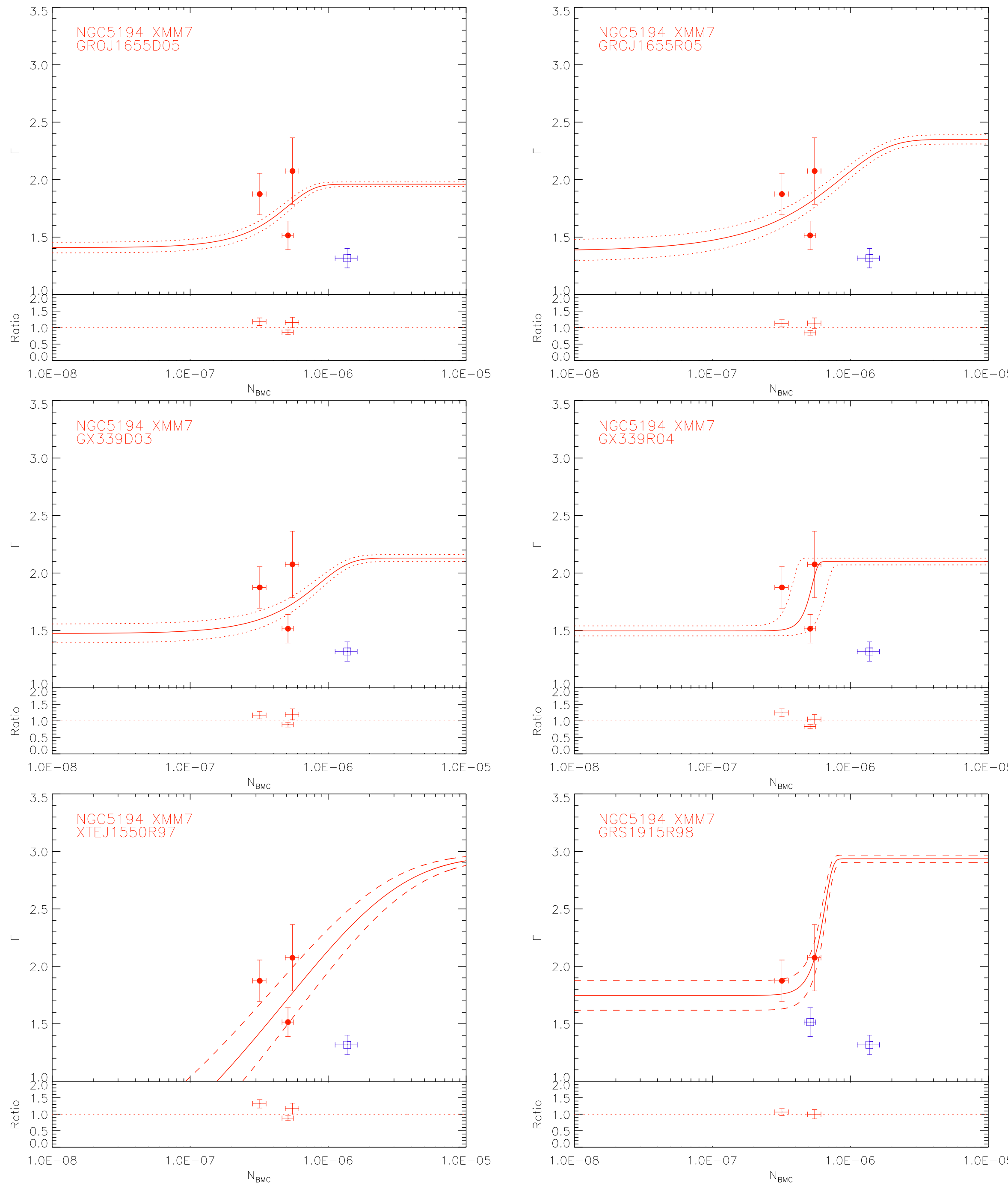

Figure B.33: $\Gamma - N_{\rm BMC}$ diagram of NGC 5194 XMM7. The solid line in aach panel shows the best-fit of reference spectral transit pattern and its 1σ uncertainty with the dashed line. Any data point used for the best-fit with the filled red circle and the empty blue box for any excluded point. The name of ULX and the used reference pattern are inidcated at the top-left coner in each panel.

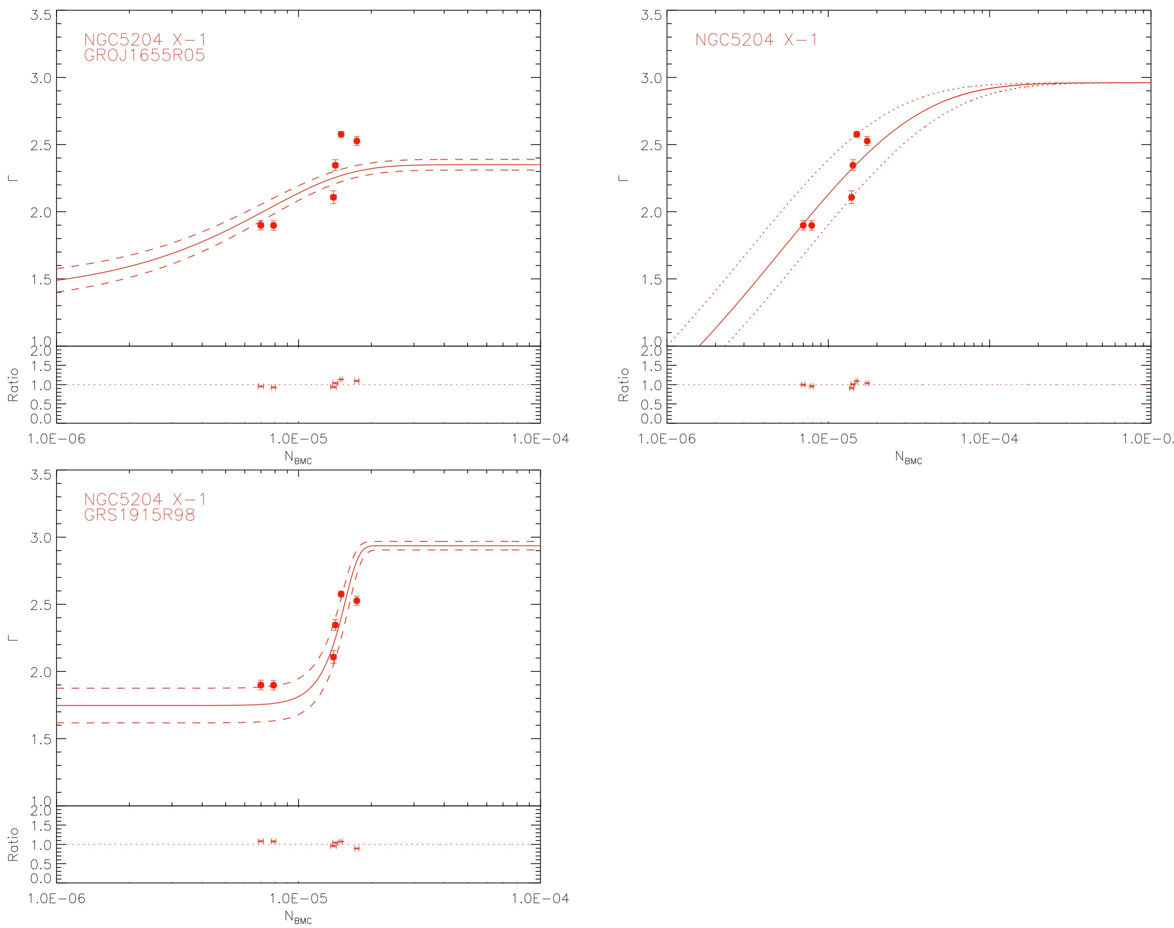

Figure B.34: $\Gamma - N_{\rm BMC}$ diagram of NGC 5204 X-1. The solid line in aach panel shows the best-fit of reference spectral transit pattern and its 1σ uncertainty with the dashed line. Any data point used for the best-fit with the filled red circle and the empty blue box for any excluded point. The name of ULX and the used reference pattern are inidcated at the top-left coner in each panel.

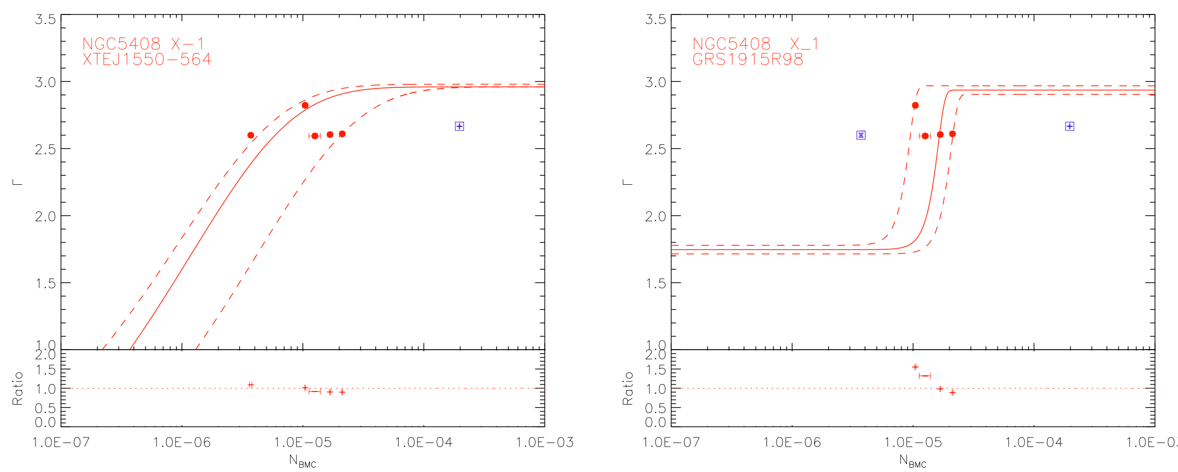

Figure B.35: $\Gamma - N_{\mathrm{BMC}}$ diagram of NGC 5408 X-1. The solid line in aach panel shows the best-fit of reference spectral transit pattern and its 1σ uncertainty with the dashed line. Any data point used for the best-fit with the filled red circle and the empty blue box for any excluded point. The name of ULX and the used reference pattern are inidcated at the top-left coner in each panel.

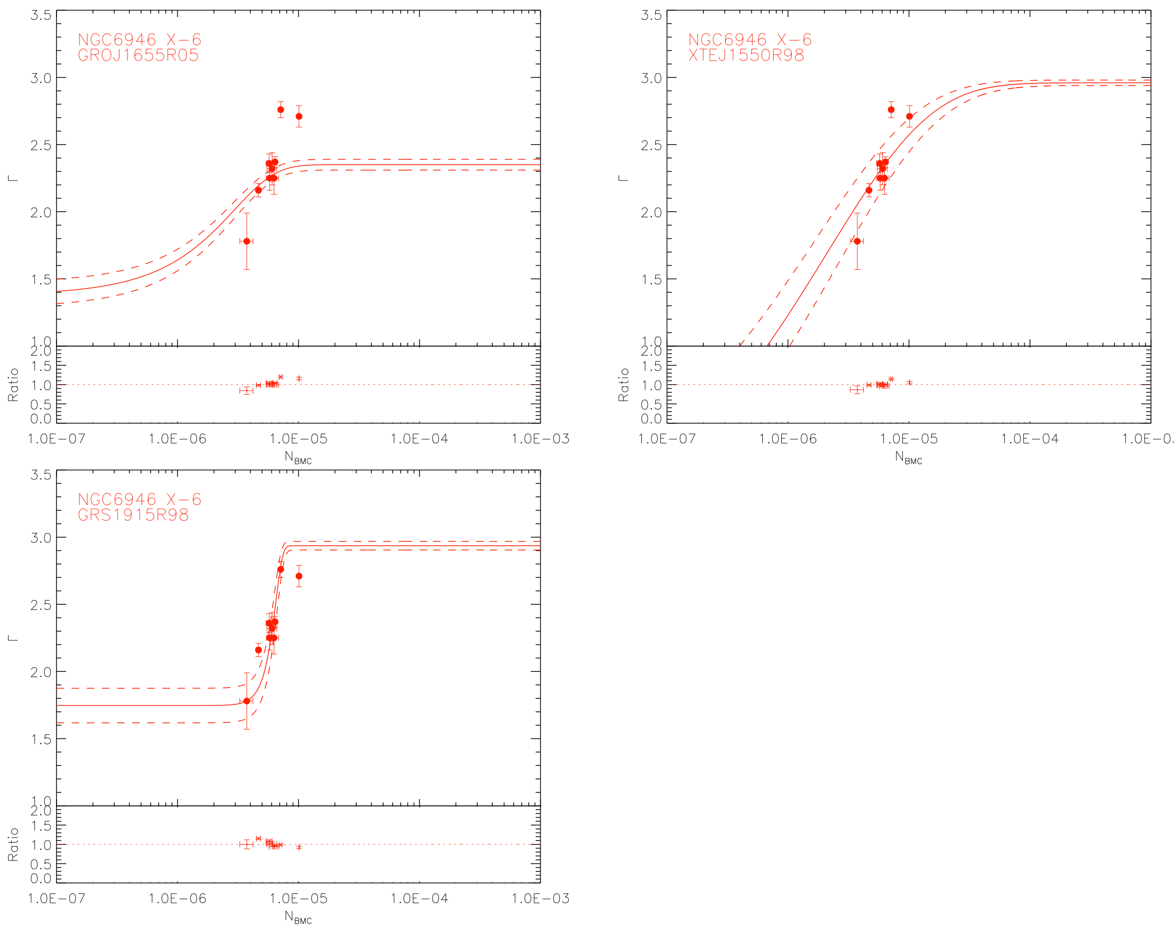

Figure B.36: $\Gamma-N_{\rm BMC}$ diagram of NGC 6946 X-6. The solid line in aach panel shows the best-fit of reference spectral transit pattern and its 1σ uncertainty with the dashed line. Any data point used for the best-fit with the filled red circle and the empty blue box for any excluded point. The name of ULX and the used reference pattern are inidcated at the top-left coner in each panel.

Appendix C: An Appendix

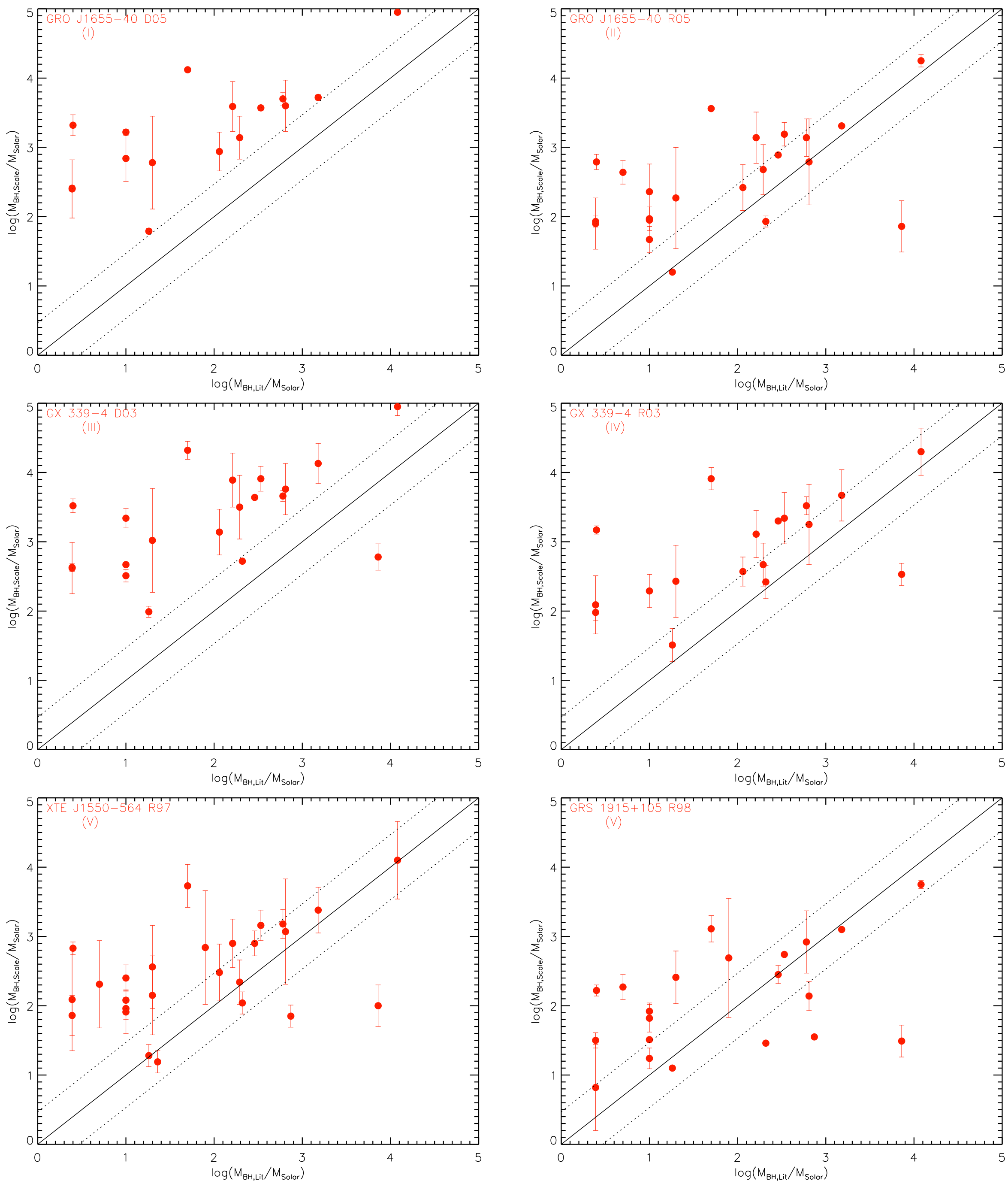

Figure C.1: Plot of $M_{\rm BH,Scale}$ vs. $M_{\rm BH,Lit,Min}$. We plotted obtained $M_{\rm BH,Scale}$ values in $y-$axis and $M_{\rm BH,Lit,Min}$ values in $x-$axis. The used different pattern is inidcated at the left-top in each panel.

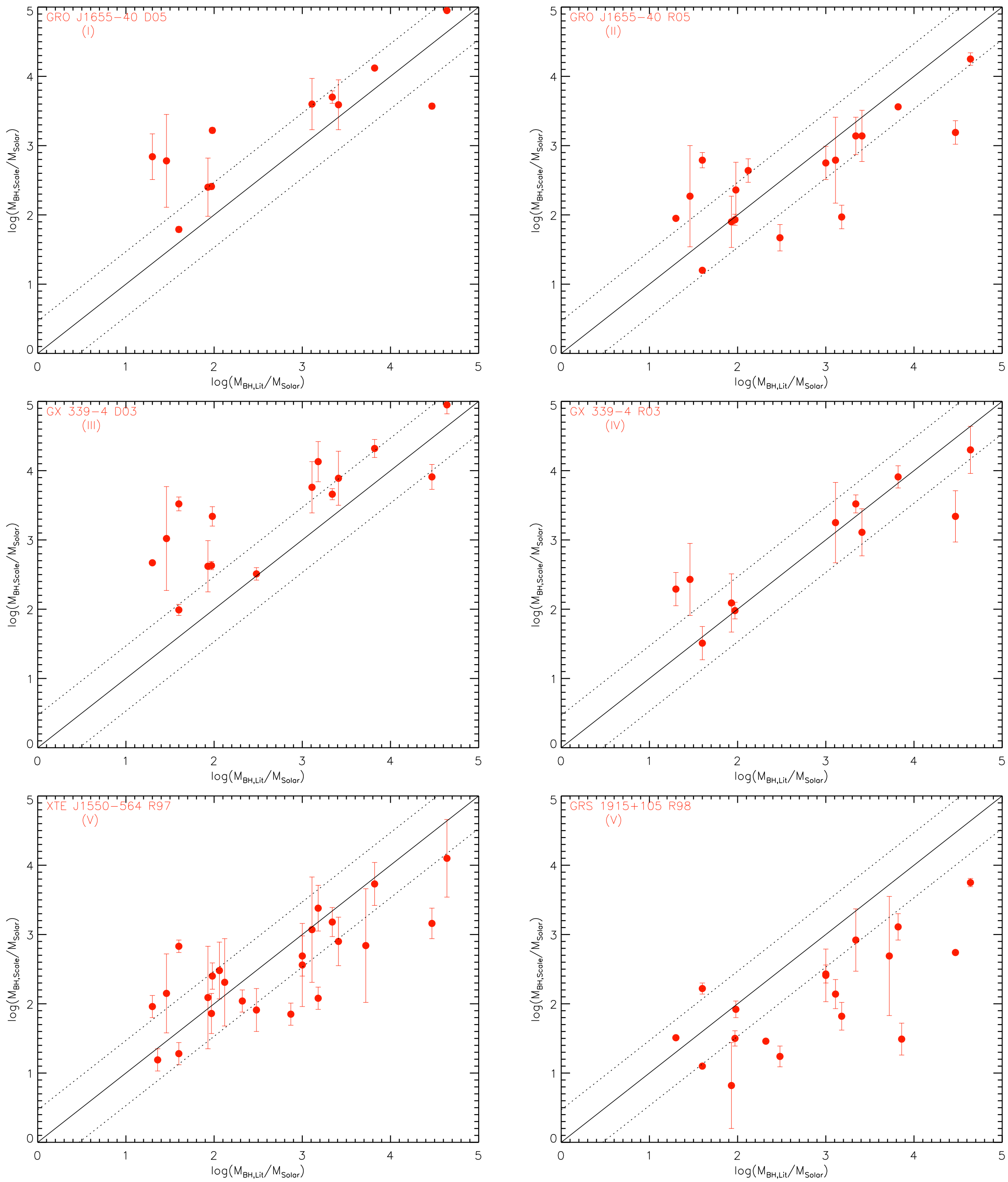

Figure C.2: Plot of $M_{\rm BH}$ vs. $M_{\rm BH,Lit,Max}$. We plotted obtained $M_{\rm BH,Scale}$ values in $y-$axis and $M_{\rm BH,Lit,Max}$ values in $x-$axis. The used different pattern is inidcated at the left-top in each panel.

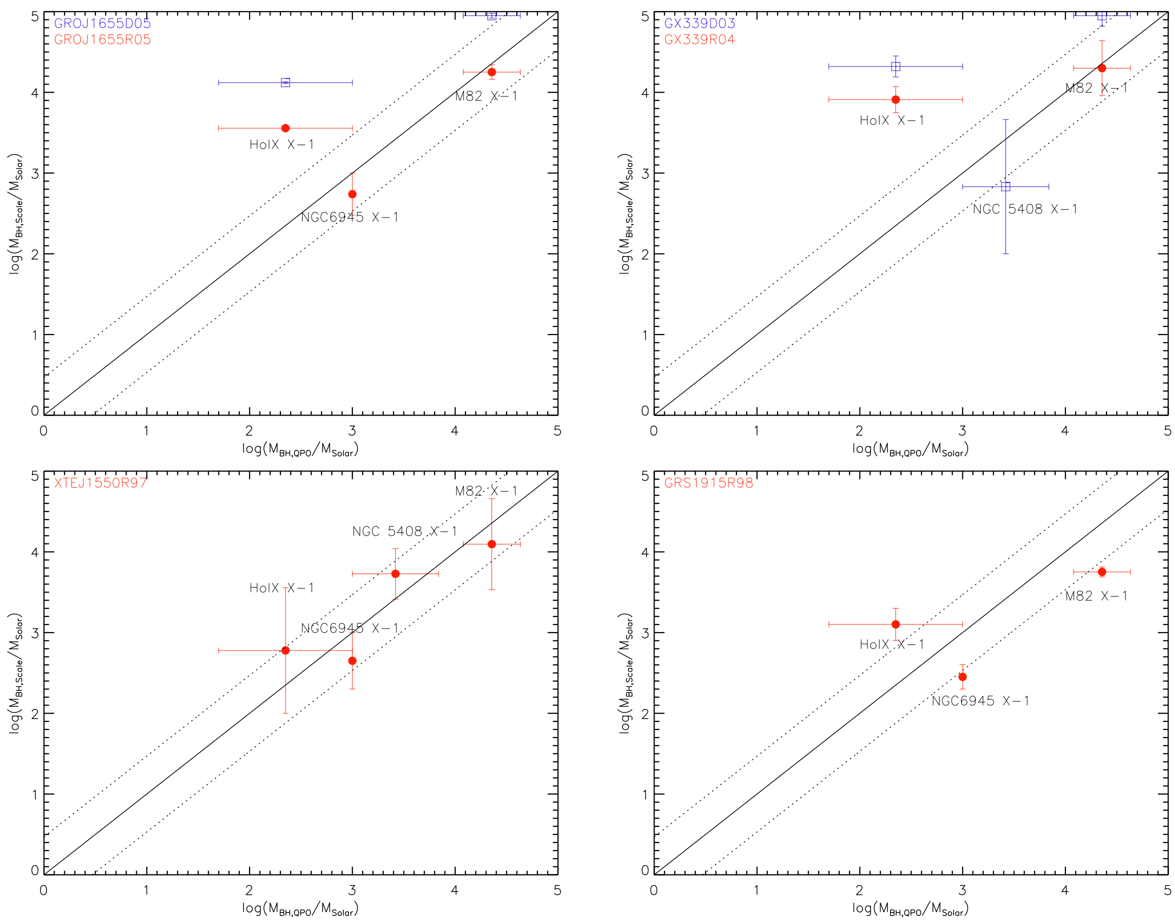

Figure C.3: Plot of $M_{\rm BH}$ vs. $M_{\rm BH,QPO}$. We compared $M_{\rm BH,Scale}$ values for ULXs whose $M_{\rm BH}$ was already determined based on QPO. We plotted $M_{\rm BH,Scale}$ on the y-axis and $M_{\rm BH,QPO}$ on the x-axis. The name of reference pattern was indicated at the top-left corner in each panel.

Bibliography

Atkinson, J. W., Collett, J. L., Marconi, A., Axon, D. J., Alonso-Herrero, A., Batcheldor, D., Binney, J. J., Capetti, A., Carollo, C. M., Dressel, L., Ford, H., Gerssen, J., Hughes, M. A., Macchetto, D., Maciejewski, W., Merrifield, M. R., Scarlata, C., Sparks, W., Stiavelli, M., Tsvetanov, Z., and van der Marel, R. P. (2005). *MNRAS*, 359:504.

Barnard, R. (2010). *MNRAS*, 404:42.

Barth, A. J., Saezi, M., Rix, H.-W., Ho, L. C., Filippenko, A, V., and Sarget, W. L. W. (2001). *ApJ*, 555:685.

Bassani, L., Dadina, M., Maiolino, R., Salvati, M., Risaliti, G., Della Ceca, R., Matt, G., and Zamorani, G. (1999). *ApJS*, 121:473.

Bauer, M.and Pietsch, W. (2005). *A&A*, 442:925.

Belloni, T., Homan, J., Casella, P., van der Klis, M., Nespoli, E., Lewin, W., Miller, J. M., and Méndex, M. (2005). *A&A*, 440:207.

Belloni, T. M. (2004). *NuPhs*, 132:337.

Belloni, T. M. (2010). *LNP*, 794:53.

Belloni, T. M. (2011). *AN*, 332:324.

Bender, R., Kormendy, J., Bower, G., Green, R., Thomas, J., Danks, A. C., Gull, T., Hutchings, J. B., Joseph, C. L., Kaiser, M. E., Lauer, T. R., Nelson, C. H., Richstone, D., Weistrop, D., and Woodgate, B. (2005). *ApJ*, 631:280.

Berghea, C. T., Weaver, K. A., Colbert, E. J. M., and Roberts, T. P. (2008). *ApJ*, 687:471.

Bianchi, S., Piconcelli, E., Chiaberge, M., Bailón, E. J., Matt, G., and Fiore, F. (2009). *ApJ*, 695:781.

Blandford, R. D. and McKee, C. F. (1982). *ApJ*, 225:419.

Blandford, R. D. and Payne, D. G. (1981). *MNRAS*, 194:1033.

Bower, G. A., Green, R. F., Danks, A., Gull, T., Heap, S., Hutchings, J., Joseph, C., Kaiser, M. E., Kimble, R., Kraemer, S., Weistrop, D., Woodgate, B., Lindler, D., Hill, R. S., Malumuth, E. M., Baum, S., Sarajedini, V., Heckman, T. M., Wilson, A. S., and Richstone, D. O. (2001). *ApJ*, 550:75.

Bower, G. A., Green, R. F., Danks, A., Gull, T., Heap, S., Hutchings, J., Joseph, C., Kaiser, M. E., Kimble, R., Kraemer, S., Weistrop, D., Woodgate, B., Lindler, D., Hill, R. S., Malumuth, E. M., Baum, S., Sarajedini, V., Heckman, T. M., Wilson, A. S., and Richstone, D. O. (1998). *ApJ*, 492:L111.

Capetti, A., Marconi, A., Macchetto, D., and Axon, D. (2005). *A&A*, 431:465C.

Cappellari, M., Verolme, E. K., van der Marel, R. P., Kleijn, G. A. V., Illingworth, G. D., Franx, M., Carollo, C. M., and de Zeeuw, P. T. (2002). *ApJ*, 578:787.

Cappi, M., Panessa, F., Bassani, L., Dadina, M., Di Cocco, G., Comastri, A., della Ceca, R., Filippenko, A. V., Gianotti, F., Ho, L. C., Malaguti, G., Mulchaey, J. S., Palumbo, G. G. C., Piconcelli, E., Sargent, W. L. W., Stephen, J., Trifoglio, M., and Weaver, K. A. (2006). *A&A*, 446:459.

Cardullo, A., Corsini, E. M., Beifiori, A., Buson, L. M., Dalla Bont, E., Morelli, L., Pizzella, A., and Bertola, F. (2009). *A&A*, 508:641.

Carpano, S., Pollock, A. M. T., Prestwich, A., Crowther, P., Wilms, J., Yungelson, L., and Ehle, M. (2007). *A&A*, 466:17.

Cash, W. (1979). *ApJ*, 228:939.

Chiang, C. Y., Done, C., Still, M., and Godet, O. (2010). *MNRAS*, 403:1102.

Ciardullo, R., Jacoby, G. H., and Ford, H. C. (1989). *ApJ*, 344:715.

Colbert, E. J. M. and Mushotzky, R. F. (1999). *ApJ*, 519:89.

Constantin, A., Green, P., Aldcroft, T., Kim, D.-W., Haggard, D., Barkhouse, W., and Anderson, S. F. (2009). *ApJ*, 705:1336.

Corbel, S., Fender, R. P., Tzioumis, A. K., Nowak, M., McIntyre, V., Durouchoux, P., and Sood, R. (2000). *A&A*, 359:251.

Corbel, S., Nowak, M. A., Fender, R. P., Tzioumis, A. K., and Markoff, S. (2003). *A&A*, 400:1000.

Cretton, N. and van den Bosch, F. C. (1999). *ApJ*, 514:704.

Dalla Bontá, E., Ferrarese, L., Corsini, E. M., Miralda-Escud, J., Coccato, L., Sarzi, M., Pizzella, A., and Beifiori, A. (2009). *ApJ*, 690:537.

Dasyra, K. M., Tacconi, L. J., Davies, R. I., Genzel, R., Lutz, D., Peterson, B. M., Veilleux, S., Baker, A. J., Schweitzer, M., and Sturm, E. (2007). *ApJ*, 657:102.

de Francesco, G., Capetti, A., and Marconi, A. (2006). *A&A*, 460:439.

de Francesco, G., Capetti, A., and Marconi, A. (2008). *A&A*, 479:355.

Devereux, N., Ford, H., Tsvetanov, Z., and Jacoby, G. (2003). *AJ*, 125:1226.

Dewangan, G. C., Griffiths, R. E., Choudhury, M., Miyaji, T., and Schurch, N. J. (2005). *ApJ*, 635:198.

Dewangan, G. C., Misra, R., Rao, A. R., and Griffiths, R. E. (2010). *MNRAS*, 407:291.

Dewangan, G. C., Titarchuk, L., and Griffiths, R. E. (2006). *ApJ*, 637:21.

Dickey, J. M. and Lockman, F. J. (1990). *ARA&A*, 28:215.

Done, C. and Nayakshin, S. (2001). *MNRAS*, 328:616.

Ebisuzaki, T., Makino, J., Tsuru, T. G., Funato, Y., Portegies Zwart, S., Hut, P., McMillan, S., Matsushita, S., Matsumoto, H., and Kawabe, R. (2001). *ApJ*, 562:19.

Edri, H., Rafter, S. E., Cheloduche, D., Kaspi, S., and Behar, E. (2012). *ApJ*, 756:73.

Emmanoulopoulos, D., Papadakis, I. E., McHardy, I. M., Arvalo, P., Calvelo, D. E., and Uttley, P. (2012). *MNRAS*, 424:1327.

Emsellem, E., Dejonghe, H., and Bacon, R. (1999). *MNRAS*, 303:495.

Esin, A. A., McClintock, J. E., and Narayan, R. (1997). *ApJ*, 489:865.

Fabbiano, G. (1988). *ApJ*, 325:544.

Fabbiano, G. (1989). *ARA&A*, 27:87.

Fabbiano, G., Elvis, M., Markoff, S., Siemiginowska, A., Pellegrini, S., Zezas, A., Nicastro, F., Trinchieri, G., and McDowell, J. (2003). *ApJ*, 588:175.

Fabbiano, G. and Trinchieri, G. (1987). *ApJ*, 315:46.

Fabian, A. C., Sanders, J. S., Crawford, C. S., and Ettori, S. (2003). *MNRAS*, 341:729.

Falcke, H., Körding, E., and Markoff, S. (2004). *A&A*, 414:895.

Fender, R. P. (2001). *MNRAS*, 322:31.

Fender, R. P., Belloni, T. M., and Gallo, E. (2004). *MNRAS*, 335:1105.

Fender, R. P., Hjellming, R. M., Tilanus, R. P. J., Pooley, G. G., Deane, J. R., Ogley, R. N., and Spencer, R. E. (2001). *MNRAS*, 322:23.

Feng, H. and Kaaret, P. (2005). *ApJ*, 633:1052.

Feng, H. and Kaaret, P. (2006). *ApJ*, 653:536.

Feng, H. and Kaaret, P. (2007). *ApJ*, 660:113.

Feng, H. and Kaaret, P. (2009). *ApJ*, 696:1712.

Feng, H. and Kaaret, P. (2010). *ApJ*, 712:169.

Feng, H., Rao, F., and Kaaret, P. (2010). *ApJ*, 710:137.

Feng, H. and Soria, R. (2011). *NewAR*, 55:166.

Ferrarese, L. and Ford, H. C. (1999). *ApJ*, 515:583.

Ferrarese, L., Ford, H. C., and Jaffe, W. (1996). *ApJ*, 470:444.

Ferrarese, L. and Merritt, D. (2000). *ApJ*, 539:9.

Ferrarese, L., Pogge, R. W., Peterson, B. M., Merritt, D., Wandel, A., and Joseph, C. L. (2001). *ApJ*, 555:79.

Foschini, L., Rodriguez, J., Fuchs, Y., Ho, L. C., Dadina, M., Di Cocco, G., Courvoisier, T. J.-L., and Malaguti, G. (2004). *A&A*, 416:529.

Frank, J., King, A., and & Raine, D. J. (2002). *Accretion Power in Astrophysics.*

Freeman, P. E., Kashyap, V., Rosner, R., and Lamb, D. Q. (2002). *ApJS*, 138:185.

Gardner, E. and Done, C. (2012). *arXiv1207.6984G.*

Gebhardt, K., Bender, R., Bower, G., Dressler, A., Faber, S. M., Filippenko, A. V., Green, R., Grillmair, C., Ho, L. C., Kormendy, J., Lauer, T. R., Magorrian, J., Pinkney, J., Richstone, D., and Tremaine, S. (2000a). *ApJ*, 539:L13.

Gebhardt, K., Lauer, T. R., Kormendy, J., Pinkney, J., Bower, G. A., Green, R., Gull, T., Hutchings, J. B., Kaiser, M. E., Nelson, C. H., Richstone, D., and Weistrop, D. (2001). *AJ*, 122:2469.

Gebhardt, K., Lauer, T. R., Pinkney, J., Bender, R., Richstone, D., Aller, M., Bower, G., Dressler, A., Faber, S. M., Filippenko, A. V., Green, R., Ho, L. C., Kormendy, J., Siopis, C., and Tremaine, S. (2007). *ApJ*, 671:1321.

Gebhardt, K., Richstone, D., Kormendy, J., Lauer, T. R., Ajhar, E. A., Bender, R., Dressler, A., Faber, S. M., Grillmair, C., Magorrian, J., and Tremaine, S. (2000b). *ApJ*, 119:1157.

Genzel, R. and Karas, V. (2007). *IAUS*, 238:173.

Genzel, R., Pichon, C., Eckart, A., Gerhard, O. E., and Ott, T. (2000). *MNRAS*, 317:348.

George, I. M. and Fabian, I. C. (1991). *MNRAS*, 249:352.

Ghez, A. M., Salim, S., Hornstein, S. D., Tanner, A., Lu, J. R., Morris, M., Becklin, E. E., and Duchne, G. (2005). *ApJ*, 620:744.

Ghez, A. M., Salim, S., Weinberg, N. N., Lu, J. R., Do, T., Dunn, J. K., Matthews, K., Morris, M. R., Yelda, S., Becklin, E. E., Kremenek, T., Milosavljevic, M., and Naiman, J. (2008). *ApJ*, 689:1044.

Gladstone, J. C., Roberts, T. P., and Done, C. (2009). *MNRAS*, 397:1836.

Gliozzi, M., Papadakis, I. E., Grupe, D., Brinkmann, W. P., Raeth, C., and Kedziora-Chudczer, L. (2010). *ApJ*, 717:1243.

Gliozzi, M., Titarchuk, L., Satyapal, S., Price, D., and Jang, I. (2011). *ApJ*, 735:16.

Goad, M. R., Roberts, T. P., Reeves, J. N., and Uttley, P. (2006). *MNRAS*, 365:191.

González-Martín, O., Masegosa, J., Márquez, I., and Guainazzi, M. (2009). *ApJ*, 704:1570.

González-Martín, O., Papadakis, I., Reig, P., and Zezas, A. (2011). *A&A*, 526:132.

Greene, J., Bailyn, C. D., and Orosz, J. A. (2001). *ApJ*, 554:1290.

Greenhill, L. J., Moran, J. M., and Herrnstein, J. R. (1997). *ApJ*, 481:23.

Gu, M. and Cao, X. (2009). *MNRAS*, 339:349.

Gültekin, K., Cackett, E. M., Miller, J. M., Di Matteo, T., Markoff, S., and Richstone, D. O. (2009a). *ApJ*, 706:404.

Gültekin, K., Cackett, E. M., Miller, J. M., Di Matteo, T., Markoff, S., and Richstone, D. O. (2012). *ApJ*, 749:129.

Gültekin, K., Richstone, D. O., Gebhardt, K., Lauer, T. R., Pinkney, J., Aller, M. C., Bender, R., Dressler, A., Faber, S. M., Filippenko, A. V., Green, R., Ho, L. C., Kormendy, J., and Siopis, C. (2009b). *ApJ*, 695:1577.

Heil, L. M., Vaughan, S., and Roberts, T. P. (2009). *MNRAS*, 397:1061.

Herrero, A., Kudritzki, R. P., Gabler, R., Vilchez, J. M., and Gabler, A. (1995). *A&A*, 297:556.

Herrnstein, J. R., Moran, J. M., Greenhill, L. J., and Trotter, A. S. (2005). *ApJ*, 629:719.

Hicks, E. K. S. and Malkan, M. A. (2008). *ApJS*, 174:31.

Ho, L. C., Feigelson, E. D., Townsley, L. K., Sambruna, R. M., Garmire, G. P., Brandt, W. N., Filippenko, A. V., Griffiths, R. E., Ptak, A. F., and Sargent, W. L. W. (2001). *ApJ*, 549:51.

Ho, L. C., Filippenko, A. V., and Sargent, W. L. W. (1997). *ApJS*, 112:315.

Homan, J., Wijnands, R., van der Klis, M., Belloni, T., van Paradijs, J., Klein-Wolt, M., Fender, R., and Méndez, M. (2001). *ApJ*, 132:377.

Hui, Y. and Krolik, J. H. (2008). *ApJ*, 679:1405.

Ishibashi, W. and Courvoisier, T. J.-L. (2012). *A&A*, 540:2.

Kaaret, P. and Corbel, S. (2009). *ApJ*, 697:950.

Kaaret, P., Corbetl, S., Prestwich, A. H., and Zezas, A. (2003). *Science*, 299:395.

Kaaret, P. and Feng, H. (2009). *ApJ*, 702:1679.

Kaaret, P., Feng, H., and Gorski, M. (2009). *ApJ*, 692:653.

Kaaret, P., Prestwich, A. H., Zezas, A., Murray, S. S., Kim, D.-W., Kilgard, R. E., Schlegel, E. M., and Ward, M. J. (2001). *MNRAS*, 321:29.

Kaaret, P., Ward, M. J., and Zezas, A. (2004). *MNRAS*, 351:83.

Kajava, J. J. E. and Poutanen, J. (2009). *MNRAS*, 398:1450.

Kalemci, E. (2002). *PhDT*, 12K.

Kaspi, S., Smith, P. S., Netzer, H., Maoz, D., Jannuzi, B. T., and Giveon, U. (2000). *ApJ*, 533:631.

Katz, J. I. (1976). *ApJ*, 206:910.

Kawaguchi, T., Kawasaki, M., Takayama, T., Yamaguchi, M., and Yokoyama, J. (2008). *MNRAS*, 388:1426.

King, A. R. (2009). *MNRAS*, 393:41.

King, A. R., Davies, M. B., Ward, M. J., Fabbiano, G., and Elvis, M. (2001). *ApJ*, 552:109.

Körding, E. G., Jester, S., and Fender, R. (2006). *MNRAS*, 372:1366.

Kormendy, J. (1988). *ApJ*, 335:40.

Kormendy, J. and Richstone, D. (1995). *ARA&A*, 33:581.

Kubota, A., Makishima, K., and Ebisawa, K. (2001a). *ApJ*, 561:147.

Kubota, A., Mizuno, T., Makishima, K., Fukazawa, Y., Kotoku, J., Ohnishi, T., and Tashiro, M. (2001b). *ApJ*, 547:119.

Laor, A. (1998). *ApJ*, 505:83.

Leahy, D. A., Darbro, W., Elsner, R. F., Weisskopf, M. C., Kahn, S., Sutherland, P. G., and Grindlay, J. E. (1983). *ApJ*, 266:160.

Lehmann, I., Becker, T., Fabrika, S., Roth, M., Miyaji, T., Afanasiev, V., Sholukhova, O., Sánchez, S. F., Greiner, J., Hasinger, G., Costantini, E., Surkov, A., and Burenkov, A. (2005). *A&A*, 431:847.

Liu, J. F. and Bregman, J. N. (2005). *ApJS*, 157:59.

Liu, J. F. and Di Stefano, R. (2008). *ApJ*, 674:73.

Liu, Q. Z. and Mirabel, I. F. (2005). *A&A*, 429:1125.

Lodato, G. and Bertin, G. (2003). *A&A*, 398:517.

Long, K. S. and van Speybroeck, L. P. (1983). *Accretion-Driven Stellar X-ray Sources*, 315:117–146.

Macchetto, F., Marconi, A., Axon, D. J., Capetti, A., Sparks, W., and Crane, P. (1997). *ApJ*, 489:579.

Magorrian, J., Tremaine, S., Richstone, D., Bender, R., Bower, G., Dressler, A., Faber, S. M., Gebhardt, K., Green, R., Grillmair, C., Kormendy, J., and Lauer, T. (1998). *ApJ*, 115:2285.

Maiolino, R., Salvati, M., Bassani, L., Dadina, M., della Ceca, R., Matt, G., Risaliti, G., and Zamorani, G. (1998). *A&A*, 338:781.

Makishima, K., Kubota, A., Mizuno, T., Ohnishi, T., Tashiro, M., Aruga, Y., Asai, K., Dotani, T., Mitsuda, K., Ueda, Y., Uno, S., Yamaoka, K., Ebisawa, K., Kohmura, Y., and Okada, K. (2000). *ApJ*, 535:632.

Makishima, K., Maejima, Y., Mitsuda, K., Bradt, H. V., Remillard, R. A., Tuohy, I. R., Hoshi, R., and Nakagawa, M. (1986). *ApJ*, 308:635.

Margon, B. and Ostriker, J. P. (1973). *ApJ*, 186:91.

Marinucci, A., Risaliti, G., Wang, J., Nardini, E., Elvis, M., Fabbiano, G., Bianchi, S., and Matt, G. (2012). *MNRAS*, 423:6.

Markowitz, A. and Edelson, R. (2001). *ApJ*, 547:684.

Markowitz, A., Edelson, R., Vaughan, S., Uttley, P., George, I. M., Griffiths, R. E., Kaspi, S., Lawrence, A., McHardy, I., Nandra, K., Pounds, K., Reeves, J., Schurch, N., and Warwick, R. (2003). *ApJ*, 593:96.

Markwardt, C. B. (2009). in Astronomical Data Analysis Software and Systems XVIII.

McHardy, I. M., Koerding, E., Knigge, C., Uttley, P., and Fender, R. P. (2006). *Nature*, 444:730.

McNamara, B. R., Wise, M., Nulsen, P. E. J., David, L. P., Sarazin, C. L., Bautz, M., Markevitch, M., Vikhlinin, A., Forman, W. R., Jones, C., and Harris, D. E. (2000). *ApJ*, 534:135.

Méndez, R. H., Thomas, D., Saglia, R. P., Maraston, C., Kudritzki, R. P., and Bender, R. (2005). *ApJ*, 627:767.

Menou, Kristen; Esin, A. A., Narayan, R., Garcia, M. R., Lasota, J.-P., and McClintock, J. E. (1999). *ApJ*, 520:276.

Merloni, A., Heinz, S., and di Matteo, T. (2003). *MNRAS*, 345:1057.

Miller, J. M., Fabbiano, G., Miller, M. C., and Fabian, A. C. (2003). *ApJ*, 585:37.

Miller, M. C. and Hamilton, D. P. (2002). *MNRAS*, 330:232.

Mineshige, S. and Ohsuga, K. (2011). *Astronomische Nashrichten*, 332:402.

Mitsuda, K., Inoue, H., Koyama, K., Makishima, K., Matsuoka, M., Ogawara, Y., Suzuki, K., Tanaka, Y., Shibazaki, N., and Hirano, T. (1984). *PASJ*, 36:741.

Mitzuno, T., Ohnishi, T., Kubota, A., Makishima, K., and Tashiro, M. (1999). *PASJ*, 51:663.

Miyoshi, M., Moran, J., Herrnstein, J., Greenhill, L., Nakai, N., Diamond, P., and Inoue, M. (1995). *Nature*, 373:127.

Mundell, C. G., Pedlar, A., Shone, D. L., and Robinson, A. (1999). *MNRAS*, 304:481.

Naim, A., Lahav, O., Buta, R. J., Corwin, H. G., J., de Vaucouleurs, G., Dressler, A., Huchra, J. P., van den Bergh, S., Raychaudhury, S., Sodre, L., J., and Storrie-Lombardi, M. C. (1995). *MNRAS*, 274:1107.

Narayan, R., Garcia, M. R., and McClintock, J. E. (2002). *THE NINTH MARCEL GROSSMANN MEETING*. World Scientific Publishing Co. Pte. Ltd.

Narayan, R. and Yi, I. (1994). *ApJ*, 428:13.

Narayan, R. and Yi, I. (1995). *ApJ*, 452:710.

Nelson, C. H., Green, R. F., Bower, G., Gebhardt, K., and Weistrop, D. (2004). *ApJ*, 615:652.

Nikolajuk, M., Papadakis, I. E., and Czerny, B. (2004). *MNRAS*, 350:26.

Nikoajuk, M., Czerny, B., and Gurynowicz, P. (2009). *MNRAS*, 934:214.

Nikoajuk, M., Czerny, B., and Ziókowski, J.; Gierliński, M. (2006). *MNRAS*, 370:1534.

Nowak, N., Saglia, R. P., Thomas, J., Bender, R., Pannella, M., Gebhardt, K., and Davies, R. I. (2007). *MNRAS*, 379:909.

Ohsuga, K. and Mineshige, S. (2011). *ApJ*, 736:2.

Okada, K., Dotani, T., Makishima, K., Mitsuda, K., and Mihara, T. (1998). *PASJ*, 50:25.

Onken, C. A., Ferrarese, L., Merritt, D., Peterson, B. M., Pogge, R. W., Vestergaard, M., and Wandel, A. (2004). *ApJ*, 615:645.

Onken, C. A., Valluri, M., Peterson, B. M., Pogge, R. W., Bentz, M. C., Ferrarese, L., Vestergaard, M., Crenshaw, D. M., Sergeev, S. G., McHardy, I. M., Merritt, D., Bower, G. A., Heckman, T. M., and Wandel, A. (2007). *ApJ*, 670:105.

Osterbrock, D. E. and Koski, A. T. (1976). *MNRAS*, 176:61.

Pakull, M. W. and Mirioni, L. (2002). *astro-ph/0202488*.

Panessa, F., Barcons, X., Bassani, L., Cappi, M., Carrera, F. J., Ho, L. C., and Pellegrini, S. (2007). *A&A*, 467:519.

Papadakis, I. E. (2004). *MNRAS*, 348:207.

Papadakis, I. E., Petrucci, P. O., Maraschi, L., McHardy, I. M., Uttley, P., and Haardt, F. (2002). *ApJ*, 573:92.

Park, D., Woo, J.-H., Treu, T., Barth, A. J., Bentz, M. C., Bennert, V. N., Canalizo, G., Filippenko, A. V., Gates, E., Greene, J. E., Malkan, M. A., and Walsh, J. (2012). *ApJ*, 747:30.

Pastorini, G., Marconi, A., Capetti, A., Axon, D. J., Alonso-Herrero, A., Atkinson, J., Batcheldor, D., Carollo, C. M., Collett, J., Dressel, L., Hughes, M. A., Macchetto, D., Maciejewski, W., Sparks, W., and van der Marel, R. (2007). *A&A*, 469:405.

Peterson, B. M. (1993). *PASP*, 105:247.

Peterson, B. M. (2001). *in The Starburst-AGN Connection*, page 3p.

Peterson, B. M., Ferrarese, L., Gilbert, K. M., Kaspi, S., Malkan, M. A., Maoz, D., Merritt, D., Netzer, H., Onken, C. A., Pogge, R. W., Vestergaard, M., and Wandel, A. (2004). *ApJ*, 613:682.

Ponti, G., Fender, R. P., Begelman, M. C., Dunn, R. J. H., Neilsen, J., and Coriat, M. (2012). *MNRAS*, 422:11.

Poutanen, J., Lipunova, G., Fabrika, S., Butkevich, A. G., and Abolmasov, P. (2007). *MNRAS*, 337:1187.

Press, W. H., Teukolsky, S. P., Vetterling, W. T., and Flannery, B. P. (1997). *Numerical Recipes*. Cambridge: Cambridge Univ. Press.

Qiao, E. and Liu, B. F. (2013). *ApJ*, 764:2.

Rao, F., Feng, H., and Kaaret, P. (2010). *ApJ*, 722:620.

Remillard, R. A. and McClintock, J. E. (2006). *ARA&A*, 44:49.

Remillard, R. A., Muno, M. P., McClintock, J. E., and Orosz, J. A. (2002). *ApJ*, 580:1030.

Research Systems, I. (1988-1999).

Rieke, G. H. and Lebofsky, M. J. (1979). *ARA&A*, 17:477.

Rybicki, G. B. and Lightman, A. P. (1979). *Radiative processes in astrophysics*. New York, Wiley-Interscience.

Sarzi, M., Rix, H.-W., Shields, J. C., Rudnick, G., Ho, L. C., McIntosh, D. H., Filippenko, A. V., and Sargent, W. L. W. (2001). *ApJ*, 550:65.

Shakura, N. I. and Sunyaev, R. A. (1973). *A&A*, 24:337.

Shapiro, S. L., Lightman, A. P., and Eardley, D. M. (1976). *ApJ*, 204:187.

Shaposhnikov, N. and Titarchuk, L. (2009). *ApJ*, 699:453.

Shemmer, O., Brandt, W. N., Netzer, H., Maiolino, R., and Kaspi, S. (2008). *ApJ*, 682:81.

Sikora, M., Stawarz, u., and Lasota, J.-P. (2007). *ApJ*, 658:815.

Silge, J. D., Gebhardt, K., Bergmann, M., and Richstone, D. (2005). *AJ*, 130:406.

Sobolewska, M. A., Gierliński, M., and Siemiginowska, A. (2009). *MNRAS*, 394:1640.

Sobolewska, M. A., Siemiginowska, A., and Gierliński, M. (2011). *MNRAS*, 413:2259.

Soria, R. (2007). *Ap&SS*, 311:213.

Soria, R. (2011). *AN*, 332:330.

Soria, R. and Ghosh, K. K. (2009). *ApJ*, 696:287.

Soria, R., Motch, C., Read, A. M., and Stevens, I. R. (2004). *A&A*, 423:955.

Stocke, J. T., Morris, S. L., Gioia, I. M., Maccacaro, T., Schild, R., Wolter, A., Fleming, T. A., and Henry, J. P. (1991a). *ApJS*, 76:813.

Stocke, J. T., Wurtz, R., and Kuehr, H. (1991b). *AJ*, 102:1724.

Strohmayer, T. E., Mushotzky, R. F., Winter, L., Soria, R., Uttley, P., and Cropper, M. (2007). *ApJ*, 660:580.

Swartz, D. A., Ghosh, K. K., Tennant, A. F., and Wu, K. (2004). *ApJS*, 154:519.

Tanaka, T. and Haiman, Z. (2009). *ApJ*, 696:1798.

Tananbaum, H., Gursky, H., Kellogg, E., Giacconi, R., and Jones, C. (1972). *ApJ*, 177:5.

Terashima, Y. and Wilson, A. S. (2003). *ApJ*, 583:145.

Terrell, N. James, J. (1972). *ApJ*, 174:35.

Titarchuk, L. and Seifina, E. (2009). *ApJ*, 706:1463.

Titarchuk, L. G., Mastichiadis, A., and Kylafis, N. D. (1997). *ApJ*, 487:834.

Tomsick, J. A., Kaaret, P., Kroeger, R. A., and Remillard, R. A. (1999). *ApJ*, 512:892.

Tremaine, S., Gebhardt, K., Bender, R., Bower, G., Dressler, A., Faber, S. M., Filippenko, A. V., Green, R., Grillmair, C., Ho, L. C., Kormendy, J., Lauer, T. R., Magorrian, J., Pinkney, J., and Richstone, D. (2002). *ApJ*, 574:740.

Trump, J. R., Impey, C. D., Kelly, B. C., Civano, F., Gabor, J. M., Diamond-Stanic, A. M., Merloni, A., Urry, C. M., Hao, H., Jahnke, K., Nagao, T., Taniguchi, Y., Koekemoer, A. M., Lanzuisi, G., Liu, C., Mainieri, V., Salvato, M., and Scoville, N. Z. (2011). *ApJ*, 733:60.

Tsunoda, N., Kubota, A., Namiki, M., Sugiho, M., Kawabata, K., and Makishima, K. (2006). *PASJ*, 58:1081.

Urry, C. M. and Shafer, R. A. (1984). *ApJ*, 280:569.

van der Klis, M. (1994). *ApJS*, 92:511.

van der Klis, M. (2005). *A Review of Rapid Variability in X-ray Binaries*. Cambridge University Press, Cambridge.

van der Marel, R. P., Cretton, N., de Zeeuw, P. T., and Rix, H.-W. (1998). *MNRAS*, 184:389.

Vasudevan, R. V. and Fabian, A. C. (2009). *MNRAS*, 392:1124.

Verolme, E. K., Cappellari, M., Copin, Y., van der Marel, R. P., Bacon, R., Bureau, M., Davies, R. L., Miller, B. M., and de Zeeuw, P. T. (2002). *MNRAS*, 335:517.

Véron-Cetty, M.-P. and Véron, P. (2006). *A&A*, 455:773.

Vestergaard, M. (2009). *astro-ph/0904.2615*. Invited contribution to the 2007 Spring Symposium on Black Holes at the Space Telescope Science Institute.

Vierdayanti, K., Mineshige, S., Ebisawa, K., and Kawaguchi, T. (2006). *PASJ*, 58:915.

Volonteri, M., Haardt, F., and Madau, P. (2003a). *ApJ*, 582:559.

Volonteri, M., Madau, P., and Haardt, F. (2003b). *ApJ*, 593:661.

Walsh, J. R., Jacoby, G. H., Peletier, R. F., and Walton, N. A. (2012). *A&A*, 544:70.

Walton, D. J., Roberts, T. P., Mateos, S., and Heard, V. (2011). *MNRAS*, 416:1844.

Wandel, A., Peterson, B. M., and Malkan, M. A. (1999). *ApJ*, 526:579.

Wang, Q. D., Yao, Y., Fukui, W., Zhang, S. N., and Williams, R. (2004). *ApJ*, 609:113.

Watson, L. C., Martini, P., Dasyra, K. M., Bentz, M. C., Ferrarese, L., Peterson, B. M., Pogge, R. W., and Tacconi, L. J. (2008). *ApJ*, 682:21.

Williams, M. J., Bureau, M., and Cappellari, M. (2010). *MNRAS*, 409:1330.

Winter, L. M., Mushotzky, R. F., and Reynolds, C. S. (2006). *ApJ*, 649:730.

Wold, M., Lacy, M., Käufl, H. U., and Siebenmorgen, R. (2006). *A&A*, 460:449.

Woo, J.-H., Treu, T., Barth, A. J., Wright, S. A., Walsh, J. L., Bentz, M. C., Martini, P., Bennert, V. N., Canalizo, G., Filippenko, A. V., Gates, E., Greene, J., Li, W., Malkan, M. A., Stern, D., and Minezaki, T. (2010). *ApJ*, 716:269.

Wu, Q. and Gu, M. (2008). *ApJ*, 682:212.

Yaqoob, T. (2012). *MNRAS*, 423:3360.

Yoshida, T., Ebisawa, K., Matsushita, K., Tsujimoto, M., and Kawaguchi, T. (2010). *ApJ*, 722:760.

Younes, G., Porquet, D., Sabra, B., and Reeves, J. N. (2011). *A&A*, 530:149.

Younis, S., Meaburn, J., and Stewart, P. (1985). *A&A*, 147:178.

Yuan, F. and Cui, W. (2005). *ApJ*, 620:905.

Yuan, F., Taam, R. E., Misra, R., Wu, X. B., and Xue, Y. Q. (2007). *ApJ*, 658:282.

Zampieri, L. and Roberts, T. P. (2009). *MNRAS*, 400:677.

Zdziarski, A. A., Gierliski, M., Mikoajewska, J., Wardziski, G., Smith, D. M., Harmon, B. A., and Kitamoto, S. (2004). *MNRAS*, 351:791.

Curriculum Vitae

Insuk Jang came to Hawaii in 1995 and was graduated from University of Hawaii. He moved to Pittsburg, Kansas for his masters in 2006 and came to George Mason University in 2008. He taught general university physics labs, both I and II, when he was in Pittsburg and in GMU.